Structural, electrical and electrochemical characterization of high frequency magnetron sputtered spinel oxide cathode films for lithium ion battery applications

Thesis submitted to

Cochin University of Science & Technology

In partial fulfillment of the requirements for the award of

Doctor of Philosophy

by

Rajive Tomy M

Department of Physics,
Cochin University of Science & Technology,
Kochi- 682022, India

July, 2012

Structural, electrical and electrochemical characterization of high frequency magnetron sputtered spinel oxide cathode films for lithium ion battery applications

Ph.D thesis in the field of material science

Author:

Rajive Tomy M

Division for Research in Advanced Materials
Department of Physics
Cochin University of Science and Technology
Cochin-682022, Kerala, India
Email: rajivetomy@gmail.com

Supervisor:

Dr. S. Jayalekshmi

Professor,
Division for Research in Advanced Materials
Department of Physics
Cochin University of Science and Technology
Cochin-682022, Kerala, India
Email: jayalekshmi@cusat.ac.in

July 2012

Department of Physics,
Cochin University of Science and Technology,
Kochi-682022, India

20th July 2012

Dr. S Jayalekshmi
Professor

Certificate

Certified that the work presented in the thesis entitled "Structural, electrical and electrochemical characterization of high frequency magnetron sputtered spinel oxide cathode films for lithium ion battery applications " is an authentic record of the bonafide research work done by Mr. Rajive Tomy M, under my guidance and supervision in the Department of Physics, Cochin University of Science and Technology, Kochi-682022, and no part of it has been included in any other thesis submitted previously for the award of any degree.

Dr. S Jayalekshmi
Supervising Guide

Declaration

I hereby declare that the work presented in the thesis entitled "Structural, electrical and electrochemical characterization of high frequency magnetron sputtered spinel oxide cathode films for lithium ion battery applications" is based on the original research work done by me under the guidance and supervision of Dr. S Jayalekshmi, Professor, Department of Physics, Cochin University of science and Technology, Kochi-682 022 and no part of it has been included in any other thesis submitted previously for the award of any degree.

Rajive Tomy M

Kochi-682 022
20th July 2012

Dedicated to

My family

Words of gratitude

"We are like dwarfs sitting on the shoulders of giants. We see more, and things that are more distant, than they did, not because our sight is superior or because we are taller than they, but because they raise us up, and by their great stature add to ours."

Throughout my education and research, I have had the pleasure of working with and learning from many wonderful individuals to whom I am deeply indebted to and thankful to have met. It is with immense pleasure that I record the acknowledgment to convey my deep sense gratitude to each and every one.

With much happiness, I place on record my deep sense of gratitude to Dr. S. Jayalekshmi, Professor, Department of Physics, Cochin University of Science and Technology, for being my supervising guide and also for giving me proper encouragement and guidance throughout the work. Her scrupulous dynamic guidance, scholastic suggestions, constant encouragement and comprehensive discussions at every stage of my work, helped me a lot to bring this thesis to a satisfactory completion.

I am extremely thankful to Prof. B. Pradeep, Head of the Department of Physics, CUSAT, Kochi, and former HODs, Prof. M.R. Anantharaman, Prof. Godfrey Louis, Prof. Ramesh Babu T, and Prof. V C Kuriakose, for providing the necessary library and laboratory facilities. I have been privileged throughout the period of my research work to have the advice and help of Prof. M. K. Jayaraj, Department of Physics, CUSAT. I take this opportunity to thank all the faculty members of the Department of Physics, CUSAT for the encouragement and timely help.

I am very much thankful to Mr. S Prasanth, MD, HHV Pvt. Ltd, Bangalore, for permitting me to use the R&D facilities at HHV Bangalore. I express my deep sense of gratitude to Dr. K Mohanchandran, VP R&D, HHV Pvt. Ltd, Bangalore, Dr. Chandan Banerjee, Dr. Ratheesh Kumar and Dr. M G Sreenivasan (HHV Pvt. Ltd, Bangalore) for their genuine approaches towards my research work. I am much indebted to them for their help and support, without which it would have been almost impossible to complete this work.

I would like to express my sincere thanks to Prof. N. Munichandraiah, Professor, IPC, IISc, Bangalore, for helping me to understand the electrochemical characterization techniques. I am also indebted to Dr. N N Sinha, IPC, IISc, Bangalore, Dr. Haridas M, Department of Physics, IISc, Bangalore, Mrs Ambili M, and Ms Nimish, Department of Instrumentation, IISc, Bangalore for their help in various stages of my work.

I would like to remember with gratitude the wonderful and fruitful moments spent with (Late) Dr. K Raveendranath, my beloved colleague in DREAM laboratory, whose attitude towards research has inspired me quite a lot. I express my sincere gratitude to Dr. M Amrithesh, Dr. Arun K J, Mr. Sreekanth Varma, Mr. Anil Kumar, Mr. Anand P B, Mr. Francis Xavier, Mrs. Sreevalsa, Dr (Mrs). Vanaja.K.A, Mrs. Jeeju, Mrs. Dhanya, Mrs. Sajimol, Mr. S Aravind and Mr. Joseph John, my other colleagues in DREAM lab, for their help, love and support.

It is my pleasure to acknowledge with gratitude the kind support extended by Dr. Reshmi R, Dr. R Manoj, Dr.Saji K J, Dr.Ajimshah, Dr.Anoop, Dr.Sreekumar, Dr.Asha, Dr.Sreekumar, Dr.Aneesh, Dr. Mini Krishna, Dr. Narayanan T N, Dr. R Jayakrishnan, Dr.Joshy N V, Dr.Vimal Kumar, MrSajeesh and Dr.Sinoy, of the Department of Physics, all through my research career. I convey my sincere thanks to the administrative, library and laboratory staff of the Department of Physics for their timely help and assistance.

I would like to thank, my colleagues at the HHV Pvt. Ltd, Bangalore for the advices and moral boosting extended to me. It is my pleasure to specially thank Mr. Sanjith K K, Mr. Rajeev R Pillai, Mr. A Suresh, Mr. U Basavaraju, Mr. Srikanth, Ms.Sunitha N H, Mrs. Srimathy N, Mr. Pavan Kumar and Mr. Naveen Kumar for their help and support.

Above all, I bend my head in humble gratitude before the Omnipotent God Almighty for all the blessings bestowed upon me.

Rajive Tomy M

Contents

Preface

Thin film battery is an electrochemical device which is used to power smaller and portable electronic gadgets and emerging technologies, such as the Micro-Electro-Mechanical Systems (MEMS). These batteries have an all solid-state construction, which includes a cathode and anode and most importantly the electrolyte in solid state, compared to the conventional type of batteries. The greatest advantage of this solid state structure is that, these batteries can withstand a wide temperature range from -20°C to 140°C and have the highest specific energy (Wh/kg) and energy density (Wh/L). These batteries can undergo thousands of charge discharge cycles without much degradation in performance. They possess the required power and energy to drive small devices, such as micro-machines, sensors, transmitters, RFID, and implanted medical components. Commercially available thin film batteries are based on rechargeable lithium ion battery technology, which is still in its early stages of development, providing much scope for future innovations in the years ahead.

The present day thin film lithium ion battery research is focused on the development of nanostructured active materials in order to improve the energy density, capacity and cycling performance. The nature of the active materials used for the assembling of the cell plays an important role in achieving these goals. Out of the three active materials involved in the assembling of an all solid state thin film cell, the cathode material significantly influences the performance of the thin film Li ion cell, The techniques used for the deposition of the various thin film layers of the cell also have high impact on its overall performance.

The most important features of an ideal cathode material include high specific energy density, good electronic conductivity and high voltage. Out of the various materials identified as suitable, the most commonly used cathode material for thin film lithium ion cell is $LiCoO_2$. Even though $LiCoO_2$ is a successful thin film cathode material, its comparatively high cost and toxic nature, call for developing cheaper and eco-friendly, alternate cathode materials. Among them $LiMn_2O_4$ is the most viable option owing to the excellent structural stability during lithium intercalation/deintercalation process, and the environmentally benign nature. The possibility of obtaining higher operating

voltages and the availability of much cheaper precursors for its synthesis make it the most favored alternate option.

The main challenges in the deposition of cathode materials in thin film form are the reproduction of stoichiometry close to the bulk material and attaining higher rates of deposition and excellent crystallinity at comparatively lower annealing temperatures. There are several methods available to develop stoichiometric thin film cathode materials including pulsed laser deposition; plasma enhanced chemical vapor deposition, electron beam evaporation, electrostatic spray deposition and RF magnetron sputtering. Among them the most versatile method is the sputtering technique, owing to its suitability for micro-fabricating the thin film batteries directly on chips in any shape or size, and on flexible substrates, with good capacity and cycle life. The main drawback of the conventional sputtering technique using RF frequency of 13.56MHz is its lower rate of deposition, compared to other deposition techniques A typical cathode layer for a thin film battery requires a thickness around one micron. To deposit such thick layers using convention RF sputtering, longer time of deposition is required, since the deposition rate is very low, which is typically 10-20 Å/min. This makes the conventional RF sputtering technique a less viable option for mass production in an economical way.

There exists a host of theoretical and experimental evidences and results that higher excitation frequency can be efficiently used to deposit good quality films at higher deposition rates with glow discharge plasma. The effect of frequencies higher than the conventional one (13.56MHz) on the RF magnetron sputtering process has not been subjected to detailed investigations. Attempts have been made in the present work, to sputter deposit spinel oxide cathode films, using high frequency RF excitation source.

Most importantly, the major challenge faced by the thin film battery based on the $LiMn_2O_4$ cathode material is the poor capacity retention during charge discharge cycling. The major causes for the capacity fading reported in $LiMn_2O_4$cathode materials are due to, Jahn-Teller distortion, Mn^{2+} dissolution into the electrolyte and oxygen loss in cathode material during cycling. The work discussed in this thesis is an attempt on overcoming the above said challenges and developing a high capacity thin film cathode material.

Chapter 1 presents a brief description of the fundamentals of electrochemical cell and its working. It gives a brief introduction to the various battery technologies available today and describes the fundamentals of the lithium ion battery technology and its advantages. The basics of thin film batteries and the materials used for thin film battery applications are also addressed in detail. A detailed discussion on the advantages of the spinel oxide cathode materials with special emphasis on $LiMn_2O_4$as a suitable cathode material for thin film lithium ion cells, follows subsequently. The challenges faced by $LiMn_2O_4$ as a cathode material and the ways to overcome these challenges are also dealt with. The motivation for carrying out the present investigations and the objectives of the research work also form a integral part of this chapter.

Chapter 2 gives a detailed description of the thin film deposition techniques and the various characterization tools employed in the present work. The important aspects of the RF magnetron sputtering under high excitation frequency and biased sputtering are discussed. The details of assembling and working of an in-house built electrochemical characterization system for battery testing form one of the highlights of this chapter.

Chapter 3starts with the details of the synthesis of pristine as well as doped $LiMn_2O_4$ targets for sputtering and their characterization. Details of the experimental set up for high frequency magnetron sputtering and the optimization of the various sputtering parameters, for realizing good quality, sputtered films of $LiMn_2O_4$ cathode materials are dealt with subsequently.

The structural, electrical and electrochemical characteristics of the ‘as deposited’ Li-Mn-O films grown by high frequency RF (27.12MHz) sputtering are detailed in chapter 4. The dependence of the cathode film properties on sputtering pressure has been investigated in depth. It is observed that sputtering under high pressure leads to lithium deficiency in the sputtered films which results in inferior electrical and electrochemical film characteristics.

The as deposited $LiMn_2O_4$cathode films without post annealing are found to be amorphous in nature which leads to inferior film properties. Hence post annealing of the sputtered films is mandatory. This chapter also gives an

account of the detailed post annealing studies of the films deposited at lower pressures. Based on the detailed analysis of the structural, electrical and electrochemical characteristics of the sputtered films on the annealing temperature, the optimum annealing temperature has been identified. The electrochemical characteristics of the half cell devices assembled using the suitably annealed films are found to be quite promising. The present studies emphasize the significance of post annealing on improving the structural, electrical and electrochemical characteristics of sputtered Li-Mn-O thin films.

Chapter 5 deals with the detailed analysis of the effect of in-situ substrate bias on the structural, electrical and electrochemical characteristic of both the 'as deposited' and post annealed Li-Mn-O films grown by high frequency RF (27.12MHz) magnetron sputtering. The presence of substrate bias has been found to promote ordered columnar growth perpendicular to the substrate for both as deposited and post annealed films. The presence of low substrate bias improves the electrical and electrochemical characteristic of Li-Mn-O films significantly. One of the most significant observations is that the presence of substrate bias can considerably reduce the required optimum annealing temperatures for achieving best film properties.

In spite of the improved structural and electrochemical characteristics achieved by through post annealing treatment and application of substrate bias the high frequency sputtered Li-Mn-O films suffer from capacity fading after repeated charge discharge cycling process. One of the possible methods to overcome this challenge is to substitute some of the manganese ions with suitable transition metal ions. Chapter 6is devoted to the detailed studies on the effect of Zn and Ni doping on the structural, electrical and electrochemical characteristics of high frequency magnetron sputtering technique. One of the highlights of these studies is the observation that Zn and Ni doping can almost eliminate the Jahn-Teller distortions suffered by Li-Mn-O films, at temperature close to room temperature. The doping is also found to improve the cycling performance of the sputter deposited Li-Mn-O films.

The highlights of the present investigations are summarized in chapter 7. The prospects of future investigations based on the results of the present work are also emphasized in this chapter.

List of publications

Publications in peer reviewed journals

1. **Rajive Tomy M**, Anil Kumar K M, Anand P B and S Jayalekshmi, Effect of annealing on the electrochemical properties of the Li-Mn-O thin films, prepared by high frequency RF magnetron sputtering. Journal of Physics and Chemistry of Solids, 73 (2012) 559–563. doi: 10.1016/j.jpcs.2011.12.008

2. **RajiveTomy M**, Anil Kumar K M, Anand P B and S Jayalekshmi, Effect of annealing on structural and electrical properties of the Li-Mn-O thin films, prepared by high frequency RF magnetron sputtering, Journal of Physics and Chemistry of Solids. 72 (2011) 1251 doi:10.1016/j.jpcs.2011.07.018

3. **RajiveTomy M**, Anil Kumar K M and S Jayalekshmi, A Cost effective, fully automated electrochemical Characterization setup for thin film LI-ion battery research, Journal of Instrument Society of India, Vol 41, No. 2, June 20

4. **RajiveTomy M**, Anil Kumar K M, Anand P B and S Jayalekshmi, 'Development of Li-Mn-O thin films by high frequency RF magnetron sputtering for lithium ion battery applications' (Under review)

5. **RajiveTomy M**, Anil Kumar K M, Anand P B and S Jayalekshmi, 'Effect of substrate bias on the physical and electrochemical properties of Li-Mn-O films prepared by high frequency magnetron sputtering.', (communicated)

6. **RajiveTomy M**, Anil Kumar K M, Anand P B and S Jayalekshmi, 'Effect of transition metal doping on the physical and electrochemical properties of Li-Mn-O films prepared by high frequency magnetron sputtering.', (communicated)

Contributed publications

7. S. Thomas Lee, K. Raveendranath, **M. RajiveTomy**. Paulraj, S. Jayalekshmi& J. Ravi, Evidence of band structure modification of $LiMn_2O_4$ upon lithium deintercalation by photoacoustic spectroscopy, Applied Physics Letters 90, 1 (2007) (doi:10.1063/1.2728033)

8. S Thomas Lee, K Raveendranath, **Rajive M Tomy**, Nibu A George, S Jayalekshmi and Jyotsna Ravi "Evidence of band structure modification due to Jahn–Teller distortion in LixMn2O4 by photo acoustic

spectroscopy", J. Phys. D: Appl. Phys. 40 (2007) 1–4 (doi: 10.1088/0022-3727/40/12/038)

9. S. Thomas Lee, K. Raveendranath, **M. RajiveTomy**, Paulraj, S. Jayalekshmi& J. Ravi "Effect of Lithium Concentration on the Thermal and Optical Properties of $Li_xMn_2O_4$ Investigated Using Photoacoustic Technique", Physical Rev. B 76, 115112 2007 (doi: 10.1103/PhysRevB.76.115112)

10. K. Raveendranath, **Rajive M. Tomy**, S. Jayalekshmi, R. V. Mangalaraja, J. Ravi and S. Thomas Lee "Evidence of Jahn-Teller Distortion in Li_xMn2O4 by Thermal Diffusivity Measurements" Applied Physics A, Volume 90, Issue 3, pp.437-440 (doi: 10.1007/s00339-007-4294-0)

Conference proceedings

1. **M. RajiveTomy**, R. Reshmi, K. Raveendranath, S. Jayalekshmi, M.K. Jayaraj, Optical absorption studies on $LiMn_2O_4$ films prepared by Pulsed Laser Deposition, presented at the 9^{th} international conference on laser ablation, 'COLA-07', September 24-28, 2007, Spain

2. **M. RajiveTomy**, K.Raveendranath, Rini Thomas, S. Jayalekshmi "A comparative study of electrical properties of $LiMn_2O_4$ and its de-lithiated form" presented at the 17th Annual General Meeting, Materials Research Society of India (MRSI) Conference, February 13-15, 2006, Lucknow University.

3. **M. RajiveTomy**, K.C. Haridas, K. Raveendranath, S. Jayalekshmi, "Effect of Ag^+ ion concentration on the optical absorption and photoluminescence observed in the silver–glass nanocomposites", presented at the International Symposium for Research Scholars on Metallurgy, Materials Science & Engineering , December 18-20, 2006, IIT Madras.

4. **RajiveTomy M**, Anil Kumar K M, S. Jayalekshmi, Fully Automated Charge-Discharge Cycling and Cyclic Voltametry Measurements Setup Using Keithley 2400 and LabVIEW, for Lithium Ion Battery Research, National instruments- VI Mantra 2009

5. K. Raveendranath, S. Thomas Lee, Jyotsna Ravi, **M RajiveTomy**, and S. Jayalekshmi, "Evidence of Jahn-Teller Distortion in $Li_xMn_2O_4$ by Thermal Diffusivity Measurements", to be presented at International

conference on advances in energy research(ICAER), December 12-14, 2007 Indian Institute of Technology, Bombay.

6. S. Thomas Lee K. Raveendranath, **Rajive M. Tomy**, R. V. Mangalaraja, S. Jayalekshmi&Jyotsna Ravi "Spectroscopic Evidence of Band Structure Modification in $Li_xMn_2O_4$ due to Jahn-Teller Distortion" to be presented at International conference on advances in energy research(ICAER), December 12-14, 2007 Indian Institute of Technology, Bombay

7. K.Raveendranath, **M. RajiveTomy**, S.Jayalekshmi, Investigations on the Electrical properties of $Li_xMn_2O_4$ Nanocomposite, presented at the National conference on current trends in material science (CTMS-07), march 25-27, 2007 Christian college Chengannur, Kottayam, India.

8. K.Raveendranath, **M. RajiveTomy**, S.Jayalekshmi, "Synthesis, Characterization and Electrical properties of a Novel High Energy Density $LiNiPO_4$Nanocomposite", presented at the national conference on smart electro ceramics (NCSE-2007), March 8-9 2007, C-MET, Thrissur, Kerala

9. K. Raveendranath, S. Thomas Lee, Jyotsna Ravi, **Rajive M. Tomy**, and S. Jayalekshmi "Determination of Band Gap of Pure and Carbon Nanotubes Doped $LiFePO_4$ by Diffuse Reflectance Measurements" National Conference on New Horizons in Theoretical and Experimental Physics"(NHTEP) October8-10, 2007, Cochin University of Science & Technology, Kochi

10. K. Raveendranath, **Rajive M. Tomy**, S. Thomas Lee, Jyotsna Ravi, , and S. Jayalekshmi"A comparison of Electrical transport Properties of the important battery material $LiMn_2O_4$ and $LiFePO_4$"International Conference on Solar cells IC-SOLACE 2008, 21-23 January 2008 Cochin University of Science & Technology, Kochi

11. S. Thomas Lee, K. Raveendranath, **Rajive M. Tomy**, S. Jayalekshmi and Jyotsna Ravi "Optical absorption spectrum of $Li_xMn_2O_4$ by Photo Acoustic spectroscopy "International Conference on Condensed Matter Physics (ICCMP-2007) 25-28 November 2007 Jaipur, Rajasthan

Chapter 1

Introduction to thin film battery technology

Abstract: This chapter starts with a brief account of the history of battery technology and then evolves into the fundamental working principles of rechargeable lithium ion cells, along with their advantages, shortcomings and applications. The merits of thin film lithium ion cells and the various electrode materials used to realize them in practice are addressed subsequently. The objectives of the present investigations and the motivation behind the work also form an integral part of the present chapter.

1.1 Introduction

United Nations has estimated that the world population will increase to about 10 billion people by 2050. This explosion in population will trigger the global energy crisis despite all efforts concerning the rational use of energy. The main reason for this is the rapid development of innovative technologies and growing environmental concerns. The mounting concern over global warming and air pollution has triggered the thought of finding suitable substitutes for internal combustion engines by alternative power sources. These circumstances have fashioned vast interest in the development of more efficient, pollution free, and safe power sources.

Incidentally, electrochemical power sources such as batteries and fuel cells are among the most promising alternative energy sources. These systems will provide a clean energy and decrease our reliance on fossil fuels. But these systems are still under developing stage and a lot of research has to be done to fulfill the future energy requirements. In the present day scenario, the quest for energy storage systems that are compact, lightweight, powerful and green is on the soar with the worldwide proliferation of portable electronics devices, including notebook and tablet computers, PDAs, camcorders, mobile phones, digital cameras and specialized devices like medical implants and MEMS. Here comes the importance for the development of batteries as portable energy devices. Despite the remarkable growth in commercializing the different battery technologies worldwide, the science underlying these technologies is often criticized for its slow progress. The present day battery technology provides only a limited power density and has shown only slow improvement. Moore's Law predicts that computing capability is doubling in capacity every two years or so. But increases in battery capacity have not kept pace. In the present scenario, the progress in battery capacity is in the neighborhood of 10% on average every year [1].

As the demand for better, safer and long lasting batteries continues, researchers around the globe are looking forward to the technologies like nanotechnology for a breakthrough in this field. It has been reported that the three-dimensional nanostructured thin film batteries can significantly increase surface area, and

therefore bump up the energy storage capacity. These batteries have much longer shelf life and can be charged 10 to 100 times faster.

1.2 Basics of electrochemical cell

The electrochemical cell converts the chemical energy stored in the active materials into electrical energy or vice-versa by electrochemical oxidation-reduction reactions. An electrochemical cell consists of three major components. The anode (negative electrode) undergoes oxidation during the electrochemical reaction and gives up electrons to the external circuit. The cathode (positive electrode) undergoes reduction during the electrochemical reaction and accepts electrons from the external circuit. The third component is the electrolyte which acts as a medium for the transfer of electric charge, as ions, between the anode and the cathode. The most important criterion for an electrolyte is that, it should be a good ionic conductor and an electronic insulator, while the electrodes used are preferred to be both good ionic and electronic conductors. Schematic diagram of an electrochemical cell is shown in figure 1.1.

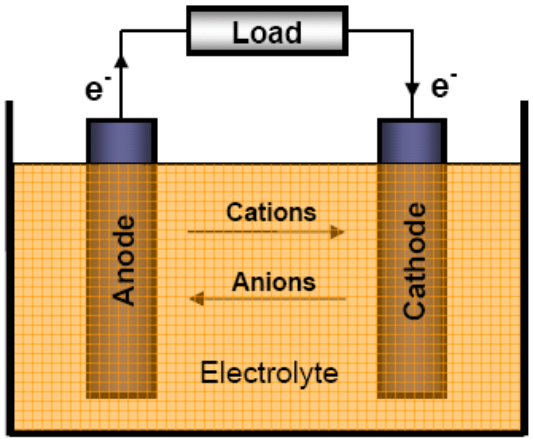

Fig.1.1: Schematic diagram of an electrochemical cell [139].

Electrochemical cells are broadly classified into two categories depending upon the reaction mechanisms. The first type is termed as Electrolytic cell and the second as Galvanic (or Voltaic) cell [2].

In an electrolytic cell, an external voltage is applied across the electrodes so that the electrochemical reaction takes place inside the cell. Electrolytic process is used in electroplating, electrolytic synthesis, and while charging a secondary battery. In a galvanic cell, the reactions occur spontaneously at the electrodes, resulting in the flow of electrons through the external circuit or load. Basically a voltaic cell converts chemical energy into electrical energy. Batteries and fuel cells belong to this category.

A battery is an energy storage device that directly converts the chemical energy stored in the active materials into electrical energy by electrochemical oxidation/reduction reactions. Based on the reversibility of the electrochemical processes, batteries can be broadly classified into (a) primary or non-rechargeable batteries and (b) secondary or rechargeable batteries. In primary batteries, the active materials undergo an irreversible chemical reaction. On the other hand, they exhibit reversible chemical reactions in secondary batteries.

A battery can deliver certain cell potential depending on the combination of the electrode materials and the type of chemical reactions involved. The basic approximation for calculating the cell voltage (V_{op}) of a battery is given as the difference between the cathode potential (E_c) and the anode potential (E_a).

$$V_{op} = E_c - E_a \qquad (1.1)$$

The cathode/anode potential of each individual electrode is the standard electrode potential with reference to the standard hydrogen electrode (SHE). In practice, the actual battery potential may show a lower and varying potential depending on the operating conditions. This is because, a small fraction of the energy delivered by the battery is lost as waste heat due to polarization losses in the cell.

The energy stored in a battery, is called the battery capacity. If a battery delivers a current of ‘I’ amperes for ‘t’ seconds, then the capacity (Q) of the battery is given by

$$Q = I \times t \text{ (in Ampere second)} \qquad (1.2)$$

The theoretical capacity of a cell is determined by the amount of active materials in the electrodes of the cell. It is expressed as the total quantity of electronic charge involved in the electrochemical reaction and is defined in terms of coulombs or ampere-hours. The capacity of a battery expressed in "ampere-hour" is directly associated with the quantity of electricity obtained from the active materials. Theoretically, 1 gram-equivalent weight of material will deliver 96,487 C or 26.8 Ah. (A gram-equivalent weight is the atomic or molecular weight of the active material in grams divided by the number of electrons involved in the reaction.)

The Faraday constant (F), which is the capacity of 1 mol of electrons is calculated as

$$1\ F = e\ N_A = 96487\ C/mol = 26.8\ Ah \qquad (1.3)$$

where 'e' is the electronic charge and 'N_A' is the Avogadro's number.

1.3 Overview of battery technology

1.3.1 Brief history.

The earliest available record on the use of battery is from Bagdad, where archeologists have uncovered a 2500 year old electrochemical cell that would qualify as a battery under today's definition [3].The first modern battery was discovered by Alessandro Volta, following the footsteps of the experiment conducted by Luigi Galvani. The first cell is generally known as Volta cell. A Volta cell consists of a stack of small disks, alternating zinc and copper, with a disk of leather saturated with salt solution separating each part of metal disks. The Volta cell (also known as Voltaic pile), generates a substantial electrical current and can be considered as the first practical battery [4].

Later, the experiments performed by Faraday on Voltaic pile ultimately led to derive the quantitative laws of electrochemistry. These laws form the basis of modern electrochemistry. Various commercially significant primary cells were produced based on Faraday's theoretical contribution [5]. Following the

footsteps of Voltaic pile, the British chemist, Daniel, introduced an improved form of electric cell consisting of copper and zinc in sulfuric acid. The Daniel cell was found to deliver sustained currents during continuous operation far more efficiently than Volta's device. Improved versions of this device were in use for long time for telegraphic applications.

None of the above mentioned battery technologies remain in use today. The first enduring invention came from Gaston Planté, of France, who developed the lead-acid cell in 1859. This device was the first successful rechargeable storage cell. Even today the same electro-chemistry, refined mostly in packaging, is used in automobile batteries and the gelled-electrolyte batteries used in uninterruptible power systems.

The next major development was the invention of wet cell by French engineer Georges Leclanché. Leclanché cells consist of a cathode of manganese dioxide mixed with carbon and an anode of metallic zinc. The electrolyte is a solution of ammonium chloride in which the electrodes are immersed. In its original wet form, the Leclanché electrochemistry is neither portable nor practical. But this basic chemistry was employed in developing the dry cell which was introduced in the late 1880s, which continues to flourish even today.

During the last century, only three battery technologies, the MnO_2 primary battery and the secondary batteries based on lead acid and nickel were in use. These old battery technologies are close to reaching their technical limit and need to be replaced with a newer technology.

1.3.2 Present day battery technology.

Modern day battery technologies use a variety of chemical systems. The development of the chemistry behind these technologies is a consequence of the research and development activities in the 20th Century. The scientific knowhow developed enables one to understand the principles of battery design and operation. Present efforts in battery design are focused on making the optimal chemistry work in practical cells. The diversity in battery technology results from each having distinct benefits for particular applications [6].

The most reliable battery technologies which form the back bone of today's portable power systems are zinc carbon , lead acid , nickel-cadmium, nickel-metal hydride and lithium ion batteries. In the following section, a brief description of the present day, major battery technologies is analyzed.

Carbon-zinc cells are perhaps the most common batteries in the world, known under a variety of names such as dry cells or flashlight batteries. In the basic carbon-zinc cell, the "carbon" in the name is a cathode current collector which is in the form of a carbon rod in the center of the cell. The actual material of the cathode is a mixture of manganese dioxide, carbon conductor and electrolyte. The zinc serves as the anode and forms the metal shell of the battery. The electrolyte is a complex mixture of chemicals that typically includes ammonium chloride, manganese dioxide, and zinc chloride. Another variety of carbon-zinc battery is the alkaline cell which uses a mixture of strong alkaline potassium hydroxide as electrolyte, has a higher energy density and longer shelf-life, with the same voltage. The main draw back with the carbon-zinc technology is that these cells cannot be recharged because the chemical reactions in the cell cannot be readily reversed. The energy density is low, and so the battery is limited for certain types of applications only. Other prominent primary battery technologies are Zinc-HgO, Zinc-air, Li-SO_2, and Li-MnO_2

Lead acid batteries offer the technology of choice for automotive applications because they are robust, tolerant to abuse, tried and tested and are of low cost. Other advantages include the tolerance to overcharging, low internal impedance, permission of very high currents, indefinite shelf life if stored without electrolyte etc. These batteries are generally too big and heavy and they suffer from a shorter cycle life and typical usable power is down to only 50% depth of discharge. Most importantly the power density (Wh/kg) is only half of that of the carbon zinc batteries.

In most of the consumer electronic equipment used during the last decade, the most popular choice of rechargeable batteries is nickel cadmium cells. These batteries use nickel and cadmium as cathode and anode respectively. Compared to the contemporary technology, their most endearing characteristic is the capability to withstand a large number of charge/discharge cycles, without much deterioration. Nickel-cadmium cells are relatively lightweight and have a

good energy storage density(about half that of alkaline cells). Its main drawback is the toxicity of the cathode material cadmium, and the memory effect.

Certain metal alloys have the capability to store atomic hydrogen 1000 times more than their own volume. These metallic alloys are termed hydrides and typically are based on compounds such as $LiNi_5$ or $ZrNi_2$. In a typical Nickel-Metal Hydride battery system, hydrides provide a storage sink of hydrogen that can reversibly react in battery cell chemistry. Additionally, hydrogen is so much superior as a cathode material that cells based on nickel and metal hydrides have a storage density about fifty percent higher than nickel-cadmium cells. The cells based on nickel and metal hydrides are not faultless and their main drawback is higher self-discharge rate than nickel-cadmium cells.

Lithium is the most chemically reactive metal and offers the foundation of present day portable energy systems. Nearly all high-density storage systems used today employ lithium because it has an inherent chemical advantage. Lithium has a specific capacity to store 3860 Ampere-hours per kilogram (Ah/kg) of mass compared to 820 Ah/kg for zinc and 260 Ah/kg for lead. By coupling with various anodes, a typical lithium battery can produce voltages between 1.5V to 3.6 V per cell, which is higher than the voltage obtained using any other chemistry. Due to safety problems lithium metal cannot be used directly in a battery. So manufacturers have come up with a cell design which uses lithium in its ionic state rather than lithium metal.

In 1991, the Sony Corporation commercialized the first lithium-ion battery. In lithium-ion cells, the lithium ions are absorbed into the active material of the electrodes rather than being plated out as metal. The typical lithium-ion cells use carbon for its anode and lithium cobalt dioxide as the cathode. The electrolyte is usually based on a lithium salt in solution. Lithium batteries offer higher storage densities than nickel-metal hydride cells and are devoid of any memory effect. On the counter, current lithium cells have a higher internal resistance than nickel-cadmium cells and consequently cannot deliver high currents. It requires protection circuit to maintain voltage and current within safe limits and is expensive to manufacture.

1.4 Fundamentals of lithium ion battery technology.

1.4.1 Overview of lithium battery technology

The basic working principle behind the battery is the conversion of chemical potential energy into electrical energy. This means, each time the battery transfers an electron, it consumes a small portion of its chemical potential energy. When all the stored chemical potential energy is exhausted, electrical energy released from the battery dies out.

The chemical potential energy stored in the battery arises due to the electronic transfer between the battery materials, i.e. anode and cathode. The anode and cathode of a battery is made up of two different types' atoms/compound. The electron affinity for the valence electrons for each of this atoms/compound is different, which result in release of energy during electrochemical interaction. More precisely, an atom that binds its valence electrons quite strongly, and requires an electron to complete octet, may extract electrons from another atom that binds them relatively weakly. In general, the electrons move from one atom to the other and some potential energy is released. The tendency of an atom to attract electrons depends on its electronegativity, which means the more strongly an atom attracts electrons, the higher its electronegativity. So these differences in electron affinity enable batteries to produce electricity by transferring electrons from atoms with low electronegativities to ones with high electronegativities. This process is the key source of a battery's energy.

Metallic lithium is the lightest metal and shows extremely low electronegativity, which means it gives up an electron so easily that it reacts violently with many chemicals. These features of the metallic lithium can be utilized in designing a battery with very high energy density. In a typical primary lithium cell, the negative electrode is lithium metal and the positive electrode could be some salts with suitable properties that undergo electrochemical reactions with lithium atoms. The electrochemical reaction enables the release of chemical potential energy as electrical energy. The main advantage for the use of lithium metal in batteries is its high electrochemical

potential (–3.04 V) and low equivalent weight (46.94 g/mol). As a result, it offers a high energy density of the order of 3.86 Ah/g.

The first primary (non rechargeable) battery using lithium metal was demonstrated in the 1970s. These cells had very high capacity and variable discharge rate, and rapidly found applications as power sources for calculators, watches or for implantable medical devices.

During the same period, with the invention of intercalation compound, which reacts reversibly with the alkali metals, crucial developments were made in the area of high energy rechargeable lithium batteries. Following the breakthrough, in 1972, Exxon come up with a lithium rechargeable cell which uses TiS_2 as the positive electrode, Li metal as the negative electrode and lithium per-chlorate in dioxolane as the electrolyte [7, 8]. Even though TiS_2 has a favorable layered-type structure with good features as a lithium ion intercalation compound, the system is not feasible. It was found that cycling causes changes on the lithium electrode, due to the formation of uneven (dendritic) Li growth as the metal was replated during each consequent discharge–recharge cycle, which led to explosion hazards [1].

Due to the inherent instability of the lithium metal, especially during charging, focus of research shifted to a non-metallic lithium battery, which uses only lithium ions. Compared with lithium metal, lithium ion batteries have slightly lower energy density but are safe, provided certain precautions are met when charging and discharging. In 1991, the first Li-ion battery was commercialized by Sony Corporation.

1.4.2 Working of lithium ion battery.

Similar to any electrochemical power sources, the modern day lithium ion battery consist of three main components, a cathode, an anode and the electrolyte. The cathode material is a lithium metal oxide, while an insertion compound like carbon/graphite is used as the anode, instead of metallic lithium [9]. The electrolyte material can be an organic liquid containing dissolved electrolyte salts or a polymer electrolyte.

A lithium ion rechargeable battery is known as a rocking chair battery due to the two-way motion of lithium ions. The lithium ions are shuttled between the anode and the cathode through the electrolyte. During charging cycle, the lithium ions undergo deintercalation from the cathode in to the electrolyte, concurrently lithium ions intercalate from the electrolyte in to the anode. While in discharge process, lithium ions are intercalated in to the cathode via electrolyte. The Intercalation/deintercalation is the process of inserting lithium ions into the structural matrix of the electrodes. The insertion process consists of an electrochemical reaction by which the electrons and lithium ion are incorporated into or extracted from a solid matrix. During this process the core matrix structure will remain intact and such reactions are called topotactic reactions and the materials for which such reversible reactions proceed are called insertion compounds.

During deintercalation/intercalation processes, the shift in charge, due to Li+ movement is compensated by electron flow through the external circuit. The topotactic Li-intercalation mechanism is the prime factor for the material's application as an electrode in a rechargeable battery. It is believed that Li is fully ionized in most lithium-metal oxides and donates its electron to the host without affecting their structural aspects much. This substantial charge transfer to the anion is responsible for the voltage difference between oxides and sulphides. This makes it possible to control the band filling of the host material by varying the Li content electrochemically. [10-12]

The basic working of the lithium ion battery scheme proposed by John Bannister Goodenough using layered Li_xMO_2 (where M is Co, Ni, or Mn) as cathode and carbon/graphite as anode is shown in figure 1.2. In this scheme the cathode (i.e. positive electrode), is the original source of lithium ions. A Li-ion cell in the as assembled state is in its discharged state. Li+ ions are included in the cathode material ($LiCoO_2$ for example), and they need to be de-intercalated from the cathode to the anode in order to charge the cell. This means that, during charging, lithium ions (Li+) travel from the positive to the negative electrode (i.e. anode), creating the compounds $Li_{1-x}CoO_2$ and Li_xC_6. When the cell is discharged, Li^+ ions are intercalated into the positive electrode, leading to the original situation [13].

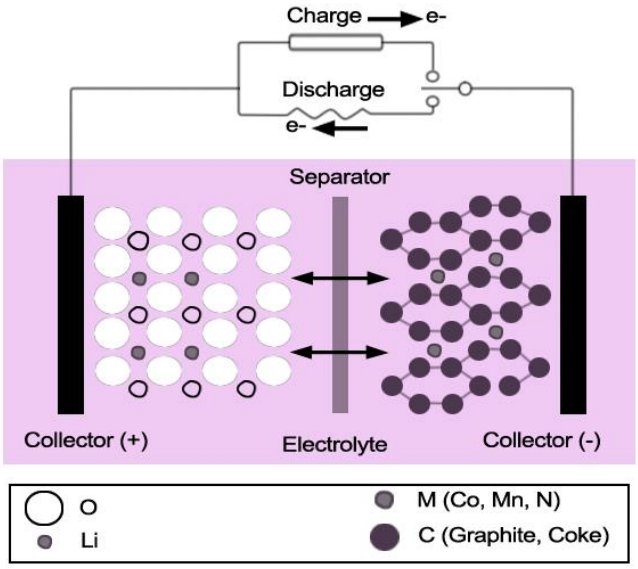

Fig.1.2: Schematic diagram of the charge and discharge processes in a lithium ion cell.

During the charge process the positive electrode is oxidized, and the negative electrode is reduced following the reactions given below:

$6C + xLi^+ + xe^- \rightarrow Li_xC_6$ (anode)

$Li_{1-x}CoO_2 + xLi^+ + xe^- \rightarrow LiCoO_2$ (cathode)

In reality, not all Li^+ ions are transported back and forth, i.e. $0 < x < 1$. In a typical lithium ion cell, the electrodes are separated by a polymeric membrane which is permeable to the electrolyte but electrically isolate the anode and the cathode [14]. The electrolyte is chosen in such a way that it only allows transfer of Li ions between the anode and cathode while any electron transport is blocked. In most applications, the electrolyte is in the liquid form, although glasses and solid polymers are being investigated as more flexible alternatives.

In general, for a lithium ion battery, electrochemical reactions can be separately studied as half cell reaction processes corresponding to the cathode or anode. It means that at the anode, the half cell reaction involving the oxidation of a given species will take place, while at the cathode another half cell reaction involving

the reduction of the other species will occur. During the oxidation half cell reaction, the species undergoing oxidation release an electron to the external circuit. This electron enters the other end of the battery, thereby reducing the other species at the opposite electrode.

Each of the half cell reaction is related to a standard electrode potential which can be calculated from the thermodynamic data of the reaction. For a reaction which is under equilibrium conditions, the electrode potential E^o is given by the equation,

$$E^o = \frac{-\Delta G^o}{nF} \quad (1.4)$$

where, '$-\Delta G^o$' is the standard Gibbs free energy,
'n' is the number of electrons, F is the Faraday constant.

Since it is impossible to measure individual electrode potentials in an absolute sense, they are measured with reference to a standard electrode. The standard electrode normally used for this purpose is the standard hydrogen electrode(SHE), kept at the temperature of 25°C and the pressure of 1 bar, and all the species are at unity activity. For other non-standard conditions, the Nernst equation can be used to calculate the potential of the half-reactions (*E*) at equilibrium:

$$E = E^o - \frac{RT}{nF}\sum lna_i^{v_i} \quad (1.5)$$

Where, a_i is the activity of the relevant species, v_i is the stoichiometric coefficient, R is the universal gas constant and T is the absolute temperature.

The cell voltage of an electrochemical cell is calculated from the electrode potentials (reduction potentials) of the half-reactions [15]. The overall theoretical cell voltage, ΔE^0or U^0, is obtained by subtracting the negative electrode potential, $E^{0,(-)}$, from the positive electrode potential, $E^{0,(+)}$:

$$U^0 = \Delta E^0 = E^{0,(+)} - E^{0,(-)} \quad (1.6)$$

It is clear from equation (1.6) that a cell with a higher cell voltage can be realized by combining two half electrode systems with potentials opposite in nature. Lithium ion cells have a relatively broad potential window, with an extreme negative potential at the anode and high potential at the cathode.

Standard potential ranges of some of the well studied electrodes versus. Li metals are given in figure1.3.

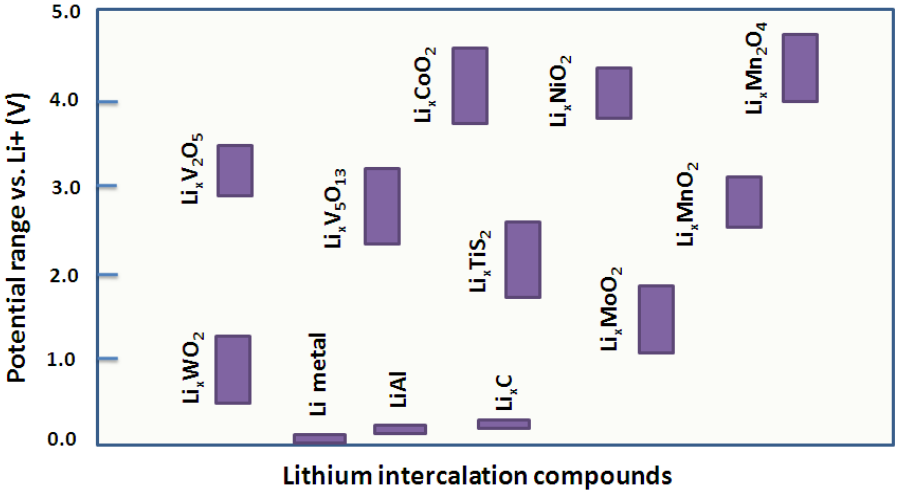

Fig. 1.3: Potential ranges of different electrode materials versus Li [15].

Theoretical values of the energy available can be calculated from the thermodynamics of the electrochemical cell reaction. The maximum energy which can be extracted from the cell reaction is the free energy of the reaction, ΔG. This means, the amount of energy released depends on the choice of the electrode. A higher amount of energy can be realized by choosing electrodes with the largest difference of electrochemical potential, μ [16].

1.4.3 Standard battery terminology.

In order to study and evaluate the properties of the electrodes used in a secondary battery, International Union of Pure and Applied Chemistry (IUPAC) has introduced some standards and guidelines. Brief descriptions of these guideline are given below [17].

Charge capacity Q (SI unit: mAh or C)

The charge capacity is the total amount of charge obtainable from a cell.

$$Q = \int I(t)dt \qquad (1.7)$$

Specific charge q (SI unit: mAh g^{-1} or Ah kg^{-1} or C kg^{-1})

The specific charge is the total charge obtainable under specified discharge conditions from a practical cell in one discharge cycle divided by the total mass of the cell (m_b).

$$\left|\frac{Q}{m_b}\right| \qquad (1.8)$$

The specific charge is often incorrectly called charge density/ specific capacity.

Specific energy w (SI unit: Wh kg^{-1} or J kg^{-1})

The specific energy is the total electrical energy (W_c) obtainable from a cell in one discharge cycle divided by the mass of the respective cell (m_b). This quantity is often incorrectly called energy density.

$$w = \frac{W_c}{m_b};\ W_c = \int U(t)\, I(t) dt \qquad (1.9)$$

Energy density W_V (SI unit: Wh dm^{-3} or J dm^{-3})

The energy density is the total electrical energy obtainable (W_c) from a cell under specified discharge conditions divided by the volume of the cell.

$$W_V = \frac{W_c}{V} \qquad (1.10)$$

Specific power *p* (SI unit: W kg^{-1})

The specific power is the capability to deliver power per mass of a primary or secondary battery. The specific power of a cell depends on the discharge current and decreases during discharge. The specific power is often incorrectly called power density.

$$p = \frac{IU^o}{m_b} \qquad (1.11)$$

Power density P_v (SI unit: W dm^{-3})

The power density is the power divided by the volume of the cell

$$P_V = \frac{IU^o}{V} \qquad (1.12)$$

Coulombic Efficiency, Φ_Q (SI unit: %)

For secondary cells, the Coulomb efficiency represents the ratio of charge released during the discharge (Q_{dis}) to the charge necessary for charging the battery (Q_{ch}).

$$\mathbf{\Phi}_Q = \frac{Q_{dis}}{Q_{ch}} \times 100 \qquad (1.13)$$

Both Q_{dis} and Q_{ch} are obtained by integrating the respective currents over the discharging and charging time, respectively. They depend on the conditions for charging and discharging.

The charge-discharge rate C-rate(SI unit: h^{-1})

When electrochemically cycling a cell, the term charge-discharge rate or C-rate ($C/\Delta t$) is often employed to explain the time frame for either one full charge or discharge. *C* denotes either the theoretical charge capacity of a cell or battery (Ah) or the nominal capacity of a cell or battery. A 'C' rate of C/10 means that the cell is charged/discharged with a current which theoretically allows a full charge/discharge of the cell in 10 hours.

Irreversible capacity loss (SI unit: %)

It is also important to define how much capacity is lost after each cycle. Irreversible capacity loss is therefore explained by the following equation:

$$IrreversibleCap.Loss = \frac{Char.cap.(n) - dischar.cap.(n)}{chargecap.(n)} \times 100 \qquad (1.14)$$

1.5 Thin film lithium ion battery technology.

The new millennium has witnessed tremendous development in the field of information technology globally. As a result of this information explosion and growing environmental concerns, modern society is now more aware of the importance of clean energy. As more and more people have access to the modern way of living, the requirement of energy is soaring high. One of the most formidable challenges faced by the contemporary society is the practical

realization of low cost and environmentally friendly energy conversion and storage systems.

The recent developments in nanoscience and technology have marked significant growth in the battery technology. Nanomaterials in thin film form have attracted enormous interest in modern times because of their remarkable mechanical, electrical and optical properties. The astounding developments in the microelectronics industry, have paved ways to develop feasible thin film battery technology with reduced dimensions and higher capacity.

Thin-film battery technology has gained significance due to the prospects of powering smaller electronic devices such as transmitters, wireless sensors, static RAM backup devices, real-time clocks, and implantable medical devices. This technology has the inherent potential to revolutionize the size of electronic equipments, by reducing their size and weight. Understanding the potential of this technology, many companies have invested huge funds to develop suitable thin-film batteries for their products. RFID (radio frequency identification) application is anticipated to drive this market to a large extent, followed by sensors and smart card solutions. The thin-film battery technology has the potential to generate huge amount of revenues once these batteries are made widely available on a commercial scale at an affordable price. The environment-friendliness of this technology is an added advantage, which promotes widespread usage of thin film batteries.

Thin film battery` is basically an electrochemical cell with an all solid-state construction, which includes the cathode (positive electrode), the anode (negative electrode) and most importantly the electrolyte in solid state, contrary to the conventional liquid/gel type. The greatest advantage of this solid state structure is that, these batteries can withstand a wide temperature range, extending from -20°C to 140°C. Another advantage is that this structure has got the highest specific energy (Wh/kg) and energy density (Wh/l). Moreover, these batteries can undergo thousands of charge discharge cycles without much degradation in performance. On comparison with the available technologies, thin film lithium battery technology is considered as the most competitive power storage technology owing to its high volumetric and gravimetric energy density, superior power capability and design flexibility. A comparison of the

volumetric and gravimetric energy density of various available technologies [18] is depicted in figure 1.4.

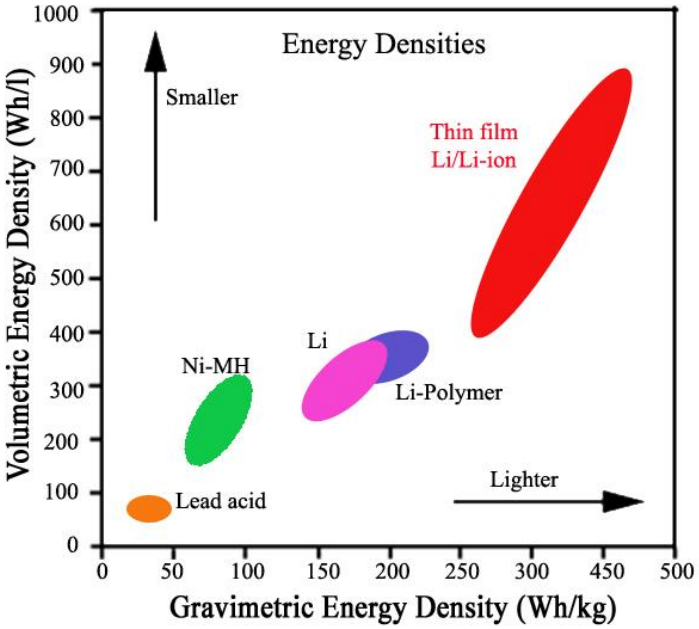

Fig. 1.4: Comparison of the volumetric and gravimetric energy density of various battery systems [18].

1.5.1 History of thin film battery.

For a thin film battery, it is necessary to arrange all the battery components, as an anode, a solid electrolyte, a cathode and current leads into multi-layered thin films by suitable techniques. Usually, the lithium metal used for anode is deposited by vacuum thermal vapor deposition (VD). Solid electrolytes and cathode and anode materials based on metal oxides are deposited as thin films by various sputtering techniques such as RF sputtering (RFS), RF magnetron sputtering (RFMS) etc. In some cases chemical vapor deposition (CVD) and electrostatic spray deposition (ESD) are used. Recently, pulsed laser deposition (PLD) has emerged as an advantageous technique, especially for cathode materials. Due to the huge initial investment cost for the construction of the cluster vacuum chambers and expensive preparation devices, only some restricted groups, mainly in

Japan, France and USA have succeeded in the fabrication of thin film batteries with the required performance perfection.

The first practical thin film battery was developed in 1982 by Hitachi Co. Japan. This was an all solid state battery with the cathode material TiS_2 deposited by CVD, $Li_{3.6}Si_{0.6}P_{0.4}O_4$ glass electrolyte layer, deposited by RF sputtering and metallic lithium film as anode, deposited by vacuum evaporation [19-20]. The first thin film battery was 4x4 mm in dimension, with a total thickness of the order of 6~8μm comprising of 1~3.7 μm thick TiS_2 cathode, 2~4μm thick electrolyte and 4μm thick lithium anode, which generated 2.5 V and a maximum current density of 3~16 $\mu A/cm^2$ and capacity of 45~150$\mu Ah/cm^2$ [21].

NTT Co. Group in Japan has developed thin film batteries by using $LiCoO_2$ and $LiMn_2O_4$ as cathode films deposited by RF sputtering [22-25]. The battery size was about $1cm^2$ and the thickness of the cathode layer was 1~5 um, the electrolyte was 1mm thick and the thickness of lithium anode film was4~8 μm.

In the 1980s, thin film batteries were also developed by Ever-ready Battery Co. and Bellcore Co. USA using sulfide glass of $Li_4P_2S_7$ or Li_3PO_4-P_2S_5as electrolyte, TiS_2 as cathode and Li and LiI as anode. [26, 27].These batteries were capable of delivering 1.5~2.8 V and 10~135 $\mu A/cm^2$ and could be operated for more than 1000 cycles [28]. Bellcore Co. also announced the lithium cell consisting of $LiMn_2O_4$ cathode, lithium boro-phosphate (LiBP) glass or lithium phosphorus oxynitride glass (LiPON) electrolyte and metallic lithium anode. The cell generated 4.2V open circuit voltage(OCV) and was capable of operating at 3.5~4.3V and $70\mu A/cm^2$ for more than 150 cycles.

The Oak Ride National Laboratory (ORNL) group in USA [29, 30] has been actively working on thin film batteries using lithium phosphonitroxide glass (LiPON) as electrolyte for the past two decades. The LiPON can be deposited by RF sputtering of Li_3PO_4 target in nitrogen gas, and has been found to be more stable compared to other lithium oxide or sulfide based glasses. These glasses have ionic conductivity of the order of $2.3x10^{-6}$ S/cm at room temperature and activation energy of 0.55 eV [31]. More over these electrolytes are stable for a potential window of 0 - 5.5V with respect to Li

electrode. The basic structure of these thin film cells consists of lithium metal anode layer deposited by vacuum evaporation, and LiPON electrolyte and cathode layers ($LiCoO_2$, $LiMn_2O_4$ etc.)deposited by RF sputtering. This group has reported various combinations of anodes and cathodes with LiPON electrolyte, exhibiting very good performance with cell voltage ranging from 2~5V, current density up to 10 mA/cm^2 and cyclability more than 10000 [32, 33].

The practical realization of all solid state thin film lithium-ion batteries is one of the greatest accomplishments of modern electrochemistry. The most astonishing feature of an all solid state battery is its ability to achieve higher energy densities than liquid electrolyte batteries. Solid electrolytes are much less temperature sensitive than liquid electrolytes, which makes them more suitable for microelectronic applications. The concept of the thin film battery is very simple and requires the arrangements of solid films of anode, solid electrolyte and cathode sequentially on a substrate. The schematic cross-section of a thin film lithium battery structure is shown in figure 1.5 [34].

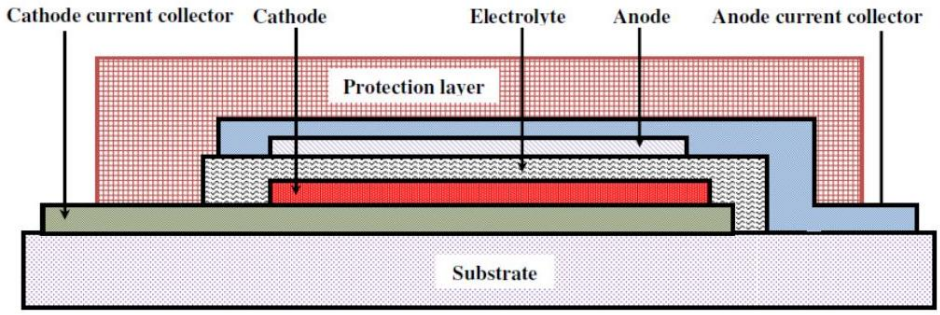

Fig.1.5: Schematic diagram of the cross section of a thin film lithium battery.

In thin film lithium ion battery both electrodes are capable of reversible lithium insertion. Because of the difference in chemical potentials of lithium in the two electrodes, the transfer of lithium ions from the anode through the electrolyte into the cathode (discharge) delivers energy, whereas the reverse lithium transfer (charge) consumes energy. When the battery is discharged, the lithium ions in the anode material migrate to the cathode material, and discharging current flows, and when the battery is charged, the lithium ions in the cathode

material migrate between the layers to form the anode, and charging current flows. In order to realize a practical thin film battery, it is necessary to make the battery components, as an anode, a solid electrolyte, a cathode and current leads into multi-layered thin films by suitable techniques as explained earlier.

1.5.2 Materials for thin film lithium ion batteries.

(A) Cathode materials

The most important feature of a cathode material is that it should have good electronic conductivity and should be capable of attaining high specific energy density, and high voltage. Numerous materials with these properties have been proposed for the cathodes of rechargeable thin film lithium batteries [35, 36]. Generally the compounds for positive electrode materials are divided into five major categories: the layered transition metal oxides, the spinel oxides, the olivines, the vanadates and metal chalcogenides. Among these, the vanadates and metal chalcogenides do not contain lithium after their synthesis. So they are in the charged state, making it essential to be coupled with the anode that serves as a lithium source in the first discharge cycle. These non lithiated electro-active cathode materials usually insert lithium electrochemically at potentials of 3 V versus Li/Li^+. In the lithiated state they are generally not stable to air and moisture. In contrast, there are various lithium-containing materials that can serve as lithium source in electrochemical cells. They must be charged (lithium must be deinserted) in the first formation cycle. These lithium containing materials are normally stable in air and moisture, and can electrochemically de-insert lithium in the 4 V potential regions.

Lithium cobalt oxide ($LiCoO_2$)

The $LiCoO_2$ as cathode electro-active material was first reported by John Goodenough in 1980[20]. $LiCoO_2$ has a layered structure with an anion close-packed or almost close-packed lattice in which alternate layers between the anion sheets are occupied by a redox-active transition metal and lithium inserts itself into the essentially empty remaining layers. The most widespread cathode material for Li-ion cell, $LiCoO_2$, shows a flat operating voltage at 3.9 V versus

Li/Li+. However, the actual specific charge of $LiCoO_2$ is only~135 mAh/g. This is because only 50 % of the Li+ ions can be removed from the structure. The complete removal of the Li^+ ions will result in structural changes and phase transitions. It is superior in cycling behavior due to its high structural stability and can be cycled more than 500 times with 80–90% capacity retention. Thin film $LiCoO_2$ cathodes discharged between 4.2 and 3.0 V give the best power densities [37]. This is due to the high diffusivity of lithium in the layered $LiCoO_2$ structure. However $LiCoO_2$ is not the perfect cathode material, and there are particular concerns related to the safety of the battery, pollution, health issues, and the rather higher cost of the cobalt oxide.

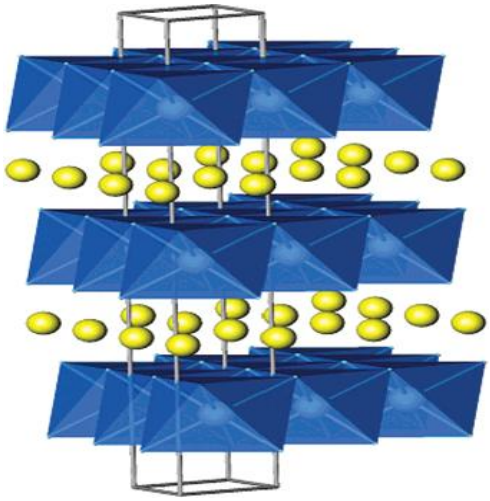

Fig 1.6: Layered structure of $LiCoO_2$ showing lithium ions between the transition-metal oxide sheets. The actual stacking of the metal oxide sheets depends on the transition metal and the anion [37].

Layered lithium manganese oxide ($LiMnO_2$).

Among the electrode materials with layered structure, the lithium manganese oxide $LiMnO_2$ is the most attractive one due to its environmental safety and cost-effective nature. Its structure might be described as a modified rock-salt type with a distorted cubic close packed oxygen anion array. The lithium and manganese cations occupy the octahedral interstitial sites in such a way that alternating zigzag layers of edge-sharing [LiO_6] and [MnO_6] octahedral are generated. Even though the structure of the $LiMnO_2$ can be described as

layered, it is slightly different from the layered structure of $LiCoO_2$. It is capable of delivering a specific charge of 190 Ah/kg in the potential interval between 2.0 and 4.25 V versus Li/Li+. However,$LiMnO_2$ based materials suffer from a limited cycling stability. On cycling, the orthorhombic $LiMnO_2$ component transforms slowly into a tetragonal lithiated spinel compound, leading to poor cycle ability of the electrode [38, 39].

Lithium nickel oxide ($LiNiO_2$)

Lithium nickel oxide ($LiNiO_2$) has a layered structure similar to that of $LiCoO_2$. The main advantage with the $LiNiO_2$ is its low cost and higher specific capacity (up to 200 Ah/kg) compared to $LiCoO_2$. But on the downside, it has a lower operating voltage, with a sloping charge-discharge profile. This nickel compound has several disadvantages for practical usage. Reported studies on this compound imply that its synthesis is difficult due to lithium volatility, leading to a highly disordered structure [40]. Moreover, the de-intercalated compound seems to be unstable and therefore dangerous in contact with organic liquids [41].

Lithium nickel manganese cobalt oxide (NMC compound)

In 2001, the fully symmetric compound, lithium nickel manganese cobalt oxide, Li ($Ni_yMn_zCo_{1-y-z}$) O2 (NMC compound) was proposed. These compounds represent the third generation of active materials for the positive electrode of lithium-ion batteries. Among these, the most studied compounds are the ones with z = y, in particular the z = y = 1/3 compound. As a general rule, manganese and cobalt are present in the structure as Mn^{4+} and Co^{3+}, respectively, while nickel [42] is observed as a combination of Ni^{2+} and Ni^{3+}. Manganese seems to be needed for structure stabilization, nickel offers most of the electrochemical activity, cobalt tends to help the rate capability, and excess lithium increases the capacity [41]. It has been shown that upon lithium removal, the unit cell volume change in Li ($Ni_{1/3}Mn_{1/3}Co_{1/3}$) O2 is less than 2% [43], which is one of the factors that might explain the high cyclability of this material. The NMC compounds can achieve high specific capacity(~170 mAh/g) with long cycle life. NMC includes a range of materials that are

regarded as promising substitutes for today's industry standard $LiCoO_2$, because of their improved electrochemical performance and thermal stability in the charged state.

Lithium containing spinel oxides.

The lithium spinels Li [M_2] O4 (M = Ti, V, Mn) and their derivatives have gained wide spread attention as alternatives to lithium cobalt oxide ($LiCoO_2$) [44, 45]. Among them, $LiMn_2O_4$ is the well studied one with many desirable advantages, including high rate performance due to its three dimensional framework, high energy density, low cost, low toxicity, and simplicity of synthesis [46]. Moreover, because of their higher bulk electrical conductivity, the $LiMn_2O_4$spinel materials can yield higher power densities than other cathode materials. In fact, spinel oxide cathode materials are thermally very stable and not prone to the thermal runaway reactions. Coupled with cobalt oxide cathode materials, spinel cathodes are fundamentally much safer.

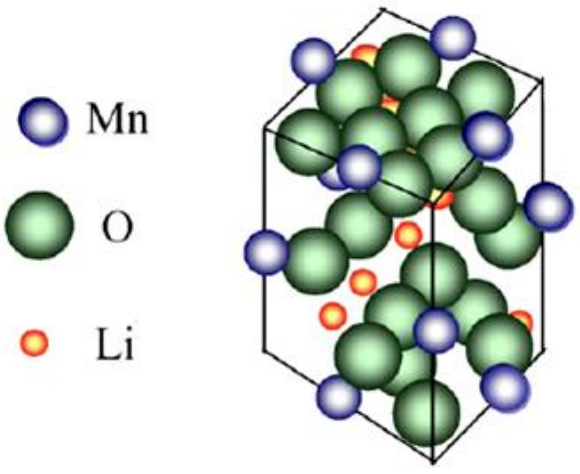

Fig.1.7: Cubic spinel structure of $LiMn_2O_4$ [45]

$LiMn_2O_4$ has a cubic spinel structure, and has three equilibrium potentials for lithium ion intercalation of which two are in the 4 V potential region (4.0 and 4.1 V vs. Li/Li^+), and the third one is in the 3 V potential region (3.1 V vs. Li/Li^+). The average oxidation state of the manganese is critical to obtain an

effective cycle life. When the oxidized state of the manganese experiences the 3 V potential region (normally below 3.50 V vs. Li/Li^+), dissolution of the manganese will occur, and the Jahn-Teller distortion connected with Mn^{3+} ions will result. As a result of the asymmetric change of cell parameters, the cubic crystal symmetry of the spinel is transformed into tetragonal symmetry. This will lead to the poor cycling performance.

Most of the research activities initiated to stabilize cubic spinel structure in recent years have been directed towards the synthesis of non stoichiometric Li-Mn spinels and Mn-substituted stoichiometric $LiMn_2O_4$ by low valence cations(＜4) [47-50].A detailed discussion of the $LiMn_2O_4$ spinel cathode materials is included in the section 1.6.

Olivine lithium metal phosphates

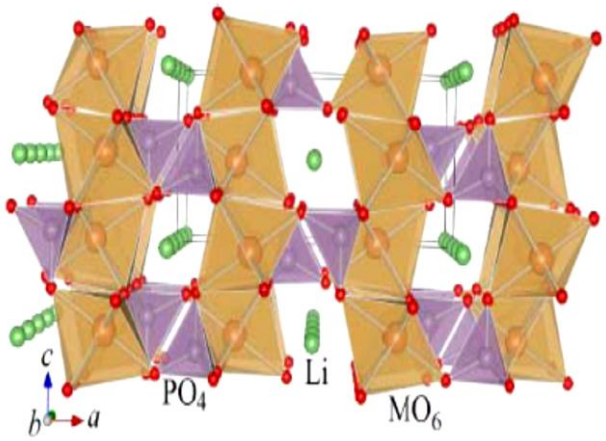

Fig 1.8: Polyhedra representation of the structure of $LiMPO_4$, with arrays of Li-ions along b axis, nearly co-planar MO_6 octahedral and PO_4 tetrahedra [50].

Olivine lithium metal phosphates, $LiMPO_4$ (M=Fe, Mn, Co, Ni) have attracted particular attention due to comparatively lower cost and good environmental compatibility of their basic constituents. Their reasonable theoretical electrochemical capacity of 170 mAh/g makes them well-suited cathode materials for large-scale battery applications. Moreover, these compounds display high redox potentials, fast Li^+ ion transport, excellent thermal stability,

high lithium intercalation potential (not too high to decompose the electrolyte) and energy density comparable to that of conventional lithium metal oxides. [51-56].

Lithium metal phosphates (LMPs) adopt an olivine-related structure, which consists of a hexagonal closed-packing (hcp) of oxygen ions with Li^{+} and M^{2+}cations located in half of the octahedral sites and P^{5+}cations in 1/8 of the tetrahedral sites as shown in Figure 1.8.[57-59, 1]. This structure may be described as chains (along the c direction) of edge-sharing MO_6octahedra, which are cross-linked by the PO_4 groups forming a three-dimensional (3-D) network. Tunnels perpendicular to the [001] and [100] directions contain octahedrally coordinated Li+ cations (along the b axis) which are mobile in these cavities. These compounds generally crystallize in the orthorhombic (Pnma space group) system [60, 61]. In phospho-olivines, all of the oxygen ions form strong covalent bonds with P^{5+} to form the PO_4^{3-} tetrahedral polyanions and stabilize the entire three-dimensional framework. This assures stable operation at higher temperatures and extreme safety under abusive conditions, and enhances the attractiveness of the olivine-type cathodes [62-64].

The major problem faced by the commercial use of these Lithium Metal Phosphates (LMPs) is their poor rate capability, which is attributed to their low electronic conductivity and slow kinetics of Li diffusion through the interfaces. Two approaches have been attempted to overcome this problem. One is to enhance electrical conductivity by coating an electron-conducting layer around the particles, such as carbon [65, 66], copper [67] and silver [68], or by doping with guest cations [69]. The other is to minimize particle size by modifying the synthesis conditions, such as using solution method [70] or lowering the sintering temperature.

Vanadates.

Oxides of vanadium, chromium, niobium as well as molybdenum are well known for their ability to electrochemically insert lithium in large quantities [71-73].

Fig. 1.9: Structures of layered LiV_2O_5 with VO_5 square pyramids [73].

Among these, vanadium oxide is an attractive cathode material due to the three stable oxidation states (V^{5+}, V^{4+} and V^{3+}) of vanadium within its closely packed oxygen structure. Vanadium oxides have been studied for use as cathodes in lithium batteries for the last three decades, because of the attractive characteristics such as high specific energy and good rate capacity [74] Initial studies were conducted on vanadium pentoxide, (V_2O_5) which has a complex intercalation behavior, involving several phases in relation to the lithium content. Due to this, V_2O_5 was an unappealing cathode material for practical applications. V_2O_5 has a layered structure with a distorted close-packed oxygen array. Its theoretical capacity is the highest within the vanadium oxide family (442 mAh/g). The structure of this compound is shown in figure 1.9.

B). Materials for anode

Metallic lithium, with a specific capacity of 3860 mAh/g, is the perfect anode material for primary lithium cells. However, it cannot be used in secondary lithium cells due to a lower cycling efficiency and inherent safety issues such as reactivity and dendrite formation during cycling. In this regard, several lithium insertion materials have been pursued as anode materials. Since both the anode and the cathode are Li insertion materials, the secondary, lithium ion cell is referred to as a "shuttle" cell or a "rocking chair" cell. However, to be a good anode insertion material, the chosen material should exhibit a lower discharge

voltage vs. Li/Li+ and it should also be able to store a reasonably large quantity of lithium ions in its structure.

The most widely used active material for anode or the negative electrode in practical lithium-ion battery system is graphite. Graphite has a layered structure which is suitable for the intercalation of Li ions. More over graphite exhibits higher specific charge and more negative redox potentials than most metal oxides, chalcogenides and polymers. During the electrochemical reduction (charging cycle) of the carbon host, lithium ions from the electrolyte penetrate into the carbon and form a lithium/carbon intercalation compound, Li_xC_n. This reaction is a reversible reaction and the reversibility of the lithium/carbon intercalation reaction strongly depends on the crystallinity, the microstructure, and the micro morphology of the carbonaceous material [75-84]. The nature and surface of graphite also strongly influence the cycle life of the battery [85].

Recently, with the discovery of new crystalline carbon nanotubes (CNTs), a new pattern in carbonaceous-based battery electrode materials has emerged. The unique properties of these nanotubes enable them to exhibit increased capacity as an active material and induce highly superior cyclic characteristics as an additive to the anode material [86-90]. A scientific report by Meunier*et al.* (2002), showed that it is possible to charge SWCNTs up to one lithium for every three carbon atoms and higher. This lead to a significant rise in the reversible capacity, which can be up to 1000 $mAhg^{-1}$ for SWCNTs and 780 $mAhg^{-1}$ for MWCNTs [91]. However, there are certain drawbacks with these nanotubes; the large irreversible component of the capacity (coexisting with the large reversible storage capacity), the large hysteresis in voltage between charge and discharge, and the absence of a voltage plateau during lithium de-intercalation [92].

Most of the present day research is moving towards replacing carbonaceous anode with non-carbonaceous anode, as well as with metal alloys and titanates. The driving force behind this current research trend is to obtain a new generation of anode materials with higher specific capacities and high power, while retaining the good properties of carbonaceous materials, such as cyclability, cost, and safety features.

Lithium metal alloys are among the most attractive and competitive candidates for new types of anodes for lithium-ion battery applications. There are a number of metals and semiconductors, for example aluminum, tin and silicon, which react with lithium to form binary and ternary Li alloys by electrochemical processes that are partially reversible. Moreover they have low operating voltage, and involve a large number of atoms per formula unit. It has been shown that these alloys can provide a specific capacity much larger than that offered by conventional carbon based anodes [93, 94].

Due to the high ionic character of the lithium alloys, they are usually quite brittle. As a result, mechanical stresses, associated with the volume changes, induce a rapid decay in mechanical properties leading to pulverization of the electrode [95]. The metallurgical structure and morphology of Li alloys such as grain size, shape, texture, and orientation strongly influence their dimensional stability [96-98].

Among all lithium alloy anodes, amorphous tin-based composite oxide introduced by the Fuji film Celltech Co. Ltd. offered the best cycle life, a high specific charge (>600 Ah/kg) and charge density (>2200 Ah/L) [99].

A new approach to alleviate the problems of alloy expansion, involves the selection of intermetallic alloys such as Cu_6Sn_5, InSb and Cu_2Sb that show a strong structural relationship to their lithiated products, Li_2CuSn and Li_3Sb for the Sn and Sb compounds, respectively. InSb and Cu_2Sb thin film electrodes are particularly attractive candidates because they operate through a reversible process of lithium insertion and metal extrusion. InSb and Cu2Sb electrodes provide reversible capacities between 250 and 300 mAh/g. Cu_6Sn_5 in which, lithium can reversibly intercalate and deintercalateis a promising alloy anode for thin film lithium batteries [100].

Thin amorphous silicon films deposited on a copper foil surface by sputtering process were shown to have close to 100% reversibility at capacities larger than 3000 mAh/g [101]. Exceptional capacity retention was also observed for silicon electrodes prepared with a nanopillar surface morphology because size confinement alters particle deformation and reduces fracturing. However, the

greatest disadvantage of these nanoparticles is the possibility of side-reactions with the electrolyte leading to poor calendar life of the cell.

A nanostructured anode based on transition metal oxides has recently been illustrated. The full electrochemical reduction of oxides such as CoO, CuO, NiO, Co_3O_4 and MnO versus lithium, involving two or more electrons per 3dmetal, was shown to lead to composite materials consisting of nanometer-scale metallic clusters dispersed in an amorphous Li_2O matrix [102]. Owing to the nanocomposite nature of these electrodes, the reactions are termed 'conversion reactions' which are highly reversible. The new results, in stark contrast, turn out not to be specific to oxides but can be extended to sulfides, nitrides or fluorides [103].

Titanium containing compounds, such as the titanium dioxide (TiO_2) and titanium spinel ($Li_4Ti_5O_{12}$) [104] are included in the list of negative intercalation electrodes for lithium-ion batteries. The advantages of using these electrodes are related to the more anodic equilibrium potential of the intercalated compound, which is favorable for high power and fast charge/discharge.

C). Solid electrolytes.

The fundamental solution for the basic safety issue with the lithium batteries can be solved by the development of solid state batteries. These batteries use solid state electrolytes and can be used to fabricate thin film rechargeable lithium batteries, which has a wide range of applications [105-111]. Solid electrolytes for battery applications require high ionic conductivities, a very low electronic conductivity and a wide range of appropriate thermodynamic stability. There are mainly four major aspects which has to be taken into consideration while designing a solid electrolyte; They are - optimization of the lattice structure spatially and energetically to improve the number and mobility of ionic defects, development of synthesis routes to prepare materials with amorphous or polycrystalline structure and with high conductivity, optimizing the stability range to prevent chemical reactions with the electrodes, and the optimization of the electrolytic domain with negligible electronic conduction over the activity range employed.

Solid polymer electrolytes are currently the most accepted electrolytes for lithium ion batteries, because they can offer an all-solid-state construction, ease of manufacture, good mechanical and electrochemical properties, and can be manufactured in a wide variety of shapes and sizes and have a higher energy density. These electrolytes are non corrosive and less probable for internal short-circuits, enabling the device a safer one. In an ideal solid electrolyte, only Li+ ions are mobile, other less mobile ions are arranged in a crystalline or glassy matrix in which Li+ moves between the vacant and/or interstitial sites. Typically this type of Li+ transport takes place in inorganic solid electrolytes. For these electrolytes, the ionic conductivity at ambient temperature is very low. A typical example for this kind of polymer electrolyte includes materials like poly(ethylene oxide)(PEO), and a lithium salt(LiX), like $LiPF_6$ or $LiCF_3SO_3$.

For the all solid state thin film lithium batteries, the electrolyte generally used is lithium phosphorus oxynitride, which is otherwise known as LiPON. LiPON has a good lithium ion conductivity, low electronic conductivity, and good electrochemical stability with both metallic lithium and the transition metal cathodes at cell potentials up to 5.5 V versus Li. Current thin-film solid-state lithium batteries based on LiPON electrolytes have shown reasonable cycle life. However, LiPON has a low ionic conductivity (~10^{-6} S/cm at 25 ºC), which limits its performance particularly at low temperatures. In addition, thin-film solid-state batteries have limited capacities based on the limitations of the thickness of the electrodes within the thin-film design.

Solid inorganic lithium-ion electrolyte based on thio-LISICON (LIthiumSuper IonicCONductor) has shown the highest reported ionic conductivities (>10^{-3} S/cm at 25 ºC)[112-115] than any solid-state inorganic lithium-ion conductors [116].Thio-LISICON materials, usually described by the formula, $Li_xM_{1-y}M'_yS_4$ (M = Si, Ge, and M′= P, Al, Zn, Ga, Sb) have been synthesized with different compositions using both high temperature and low temperature methods. The low temperature process yields thio-LISICON materials which show high ionic conductivities (3.2 x 10^{-3} S/cm at 25^{o}C) and wide electrochemical stability windows (up to 10 V vs Li)[117]. These excellent properties of the thio-

LISICON make it the most promising thin film solid electrolyte for the thin film rechargeable lithium batteries.

1.6 $LiMn_2O_4$ as cathode materials for thin film battery

The performance characteristics of a lithium ion battery directly depend on the properties of cathode materials. In general, a lower chemical potential and a large intercalation capacity for lithium ions are necessary, as these are the basic factors which determine the cell voltage and charge capacity of the battery. Moreover, good chemical and mechanical stability of the cathode material is essential in order to retain capacity during the charge discharge cycling. There are many cathode materials which qualify these criteria, and among these one of the well studied ones is the $LiCoO_2$ with a layered structure, $LiMn_2O_4$ with a 3D spinel structure and $LiFePO_4$ with an olivine structure.

$LiMn_2O_4$belongs to the third generation cathode material for lithium ion battery applications. The $LiMn_2O_4$ and its derivatives remain the most attractive cathode materials in terms of cost, abundance, and nontoxicity compared to other cathode systems. Moreover $LiMn_2O_4$ is widely recognized as a potential substitute for $LiCoO_2$ and is used in high energy density batteries for high power cell applications. The possibility of cycling 0.8 Li per Mn_2O_4 unit electrochemically from its core spinel structure corresponding to a complete utilization capacity has prompted its usefulness in terms of charge-discharge control when employed as cathode in Li-ion batteries.

Moreover and more importantly, the high rate capability of the Mn-O system could be advantageous not only for discharge, but also for rapid recharge of the cell. The above features have recently occupied a place of pride among the battery manufactures to utilize the spinel $LiMn_2O_4$ as a Li^+ source electrode for practical high voltage Li-ion technology. Interest in the spinel $LiMn_2O_4$ as electrode in rechargeable lithium-ion batteries stems from the fact that the lithium ions can be removed (de-intercalated) and reinserted (intercalated) into this compound topotactically. This spinel can de-intercalate Li+ ions at ~4 volts becoming λ-MnO_2 (spinel structure) and intercalate Li+ ions at approximately 3 V to yield $LiMn_2O_4$. The good voltage regulation during cycling, the excellent

electro-chemical reversibility, and the theoretical specific capacity (148 mAh/g) make the spinel $LiMn_2O_4$an attractive cathode material.

Moreover, unlike layered structured cobalt oxide materials, all atoms in spinel shaped manganese oxides are connected via genuine chemical bonds with large channels in the lattice for Li insertion and hence they have low discharge capacity and structural stability at moderately high temperatures. However, batteries made of $LiMn_2O_4$ electrodes show drastic capacity fading after each charge-discharge cycle which may be due to the dissolution of $LixMn_2O_4$electrode in the electrolyte as Mn^{2+} ions and onset of Jahn-Teller effect in deeply discharged $LiMn_2O_4$ electrodes.

1.6.1 Structure of $LiMn_2O_4$.

Manganese oxide exists in nature in many structural forms, [118] out of which most promising cathode material for the lithium ion battery application is the spinel manganese compounds. In present topic mainly discusses the structural features of the spinel $LiMn_2O_4$ cathode material as because structure and electrochemical properties provide more information about its behavior as a cathode in secondary lithium-ion batteries.

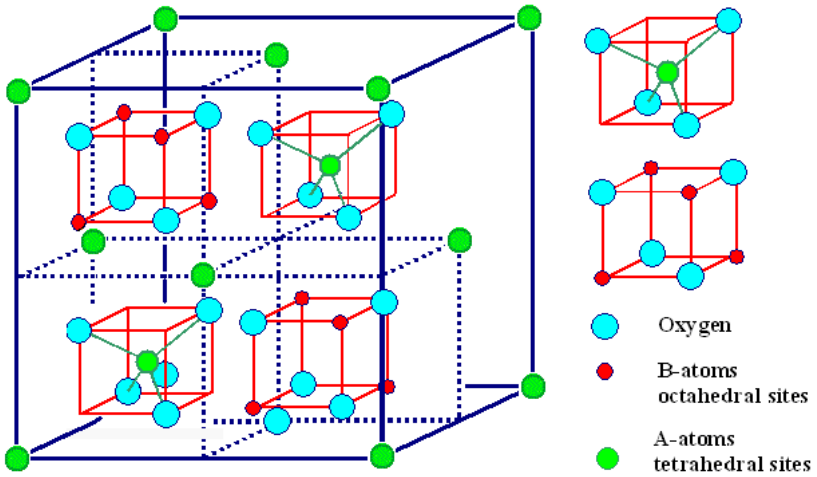

AB_2O_4 spinel The red cubes are also contained in the back half of the unit cell

Fig. 1.10: Schematic illustration of the spinel crystal structure [118].

Generally spinel structure is represented as AB_2O_4 where A ion is surrounded by four oxygen ions, forming a unit tetrahedron, usually in its divalent (or monovalent) state, and B ion is surrounded by six oxygen ions, forming a unit octahedron, usually in trivalent (and/or tetravalent) states. Figure 1.10 represents the general spinel structure with B atoms at octahedral sites and A atoms at tetrahedral sites. There are eight occupied tetrahedral (or A) sites and 16 occupied octahedral (or B) sites in a unit cube.

In the $LiMn_2O_4$ spinel, the Li ions occupy tetrahedral sites [119] each surrounded by four oxygen ions; the Mn ions occupy octahedral sites, each surrounded by six oxygen ions. Here the oxygen anions form the face centered cubic packing**.** For every four oxygen anions, there are four octahedral sites and eight tetrahedral sites. Out of these twelve, only three are needed to fill the cations of the above formula. In the normal spinel structure, 'A' cations are in the tetrahedral voids and 'B' in the octahedral voids. The spinel phase of $LiMn_2O_4$ belongs to the Li-Mn-O system that has been studied in detail as an insertion electrode for secondary lithium cells. In the system the lithium ions occupy the 8a tetrahedral interstitials **a**nd manganese cations occupy 16d octahedral interstitials of a cubic close packed array constructed by the oxygen anions located at the 32e positions of the Fd 3m space group [119, 120]. In a crystal, point group symmetry operations can be combined with translational symmetry elements provided they are compatible. Such combinations are called space groups]

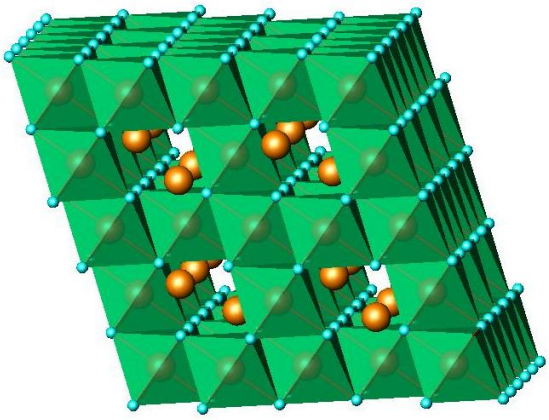

Fig. 1.11: The spinel structure with MO_6 octahedra and Li taking tetrahedral positions [121].

The spinel structure of $LiMn_2O_4$ is composed of MnO_6 octahedral frame work (Figure 1.12) within which there is tetrahedral channel sites for Li^+ to occupy [121]. As clearly seen in Figure 1.11, the spinel-framework structure has a three-dimensional (3D) channel consisting of one-dimensional (1D) tunnels. Since lithium being a light element, it can be easily inserted into or taken away from the structure without causing any structural changes. This aspect makes $LiMn_2O_4$ an important material from the point of application as electrode material in rechargeable lithium batteries.

The spinel structure can also be illustrated as being made of single chains consisting of edge-shared BO_6 octahedra. The layers consisting of BO_6octahedral chains parallel to each other stack up along the *c* axis with 90^o rotation to form the spinel structure. Because the single chains in the adjacent layers are at right angles to each other, the chains in the spinel structure run in two orthogonal directions. For example, stoichiometric $LiMn_2O_4$ismade up of single chains of edge-shared MnO_6 octahedra, i.e., Mn^{3+}–Mn^{4+}–Mn^{3+}–Mn^{4+}–Mn^{3+}–Mn^{4+} in its ideal charge order. At ambient temperature, stoichiometric $LiMn_2O_4$ is cubic. But at low temperatures, phase transition from cubic to tetragonal (or orthorhombic) is observed, which reminds one of a Peierls transition coupled with localized/delocalized electrons associated with Jahn–Teller effect, although this is not well supported by the experimental facts. Cubic to tetragonal transformation during the reduction of $LiMn_2O_4$ to $Li_2Mn_2O_4$, can also be explained using this structural description.

The general composition for the spinel structure described above, represented as $A[B_2]O4$ is called a normal spinel. However, the spinel structure is flexible with regard to the distribution of A and B ions at tetrahedral and octahedral sites. When A ions occupy one-half of the octahedral 16d sites and B ions occupy the other half of the octahedral 16d sites as well as all of the tetrahedral 8a sites, the structure is called an inverse spinel. The inverse spinel is represented by $B[AB]O_4$ in which A and B ions in the square brackets occupy the octahedral 16d sites.

The electronic structure of any material is perhaps its most important signature, which is responsible for most of its properties and is dependent on several

factors including its crystal structure and bond formation. Since the Mn-ion is in octahedral symmetry, the electronic structure of $Li_xMn_2O_4$ compound is governed by a strong hybridization between the manganese d and oxygen p atomic orbitals where its d_{z2} and d_{x2-y2} atomic orbitals directly overlap with the p_x, p_y and p_z orbitals of oxygen along the octahedral directions. This σ overlap creates the $e_g$bands, of which the bonding band, e^b_g, has a predominant oxygen p character and the antibonding band, e^*_g, has a predominant metallic d character. The remaining d_{xy}, $d_{yz}$and d_{xz}orbitals point away from oxygen and have only a minor π overlap giving rise to the nonbonding t_{2g}bands. In $Li_xMn_2O_4$spinels, the Fermi level $E_F$lies within the nonbonding t_{2g}bands. Similarly, the overlap of oxygen p with manganese p and oxygen p with manganese s gives rise to $t_{1u}$and a_{1g}bands, respectively. There is considerable amount of intermixing between e^b_g, $t_{1u}$and a_{1g}bands and are collectively known as oxygen 2p bands because of their predominant oxygen p character [122-125]. The band gap of $Li_xMn_2O_4$ is reported to be around 1 eV [126]. However, there are also other absorption peaks apart from the fundamental absorption edge [18,19] Berg et al have observed that when a cubic crystal undergoes a tetragonal Jahn–Teller distortion as in $LiMn_2O_4$,its electronic structure gets modified in the form of splitting up of each of$Mnt_{2g}$and Mn e^*_g bands into two [127]. Another challenge in the study of Li transfer in lithium manganese oxides (LMOs) is its effect on the band structure of LMOs [128]. In the rigid band picture, Li intercalation into LMO raises the host Fermi level due to band filling of the host material. On the contrary, in the non-rigid band picture, Li intercalation does not affect the host Fermi level, but its density of states translates to lower energies due to electron transfer from lithium to oxygen [129].

1.6.2 Li^+ Extraction/Insertion mechanism in the Spinel $LiMn_2O_4$.

In a typical lithium ion cell, during the discharge cycle, Li^+ ions are transported through the electrolyte to the cathode where they get inserted into the crystal structure of the host cathode material. The insertion of Li^+ ions is generally termed as ‘intercalation’ since they intercalate into the cathode materials often having the layered or three dimensional structures, which provide easy access, and mobility for the incoming and outgoing lithium ions. When the battery is charged, a reverse operation occurs, where Li^+ ions are moved out of the

cathode and inserted into the anode material. Simultaneously, electrons travel via the external circuit, compensating for the positively charged lithium ions in the crystal structure. The electrochemical process at the cathode is the up taking of lithium ions during discharging and the releasing of lithium ions during charging of the battery. The overall battery process can hence be described as the insertion-extraction of both the mobile lithium ions and the charge compensating electrons into the rigid host. The former induces reversible modifications of the unit cell in the cathode and the latter induces reversible changes in the oxidation state of the transition metal atom. Since the lithium ions are traveling between the cathode and the anode during the electrochemical process of charging and discharging, this type of rechargeable batteries is also known [130] as the 'rocking-chair' batteries.

For a lithium ion cell with spinel $LiMn_2O_4$ as cathode material and graphite as anode, the overall cell reaction can be written as,

$$LiMn_2O_4 + C_6 \rightarrow Li_{1-x}Mn_2O_4Li_xC$$

This electrochemical process can be described by extraction/insertion of Li ions into the cathode material. The flow of Li^+ ions induces a voltage difference between the anode and the cathode of the battery when it is used as a power supply. Intercalation and de-intercalation of lithium ions in $LiMn_2O_4$ spinel take place at two characteristic voltages of ~3V and ~4V (vs. Li/Li+ electrode), respectively. The average oxidation state of manganese is 3.5 in $LiMn_2O_4$.

The phase diagram of the Li-Mn-O system is shown in figure1.12. It is clear from the phase diagram that, extraction of Li^+ ions leads to composition change from $LiMn_2O_4$ towards Mn_2O_4 (λ-MnO_2) with Mn^{4+} oxidation state, while the insertion of excess Li+ leads to the formation of $Li_2Mn_2O_4$ (i.e. $LiMnO_2$)) with Mn^{3+} oxidation state. For the cubic spinel-related structure within the phase field of λ-MnO_2-$LiMn_2O_4$-$LiMnO_2$-$Li_5Mn_4O_9$, lithium intercalation-deintercalation or the 'rock-chair' mechanism is possible [131].

The removal of Li from $LiMn_2O_4$ occurs through a two - step reaction around 4V. Two potential plateaus can be discerned in the charge /discharge curve,

separated by 100-150mV. Studies have shown that the material goes through at least one two–phase regions, during charge /discharge [132-133]. The structures of these intermediate phases are not clear, but single crystal studies have shown that super structures may occur in the upper part of the potential curve [134].

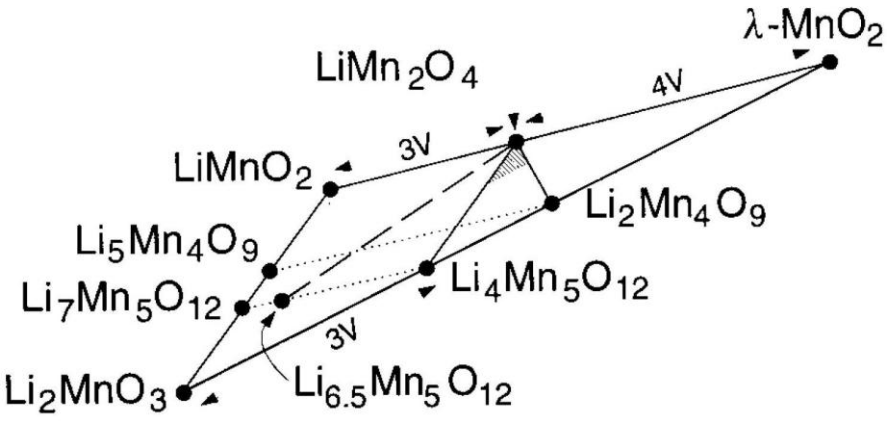

Fig.1.12: Li-Mn-O phase diagram at room temperature [131].

The transformation from $LiMn_2O_4$ to $Li_2Mn_2O_4$ involves a distinct first order phase transition. When Li ions are inserted into the spinel host structure, they occupy the octahedral 16csites. Since each of the 8a-tetrahedron faces is shared with an adjacent, vacant 16c site, the Li ions in the tetrahedral sites are instantly displaced into the vacant 16c site, causing a first-order phase transition. When the Mn^{3+} (d^4) concentration increases, Jahn-Teller (JT) distortion occurs. The crystal symmetry decreases from cubic to tetragonal, imposing a large strain on the individual spinel particles that ultimately results in electromechanical grinding. The reversibility of this phase transition is poor [135, 132].

1.6.3 $LiMn_2O_4$ and Jahn Teller effect.

The Jahn-Teller theorem states that "For non-linear molecules, a nuclear configuration which begets an orbitally degenerate occupied state is unstable with respect to one without such orbital degeneracy.[136].This means that there cannot be unequal occupation of orbitals with identical energies. To avoid such unequal occupation, the molecule distorts so that these orbitals are no longer degenerate.

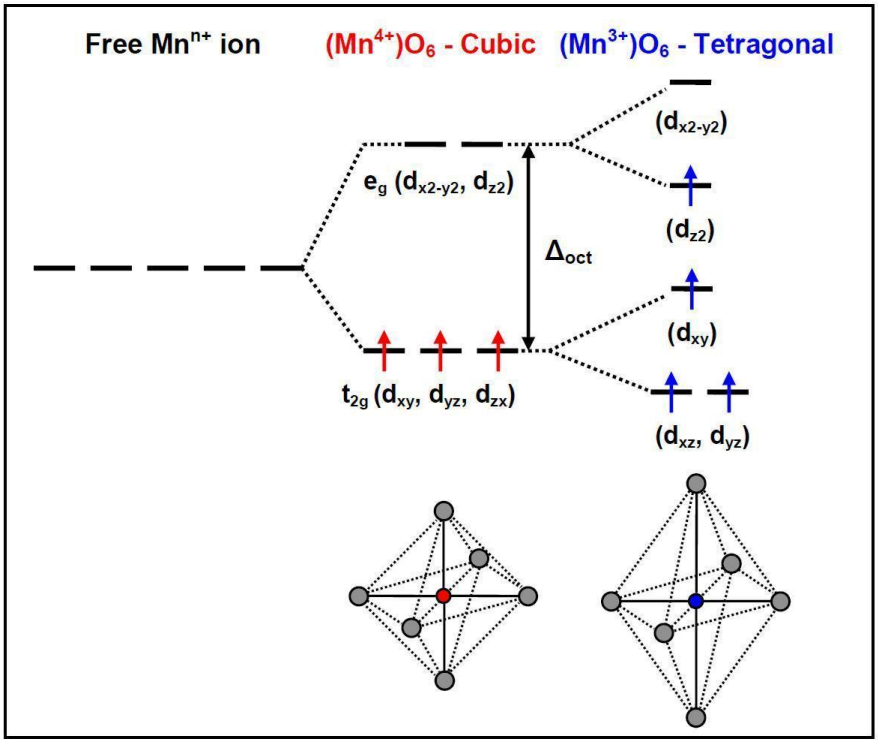

Fig 1.13: Cubic to tetragonal (Jahn-Teller) distortion arising from Mn^{3+}:$3d^4$ due to the single electron present in the e_g orbital [139].

The cyclability of lithium secondary batteries depends greatly on the structural integrity of the host materials during charging and discharging processes. $LiMn_2O_4$, which has a cubic spinel structure (space group Fd3m, with Li on 8a tetrahedral sites, Mn on 16d octahedral sites, and O ions on 32e positions) is a stable phase at room temperature [137-139]. However, the cooperative Jahn-Teller (JT) distortion in $LiMn_2O_4$ occurring below 290K, which transforms its cubic phase to tetragonal phase, is an order to disorder, first-order type phase transition [140, 141]. Figure 1.13 shows the molecular orbitals of d^4 complex for Jahn-Teller effect.

In the case of $LiMn_2O_4$, the Jahn-Teller distortion is accompanied by an increase in the unit-cell volume. The increased concentration of Mn^{3+} ions in the host structure reduces the crystal symmetry from cubic (c/a = 1) to tetragonal. (c/a = 1.16)[142].This structural distortion is too large for the spinel

framework to maintain its structural integrity during cycling. This limits the usage of $LiMn_2O_4$ cathodes only to the 4 V regions corresponding to the extraction/insertion of Li+ ions from/into the 8a tetrahedral sites. Moreover this lattice instability due to the Jahn-Teller distortion together with a subsequent volume increase upon Li intercalation into $LiMn_2O_4$ occurring at near to ambient temperatures leads to its fracture with a probable loss of electrical contact with the current collector on repeated cycling or over discharging and is a major problem with the commercial use of $LiMn_2O_4$ spinel.

1.6.4 Capacity fading in $Li_xMn_2O_4$ system

The capacity fading reported in $LiMn_2O_4$ cathode materials is a consequence of various factors. Some of the major causes are given below.

The capacity fading in $LiMn_2O_4$ cathode material is mainly due to the Jahn-Teller distortion. This distortion is accompanied by an increase in the unit-cell volume, which is detrimental to the structural integrity and inter-particle contact during repeated charge-discharge cycles. Under dynamic, non equilibrium conditions above 3 V, it has been proposed that some particles can be more lithiated than others, thereby driving the composition of the electrode surface into a Mn^{3+} rich $Li_{1+x}[Mn_2]O_4$ region [143]. Recent data shows that under high-rate conditions, the tetragonal $Li_2Mn_2O_4$ phase is formed at the surface of some spinel particles above the expected thermodynamic voltage (2.96 V), thus causing structural damage to the electrode [144]

Another reason for capacity fading is the Mn^{2+} dissolution in to the electrolyte. This arises due to the partial solubility of the spinel oxide electrode in the electrolyte solution and can cause disproportionate reaction at the particle surface. Manganese dissolution was reported to be induced by acids generated by reactions of fluorinated anions with water impurities present in the cell components (electrodes, electrolytes), oxidation of the solvent etc. [145-147]

Capacity fading and poor performance can also be caused by over de-lithiation of spinel $LiMn_2O_4$, which results in oxygen loss. Electrolyte decomposition due to overcharging, polarization of electrodes due to electronic contact loss etc. are some of the other factors responsible for capacity fading.

1.6.5 Effect of transition metal doping on $LiMn_2O_4$.

As seen earlier, $LiMn_2O_4$ has a cubic spinel structure at room temperature. As the temperature decreases, the cubic spinel gets transformed to the orthorhombic phase at around 280^oK. Since this transition temperature is very close to the room temperature, continuous charge discharge cycling results in a rapid fall of the capacity and hence poor performance of the battery. On further reduction in temperature to about 65^oK, the structure totally gets converted to a single phase of tetragonal spinel. In order to use $LiMn_2O_4$ as a successful cathode material it is very crucial to stabilize the cubic spinel structure.

$LiMn_2O_4$ spinel can be equivalently represented as $LiMn^{3+}Mn^{4+}O_4$ with an equal number of isotropic $Mn^{4+}O_4$octahedra and JT-distorted $Mn^{3+}O_4$octahedra because only the high spin Mn^{3+} ions favor dynamic Jahnn Teller distortion. It is also observed that substitutions of other transition metal ions ($LiMn_{2-x}M_xO_4$, where M= Cr, Co, Ni, Fe, and Cu) [148, 149] for manganese will reduce the extent of JT distortion in spinel $LiMn_2O_4$, thereby improving the electrochemical performance of the cathode. This is due to the reduction in the number of Mn^{3+} ions because of their substitution by M ions.

1.6.6 Objectives of the present investigations

Thin film Li ion cells based on $LiMn_2O_4$ cathode material can be developed by using a variety of techniques and among them, RF magnetron sputtering has been identified as a versatile and advantageous technique for achieving the satisfactory deposition of thin film battery layers. It offers the possibility to micro-fabricate the thin film batteries directly onto chips in any shape or size, and on flexible substrates, with good capacity and cycle life. High quality crystalline films of battery layers can be effectively developed using sputtering technique. It is also possible to process large area substrates easily and with high efficiency using this technique. However, the successful deposition of thin film battery cathode materials with the required film qualities is always challenging due to several reasons. These include the selection and optimization of the most suitable deposition technique and the assembling of the devices with the required characteristics. Thin film batteries made of $LiMn_2O_4$ electrodes show drastic capacity fading after each charge-discharge cycle due to the inherent property of the material arising from the Jahn-Teller effect

There are several other challenges in developing thin film battery layers by using RF sputtering technique. These include comparatively high initial investment costs of equipments and most importantly the low deposition rates of the individual layers, which make the battery fabrication a lengthy affair, affecting the throughput of production and production cost.

The electrochemical properties of the ‘as deposited’ cathode films by sputtering technique are inferior and hence these films are not suitable for the assembling of a practical thin film battery. In order to achieve good electrochemically active cathode films, the ‘as deposited’ films should undergo a high temperature post annealing cycle, which enhances the crystallinity and improves the stability of the films

Most importantly, the major challenge faced by the thin film cells based on the $LiMn_2O_4$ cathode material is the poor capacity retention during charge discharge cycling. The major factors responsible for the capacity fading reported in $LiMn_2O_4$ cathode materials are the Jahn-Teller distortion,

Mn^{2+}dissolution into the electrolyte and oxygen loss in the cathode materials during cycling.

Based on the above challenges, the objectives of the present work can be summarized as follows:

Increase the rate of sputter deposition of the thin film battery cathode layer by using high frequency excitation source.

Reduce the post annealing temperature of the ‘as deposited’ thin film battery cathode layers by using in situ-substrate bias.

Improve the discharge capacity of the thin film battery by optimizing the deposition conditions cathode layer.

Improve the cycle life of the thin film battery cathode layer by doping with suitable metal ions.

1.7 Reference.

[1] Tarascon J.M and Armand M, 2001, Nature 414, 359.
[2] A. J. Bard and L. R. Faulkner, Electrochemical Methods, John Wiley and Sons (1980).
[3] Welfare, S. and Fairley, J. Arthur C Clarke's Mysterious World, Collins-1980, pp. 62-64.
[4] Paul FleuryMottelay, Bibliographical History of Electricity and Magnetism, (2008), ISBN 1443728446.
[5] Strong F. C. Faraday's Laws in One Equation, Journal of Chemical Education, doi:10.1021/ed038p98.
[6] Batteries: History, Present, and Future of Battery Technology by Wrosch: http://www.extremetech.com/computing/49004-batteries-history-present-and-future-of-battery-technology?print].
[7] Whittingham, M. S. Electrochemical energy storage and intercalation chemistry. Science 192, 1226 (1976).
[8] Whittingham, M. S. Chalcogenide battery. US Patent 4009052.
[9] Samar B, Somerset NJ. Rechargeable Battery.USPTO 1981; US4304825.
[10] Handbook of Batteries, 2nd edition, D. Linden, Ed., McGraw-Hill, Inc., NewYork (1995).
[11] Modern Batteries: An introduction to Power sources Colin A. et.al Edward Arnold (1984).
[12] "Advanced Secondary Batteries" A review. R.M Dell U.K. Atomic Energy Authority (1979).
[13] Ozawa K. Solid State Ionics 1994; 69: 212-21.
[14] Xu K. Nonaqueous liquid electrolytes for lithium-based rechargeable batteries. Chem. Rev 2004; 104: 4303-417.
[15] Electrochemistry: Principles, Methods, and Applications, C. M. A. Brett, and A. M. O. Brett, Oxford University Press, Oxford, 1993.
[16] D. Pletcher, AFirst Course in Electrode Processes, The Electrochemical Consultancy, Alresford Press Ltd., 1991.
[17] Gritzner G, Kreysa G. Pure &ApplChem 1993; 65: 1009-20.
[18] Arun Patil, Vaishali Patil, Dong Wook Shin, Ji-Won Choi, Dong-Soo Paik, Seok-Jin Yoon, Materials Research Bulletin, 43 (2008) 913–1942.
[19] K. Kanehori, Y. Ito, F. Kirino, K. Miyauchi, and T. Kudo, Solid State Ionics 18/19 (1986) 818.

[20] K. Mizushima, P.C. Jones, P.J. Wiseman, J.B. Goodenough, Mater. Res. Bull. 15 (1980) 783.
[21] Solid State Ionics for Batteries, M. Tatsumisago et.al.Springer, 2005.
[22] J. Yamaki, H. Ohtsuka, and T. Shodai, Solid State Ionics 86-88 (1996) 1279.
[23]. H. Ohtsuka and A. Yamaji, Solid State Ionics 8 (1983) 43 .
[24] H. Ohtsuka, Okada, S.,Yamaki, J., Solid State Ionics 40-1 (1990) 964.
[25] H. Ohtsuka and J. Yamaki, Jpan.J.Appl.Phys. 28 (1989) 2264.
[26] S. D. Jones, Akridge, J.R., Solid State Ionics 53-6 (1992) 628.
[27] J. R. Akridge and H. Vourlis, Solid State Ionics 18-19 (1986) 1082.
[28] S. D. Jones, J. R. Akridge, and F. K. Shokoohi, Solid State Ionics 69 (1994) 357.
[29] J. B. Bates, Gruzalski, G.R., Dudney, N.J., Luck, C.F., Yu, X.H., Solid State Ionics 70 (1994) 619.
[30] J. B. Bates, N. J. Dudney, B. Neudecker, A. Ueda, and C. D. Evans, Solid State Ionics 135 (2000) 33.
[31] X. Yu, J. B. Bates , G. E. Jellison, and F. X. Hart, J. Electrochem. Soc., 144 (1997) 524.
[32] B. Wang, J. B. Bates, F. X. Hart, B. C. Sales, R. A. Zuhr, and J. D. Robertson, Journal of the Electrochemical Society 143 (1996) 3203 6.
[33] B. J. Neudecker, N. J. Dudney, and J. B. Bates, J. Electrochem. Soc., 147 (2000) 517.
[34] Zhang et al., US Patent 10,207,445 (2002).
[35] M. Winter, J.O. Besenhard, M.E. Spahr, P. Novak, Adv. Mater. 10 (1998) 725.
[36] A.S. Arico, P. Bruce, B. Scrosati, J.-M. Tarascon, W. Van Schalkwijk, Nature 4 (2005) 366.
[37] C. Kim, T. Fujino, K. Miyashita, T. Hayashi, M. Endo, M.S. Dresselhaus, J. Electrochem. Soc. 147 (2000) 1257.
[38] R.J. Gummow, D.C. Liles, M.M. Thackeray, Mater. Res. Bull. 28 (1993) 1249.
[39] R.J. Gummow, M.M. Thackeray, J. Electrochem. Soc. 141 (1994) 1178.
[40] Winter M, Besenhard JO, Spahr ME, Novák P, Adv Mater 10(1998b) 738.
[41] Whittingam MS, Chem Rev 104 (2004) 4271.
[42] Ohzuku T, Makimura Y., Chemistry Letters 30 (2001) 642.

[43] Kim JM, Chung HT, ElectrochimicaActa 49(2004) 937,
[44] Thackeray MM, David WIF, Bruce PG, Goodenough JB., Mat Res Bull 18 (1983) 461.
[45] M.M. Thackeray, L.A. de Picciottoa, A. de Kocka, P.J. Johnsona, V.A. Nicholasa and K.T. Adendorffa, Journal of Power Sources , 21(1987)1.
[46] J.M. Tarascon, W.R. McKinnon, F. Coowar, T.N. Bowmer, G. Amatucci, D. Guyomard, J. Electrochem. Soc. 141 (1994) 1421.
[47] Thirunakarana R, Kimb K T, Kangb YM, Yong-lee J. Mater Res Bull, 40 (2005)177.
[48] Sun YK, Jeon YS, LeebHJ.,Electrochem Solid-State Lett, 3(1)(2000) 7.
[49] Julien C, Mangani IR, Selladurai S, Massot A., Solid State Sci. 4(2002) 1031.
[50] Zhao Ming-shu, Song Xiao-ping., Trans Nonferrous Met Soc China 14 (2004) 8118.
[51] Padhi, A. K.; Nanjundaswamy, K. S.; Goodenough, J. B. J., Electrochem. Soc., 144(1997)1188.
[52] Yamada, A.; Chung, S. C.; Hinokuma, K. J. Electrochem. Soc.,148, A224 (2001).
[53] Masquelier, C.; Padhi, A. K.; Nanjundaswamy, K. S.; Goodenough, J. B. J. Solid State Chem. 135, 22 (1998).
[54] K.Amine, H.Yasuda, M.Yamachi, Electrochem and solid state, Lett. 3, 178 (2000).
[55] A.Yamada, Y.Kudo., K Y Liu, J.Electrochem.Soc.148 A 1153, (2001).
[56] A.Yamada, Y.Kudo., K Y Liu, J.Electrochem.Soc.148 A 747 (2001).
[57] S. Geller., J.L.Durand., ActaCrystallogr., 13, 325 (1960).
[58] F.Zhou, C A Marianetti, M.Cococcioni, D.Morgan and G.Ceder, Phy.Rev B. 69, 201101(R) (2004).
[59] C. V. Ramana, A. Ait-Salah, S. Utsunomiya,U Becker, A.Mauger, F. Gendron,C. M. Julien Chem. Mater. 18, 3788 (2006)
[60] A. Yamada, M. Hosoya, S.-C.Chung, K. Hinokuma, Y. Kudo, K.-Y. Liu, in: A. Manthiram, P.N. Kumta, S.K. Sundaram and G. Ceder (Eds.), Materials for Electrochemical Energy Conversion and Storage, American Ceramic Society, Westerville,189 (2002).
[61] A. Yamada, M. Hosoya, S.C. Chung, Y. Kudo, K.Y. Liu, in: G. Nadri, R. Koetz, B. Scrosati, P.A. Moro, E.S. Takeuchi (Eds.),Advanced Batteries and

Super capacitors, The Electrochemical Society, Pennington, NJ, PV2001 (2001).
[62] S-Y Chung, J.T. Bloking., Y.-M. Chiang, Nature Materials, 1, 123-128 (2002).
[63] P. SubramanyaHerle, B. Ellis, N. Coombs and l. F. Nazar, Nature materials 3, 147 (2004).
[64] H.Huang, S.-C.Yin, L. F. Nazar, Electrochem. Solid-State Lett., 4, A170 (2001).
[65] Y.Inabaetal.Extended abstracts of the 22nd symposium on Solid state Ionics in Japan .53(1993).
[66] S. S. Zhang , J. L. Allen, K. Xu and T. R. Jow, J. Power, Sources, 147, 234 (2005).
[67] F. Croce, A. D'Epifanio, J. Hassoun, A. Deptula, T. Olczac and B. Scrosati, Electrochem. Solid State Lett.5 A47 (2002).
[68] K.S. Park, J.T. Son, H.T. Chung, S.J. Kim, C.H. Lee, K.T. Kang, H.G. Kim, Solid State Commun. 129, 311 (2004).
[69] S. Shi, L. Liu, C. Ouyang, D.S. Wang, Z. Wang, L. Chen, X. Huang, Phys. Rev. B 68, 195108 (2003).
[70] A. Singhal, G. Skandan, G. Amatucci, F. Badway, N. Ye, A. Manthiram, H. Ye, J.J. Xu, J. Power Sources 129,38 (2004).
[71] A.J. Jacobson, R.R. Chilannelli, M.S. Whittingham, J. Electrochem. Soc. 12 (1979) 2277.
[72] J. Desilvestro, O. Haas, J. Electrochem. Soc. 137 (1990) 5C.
[73] R.J. Gummow, A. De Kock, M.M. Thackeray, Solid State Ionics 69 (1994) 59.
[74] J. Kohler, H. Makihara , H. Uegaito, H. Inoue, M. Toki, ElectrochimActa 46 (2000) 59.
[75] M.-S. Park, S. Rajendran, Y.-M.Kang, K.-S.Han, Y.-S.Han, J.-Y. Lee, J. Power Sources 158 (1) (2006) 650.
[76] J.R. Dahn, A.K. Sleigh, H. Shi, B.M.Way,W.J.Weydanz, J.N. Reimers, Q. Zhong, U. von Sacken, in: G. Pistoia (Ed.), Lithium Batteries: New Materials, Developments and Perspectives, Elsevier, Amsterdam, 1994, p. 1.
[77] J.R. Dahn, A.K. Sleigh, H. Shi, B.M.Way,W.J.Weydanz, J.N. Reimers, Q. Zhong, U. von Sacken, in: G. Pistoia (Ed.), Lithium Batteries: New Materials, Developments and Perspectives, Elsevier, Amsterdam, 1994, p. 1.

[78] R. Yazami, M.Z.A. Munshi, Handbook of Solid State Batteries and Capacitors, 1995 ISBN no. 981-02-1794-3.
[79] I.A. Courtney, J.R. Dahn, J. Electrochem Soc. 144 (1997) 2045.
[80] T. Doi, K. Takeda, T. Fukutsuka, Y. Iriyama, T. Abe, Z. Ogumi, Carbon 43 (11) (2005) 2352.
[81] F. Béguin, F. Chevallier, C. Vix-Guterl, S. Saadallah, V. Bertagna, J.N. Rouzaud, E. Frackowiak, Carbon 44 (10) (2005) 2160.
[82] G. Brancolini, F. Negri, Carbon 42 (5-6) (2004) 1001.
[83] S. Pruvost, C. Hérold, A. Hérold, P. Lagrange, Carbon 42 (8-9) (2004) 1825.
[84] C. Hérold, S. Pruvost, A. Hérold, P. Lagrange, Carbon 42 (10) (2004) 2122.
[85] Goers D, Buqa H, Hardwick L, Wuersig A, Novák P, Ionics 9 (2003) 258.
[86] Endo M, Nakamura J, Sasabe Y, Takahashi T, Inagaki M, Trans IEE Jpn A 115 (1995) 349.
[87] Wu GT, Wang CS, Zhang XB, Yang HS, Qi ZF, He PM, et al., JElectrochemSoc 146 (1999) 1696.
[88] Lu W, Chung DDL, Carbon 39(4)(2001)493.
[89] Frackowiak E, Béguin F, Carbon 40(10)(2002)1775.
[90] Ng SH, Wang JZ, Guo ZP, Chen J, Wang GX, Liu HK, ElectrochimicaActa 51 (2005)23.
[91] Gao B, Sinha S, Fleming L, Zhou O, Adv Mater 13 (2001) 816.
[92] Frackowiak E, Béguin F, Carbon 40(10)(2002)1775.
[93] R.A. Huggins, in: J.O. Besenhard (Ed.), Handbook of Battery Materials, Wiley-VCH, Weinheim, 1999, Part III (chapter 4).
[94] M. Winter, J.O. Besenhard, Electrochem. Acta 45 (1999) 31.
[95] Handbook of Battery Materials by J. O. Besenhard, Jürgen O. Besenhard, Wiley-VCH, 1999, ISBN-10: 3527294694.
[96] J.O. Besenhard, J. Yang, M. Winter, J. Power Sources 68 (1997) 87.
[97] T. Nohma, S. Yoshimura, K. Nishio, Y. Yamamoto, S. Fukuoka, M. Hara, J. Power Sources 58 (1996) 205.
[98] Sanyo Electric, US Patent 4 820 599 (1989).JEC Battery Newslett.3 (1989) 15.
[99] Y. Idota, T. Kubota, A. Matsufuji, Y. Maekawa, T. Miyasaka, Science 276 (1997) 1395.

[100] M.M. Thackeray, J.T. Vaughey, A.J. Kahaian, K.D. Kelper, R. Benedek, Electrochem.Commun.1 (1999) 111.
[101] Taeho Moon, Chunjoong Kim, Byungwoo Park, Journal of Power Sources 155 (2006) 391.
[102] Y. Idota, T. Kubota, A. Matsufuji, Y. MaeKawa, T. Miyasaka, Science 276 (1997) 1395.
[103] J.-M.Tarascon, S. Grugeon, S. Laruelle, D. Larcher, P. Poizot, in: G.-A. Nazri, G. Pistoia (Eds.), Lithium Batteries Science and Technology, Kluwer Academic/Plenum, Boston, 2004 , p. 220 (chapter 7).
[104] Strobel P, LeCras F, Anne M., J Solid State Chem 124(1996) 83.
[105] F. Croce, G.B. Appetcchi, L. Persi, B. Scrosati, Nature 394 (1998) 456.
[106] B. Scrosati, F. Croce, L. Persi, J. Electrochem.Soc. 147 (2000) 1718.
[107] P.A.R.D. Jayathilaka, M.A.K.L. Dissanayake, I. Albinsson, B.E. Mellander, Electrochim.Acta 47 (2002) 3257.
[108] B.K. Mandal, A.K. Padhi, Z. Shi, S. Chakraborty, R. Filler, J. Power Sources 162 (2006) 690.
[109] B.K. Mandal, A.K. Padhi, Z. Shi, S. Chakraborty, R. Fille, J. Power Sources 161 (2006) 215.
[110] Y. Li, J.A. Yerian, S.A. Khan, P.S. Fedkiw, J. Power Sources 161 (2006) 1288.
[111] C. Korepp, H.J. Santner, T. Fujii, M. Ue, J.O. Besenhard, K.-C.Möller, M. Winter, J. Power Sources 158 (1) (2006) 578.
[112]. Kanno, R.; Maruyama, M., J. Electrochem.Soc. 148 (7) (2001) A742.
[113] Mizuno, F.; Hayashi, A.; Tadanaga, K.; Tatsumisago, M., Adv. Mater., 17(7) (2005) 918.
[114] M. Murayama, N. Sonoyama, A. Yamada, R. Kanno, Solid State Ionics 170 (2004) 173.
[115] M. Tatsumisago, F. Mizuno, A. Hayashi, J. Power Sources 159 (2006) 193.
[116] Knauth, P., Solid State Ionics, 180(2009) 911.
[117] Minami, K.; Hayashi, A.; Tatsumisago, M., Solid State Ionics, 179(2008) 1282.
[118] M.M. Thackeray, M.H. Rossouw, A. de Kock, A.P. de la harpe, R.J. Gummow, K. Pearce, and D.C. Liles, J. Power Sources 43-44 (1993) 289.

[119] Introduction to Solid state Physics" by Charles Kittel.John Wiely& Sons.INC (2000).
[120] S. Chitra, P. Kalyani et al., Ionics 4 (1998).
[121] C. Ouyang, H. Deng, Z. Ye, M. Lei and L. Chen, Thin Solid Films 503, 268 (2006).
[122] H. Berg, K. Goransson, B. Nolang and J. O. Thomas, J. Mat.Chem. 9 2813 (1999).
[123] C. Ouyang, H. Deng, Z. Ye, M. Lei and L. Chen, Thin Solid Films 503, 268 (2006).
[124] M. K. Aydinol, A. F. Kohan, G. Ceder, K. Cho and J.Joannopoulos, Phys. Rev. B, 56, 1354 (1997).
[125] A. Paolone, C. Castellano, R. Cantelli, G. Rousse and C. Masquelier, Phys. Rev. B, 68, 14108 (2003).
[126] M. K. Aydinol, A. F. Kohan, G. Ceder, K. Cho and J. Joannopoulos, Phys. Rev. B, 56, 1354 (1997).
[127] K. Kushida and K. Kuriyama, App. Phys. Lett., 77, 4154 (2000).
[128] M Wakihara, H. Ikuta and Y Uchimoto, Ionics 8, 329 (2002).
[129] M. K. Aydinol, A. F. Kohan, G. Ceder, K. Cho and J. Joannopoulos, Phys. Rev. B, 56, 1354 (1997).
[130] S. Megahed, B. Scrosati, TheElectrochem. Soc. Interface, winter 34-37 (1995).
[131] V. S. Pervov, I. A. Kedrinskii, E. V. Makhonina, Inorg. Mater., 33 [9] 869-877 (1997).
[132] M.M Thackeray, P.J.Johnson, dePiccioto, P.G.Bruce and J B Goodenough. Mat. Res. Bull. 19, 179 (1984).
[133] Guohua Li, Astuo Yamada, Yuzuru Fukushima, Kiyoshi Yamaura, Takamitsu Saito, Takuya Endo, Hideto Azuma, kojiSekai, Yoshio Nishi, Solid State Ionics 130, 221 (2000).
[134] H.Bjork, T.Gustafson, J.O.Thomas, Eelectrochem.Commun, 3,187 (2001).
[135] S.R.S Prabhakaran, Nasiman B, S.S.Michael, M.Massot, C. Julien, Solid State Ionics 112 ,25 (1998).
[136] Malcom Gerloch, Edwin C. Constable "Transition Metal Chemistry" VCH Pulishers, Newyork , NY, (USA) (1994).
[137] S. Thomas Lee, K. Raveendranath, M. RajiveTomy, M.Paulraj, S. Jayalekshmi and Jyotsna Ravi, Appl. Phys. Lett.90, 161912 (2007).

[138] S. Thomas Lee, K. Raveendranath, M. Rajive Tomy, Nibu A. George, S. Jayalekshmi and J. Ravi, J. Phys. D: Appl. Phys. 40,3807-3810 (2007).
[139] Arun Kumar T A, The University of Texas, Austin, thesis, August 2007
[140] S. K. Mishra and G. Ceder, Phys. Rev. B, 59, 6120 (1999).
[141] V. W. J. Verhoeven, I. M. de Schepper, G. Nachtegaal, A. P. M.Kentgens, E. M. Kelder, J. Schoonman and F. M. Mulder, Phys.Rev. Lett. 86, 4314 (2001)
[142] M. M. Thackeray, Prog.Solid State Chem., 25, 1 (1997).
[143] M. M. Thackeray, J. Electrochem. Soc., 142 [8] 2558-2563 (1995).
[144] N. W. Grimes, J. Phys. C: Solid State Physics, 4,L342-L344 (1971).
[145] D. H. Jang, Y. J. Shin, S. M. Oh, J. Electrochem. Soc., 143 [7] 2204-2211 (1996).
[146] D. H. Jang, S. M. Oh, J. Electrochem. Soc., 144 [10] 3342-48 (1997).
[147] D. Aurbach, Y. Gofer, J. Electrochem.Soc., 138 [12] 3529-35 (1991).
[148] K. Hong and Y. Sun, J. Power Sources, 109, 427 (2002).
[149] R. Alcantara, M. Jaraba, P. Lavela, and J. L. Tirad, J. Electroanal.chem., 566, 187 (2004).

Chapter 2

Deposition and characterization techniques

Abstract: This chapter gives an account of the various techniques available for the deposition of cathode films for all solid state lithium ion battery applications. The advantages of RF sputtering, especially high frequency RF magnetron sputtering, over other thin film deposition processes and its commercial implications are addressed in detail. The theoretical aspects of various experimental tools used in the present work including X -ray diffraction (XRD), scanning electron microscopy (SEM), energy dispersive X-Ray (EDX) analysis, atomic force microscopy, Raman spectroscopy, and electrochemical characterization techniques, are also illustrated briefly.

2.1 Thin film deposition techniques: An introduction.

Thin film technology is a major area of scientific research worldwide, because of its wide range of applications in fields such as optics, electronics, biotechnology, and the tool manufacturing industry. It enables the fabrication of miniaturized devices with high performance and reliability. Conventional bulk fabrication techniques are not suitable for the fabrication of thin film layers/devices, since such techniques do not scale down to the desired size with sufficient efficiency relative to cell volume. Therefore, micro-fabrication techniques similar to those being used in the microelectronic processes need to be used.

In any thin film micro-fabrication technique, the physical and chemical properties of the films strongly depend on the mechanism of film growth. The electrical and optical properties of the films in general are much dependent on the structure, morphology and the nature and density of defects in the films. Similarly, in the case of thin film lithium ion cells, the electrochemical properties mainly depend on the physical and chemical properties of the cathode materials. These properties vary with the deposition techniques and deposition parameters. So understanding the properties like composition, morphology, structure, crystallinity, electronic and ionic transport properties, and their relation to the deposition processes and parameters can be of help in optimizing the characteristics of the cathode materials. Thus the choice of the right deposition technique is important for obtaining films with the desired properties

Micro-fabrication techniques constitute a well established area, thanks to the wide range of applications in the semiconductor industry [1]. There are a variety of micro-fabrication techniques available to cast oxide films on to various substrates. Some of the well studied deposition processes include, sol-gel process, electrostatic spray deposition (ESD), chemical vapor deposition (CVD), electron beam gun evaporation, pulsed laser deposition (PLD), and magnetron sputtering. In most of the commercial all solid state thin film battery manufacturing processes, the thin film cathode materials are deposited by using variations of these techniques. Each deposition technology has its own unique

features, advantages and disadvantages. This chapter gives a brief review of some of the techniques widely used for the deposition of oxide thin films for lithium ion battery applications.

2.2 Thin film preparation techniques: An over view

The thin film deposition techniques used for oxide materials are broadly classified into two categories, such as physical methods and chemical methods. The chemical methods consist of chemical vapor deposition, sol gel techniques and electrostatic spray deposition (ESD). The physical methods are mainly constituted by evaporation, sputtering and pulsed laser deposition (PLD). The following sections portray the methodology and experimental set-up used in various thin film deposition techniques.

2.3 Chemical methods to prepare thin films

2.3.1 Chemical vapor deposition

Chemical vapor deposition (CVD) refers to the deposition of a non-volatile solid film on a substrate from the reaction of vapor phase chemical reactants containing the right constituents.

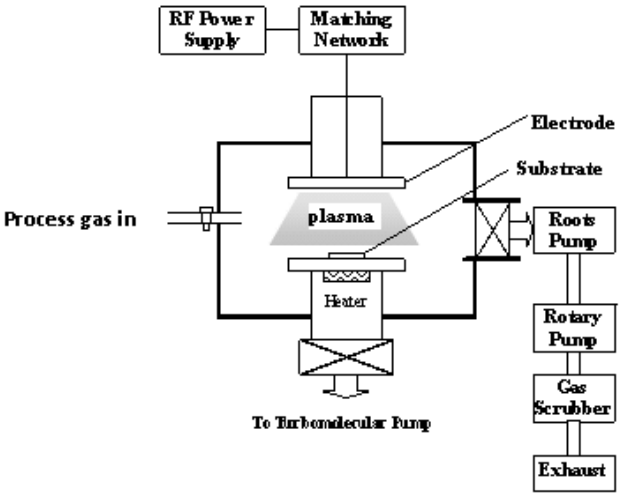

Fig. 2.1: Schematic diagram of a PECVD reactor.

A reaction chamber is used for this process, into which the reactant gases are introduced to decompose and react with the substrate to form the film. The CVD process is mainly classified as APCVD, LPCVD, and PECVD, among which PECVD is the mostly widely used technique for depositing semiconductor films [2]. Figure 2.1 shows the schematic diagram of a typical PECVD reactor.

In PECVD process, a glow discharge is created by applying an RF field to a low-pressure gas, creating free electrons within the discharge region. The electrons are sufficiently energized by the electric field, so that gas-phase dissociation and ionization of the reactant gases occur when the free electrons collide with them. Energetic species are then adsorbed on the substrate surface, where they are subjected to ion and electron bombardment, resulting in rearrangements, reactions with other species, new bond formation, film formation and growth. A typical example for oxide cathode material film formation by PECVD process is the formation of vanadium pentaoxide (V_2O_5) films [3]. In this process vanadium oxytrichloride and hydrogen are used as the precursor gases.

$$4\ VOCl_3 + 6H_2 + 3O_2 \xleftrightarrow{\text{Plasma}} 2V_2O_5 + 12HCl\uparrow$$

2.3.2 Sol-gel spin casting techniques

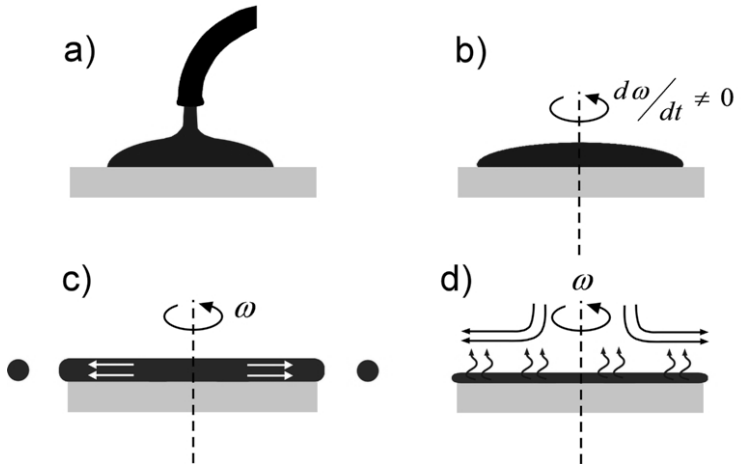

Fig.2.2: Schematic representations of sol-gel spin casting [5].

The schematic diagram of sol gel spin casting is shown in figure 2.2. Sol gel spin coating technique is a simple and cost effective method, which can be used for depositing oxide films on irregular and/or large surfaces. 'Sol gel' is a colloidal suspension of particles that is gelled to form a solid. The solution or sol is prepared by dissolving metalorganic precursors in the required ratio in deionized water and agitating at 80℃ for a few hours. The sol containing the organometallic compounds is dispensed on to a substrate in a controlled manner, and then the substrate is spun out at a constant speed forming a thin film at atmospheric conditions. This film is then baked at high temperatures to remove water and carbon groups, resulting in the formation of the required oxide film [4, 5].

Among the various thin film deposition techniques, the sol-gel technique has the special advantage of achieving large area coatings with easy control of the doping level, solution concentration and homogeneity, without using expensive and complicated equipments, compared to other methods. The low specific surface area seems to be a serious disadvantage of sol-gel films deposited on flat substrates. The other drawbacks of this technique include high cost of raw materials, shrinkage of film during processing and toxicity of some precursors.

2.3.3 Electrostatic spray deposition

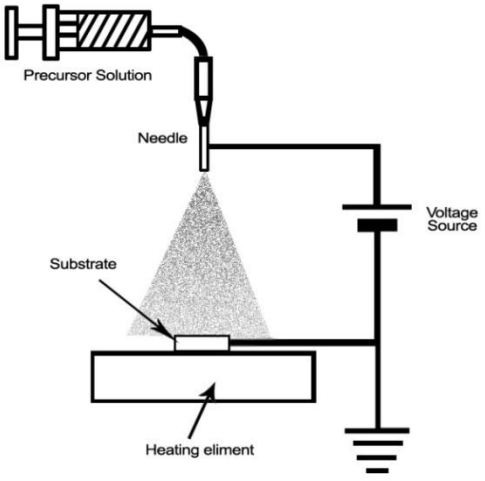

Fig. 2.3: Schematic representation of ESD technique.

Electrostatic spray deposition (ESD) technique is a widely used chemical method to deposit thin films [6-8].It involves spraying a solution, usually aqueous, containing soluble salts of the constituents of the desired compound, onto a heated substrate. The solution can be acetate, nitrate or chloride, and nitrate solution requires lower substrate temperatures to decompose while chloride needs higher temperatures. This method is quite suitable for depositing large area thin films, with good reproducibility. In this technique the solutions of precursors in the reservoir are pumped through a flexible tube to the tip of a nozzle. The nozzle is a stainless steel capillary with a slanted tip of 15° at the end. Due to the high electric field imposed by the DC power source between the nozzle and the substrate, the solution at the nozzle tip is disrupted by the electrostatic force to form fine aerosol droplets. The droplets are then attracted by the electric field, and land on the heated substrate, where evaporation, wetting, drying and decomposition take place to form oxide layers. The temperature of the substrate during deposition is maintained at a constant value by a temperature controller in conjunction with a thermocouple and heating element. The schematic diagram of ESD technique is shown in figure 2.3.

2.4 Physical methods used to deposit thin films.

One of the most common techniques which falls under the category of physical vapor deposition (PVD) processes is thermal evaporation. Thermal evaporation involves heating a solid material inside a high vacuum chamber up to a temperature high enough to produce vapors of the material. Under high vacuum conditions, even a relatively low vapor pressure is sufficient to raise a vapor cloud inside the chamber. This evaporated material now constitutes a vapor stream, which traverses the chamber and hits the substrate, sticking to it as a coating or film. There are two primary methods of heating the source material, categorized as thermal evaporation and electron beam evaporation.

2.4.1 Thermal evaporation

The thermal evaporation setup mainly consists of a simple electrical resistive heating element, or filament. There are various physical configurations of these filaments, also known as “boats”, which essentially consist of pieces of thin

metal sheets of suitable (high melting point) metals, such as tungsten in which indentations or troughs are made for placing the material. The filament source offers the safety of low voltages, although very high currents are required. The schematic of a simple thermal evaporation setup using resistive heating is shown in figure 2.4.

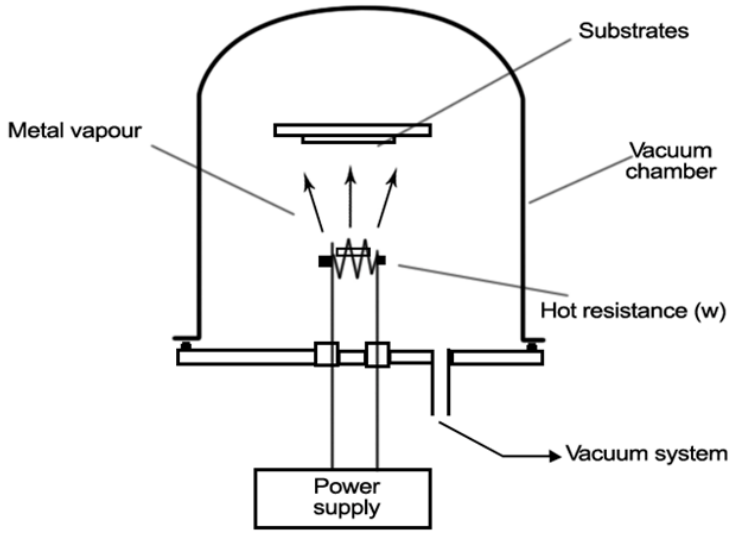

Fig. 2.4: Schematic representation of thermal evaporation technique.

The main disadvantage with thermal evaporation is that, due to high temperature of the resistive 'boat', the resistor material may react with the material under evaporation, and thus contaminate the evaporation purity and the quality of film. So this technique is primarily suitable for evaporating metals. Thermal evaporation is not suitable for depositing dielectric/ ceramic materials, because of the high evaporation temperature of these materials.

2.4.2 Electron beam evaporation.

The electron-beam evaporation, which is generally known as E-beam evaporation uses a stream of electrons for heating the evaporant material. The electron source, also known as the electron "gun" consists of a heated filament which emits electrons. These electrons are then accelerated by high voltage,

forming an electron beam with considerably high energy. This beam is magnetically directed onto the crucible in which the material to be evaporated is placed. The advantage of e-beam evaporation technique is that it can deliver highly concentrated power over a very small area, which heats up the material contained in a hearth. The crucible/hearth requires water-cooling to avoid damage due to excessive heating. The schematic of simple e-beam evaporation setup is shown in figure 2.5.

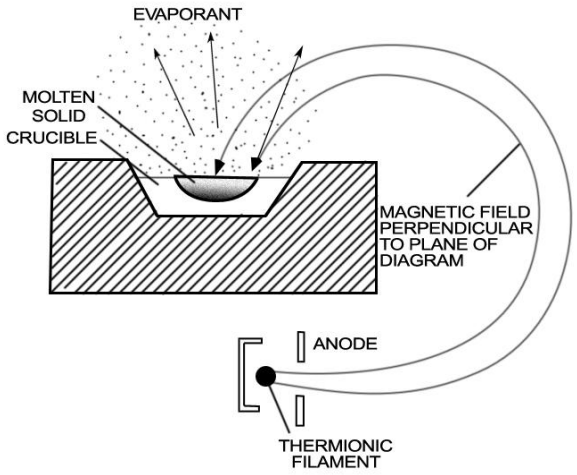

Fig. 2.5: Schematic of electron beam evaporation technique.

The deposition rate in this process can be as low as 1 nm per minute to as high as a few micrometers per minute. The material utilization efficiency is high relative to other methods and the process offers structural and morphological control of films. Due to the very high deposition rates, this process has many industrial applications. Moreover, since very high temperatures can be achieved in e-beam evaporation, it can be used for the evaporation of ceramic materials [9]. The main drawback with the e- beam evaporation technique is the lack of precise control of the stoichiometry of the compound materials.

2.4.3 Pulsed Laser Deposition (PLD).

Pulsed laser deposition (PLD) is a technique used to deposit thin films by utilizing suitable laser beams to ablate materials. PLD was the first technique used to successfully deposit the superconducting $YBa_2Cu_3O_7$ thin films [10].

Since then, many materials those are normally difficult to be deposited by other methods, especially multi-element oxides, have been successfully deposited by PLD. In the case of multi-elemental compounds such as high temperature superconductors, ferroelectrics and electro optic materials, this technique is extremely successful. This technique offers many potential applications, in integrated circuits, optoelectronics, micro mechanics and medical implants [11].

In PLD, a laser beam of sufficient intensity is focused and directed to a target located inside a vacuum chamber. The impact of the laser energy creates an expanding material plume which subsequently condenses as a solid material on a substrate. Schematic diagram of the pulsed laser deposition system is shown in figure 2.6.

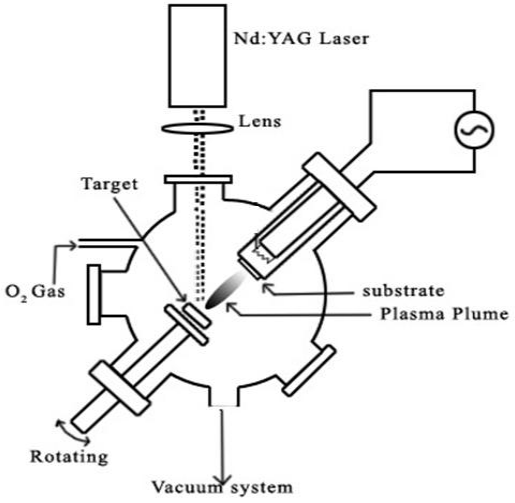

Fig. 2.6: Schematic of the PLD technique

The main advantage of PLD originates from the laser material removal mechanism. PLD relies on photon interactions to create an ejected plume of material from any target. The vapor (plume) is collected on a substrate placed at a short distance from the target. However, the actual physical mechanism of material removal is quite complex. One can consider the ejection of material to occur due to rapid explosion of the target surface due to superheating. Unlike thermal evaporation, which produces a vapor composition dependent on the vapor pressures of elements in the target material, the laser-induced expulsion

produces a plume of material with stoichiometry similar to the target. It is generally easier to obtain the desired film stoichiometry from multi-element materials using PLD than with any other deposition techniques [12]. The main disadvantage with the PLD technique is that, the deposition is limited to small areas, and so the possibility of scaling up to large area deposition is difficult.

2.4.4 Sputtering.

Sputtering is a process by which atoms are knocked out from a solid target material due to bombardment of energetic ions. The deposition of these ejected atoms on a substrate under suitable conditions is known as sputter deposition. The most important characteristic of sputtering is its universality. As the cathode target atoms are ejected by physical momentum-exchange process, practically almost any solid material can be sputtered. Sputtering has two main advantages over other compound deposition methods. It takes place from a solid target source, and the composition of the source material is reproduced in the final coating. Sputter deposition has led to the development of a number of commercial applications ranging from microelectronics fabrication to simple decorative coatings.

2.4.5 Sputtering Phenomena.

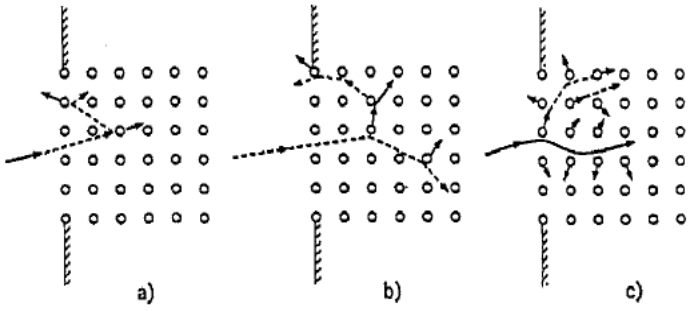

Fig. 2.7: A schematic representation of sputtering by elastic collision: (a) the single knock-on regime; (b) the linear cascade regime; (c) the non-linear or spike regime in which there is a high density of recoil atoms so that most atoms in a certain volume are moving [13].

When the target material is bombarded with energetic ions, these ions may get reflected back, coalesce, scatter, sputter surface atoms, or get buried in sub-surface layers. This in turn results in surface heating, chemical reactions, atom mixing and alteration of surface topography. If ion-surface collisions are successful in setting target atoms in motion, and if enough energy is transferred to target atoms, they overcome the force of binding energy and sputtering takes place. Depending on the energy of the recoiling target atoms after collision with the ions, and on the spatial density of the recoils, different collision cascade regimes can be distinguished as single knock on regime, linear cascade regime and nonlinear cascade regime.

In the single knock-on regime (Fig. 2.7a), only a small amount energy is transferred between the ions and target atoms. The recoil atoms at the target surface may receive sufficient energy to overcome the surface binding energy, and thus may be sputtered. The minimum energy required for this is called the threshold energy (E_t). Typical values for E_t range from 5 to 40 eV depending on the nature of the incident ions, mass and the atomic number of the target atoms and the binding energy of atoms to the surface (U_s). Typically, U_s may be assumed to be the heat of sublimation or vaporization and ranges between 2 and 5 eV. Since the received energy is not enough to generate recoil cascades, only few collisions will occur in this regime. [13].

In the linear-cascade regime, the target is bombarded with ions of medium or high masses with energies exceeding a few hundred eV. Large energies are transferred to atoms on the surface of the target, leading to the evolution of larger collision cascades, which can be thought of as collisions taking place between a moving atom and an atom at rest (Fig. 2.7b). Such a cascade is termed linear because the solution of a Boltzmann transport equation relating the collision cascade is linearized under the postulate that only collisions between a moving atom and a stationary atom occur.[14, 15]

At higher recoil densities, nonlinear cascade regime will be prominent, i.e. majority of atoms within the cascade volume are concurrently in motion or the cascade is said to have entered the spike regime. For this condition, the ions must have adequately high energies up to 10 keV and heavy atomic mass, to generate high recoil densities of atoms in the target surface (Fig. 2.7c). For such

a spike regime, both theoretical and experimental work reveals that the number of sputtered atoms rises non-linearly with the energy falling at the target surface, and thus such a cascade has been termed nonlinear [16]. The difference between a linear collision cascade and a spike regime is that only a small fraction of the atoms is in motion in a certain cascade volume in a linear cascade, whereas all atoms move in a certain spike volume.

The sputter yield, S i.e. number of sputtered target atoms per incident ion, mainly depends on the incident ion energy, E. In the low-energy region near the threshold, S obeys the relation $S^2 \propto E$, as seen in figure 2.8. For ion energies of the order of 100 eV, S is expressed by $S \propto E$. In this energy region, the incident ions collide with the surface atoms of the target, and the number of displaced atoms due to the collision will be proportional to the incident energy. At higher ion energies of 10 to 100 keV, the incident ions travel beneath the surface and the sputter yields are not governed by surface scattering, but by the scattering inside the target. Above 10 keV, the sputter yields will decrease due to energy dissipation of the incident ions deep in the target. Maximum sputter yields are seen for ion energies in the region of about 10 keV.

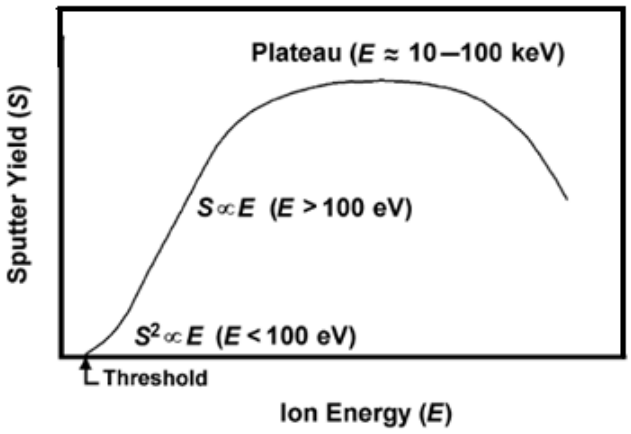

Fig. 2.8: Variation of sputter yield with ion energy [13].

There are different types of sputter depositions in use today, such as direct current sputtering (DC sputtering), radio frequency sputtering (RF sputtering) and magnetron sputtering, but all these are variants of the same physical phenomenon.

2.4.6 DC sputtering

The dc sputtering system is comprised of a pair of planar electrodes, in which one electrode is a cold cathode and the other is an anode. The surface of the cathode is covered with the target material and is water-cooled. The substrates are placed on the anode which is generally grounded. The sputtering chamber is filled with argon gas to a pressure of a few hundred mtorr, and several kilovolts of dc voltage is applied between the electrodes, thereby triggering a glow discharge. The Ar ions in the glow discharge are accelerated towards the cathode, and bombard the target, resulting in the sputter deposition of the target material on the substrates. When the ions strike the cathode, they may sputter some of the target surface atoms, and they may also liberate secondary electrons from the target. These secondary electrons are responsible for maintaining the electron supply for sustained glow discharge. The schematic diagram of dc sputtering is shown figure 2.9.

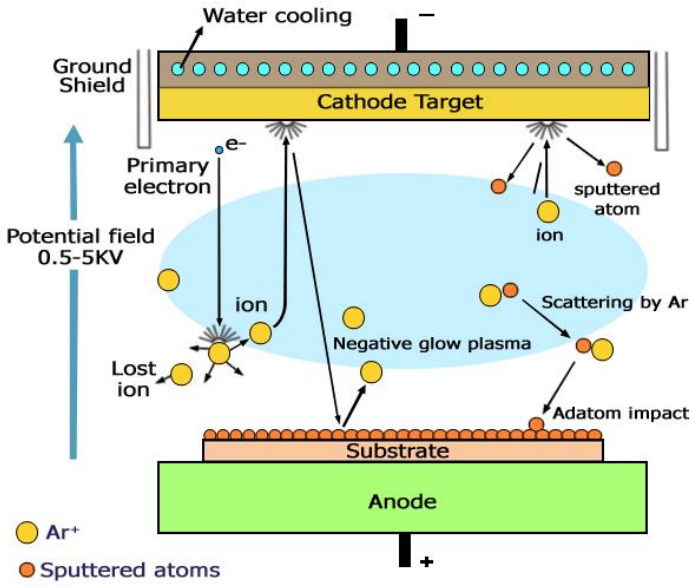

Fig. 2.9: The schematic diagram of dc sputtering

For a sputtering process, the relative thin film deposition rate depends on the operating pressure and ion current. At low pressures, the cathode plasma sheath is wide, ions are produced far from the target, and their probability of being lost to the chamber walls is more. Moreover, at lower pressures, the mean free path

of the electrons is large and so the electrons collected by the anode are not replenished by ion-impact-induced secondary electron emission at the cathode. Therefore, ionization efficiencies are low and self sustained discharges cannot be maintained below about 10 mtorr. As the pressure is increased at a fixed voltage, the electron mean free path is decreased, more and more ions are generated, and larger ion currents will flow. But if the pressure is too high, the sputtered atoms undergo increased collisional scattering and are not efficiently deposited [17].

2.4.7 RF sputtering

The main draw back with the DC sputtering technique is its inability to sputter insulator targets because of the immediate build-up of a positive surface charge on the front side of the insulator. So in order to sustain a glow discharge with an insulator target, the dc voltage power supply has to be replaced by an rf power supply.

When an ac signal of frequency of the order of 50Hz is applied to the electrodes, ions become sufficiently mobile to establish a complete discharge at each electrode on each half-cycle. In this condition, direct current sputtering takes place at both electrodes, and the electrodes behave as cathodes as well as anodes for every alternative signal cycle. When a high frequency ac signal is applied, electrons oscillating in the glow region attain enough energy to cause ionizing collisions, reducing the need for secondary electrons to sustain the discharge. The advantage is that insulating electrodes can also be used for sputtering, since the RF voltages can be coupled with any kind of impedance. This technique allows the sputtering of any material irrespective of its resistivity.

The basic working mechanism behind the RF sputtering technique is the formation of a negative self-bias (or sheath voltage) on the target surface. Due to this negative bias, it behaves like a DC target and positive ion-bombardment sputters away atoms for subsequent deposition. The negative target bias is due to the difference in electron and ion mobilities. In fact electrons are considerably more mobile than ions, and therefore have little difficulty in

following the periodic change in the electric field as compared to the ions. The discrepancy in electron and ion mobilities means that the isolated positively charged electrode draws more electron current than the positive ion current drawn by the negatively charged electrode. As a result of this, the discharge current-voltage characteristics are asymmetric. A schematic diagram of the RF sputtering is shown in figure 2.10.

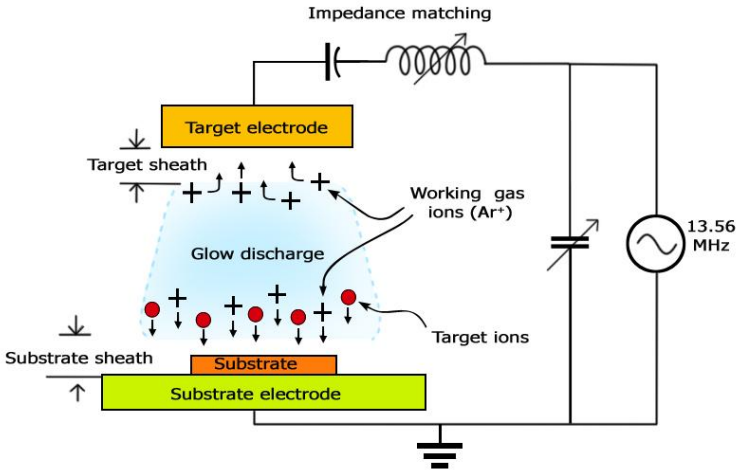

Fig. 2.10: Schematic diagram of the RF sputtering system

Since the plasma discharge has capacitive as well as resistive characteristics, for the efficient coupling of the RF power to the target, an impedance-matching network consisting of a combination of variable and fixed capacitors and inductors is required to ensure maximum power delivery. Moreover, in RF sputtering, capacitive reactance is inversely proportional to the capacitance or area. So more voltage drop will occur across the capacitor of a smaller surface area. For efficient sputtering, the area of the target electrode should be small compared with the total area of the other electrode. It has been shown that the ratio of the voltage across the sheath at the capacitively coupled electrode of smaller Area (A_c)V_c to that across the larger area (A_d) electrode V_d is given by,

$$V_c/V_d = (A_d/A_c)^4 \qquad (2.1)$$

This equation tells that smaller area will see a larger sheath voltage by a power of 4. The usefulness of this result is that $A_d > A_c$ must hold to selectively sputter

the target. This is done in practice by grounding the substrate holder to the entire chamber resulting in a very large A_d. For this reason it is extremely important that the substrate holder and the system are well grounded to ensure that resputtering of the growing film does not occur [13].

In rf diode sputtering, the cathode current density is given by

$$i_s = C\frac{dV}{dt} \qquad (2.2)$$

Where *C* is the capacitance between the discharge plasma and the target, and dV/dt denotes the time variations of the target surface potential. This indicates that the increase of the frequency increases the cathode ion currents [18].

In spite of the simplicity of the techniques, simple DC sputtering or RF sputtering is no longer employed in production environments because of low deposition rates. The low deposition rates are due to lack of secondary electrons for gas ionization. Even at optimum operating conditions, secondary electrons emitted from the cathode have an appreciable probability of reaching the anode or chamber walls without making ionizing collisions with the sputtering gas. Moreover higher sputtering pressure may not increase the rate of deposition appreciably. At higher pressures, the contaminant levels of O_2 and H_2O in chamber gases will be high, which can oxidize cathodes as well as contaminate the deposited film.

2.4.8 Magnetron Sputtering

The magnetron sputtering technique is a modified form of the classical DC/RF sputtering. In this method, an array of permanent magnets is arranged behind the cathode plate. This setup forms the planar magnetron sputtering gun/cathode. In this setup, the magnets are arranged in such a way that the magnetic field on the face of the target is normal to the electric field within a closed path, and forms a boundary "tunnel" which traps electrons close to the surface of the target. This arrangement improves the efficiency of gas ionization and confines the plasma, allowing higher current at lower gas pressure and achieves a better sputter deposition rate. A schematic diagram of magnetron sputtering is shown in figure 2.11.

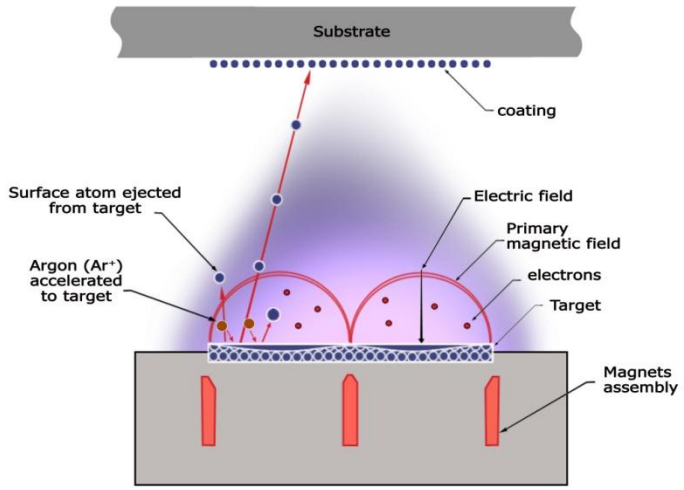

Fig. 2.11: Schematic diagram of the magnetron sputtering system

When the magnetic field is applied parallel to the surface of a target, and perpendicular to the electrical field, secondary electrons that are accelerated from the target to the substrate, are influenced by the Lorentz force given by the equation

$$\boldsymbol{F} = \frac{\boldsymbol{mdv}}{\boldsymbol{dt}} = -\boldsymbol{q}(\boldsymbol{\varepsilon} + \boldsymbol{v} \times \boldsymbol{B}), \qquad (2.3)$$

where $\boldsymbol{q}$, $\boldsymbol{m}$ and $\boldsymbol{v}$ are the electron charge, mass, and velocity, respectively.

Due to this, the secondary electrons follow a spiral path which increases the path length in the plasma and increases the probability of collisions with the background gas. This increases the ionization efficiency of the available electrons. So it is possible to sputter at lower pressures with much higher yield than those obtained in classical DC/RF sputtering.

In planar magnetron sputtering, targets erode preferentially in the confined region between the magnets arrays, where the plasma is most intense. This leaves a kind of race track ditch or depression that gradually deepens, surrounded by a much larger target area that undergoes less loss of target material. This kind of target erosion has a number of undesirable drawbacks such as low target area utilization, non uniformity in terms of film thickness and properties, reduced target life and gradual decrease in target cooling efficiency.

2.4.9 Bias Sputtering.

In bias sputtering, either a negative DC or RF bias voltage is applied externally to the substrate. Due to the bias, the electric fields near the substrate are modified, which vary the flux and energy of incident charged species, enhancing the quality of the deposited material.

In normal planar magnetron sputtering, negative bias voltage of the order of a few hundred volts is applied. Due to charge exchange processes in the anode dark space, only a few discharge ions strike the substrate with full bias voltage, and a broad low energy distribution of ions and neutrals bombard the growing film. This technique has been successfully utilized in RF as well as DC sputtering configurations.

Bias sputtering has been effective in altering a broad range of properties in deposited films like resistivity, hardness, residual stress, etch rate, optical reflectivity, film morphology, density and adhesion. The actual mechanism behind the baised sputtering is not well understood. It is thought that bias controls the sorbed gas content on the growing film surface by the re-sputtering of the gas atoms during low-energy ion bombardment. Under such a scenario, both the weakly bound physisorbed gases and strongly attached chemisorbed species may have large sputtering yields and low sputter threshold voltages. In some other cases, sorbed gases may have low sputter yields and will be incorporated within the growing film. Moreover, energetic particle bombardment before and during film formation and growth promotes numerous changes and processes at a microscopic level, including removal of contaminants, alteration of surface chemistry, enhancement of nucleation and re-nucleation, higher surface mobility of adatoms, and elevated film temperatures with attendant acceleration of atomic reaction and inter-diffusion rates. Film properties are then modified through roughening of the surface, removal of interfacial voids and subsurface porosity, formation of finer, more isotropic grain morphology and columnar grains in a way that strongly dramatizes structure-property relationships in practice. There are few ways to broadly influence such a wide variety of thin film properties, in so simple and cheap a manner, than by the application of substrate bias [13].

2.5 Characterization techniques

Thin film battery technology is an exciting area of research and this technology influences a wide range of applications in day today life. In the present scenario of thin film lithium ion battery research, the importance for assessing battery performance involves the estimation of the capacity and capacity fading of the battery. The life of the thin film battery is dependent on the aging effects of its chemical constituents which arise due to structural and phase changes, contact loss between particles, oxygen release and electrolyte decomposition. These drawbacks can be eliminated by careful study of the thin film materials used for assembling the battery.

For any technology and related applications to develop, extensive research must first be carried out to achieve the most favorable results. The initial steps in the development of thin film batteries are concerned with the identification of the optimum material synthesis conditions to achieve the required material characteristics. The expected device performance can be realized by choosing the most suitable materials through various characterization procedures.

The characterization process involves the investigation of the physical, chemical and electrochemical properties of the individual thin film battery layers obtained at different growth conditions and optimization of these properties for the best performance of the device. The basic thin film characterization techniques include, optimization of film thickness, X-ray diffraction study of the films for investigating the phase purity of the material, scanning electron microscopy with energy dispersive analysis, atomic force microscopy, Raman spectroscopy, electrical conductivity studies, and electrochemical characterization techniques including cyclic voltammetry and charge discharge cycling. This chapter describes these characterization techniques in detail, which are used to study the thin film cathode materials developed by high frequency magnetron sputtering.

2.5.1 Measurement of thin film thickness by stylus profiler

The thickness of the deposited films plays an important role in optimizing the properties of the different active layers in a device. Reproducible properties are

achieved only when the film thickness and the deposition parameters are kept constant. So thickness control is highly important in any thin film deposition process. Film thickness canbe measured either by *in-situ* monitoring of the rate of deposition or by *ex-situ* measurements after the film deposition. The ideal technique would be a highly accurate, contact/non-contact, high speed measurement with no disturbance on surfaces. In the present work, contact method using a stylus profiler has been used for film thickness measurement.

A stylus profiler consists of a diamond tip of the order of a few microns, which is kept vertically in contact with the film sample. The stylus profiler takes measurements electromechanically by moving the sample beneath the diamond tipped stylus. The high precision stage moves the sample according to a user defined scan length, speed and stylus force. The stylus is mechanically coupled to the core of a linear variable differential transformer (LVDT). When the stylus scans the sample surface, surface variations cause the stylus to be translated vertically. Electrical signals corresponding to the stylus movement are produced as the core position of the LVDT changes. The LVDT scales an ac reference signal proportional to the position change, which in turn is conditioned and converted to a digital format through a high precision, integrating, analog-to-digital converter. The film whose thickness has to be measured is deposited with a region masked. This creates a step on the sample surface. The thickness of the sample can be measured accurately by measuring the vertical motion of the stylus over the step [19].

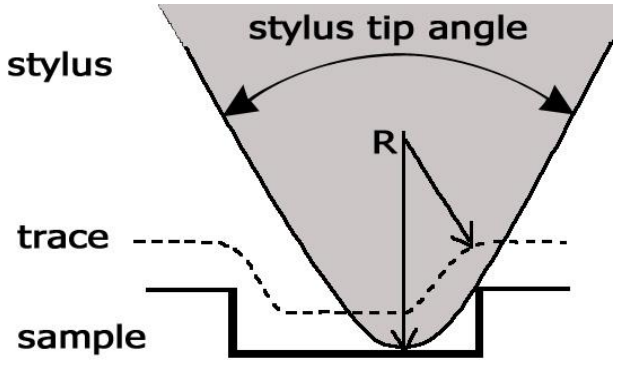

Fig. 2.12: Schematic diagram illustrating the determination of film thickness with stylus profiler

2.5.2 X-ray diffraction studies

A given crystalline substance always produces a distinctive x-ray diffraction pattern whether that substance is present in the pure state, or as one constituent of a mixture of substances. This fact is the basis for the diffraction method of chemical analysis. The advantage of x-ray diffraction analysis is that it unveils the existence of a compound and not in terms of its constituent chemical elements. Diffraction analysis is useful whenever it is crucial to know the state of chemical combination of the elements involved or the particular phase in which they are present. This feature makes the X-ray diffraction study an excellent tool to characterize the films for its structural properties. Compared with ordinary chemical analysis, the diffraction method has the advantage that it is much faster, requires only a very small amount of sample and is non destructive. The only disadvantage is that it is not a high resolution technique since it gives only microscopic information.

In X-ray diffraction (XRD) technique, a beam of X-rays incident on a crystalline material undergoes scattering by the electrons associated with the atoms. The scattered X-rays, in turn, undergo interference due to the periodic arrangement of atoms in the crystal and its symmetry. The interference is constructive in certain directions giving rise to a resultant diffracted beam in that direction with enhanced X-ray intensity. The interference is destructive in other directions.

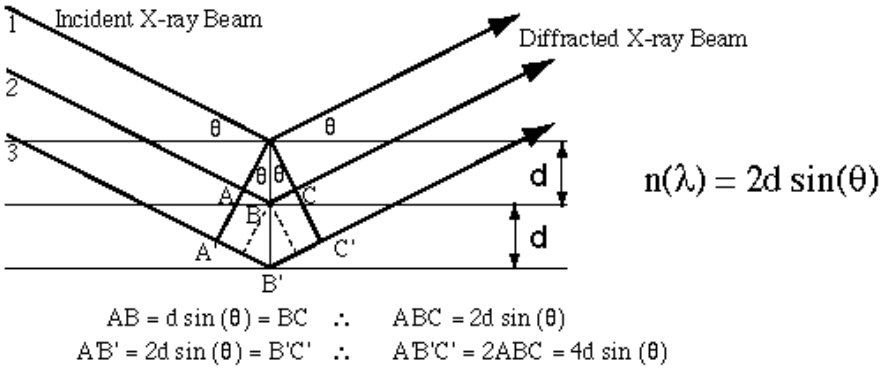

Fig. 2.13: Schematic representation of Bragg's law of diffraction in crystalline materials

The Bragg's equation forms the basis of X-ray diffraction, which determines the conditions of constructive interference of X-rays, and is given by the relation,

$$2dSin\theta = n\lambda, \qquad (2.4)$$

where n is the order of diffraction, 'λ' is the wavelength of the X-rays, 'd' is the inter atomic distance and 'θ' is the glancing angle (or the complement of the angle of incidence). The schematic diagram corresponding to crystal diffraction is given figure 2.13.

It is clear from the equation that by measuring the 2θ values for each diffraction peak, one can calculate the *d*-spacing for each diffraction peak. Each crystalline substance has a unique X-ray diffraction pattern. The number of observed peaks is related to the symmetry of the unit cell. The *d*-spacings of the observed peaks are related to the repeating distances between the planes of atoms in the structure. The intensities of the peaks are related to the nature of atoms present in the repeating planes. The scattering intensities for X-rays are directly related to the number of electrons in the atom. This means that, light atoms scatter X-rays weakly, while heavy atoms scatter X-rays more effectively. The features of a diffraction pattern like, the number of peaks, the positions of the peaks, and the intensities of the peaks, define a unique, fingerprint X-ray powder pattern for every crystalline material.

Thus X-ray diffraction study is a useful tool which gives a whole variety of information about the crystal structure, orientation, average crystalline size and stress in the films. Experimentally obtained diffraction patterns of the sample are compared with the standard powder diffraction files published by the International Centre for Diffraction Data (ICDD).

The average grain size of the film can be calculated using the Scherrer's formula,

$$d = \frac{0.9\lambda}{\beta Cos\theta} \qquad (2.5)$$

where, λ is the wavelength of the X-rays and β is the full width at half maximum intensity of the peaks in radians.

The lattice parameter values for different crystallographic systems can be calculated from the following equations using the (hkl) parameters and the inter-planar spacing d.

Cubic system,

$$\frac{1}{d^2} = \frac{h^2+k^2+l^2}{a^2} \qquad (2.6)$$

Tetragonal system

$$\frac{1}{d^2} = \frac{h^2+k^2}{a^2} + \frac{l^2}{c^2} \qquad (2.7)$$

Hexagonal system,

$$\frac{1}{d^2} = \frac{4}{3}\left[\frac{h^2+hk+k^2}{a^2}\right] + \frac{l^2}{c^2} \qquad (2.8)$$

X-ray diffraction experiments of the films in the present studies were done using Rigaku X-ray diffractometer. A filtered Cu-K_α radiation having wavelength λ = 1.542 Å was used for diffraction. The accelerating potential applied to the X ray tube is 30 kV and the tube current is 20 mA [20].

2.5.3 Scanning Electron Microscope (SEM)

Electron microscopes are instruments that use a beam of highly energetic electrons to examine objects on a very fine scale. This examination can yield information about the topography, morphology, composition and crystal structure. Electron microscopes function exactly as their optical counterparts except that they use a focused beam of electrons instead of light to "image" the specimen and gain information as to its structure and composition. The basic steps involved in all electron microscopes are the following.

A stream of electrons formed in high vacuum is accelerated towards the specimen, which is at a positive electrical potential. The sample is irradiated by the beam and interactions occur inside the irradiated sample, affecting the electron beam. This interaction causes the electrons to be absorbed, emitted, reflected, or transmitted and can, in turn, cause light or X-ray emission, and these interactions are summarized in figure 2.14.

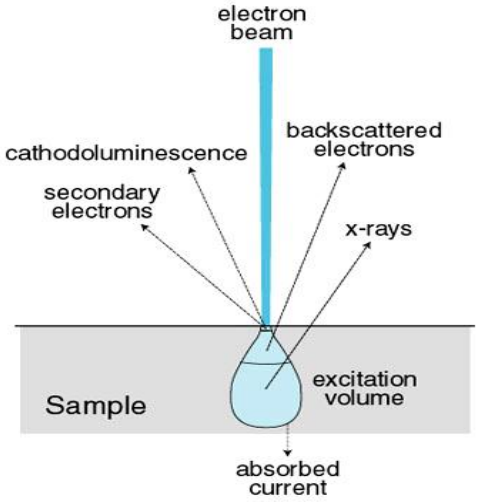

Fig. 2.14: Schematic representation of electron matter interactions

During the electron matter interaction, the electrons undergo an elastic collision with the specimen atoms and experience a trajectory change while the kinetic energy and velocity of the electrons remain constant. The strongest region of the electron energy spectrum is due to secondary electrons. The secondary electron yield depends on several factors, and is generally higher for high atomic number targets, and at higher angles of incidence. Secondary electrons are produced when an incident electron excites an electron in the sample and loses most of its energy in the process. The excited electron moves towards the surface of the sample undergoing elastic and inelastic collisions until it reaches the surface, where it can escape if it still has enough energy. Production of secondary electrons is very topography related. Due to their low energy (5eV), only secondary electrons that are very near the surface (<10 nm) can exit the sample and be examined. Any changes in topography in the sample that are larger than this sampling depth will change the yield of secondary electrons due to collection efficiencies.

Backscattered electrons consist of high-energy electrons originating in the electron beam that are reflected or back-scattered out of the specimen interaction volume. The production of backscattered electrons varies directly with the specimen's atomic number. This differing production rates cause higher atomic number elements to appear brighter than lower atomic number elements.

This interaction is utilized to differentiate parts of the specimen that have different average atomic number. Figure 2.15 shows the electron yield $N(E)$ as a function of electron energy for silicon.

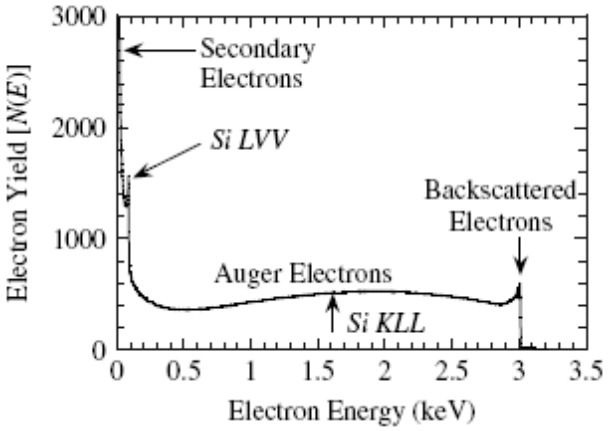

Fig. 2.15: Electron yield $N(E)$ as a function of electron energy for silicon for the entire electron energy range [13]

There are many unique advantages for using the SEM instead of an optical microscope. The main advantage of the SEM is that it has a large depth of field, which allows a great amount of the sample to be in focus at a time. Apart from this the SEM produces images of high resolution, which means that closely spaced characteristics can be examined at a high magnification. The sample preparation is relatively easy since most SEMs require that sample should be conducting. The combination of higher magnification, larger depth of focus, greater resolution, and ease of sample preparation makes the SEM one of the most successful instruments in current research and development [21].

The basic instrumentation set of SEM consists of a filament, which emits electrons, commonly made up of LaB_6 or tungsten in the shape of a hairpin gun. This filament is a kind of loop that functions as the cathode. A voltage is applied to the loop, causing it to heat up. The anode, which is kept at a positive polarity with respect to the filament, forms powerful attractive forces for electrons emitted from the cathode. This causes electrons to accelerate towards the anode. The streams of electrons are made to pass through a condenser lens, and are focused to very fine point on the sample by the objective lens. The

electron beam hits the sample, producing secondary electrons from the sample. These electrons are collected by a secondary detector or a backscatter detector and converted to a voltage and amplified. The amplified voltage is applied to the grid of the CRT that causes the intensity of the spot of light to change. The image consists of thousands of spots of varying intensity on the face of a CRT that corresponds to the topography of the sample. A simplified schematic diagram of scanning electron microscope is shown in figure 2.16.

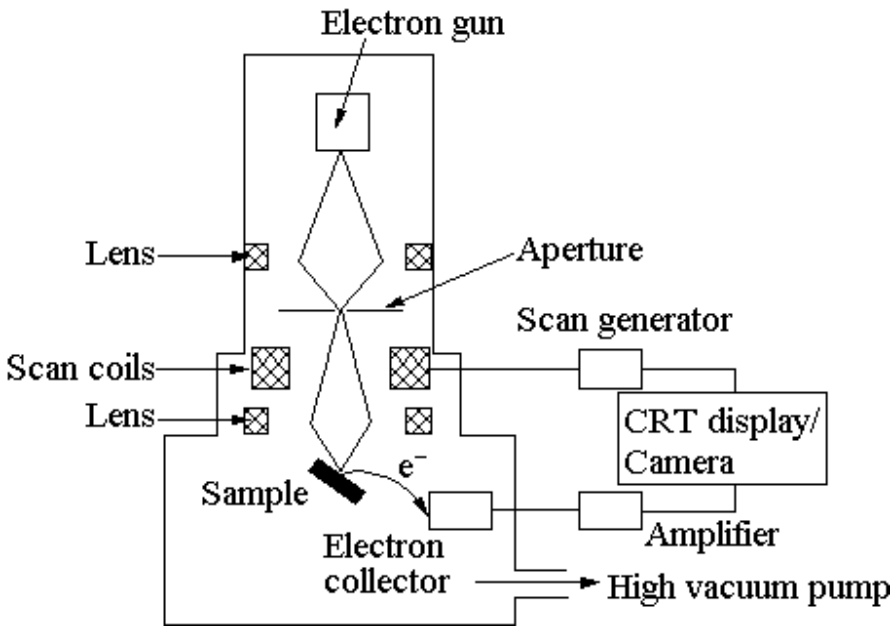

Fig. 2.16: Schematic diagram of a scanning electron microscope

2.5.4 Energy Dispersive X-Ray (EDX) Analysis

As the electrons interact with the atoms in a sample, individual incident electrons undergo scattering which can be classified as elastic and inelastic. In the elastic scattering, only the electron trajectory changes while the kinetic energy and velocity remain constant. But in the case of inelastic scattering, a few incident electrons will actually collide with sample atoms and displace electrons from their orbits around nuclei causing the atom to go in to an excited state. Atom in this excited state is unstable and returns to the ground or unexcited state by giving off the excess energy. The production of X-Rays,

Auger electrons and cathode-luminescence are three ways of relaxation. The relaxation energy is the fingerprint of each element. When the sample is bombarded by the electron beam of the SEM, electrons are ejected from the atoms on the specimen's surface. A resulting electron vacancy is filled by an electron from a higher shell, and an X-ray is emitted to balance the energy difference between the two electrons.

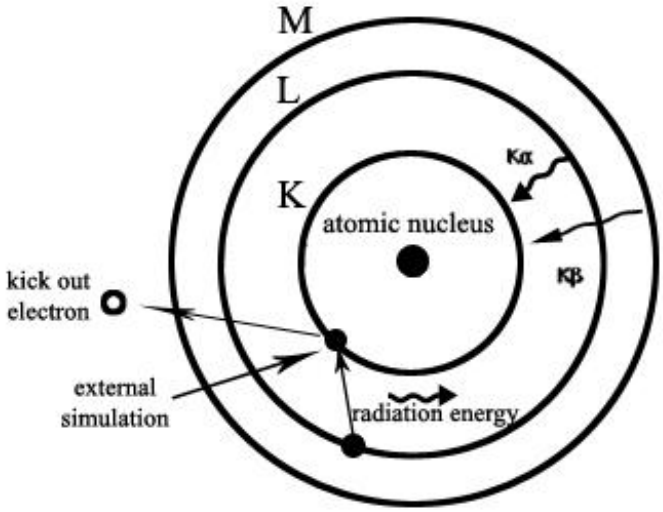

Fig. 2.17: Electronic transitions showing the emission of X rays.

The amount of energy released by the transferring electron depends on which shell it is coming from, as well as which shell it is moving to. Furthermore, the atom of every element releases X-rays with unique amounts of energy during the transferring process. Thus, by measuring the energy of the X-rays emitted by a specimen during electron beam bombardment, the identity of the atom from which the X-ray has been emitted can be established.

The EDS X-ray detector measures the number of emitted X-rays versus their energy. The energy of the X-rays is characteristic of the element from which the X-ray are emitted. In practice, EDS is most often used for qualitative elemental analysis, simply to determine which elements are present and their relative abundance. The EDX analysis system works as an integrated feature of a scanning electron microscope (SEM), and cannot operate on its own without the latter.

The EDX spectrum is the plot of intensity of X-rays vs energy of the emitted X-rays. An EDX spectrum normally displays peaks corresponding to the energy levels from which the most X-rays have been received. Each of these peaks is unique to an atom, and therefore corresponds to a single element. The higher the intensity of peaks in a spectrum, the more concentrated is the element in the specimen. An EDX spectrum plot not only identifies the element corresponding to each of its peaks, but the type of X-ray to which it corresponds as well.

Accuracy of EDX spectrum can be affected by many factors. The windows in front of the Si-Li detector can absorb low-energy X-rays which means that EDX detectors cannot detect the presence of elements with atomic number less than 5, (H, He, Li, or Be). The differing over-voltage of the EDX will result in different peak sizes. Raising over-voltage on the SEM will shift the spectrum to the larger energies making higher-energy peaks larger and lower energy peaks smaller. Also many elements will have overlapping peaks (ex. Ti Kβ and V Kα, Mn Kβ and Fe Kα). The accuracy of the spectrum can also be influenced by the nature of the sample. X-rays can be generated by any atom in the sample that is sufficiently excited by the incoming beam. These X-rays are emitted in any direction, and so may not all escape the sample. The probability of an X-ray escaping the specimen, and thus being available to detect and measure depends on the energy of the X-ray photon and the quantity and density of material it has to pass through. This can result in reduced accuracy in inhomogeneous and rough samples [22-25].

2.5.5 Atomic Force Microscopy (AFM)

Scanning Probe Microscopy is a technique used to capture images of surfaces using a physical probe that scans the specimen. An image of the surface is obtained by mechanically moving the probe in a raster scan of the specimen, line by line, and recording the probe-surface interaction as a function of position. The operation of the instruments is generally based on detecting the near-field image. There are several scanning probe microscopy techniques in which atomic force microscopy (AFM) is a unique technique with very high-resolution of the order of fractions of a nanometer, more than 1000 times better than the optical diffraction limit [26].

Atomic force microscope operates by measuring the force between a probe and the sample. This force depends on the nature of the sample, the distance between the probe and the sample, the probe geometry, and sample surface contamination. In contrast to scanning tunneling microscopy, which requires electrically conducting samples, AFM is suitable for conducting as well as insulating samples. The principle of working of AFM is illustrated in figure 2.18.

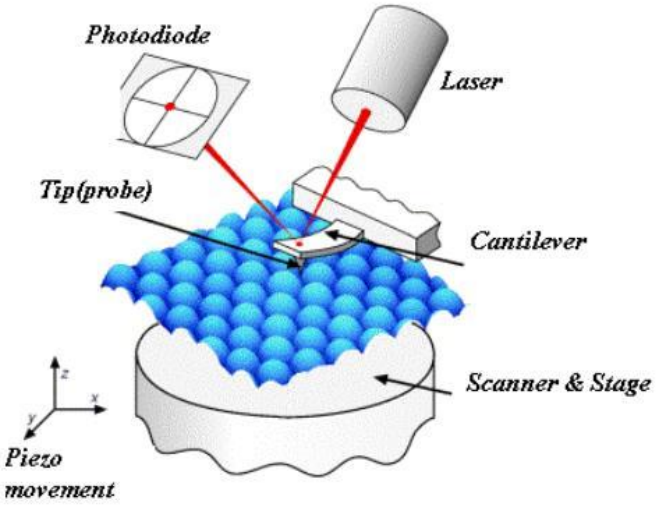

Fig. 2.18: Schematic representation of the working of atomic force microscope.

The instrument consists of a cantilever with a sharp tip mounted on its end. The cantilever is usually formed from silicon, silicon oxide or silicon nitride and is typically 100 μm long, 20 μm wide, and 0.1 μm thick, but other dimensions are also used. The vertical sensitivity depends on the cantilever length. For topographic imaging, the tip is brought into continuous or intermittent contact with the sample and scanned across the sample surface. Moving the sample is simpler because the optical detection system need not move. The motion of the cantilever can be sensed by several methods. A common technique is to sense the light reflected from the cantilever into a two-segment or four-segment, position sensitive photodiode. The cantilever motion causes the reflected light to impinge on different segments of the photodiode detector. The output of the detector is connected to a feedback controller that regulates the force between the sample and the tip by moving the sample up or down. The sample is moved

by a PZT scanning actuator. The cantilever must be soft enough to deflect a measurable amount without damaging the surface features of the sample. The amount of deflection is proportional to the force acting on the tip.

$$F_{spring} = -k.\Delta Z \qquad (2.9)$$

where F is the force on the sample, k is the spring constant of the cantilever, and, ΔZ is the deflection of the cantilever.

AFM can work in various modes, which include contact mode, non contact mode, tapping mode, dynamic force mode, and phase mode. Friction force microscope, magnetic force microscope, surface potential microscope, etc are scanning probe microscopes, with slight variation in the working principles from that described above.

2.5.6 Raman spectroscopy

Raman spectroscopy is a vibrational spectroscopic technique that can detect both organic and inorganic species and measure the crystallinity of solids. When light is scattered from a molecule or crystal, most photons are elastically scattered. The scattered photons have the same energy and, therefore, wavelength, as the incident photons. However, a small fraction of light is scattered at optical frequencies different from, and usually lower than, the frequency of the incident photons. The process leading to this inelastic scatter is termed, the Raman effect. Raman scattering can occur with a change in vibrational, rotational or electronic energy of a molecule. If the scattering is elastic, the process is called Rayleigh scattering. If it's not elastic, the process is called Raman scattering. If the substance being studied is illuminated by monochromatic light, for example from a laser, the spectrum of the scattered light consists of a strong line (the exciting line) of the same frequency as the incident illumination together with weaker lines on either side shifted from the strong line by frequencies ranging from a few to about 3500 cm^{-1}. The lines of frequency less than the exciting lines are called Stokes lines, and the others anti-Stokes lines [27].

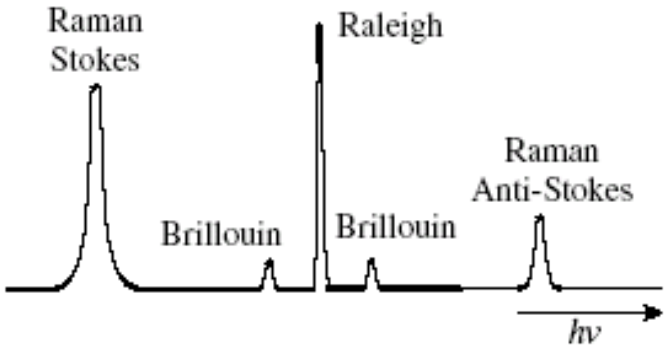

Fig. 2.19: Typical example of Raman spectra

During Raman spectroscopy experiments, a laser beam is incident on the sample. The scattered light or signal is passed through a double monochromator to reject the Raleigh scattered light and the Raman-shifted wavelengths are detected by a photodetector. In the Raman spectroscope, a laser illuminates the sample through a microscope. Laser power is usually held below 5 mW to reduce sample heating and specimen decomposition. The signal-to-noise ratio is enhanced if the Raman radiation is observed at right angles to the pump beam.

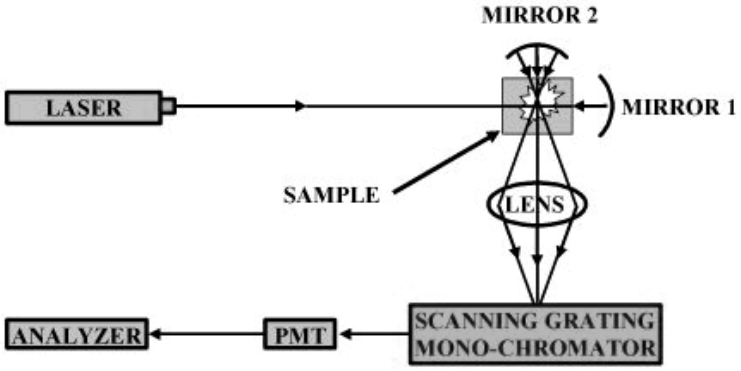

Fig. 2.20: Schematic representation of Raman spectrometer

By using lasers with varying wavelengths, different absorption depths are possible, enabling depth profiling of the sample. The technique is non-destructive and requires no contact with the sample. Most semiconductors can be characterized by Raman spectroscopy. The wavelengths of the scattered light

are analyzed and matched to known wavelengths for identification. Various properties of the sample can be characterized using this technique. It is useful in the determination of composition and crystal structure. For example, different crystal orientations give rise to slightly different Raman shifts. The Stokes line shifts, broadens and becomes asymmetric for microcrystalline samples and the lines become very broad for amorphous semiconductors, allowing a distinction to be made between single crystal, polycrystalline, and amorphous materials. The scattering frequency is also shifted by stress and strain in the thin film. Both compressive and tensile stress can be determined as the compressive stress gives an upward and tensile stress a downward shift from the unstressed samples. Raman spectroscopy, when coupled with other characterization techniques, is very effective for problem solving in semiconductor processing.

2.5.7 Electrical conductivity studies

The electrical conductivity is a measure of the electronic transport in the materials. By measuring the electrical conductivity as a function of temperature basic mechanisms of electrical conduction in solids can be studied. In the present work, an in house built setup to measure the conductivity of the thin film samples using two probe method has been used. The samples for conductivity measurements were coated on quartz substrates and co-planar aluminum electrodes were evaporated on to the films as shown in figure 2.21[28].

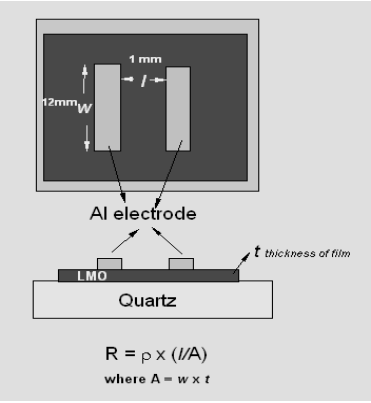

Fig. 2.21: Electrode configuration for planar two probe conductivity measurement set up

The DC conductivity of the films deposited with substrate bias (deposited on platinum coated Si wafer) was measured by two probe method in sandwich configuration.

For co-planar electrode configuration, if '*l*' is the separation between the two electrodes, '*w*' the length of the film deposited and 't' the thickness of the film, then conductivity (σ) can be expressed as

$$\sigma = (l \, . \, I) / (V \, . \, t \, . \, w) \quad [\ \mathrm{Scm^{-1}}] \qquad (2.10)$$

The temperature dependent conductivity (σ_T) of a given sample is given by the well established Arrhenius relation, which is expressed as:

$$\sigma_T = \sigma_0 \exp [-E_a/kT] \qquad [\mathrm{Scm^{-1}}] \qquad (2.11)$$

where σ_0 is the conductivity pre-factor, E_a is the thermal activation energy, k is the Boltzman constant and T is the temperature in Kelvin. This relation is also used to determine the activation energy from the slope of $\ln\sigma_T$ vs. $10^3/T$ plot. (i.e. plot between natural log of conductivity vs. 1000/T)

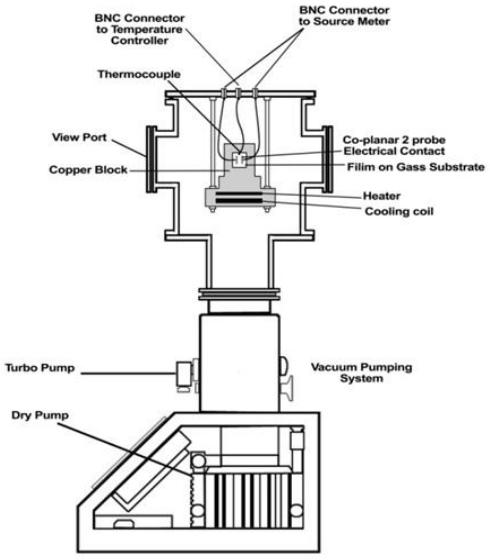

Fig. 2.22: Experimental set-up for planar two probe conductivity measurement.

Conductivity measurements were carried out in a cryostat as in Figure 2.22, consisting of a chamber with evacuation arrangement and a heating system. The chamber vacuum ~ 10^{-5}torr was attained with the help of a turbo pump. A

copper block holder was used to mount the samples using silver paint, enabling good thermal contact and a heating coil was attached to attain the desired temperature of the sample.

Ohmic contacts were made to the co-planar aluminium electrodes of the sample under test and the terminals of electrometer (Keithley, 2400) that applies the voltage as well as measures the current flowing through the sample were connected. The magnitude of the applied voltage depends upon the nature of the sample. All the samples were annealed in vacuum at 150°C for one hour prior to the measurement in order to avoid any effect of the absorbed gases. The sample was then cooled down slowly in a stepwise manner and the conductivity was measured at each of these steps.

2.5.8 Electrochemical characterization

Electrochemical properties of the battery are determined by the properties of the electrolytes, anode and cathode materials. Electrochemical characterization techniques are suitable for determining current/voltage characteristics, tests for polarity reversal (charging) of batteries, characterizing ageing effects using impedance spectroscopy, recording charge and discharge cycles, determining battery capacity, measuring the electrolyte resistance and charge transfer resistance etc. These techniques are also suitable for determining the thermodynamics of redox processes, kinetics of heterogeneous electron transfer reactions and coupled chemical reactions or adsorption processes.

A simple electrochemical system consists of a reference electrode, working electrode, and a counter electrode, which are immersed in an electrolyte solution. Such a configuration is known as three electrode set-up. When an electrochemical system is subjected to the passage of current between the two electrodes, it is deviated from the equilibrium state. The main aim of the electrochemical characterization is to investigate the electrode process of working electrode. Such investigations are carried out by controlling either the cell potential (potentiostatic control) or the current that passes through the cell (galvanostatic control). In three electrode set-up the individual electrode potential is monitored with respect to the reference electrode. In some cases

only two electrodes, i.e. the working electrode, and the counter electrode are used [29].

In a typical instrument for charge/discharge cycling and cyclic voltammetry experiment, a programmable voltage source, an ammeter, a voltmeter and a programmable electronic load are required. The charge/discharge cycling experiment is a time consuming process, often taking several hours/days to complete, depending upon the number of cycles and 'C' rate and scan speed. Hence it is always desirable to automate these tests with a computer using some standard interfacing software. In order to conduct the charge/discharge cycling and cyclic voltammetry, a number of standard instruments are available commercially, but these systems are very expensive. This section deals with the basic theory of galvanostatic charge/discharge cycling and cyclic voltammetry and describes the essentials of an in-house made instrumentation set-up to study the electrochemical properties of the assembled thin film battery.

2.5.9 Experimental set-up for galvanostatic charge/discharge cycling.

In a galvanostatic charge/discharge cycling, a constant current is applied between the working and the counter electrodes. The current is applied until the set upper or lower potential limits are reached. For the working electrode a negative current would cause reduction and a positive current, oxidation. The investigation of the variation of potential with time of an electrochemical system is also called chronopotentiometry. The major advantage of this method is that, the electrode process can be investigated under actual battery working conditions, since the current or current density is kept constant.

For an insertion/extraction process into a compound *M*,

$$Li_xM + \Delta xLi^- + \Delta xe^- \leftrightarrow Li_{x-\Delta x}M$$

The amount of inserted species Δx can be calculated as

$$\Delta x = \frac{I \Delta t \mathrm{Mr}}{nFm} \qquad (2.12)$$

where 'I' is the applied current in ampere,'Δt' is the time interval in seconds, 'Mr' is the mass of the compound in $gmol^{-1}$, 'm' is the active mass loading in grams, 'n' is the number of electrons and 'F' is Faraday's constant.

The energy stored in a battery, called the battery capacity, is measured in either watt-hours (Wh), kilowatt-hours (kWh), or ampere-hours (Ahr). The battery cycle life is defined as the number of complete charge - discharge cycles a battery can perform before its nominal capacity falls below 80% of its initial rated capacity. The basic idea of charge discharge cycling is to study the capacity fading in the lithium ion cells. The rate of charge and discharge is selected depending upon the theoretical capacity of the cathode material under investigation.

The 'C' rate is a method of expressing the constant current applied to an electrode in relation to its theoretical capacity. The specific capacity of all the cells tested was calculated by considering only the active mass of the cathode material in the electrode, and all electrochemical testing was carried out at ambient temperature (23 °C ± 5 °C) [29].

2.5.10 Charge/discharge cycling set-up using Keithley 2400 SMU.

The schematic diagram with Keithley 2400 source meter as constant current source for charge/discharge cycling is shown in figure 2.23.

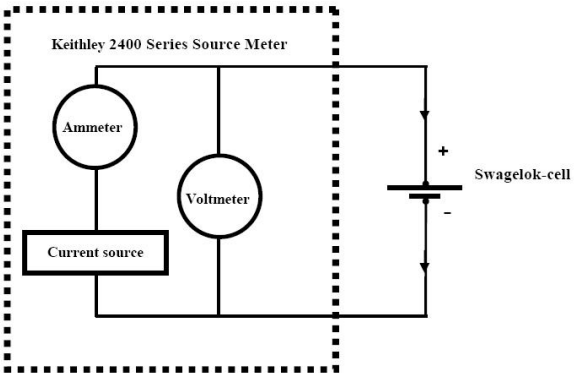

Fig. 2.23: Keithley 2400 Source Meter as constant current source for charge/ discharge cycling

The Keithley Series 2400 Source Meter includes programmable power supplies, electronic loads, voltmeters, and ammeters, and hence it is the perfect instrument to be used for battery discharge and charge testing. One of the key

features of the Keithley 2400 SMU is that it can measure either current or voltage while in the constant current source mode. It uses a positive test current for charging cycle and a negative test current for discharging. The voltage of the cell is recorded in regular intervals of time and charge/discharge curve is plotted between cell voltage and elapsed time.

One important thing that is to be noted while doing charge discharge cycling using Keithley 2400 SMU is, the setting of the compliance voltage. For charging, the compliance voltage is set to the desired battery voltage. Once the source output is turned on, the SMU will output a constant current until it reaches the desired voltage. At this juncture, the instrument will go into compliance and becomes a constant voltage source. For discharging, the compliance voltage is always set higher than the nominal voltage of the battery. It should never be set lower than the battery voltage because the instrument will go into compliance, causing the output current to be much higher than desired [30-31].

LabVIEW graphical interface software development platform has been used to interface Keithley 2400 SMU. An IEEE-488 interface has been used to communicate with the Keithley 2400, employing LabVIEW driver software for windows operating system. Figure 2.24 shows the schematic of the instrumentation set up to test the electrochemical characteristics of the assembled lithium ion cells.

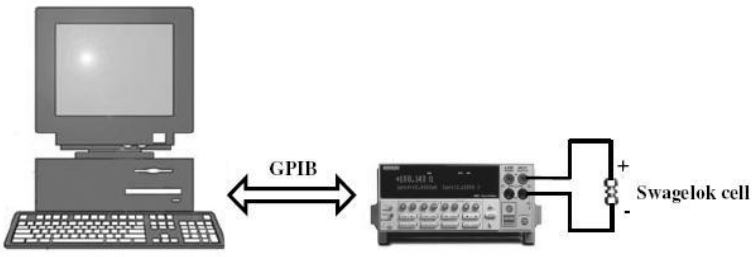

Fig. 2.24: Automating Keithley 2400 Source with PC using GPIB interface and LabVIEW

The basic programming structure using LabVIEW for charge/discharge cycling is shown in the form of a flow chart in figure 2.25[32, 33].

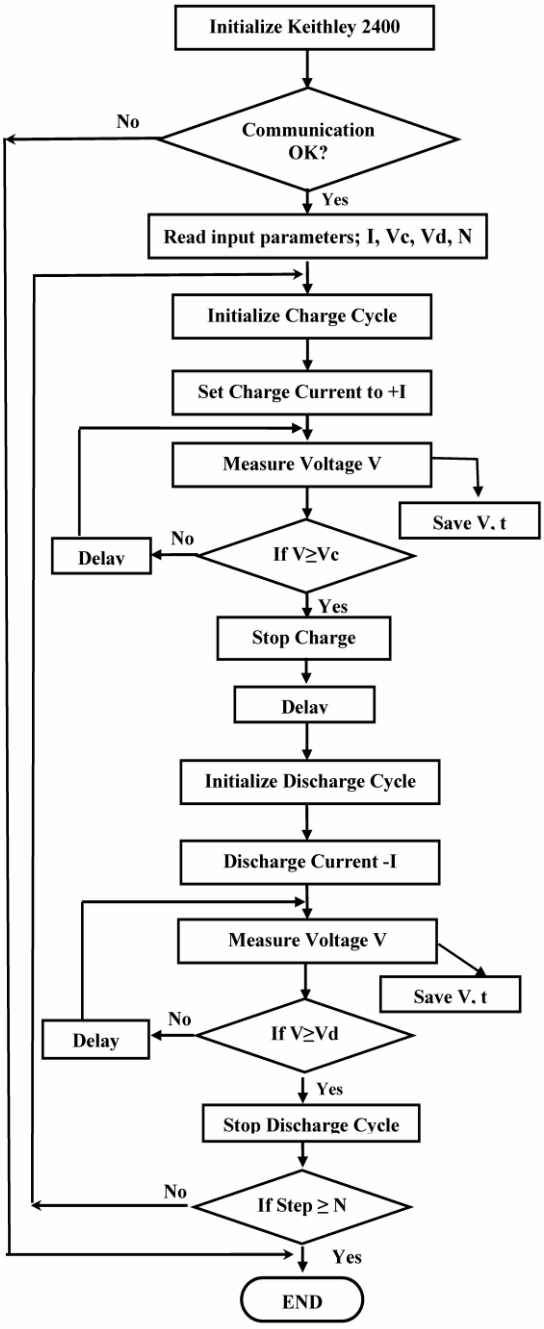

Fig.2.25: Flow chart for charge discharge cycling

The software user interface is shown in figure 2.26, which allows input of necessary conditions to the software in order to control the charge/discharge cycling experiment.

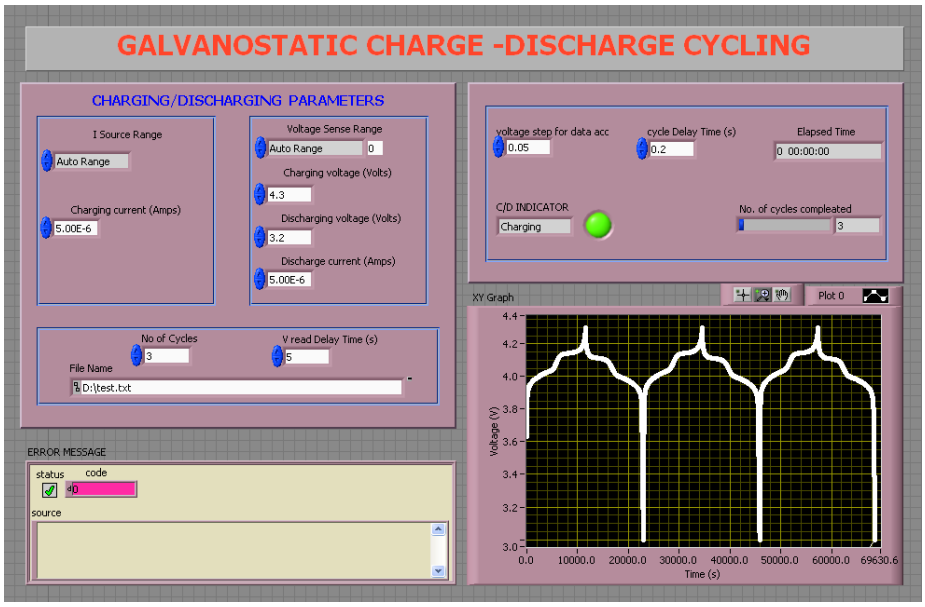

Fig. 2.26: Measuring system interface for charge discharge cycling

2.5.11 Cyclic voltammetry-Measurement principle

Cyclic voltammetry is an extensively used method for studying electrode processes, especially for the purpose of understanding the thermodynamics and kinetics of electron transfer at the electrode-electrolyte interface. This technique is often employed as the first method to characterize new electrochemical systems. In this method the cell/system under test is cycled in a potential window, where the potential applied on the working electrode is continuously changed at a constant rate. In essence, the potential is swept through the potential range where an electrode reaction occurs before the direction of scan is reversed, in order to define whether (a) the product of electron transfer is stable or (b) the reaction intermediates or the final products are electro-active. The change of potential as a function of time is called the scan rate. The potential sweep can be described by its initial (*Ei*), switching (*Es*), and final (*Ef*)

potentials, and also by the scan rate, ν. The potential as a function of time (t) is given by,

$E = E_i + \nu t$ …….(for forward voltage sweep) (2.13)

$E = E_s - \nu t$ …….(for reverse voltage sweep) (2.14)

with the scan rate (in mV/s) defined as

$$\nu = \frac{\Delta E}{\Delta t} \quad (2.15)$$

One of the most important parameters is the setting of the maximum and minimum potential ranges, which define the potential window. The cyclic voltammetry (CV) is performed by scanning the voltage between two chosen cut-off voltages at a given sweep rate, while simultaneously, measuring and recording the response current arising from the electron transfer. While choosing the cut-off voltages, the stability of the electrolyte must be taken into account in order to avoid its decomposition.

2.5.12 Cyclic voltammetry set-up using Keithley 2400 SMU

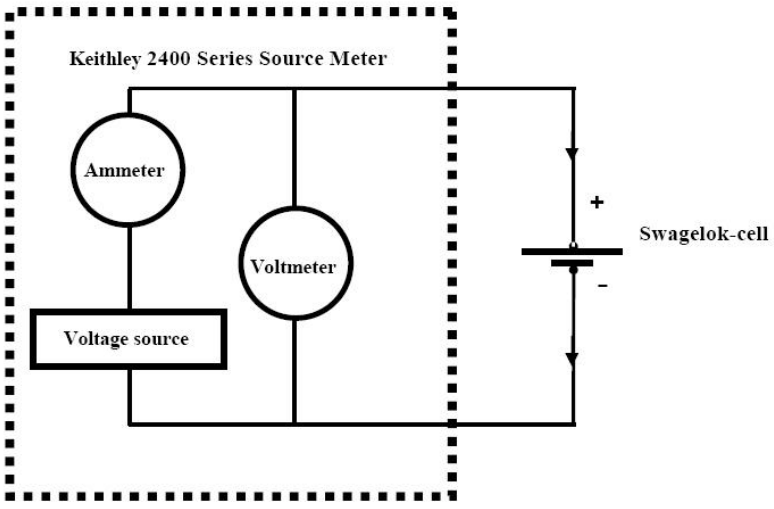

Fig. 2.27: Keithley 2400 Source Meter as Voltage source for CV experiment.

Keithley 2400 is a programmable source meter, capable of operating in the voltage sweep mode also, to perform cyclic voltammetry. When the source meter is in the voltage sweep mode, it can measure both current and voltage. It produces a positive forward sweep voltage, with a desired scan rate, for the oxidation cycle (i.e. lithium de-intercalation process in the case of a lithium cell). The corresponding cell current and voltage are monitored at regular intervals of time. A positive reverse sweep voltage with the same scan rate is used for the reduction cycle (i.e. lithium intercalation process in the case of lithium cell). The plot of the voltage vs. current, in between the cut-off voltages will give the cyclic voltammogram. The schematic diagram showing Keithley 2400 as voltage source for cyclic voltammetry experiment is shown in figure 2.27.

Similar to charge/discharge cycling, CV experiment often takes several hours to complete, depending up on the voltage scan speed, making it desirable to automate these tests with a computer. The LabVIEW based graphical user interface for CV experiment shown in figure 2.28.

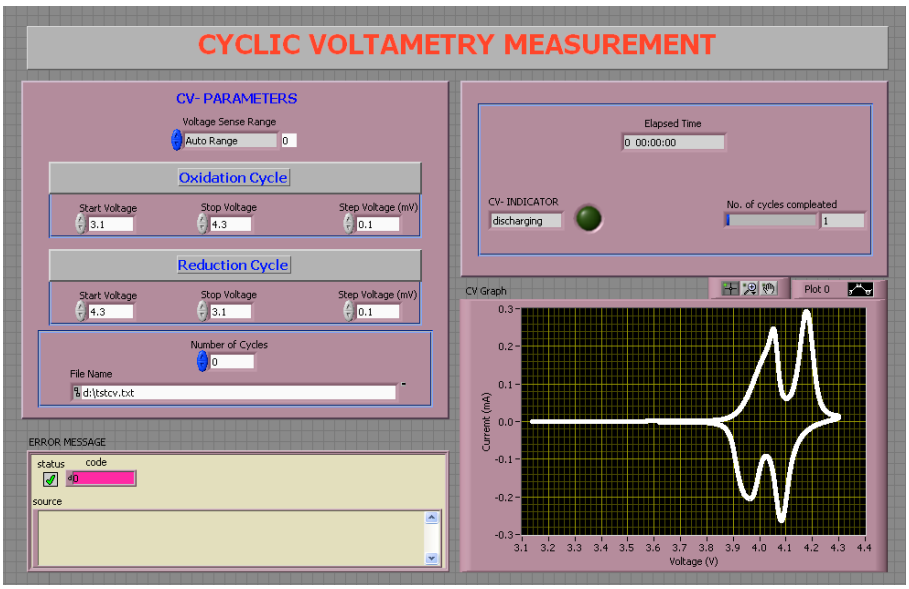

Fig. 2.28: Measuring system interface for Cyclic Voltammetry

The basic programming structure is shown in the form of a flow chart in figure 2.29

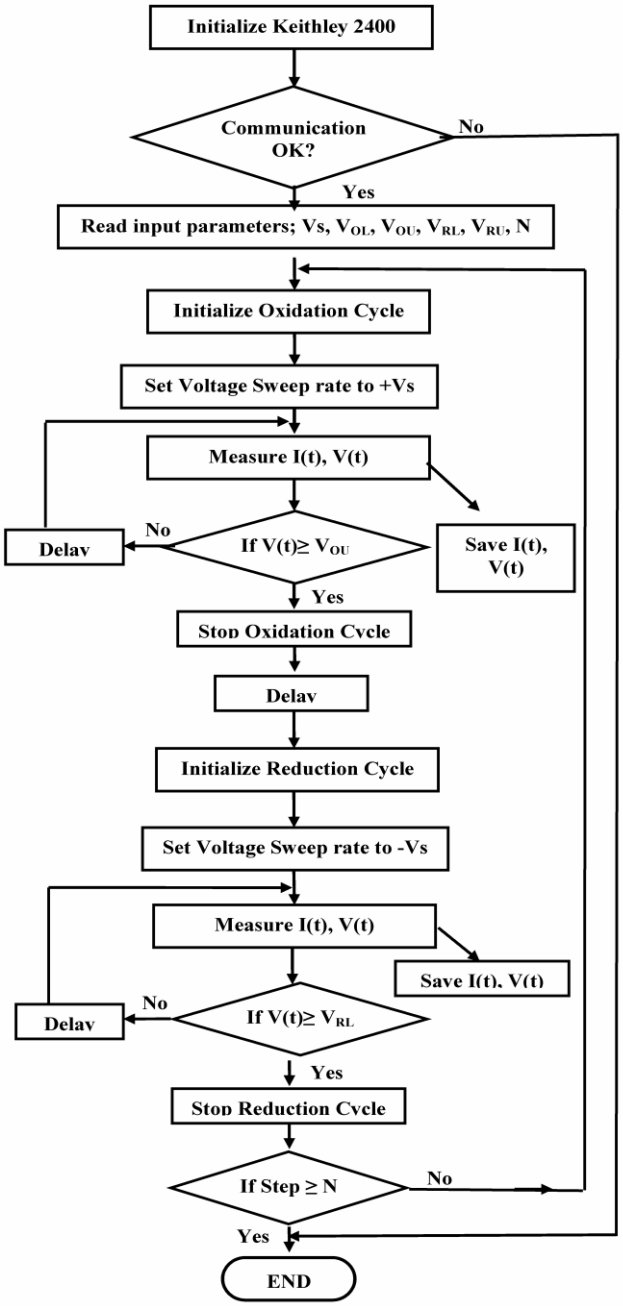

Fig. 2.29: Flow chart for Cyclic Voltammetry experiment.

2.6 References

[1] Introduction to Microfabrication by S. Franssila, ISBN 0-470-85106-6.
[2] Thin-Film Silicon Solar Cells by Arvind Victor Shah, ISBN: 978-2-940222-49-0.
[3] Ji-Guang Zhang et al. US patent No. 6156395.
[4] D. MeyerhoferJ. Appl. Phys. 49 (1978) 3993.
[5] S. Sakka et al., The sol-gel transition: formation of glass fibers & thin films, J. Non Crystalline Solids, Vol. 48, (1982) 31.
[6] Dong Shu et al. Solid State Ionics, 160, (2003) 227.
[7] Fei Cao et al. ElectrochimicaActa, 47 (2002) 1607.
[8] S.B. Tang et al. Journal of Power Sources, 164, (2007) 372
[9] S. W. Jin, J. Vac. Sci. Technol. A26 (2008) 114
[10] D. Dijkkamp et al., Appl. Phys. Lett. 51 (1987) 619
[11] Pulsed Laser Deposition of Thin Films: Applications-Led Growth of Functional Materials by Robert Eason, ISBN: 978-0-471-44709-2
[12] Pulsed Laser Deposition of thin films by D. B. Chrisey and G. K. Hubler John, Wiley and Sons, New York, 1994
[13] M. Ohring. Materials Science of Thin Films: Deposition and Structure. Academic Press, New York, 2001
[14] P. Sigmund: Theory of Sputtering. I. Sputtering Yield of Amorphous and Polycrystalline Targets Phys. Rev. 184, 383 (1969)
[15] P. Sigmund, C. Claussen: Sputtering from Elastic-Collision Spikes in heavy Ion Bombardment Metals J. Appl. Phys. 52 (1981) 990.
[16] R. Behrisch: Sputtering by Particle Bombardment -I Springer-Verlag Berlin, 1981.
[17] L. I. Maissel and R. Glang (Eds). Handbook of Thin Film Technology, McGraw-Hill, New York, 1970.
[18] K. Wasa, M. Kitabatake, and H. Adachi.Thin Film Materials Technology. Springer-Verlag GmbH & Co. KG, Germany, 2004.
[19] Dektak 6M, stylus profilometer manual.
[20] Charles Kittel, Introduction to Solid State Physics, Seventh edn,Wiley Eastern Limited, New Delhi, 1996.
[21] D. K. Schroder. Semiconductor material and device characterization. Wiley-Intersciernce, New Jersey, 1998.

[22] M.VonHeimendahl, W.Bell, G.Thomas. Applications of Kikuchi line Analyses in Electron Microscopy. Journal of Applied Physics 35 (1964) 3614.
[23] C. Richard Brundle, Charles A. Evans Jr, Shaun Wilson. Encyclopedia of materials characterization, Butterworth-Heinemann publications, 1992.
[24] P. E .J. Flewit and R. K. Wild, Physical methods for material characterization, second edition, IOP publishing, London, 2003.
[25] Goldstein, J. I. et al., Scanning Electron Microscopy and X-Ray Microanalysis. Springer (2003).
[26] Atomic force microscopy by Peter Jonathan Eaton, Peter Eaton, Paul West, ISBN-10: 0199570450.
[27] Gardiner, D.J. Practical Raman spectroscopy. ISBN 978-0387502540.
[28] Properties of amorphous silicon and its alloys, By Tim Searle, ISBN-10: 0852969228.
[29] H. Kiehne, Battery technology handbook, CRC, 2 edition (August 1, 2003).
[30] Keithley 2400 Source meter user manual.
[31] http://www.keithley.com/support/data?asset=3806
[32] LabVIEW-7.1 Documentation-Resources (http://digital.ni.com/public.nsf/allkb/06572E936282C0E486256EB0006B70B4)
[33] M. R. Tomy, K.M. A. Kumar, S. Jayalekshmi, Journal of Instrument Soc. of India 41, 88 (2011)

Chapter 3

High frequency sputtering of $LiMn_{2-x}Me_yO_4$

Abstract: Sputtering is one of the most versatile techniques used for the deposition of thin film cathode materials when device quality films are required. Sputtering process can be employed to deposit films with higher purity, better controlled composition, greater adhesion and homogeneity and better control of film thickness. This chapter deals with the details of synthesis and characterization of $LiMn_{2-x}Me_yO_4$ targets and the experimental setup designed for the high frequency (27.12MHz) RF magnetron sputtering of these targets. The optimization of sputtering conditions by varying the significant sputtering parameters is also discussed in detail.

3.1 Introduction.

Lithium manganese oxide ($LiMn_2O_4$) has attracted widespread attention as a cathode material for thin film lithium ion battery applications. The excellent structural stability during lithium intercalation/deintercalation process is one of the attractive characters of $LiMn_2O_4$[1, 2].Compared to other much familiar alternatives like $LiCoO_2$, it is environmentally benign, cost effective, has higher specific capacity and offers higher electrochemical potential[3].

$LiMn_2O_4$ in thin film form (Li-Mn-O) can be realized by various methods, like pulsed laser deposition [4, 5], plasma enhanced chemical vapor deposition [6], electron beam evaporation [7, 8] electrostatic spray deposition [9] and RF magnetron sputtering [10-12]. Among these, the most versatile method is the sputtering technique, owing to the possibility of micro-fabrication of the thin film batteries directly onto chips in any shape or size, and on flexible substrates, with good capacity and cycle life. A typical sputtering process involves the creation of gas plasma, usually of an inert gas such as argon, by applying voltage between a cathode and an anode. Here the cathode is the target material (source material) which is to be deposited, and the substrate is placed at the anode. The source material is subjected to intense bombardment by ions. By momentum transfer, particles are ejected from the surface of the cathode material and they diffuse away from it, and get deposited as a thin film on the substrate.

The electrochemical properties of thin film battery layers deposited by sputtering technique are mainly dependent on the physical and chemical properties of the cathode materials. Understanding the composition, morphology, structure, crystallinity, and charge carrier transport properties can be of help in optimizing the characteristics of the cathode materials. The properties of the $LiMn_2O_4$ cathode films deposited by RF sputtering vary with the composition of the sputtering target, target preparation techniques and sintering conditions.

This chapter gives an account of the synthesis of the pristine as well as doped $LiMn_2O_4$ sputtering targets and their characterization. It is followed by a

detailed description of the high frequency RF magnetron sputtering setup and the optimization of the sputtering conditions by varying the sputtering power and pressure. A comparative study with the conventional sputtering process using lower frequency excitation source is also attempted.

3.2 Preparation of $LiMn_{2-x}Me_yO_4$ sputtering targets.

There exists a variety of methods for the synthesis of $LiMn_{2-x}Me_yO_4$ (where Me – Mn, Ni, Zn and x, y ~ 0.05) spinel oxide cathode target materials. Among these, solid-state reaction technique via salt decomposition is the simplest and the most effective method to synthesize the spinel targets. In the present work, solid-state reactions of oxide/carbonate precursors of lithium, manganese, nickel and zinc were used for the preparation of the sputtering target materials.

The properties of the sputtering targets play an important role in controlling the stoichiometry of the thin film layers. In general, for a ceramic target, density, phase structure, pore size and its distribution, grain size and resistivity are the basic controlling parameters. These parameters mainly depend on the preparation techniques of the target materials and the sintering conditions.

Sintering of the target material is a significant factor that determines the qualities of the sputtering target. The principal objective of sintering process is to reduce porosity. It is usually accompanied by other changes within the material, desirable for a good quality target material.

Sintering mainly influences the parameters such as strength, elastic modulus, hardness, fracture toughness, distribution of grain size and shape, average pore size and shape and distribution of pore size and shape. It also influences positively, the chemical composition, crystal structure and electrical and thermal properties. The selection of sintering temperature and time is very important, since this may affect the structural stability of the spinel phase.

In the present work, the pristine lithium manganese oxide ($LiMn_2O_4$) powder was synthesized by direct solid-state reaction of Li_2CO_3 (Alfa Aesar-99.5%) and $MnCO_3$ (Alfa Aesar-99.5%) in stoichiometrically required ratio. The reaction equation is shown below.

$$2Li_2CO_3 + 8\ MnCO_3 + 3O_2 \rightarrow 4LiMn_2O_4 + 10CO_2$$

All the precursors were pre-dried at 200°C in separate crucibles for 5 hours in order to get rid of the absorbed moisture. The de-hydrated reactants were weighed out using an electronic balance to an accuracy of five decimal. The reactants were mixed thoroughly and finely ground under acetone in an agate mortar. The organic solvent acetone in this mixture gets evaporated off. The mixture was then calcinated at 600°C in high density alumina crucibles for 12 hours in order to get rid of CO_2.

The solid thus obtained was cooled to room temperature and an excess amount (5%) of $Li_2CO_3$was added to the calcinated solid (in order to compensate for lithium loss during the sputter deposition), and was again ground uniformly under acetone in the agate mortar. The powder so obtained was pressed into targets of two inch diameter under a load of 10 tons in a hydraulic pellet press. These targets were then sintered in a temperature controlled muffle furnace at 800°C for 24 hours in air. After the sintering, the contents were cooled to room temperature at a cooling rate of about 2°C/min [13]

In order to study the effect of doping on the electrochemical performance of the $LiMn_2O_4$ cathode films, targets doped with Zn and Ni were also synthesized. Nickel doped lithium nickel manganese spinel oxide targets ($LiNi_{0.05}Mn_{1.95}O_4$) were synthesized by following the same solid state process, where the precursors used were Li_2CO_3 (Alfa Aesar-99.5%), $MnCO_3$ (Alfa Aesar-99.5%) and NiO (Alfa Aesar-99.5%). Similarly the zinc doped, lithium zinc manganese spinel oxide targets were obtained by the reaction of Li_2CO_3 (Alfa aser-99.5%), $MnCO_3$ (Alfa Aesar-99.5%) and ZnO (Alfa Aesar-99.5%).

3.3 Characterization of $LiMn_{2-x}Me_xO_4$ sputtering targets.

3.3.1 Chemical composition analysis.

In order to obtain good quality sputtered films, it is necessary to know the chemical composition of the targets. Atomic emission spectroscopy (Thermo-IRIS INTREPID) was used to determine the elemental composition of the

target materials. The solutions for the ICP-AES analysis were prepared by dissolving 100 mg of the powdered target samples in 100 ml of 25% HCl solution containing a few drops of H_2O_2.

Table 3.1 shows the chemical composition of the target materials $LiMn_{2-x}Me_yO_4$ (where Me represents the dopant metal ions such as Mn, Ni, Zn and x, y ~ 0.05)

Table 3.1: Chemical composition of the pristine and doped target materials

Target	Li	Mn	Ni	Zn
$LiMn_2O_4$	1.04	2	-	-
$LiMn_{2-x}Ni_yO_4$	1.05	1.95	0.048	-
$LiMn_{2-x}Zn_yO_4$	1.04	1.95	-	0.047

3.3.2 X-ray diffraction studies.

The targets prepared by solid state reaction technique were robust and bluish black in color. The phase purity and crystal structure of the target material was confirmed using X-ray diffraction studies (Rigaku Diffractometer Model: D max C) with filtered Cu-K_α radiation having wavelength 1.542Å.

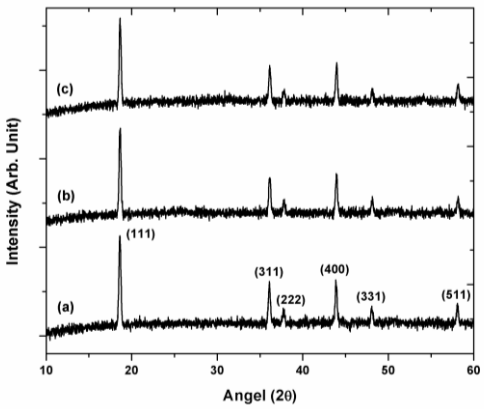

Fig. 3.1: XRD patterns of $LiMn_{2-x}Me_yO_4$ target materials; (a) Pristine $LiMn_2O_4$, (b) $LiMn_{2-x}Ni_yO_4$and (c) $LiMn_{2-x}Zn_yO_4$ with x, y ~0.05.

The XRD analysis confirms the formation of the spinel structure without any visible impurity phases. The X-ray diffraction curves of the pristine, nickel doped and zinc doped $LiMn_2O_4$ samples are shown in figure 3.1.

For all the three target materials, i.e. $LiMn_2O_4$, $LiMn_{2-x}Ni_yO_4$and $LiMn_{2-x}Zn_yO_4$ (x, y ~0.05), there are six peaks between the 2θ values of 10 and 60° out of which the three strong peaks correspond to the reflections from (111), (311) and (400) planes, and the three less intense peaks correspond to the reflections from (222), (331) and (511) planes. The reflection from the peak corresponding to the (111) plane has the highest intensity. All these peak positions and the relative intensity values are in good agreement with those of the cubic spinel structure of $LiMn_2O_4$ [14]. Moreover none of the peaks corresponding to the precursors are observable, which indicates that all the solid state reactions involved can be considered as complete and uniform.

The powder diffraction data of the target materials was used to determine the unit cell lattice parameters by the least square fitting method of the d-spacing and the hkl values. The lattice constants, and the full width at half maximum (FWHM) of the diffraction peaks of the pristine and doped targets calculated from the XRD data are given in table 3.2.

Table 3.2: The lattice constants and the full width at half maximum (FWHM) of the diffraction peaks for the pristine and doped targets calculated from the XRD data.

Target	d-values (Å)	Lattice parameter, a (Å)	FWHM (°)
$LiMn_2O_4$	4.760	8.245	0.274
$LiNi_yMn_{2-x}O_4$	4.755	8.237	0.269
$LiZn_yMn_{2-x}O_4$	4.753	8.232	0.262

The XRD data clearly shows that all the target materials have a cubic spinel structure corresponding to Fd3m space group, with Li-ions occupying the 8a

tetrahedral sites and manganese cations occupying 16d octahedral sites of a cubic closed array represented by the oxygen located in the 32e positions. The lattice parameter of $LiMn_2O_4$ is calculated to be 8.245 Å. The lattice parameters of the doped samples are found to be slightly less than that of pristine samples and are 8.237 Å and 8.232 Å respectively for $LiNi_yMn_{2-x}O_4$and $LiZn_yMn_{2-x}O_4$.

3.3.3 Surface morphology studies.

The surface morphology of the target materials was studied using scanning electron microscope (ESEM-Quanta 200). The scanning electron microscope images of the $LiMn_{2-x}Me_xO_4$ target materials are shown in figures 3.2a, b&c.

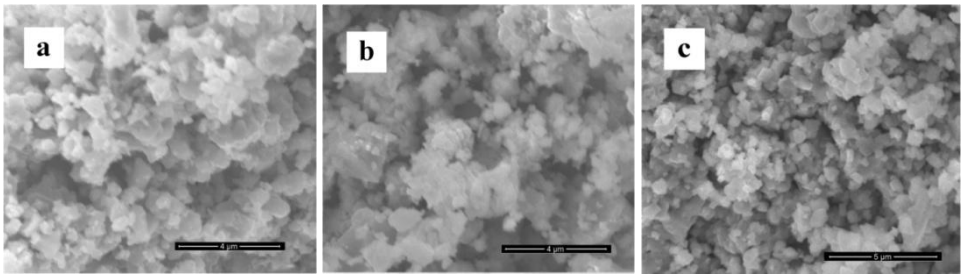

Fig. 3.2: Scanning electron micrographs of (a) $LiMn_2O_4$, (b)$LiMn_{2-x}Ni_yO_4$and (c) $LiMn_{2-x}Zn_yO_4$.

The scanning electron micrographs of the samples confirm that the shape and size of the particles in all the samples are uniform which indicates the proper stoichiometry of reacting components involved in the synthesis process. The average particle size is found to be of the order of 0.5 micron.

3.4 $LiMn_2O_4$ films by high frequency RF magnetron sputtering.

3.4.1 High frequency RF magnetron sputtering: An overview.

The most commonly used excitation frequency for radio frequency magnetron sputtering of the ceramic materials is 13.56MHz. The selection of this frequency is mainly based on the convention and availability of the RF technology suited for this frequency, rather than the optimization of the

physical processes in the discharge. [15.]. There has been a lot of theoretical and experimental evidences and results that higher excitation frequency can be efficiently used to deposit good quality films at higher deposition rates with glow discharge plasma[15].

The effect of frequencies higher than the conventional one (13.56MHz) on the RF magnetron sputtering process has not been subjected to detailed investigations. Expecting higher deposition rates and improved film quality, in the present work, attempts have been made to sputter deposit spinel oxide cathode films for thin film lithium ion battery applications, using high frequency RF excitation source. The excitation frequency of 27.12MHz has been chosen in the present work for the sputter deposition of cathode films.

3.4.2 Experimental setup for high frequency RF magnetron sputtering.

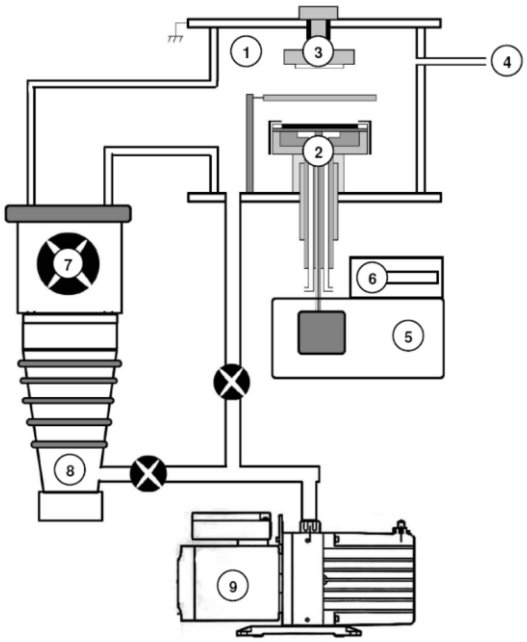

Fig. 3.3: Schematic diagram of the sputtering system, (1) Process chamber, (2) Magnetron gun, (3) Substrate holder with bias mechanism, (4) Gas inlet, (5) RF Matching network, (6) RF generator, (7) Baffle valve, (8) Diffusion pump, (9) Rotary Pump.

A planar magnetron sputtering system (MSPT 12 Sputter Coater) in sputter up configuration has been used for the present investigations. The sputtering system consists of a cylindrical chamber of diameter 12 inches and height20 inches. The vacuum pumping system consists of a water cooled diffusion pump backed by a roughing pump, which is an oil sealed rotary pump. A series of roughing, backing and high vacuum valves are used to optimize the system performance. The ultimate vacuum achievable with this pumping system is $2x10^{-6}$mbar. The vacuum inside the chamber is monitored by using a combination of pirani and penning gauges. The schematic diagram of the RF sputter coater is shown in figure 3.3

A 2 inch planar water cooled magnetron, suitably modified to feed high frequency RF power, avoiding any RF leakage, has been used for the sputter deposition. The schematic diagram of the magnetron sputter gun is shown in figure 3.4.

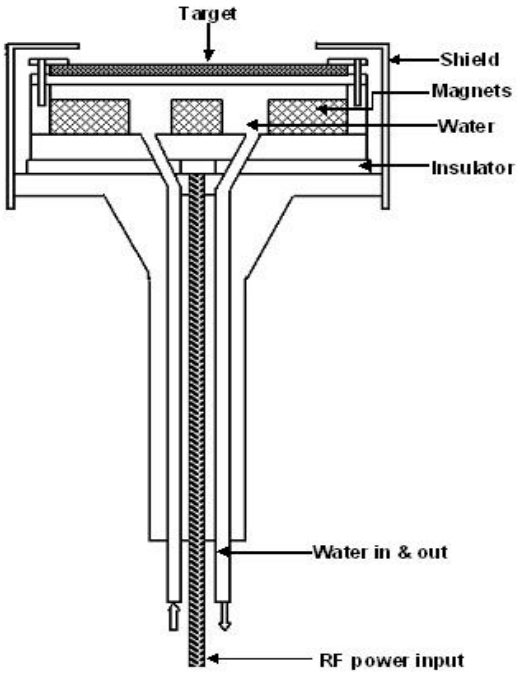

Fig. 3.4: Schematic diagram of Magnetron gun.

In the present work, 27.12 MHz power supply (Advanced Energy Dressler Cesar, see figure 3.5) has been used for the sputtering. The RF circuit basically consists of a matching network, with an auto tune facility, which is connected to the output of the high frequency RF power supply. The output of the matching network is connected to the magnetron gun. During operations, matching network is tuned automatically to transfer maximum power to the plasma and to make the reflected RF power minimum. The schematic diagram of the electrical circuits used for the high frequency RF sputtering system is shown in figure 3.6. Special care has been taken while grounding the system and matching network, which is important to avoid any RF leakage and to deliver maximum forward RF power to the magnetron gun.

Fig. 3.5: Photograph of 27.12MHz RF power supply

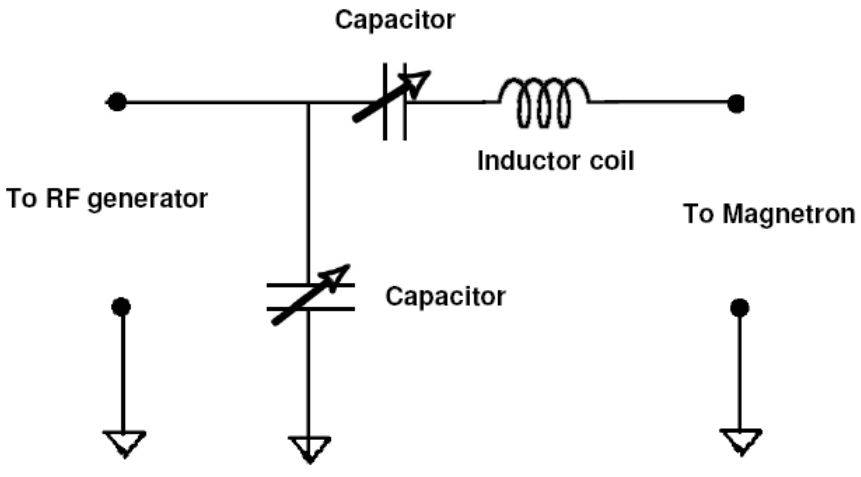

Fig. 3.6: Schematic diagram of the 27.12 MHz RF matching network.

Ultra high pure Argon gas (Ar-99.995%) was used for the film deposition. A small amount of high pure oxygen (O_2-99.995%) was also introduced during the film deposition process to avoid any possible oxygen deficiency. The gases were injected through needle valves and their flow rates were controlled by mass flow controllers (Bronkhorst High-Tech). The working pressure was adjusted by throttling the high vacuum valve. The substrates were mounted on the substrate holder, vertically above the magnetron and were grounded. In the present set up, in-situ substrate heating was not used, but the substrate temperature during the film deposition was measured and recorded.

Attempts were also carried out to study the effect of substrate bias on the properties of the deposited films. In-situ substrate bias was applied by isolating the substrate holder from the main body and applying negative dc voltage from a variable power supply to the substrate holder. During sputter deposition under substrate bias conditions, the substrates upon which films were deposited were kept in electrical contact with the substrate holder. Hence only electrically conducting substrates like stainless steel (SUS 304), metal coated silicon wafer etc. were used for film deposition under bias conditions.

Three different substrates, including stainless steel (SUS 304) discs of 0.5mm thickness, polished silicon wafer (100) and quartz plates of 1mm thickness were used in the present study. Since substrate surface preparation is important to obtain good film adhesion to the substrates, all the substrates were cleaned as per the standard procedure. Si (100), Pt coated Si wafer and quartz substrates were cleaned by rinsing in acetone, isopropyl alcohol, and then in deionized (DI) water, while SUS 304stainless steel substrates were cleaned in an ultrasonic bath sequentially using acetone, ethanol, and DI water separately. Thereafter, all the substrates were dried inN_2 gas. Films deposited on stainless steel substrates were used for electrochemical and structural studies, those on silicon wafer for morphological studies and those on quartz substrates for electrical studies.

In the present work, the magnetron in sputter up configuration was employed and the target to substrate distance was maintained to be 6 cm. The sputtering chamber was evacuated to a pressure of $4x10^{-6}$ mbar, and a mixture of argon and oxygen gases in the ratio of 20:1 was introduced into the process chamber.

The total process pressure was maintained by throttling of the high vacuum valve. The target was pre-sputtered in an argon atmosphere for 20 min to eliminate surface impurities. The experiment was conducted with different sputtering powers for a given sputtering pressure. The experiment was also repeated for different sputtering pressures in order to study the properties of the films in different sputtering pressure regimes.

Fig. 3.7: Photograph of the high frequency (27.12MHz) sputtering plasma of $LiMn_2O_4$ target.

3.5 Optimization of sputtering conditions for Li-Mn-O films

The optimization of sputter deposition conditions of $LiMn_2O_4$ target using 27.12MHz RF excitation source was carried out by investigating the variation of the rate of deposition with respect to various values of sputtering pressure and power. The sputtering pressure was varied from 0.001mbar to comparatively higher value of 0.05mbar. It was observed that the sputter deposition was not stable at the low pressure of 0.001mbar, whereas, it was quite stable at higher pressures up to 0.05mbar. However, further increase in pressure was found to cause the leakage of RF power, leading to unstable plasma.

The reason for the instability of sputtering plasma at lower pressures may be the design of dark space shield or some unknown factor, which requires further investigations. So in the present study, the investigations were limited to the sputtering pressures between 0.005mbar and 0.05mbar.

For all sputtering pressures, the rate of film deposition was found to increase with increase in sputtering power. Moreover it was also observed that when the RF power density was increased beyond 5W/cm^2, the target started to get heated up, resulting in lithium deficient films. This could probably be due to the insufficient target cooling which is one of the limitations with the magnetron gun design. Figure 3.8 shows the deposition rate of Li-Mn-O films as a function of the deposition pressure and power.

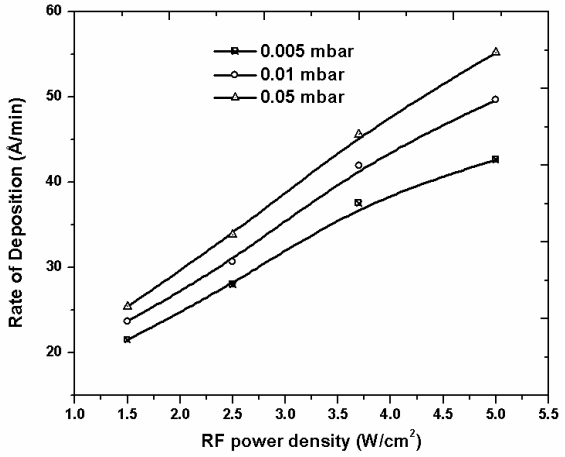

Fig 3.8: Deposition rate of Li-Mn-O films as a function of the deposition pressure and power using 27.12MHz, excitation source.

In the present work, the sputter deposition was carried out without any in-situ substrate heating. It was observed that, during the sputtering process, the substrate temperature increases linearly and an equilibrium temperature is reached after about 15 minutes from the starting of sputtering. Substrate heating during sputtering may be caused by heat of condensation, sputtered atom kinetic energy, plasma radiation or cathode reflected neutrals [16].

The sputter-deposited Li-Mn-O films using 27.12MHz excitation source are found to be physically stable and show good adhesion to substrates. In the

present work, for the characterization of the sputter deposited films, the thickness of the films has been maintained at ~300nm, by adjusting the deposition time.

A comparative study of the deposition rate as a function of pressure for a constant power of 5W/cm^2 using 27.12MHz RF source, and the conventional 13.56MHz RF source is shown in figure 3.9.The rate of sputter deposition using 27.12MHz excitation source, initially increases with increase in sputtering pressure from 0.005 mbar, and it peaks at around 0.03 mbar pressure, and any further rise in pressure leads to decrease in deposition rate. Same is the case for the films deposited using the conventional 13.56MHz RF power source. Apparently, at higher sputtering pressures, the average mean free path of gas molecules is very short, and therefore the collision of particles becomes more frequent in the chamber. Due to collision, particles lose energy, and cannot reach the substrate or in other words, they do not have enough energy to form films. This results in a reduction of deposition rate.

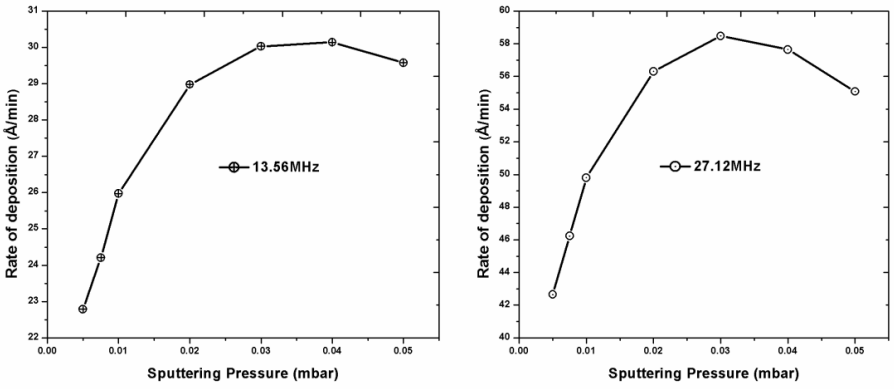

Fig. 3.9: Rate of sputter deposition as a function of pressure for a constant power of 5W/cm^2 using 13.56MHz and 27.12MHz RF excitation sources.

On comparison of the results shown in figure 3.9, it is obvious that the deposition rates obtained using 27.12MHz is much higher than that obtained using the conventional RF frequency of 13.56MHz. The deposition rate is almost doubled. A rate of 58Å/min has been obtained using 27.12MHz source as compared to the 30Å/min for the films deposited using 13.56MHz source, keeping all other conditions the same. It seems that the higher frequency RF

magnetron discharge appreciably improves the nucleation and the rate of growth of the Li-Mn-O films. Similar results were obtained for the films deposited with in situ substrate bias, but the deposition rate was slightly lower than that for the films deposited without substrate bias.

The structural, morphological and electrochemical properties of the Li-Mn-O thin films deposited using 27.12MHz RF source, with respect to sputtering pressure, are discussed in the following chapters. Three sputtering pressures i.e. 0.005, 0.01, and 0.05 mbar, corresponding to RF power of $5W/cm^2$ have been chosen for the present study. One of the reasons for selecting these pressures is the good quality of the films obtained at these pressures. These pressures can also be considered as those representing the most convenient pressure range to study the properties of these films with minimum number of experiments [17].

3.6 Conclusions

Spinel $LiMn_{2-x}Me_yO_4$ (where Me – Mn, Ni, Zn and x, y ~ 0.05) cathode target materials were synthesized by a two stage solid state reaction technique. These target materials were characterized in order to understand the compositional and structural details. These targets were used to deposit Li-Mn-O films using high frequency magnetron sputtering technique. In this study, 27.12MHz RF excitation source was used for the sputtering, and detailed investigations to optimize the deposition conditions were carried out by varying the sputtering power and pressure. The deposition rate was found to be higher for the 27.12 MHz RF source compared to that obtained using the conventional RF excitation frequency of 13.56MHz. A maximum deposition rate of 58Å/min was obtained with the higher frequency, which is almost two times the rate obtained with the conventional frequency. Present investigations reveal that the high excitation frequency magnetron discharge significantly improves nucleation and growth of Li-Mn-O films, thereby improving the rate of deposition without compromising the quality of the films. From these investigations it is inferred that the beneficial effects of the high frequency discharge are due to the reduced DC voltage at the target surface, which in turn reduces the energy of the reflected argon ions bombarding the growing film.

3.7 Reference

[1] M.M. Thackeray, W.I.F. David, P.G. Bruce, J.B. Goodenough, Mater. Res. Bull. 18 (1983), 461.
[2] M. Tarascon, E. Wang, F.K. Shokoohi, W.R. McKinnon, S. Colson, J. Electrochem. Soc. 138, (1991) 2859.
[3] H.A. Kiehne, Battery Technology Handbook, CRC Press; second edition, 2003
[4] C. Julien, E. Haro-Poniatowski, M. A. Camacho-Lopez, L. Escobar-Alarcon, and J. Jimenez-Jarquin, Mater. Sci. Eng. B 72 (2000) 36.
[5] A. Rougier, K. A. Striebel, S. J. Wen, T. J. Richardson, R. P. Reade and E. J. Cairns, Applied Surface Science 134 (1998) 107.
[6] P. Liu, J.-G.Zhang, J. A. Turner, C. E. Tracy and D. K. Benson, J. Electrochem.Soc.146 (1999) 2001.
[7] F. K. Shokoohi, J. M. Tarascon, and B. J. Wilkens, Appl. Phys. Lett. 59 (1991) 1260.
[8] F. K. Shokoohi, J. M. Tarascon, B. J. Wilkens, D. Guyomard, and C. C.Chang, J. Electrochem. Soc. 139 (1992) 1845.
[9] D Shu, K Y Chung, W I Cho and K-B Kim, Journal of Power Sources, 114 (2003) 253.
[10] K. H. Hwang, S.H. Lee, and S.K. Joo, J. Electrochem. Soc. 141 (1994) 3296
[11] B. J. Hwang, C. Y. Wang, M. Y. Cheng, and R. Santhanam, J. Phys. Chem. C 113 (2009) 11373.
[12] J. Xie, T. Tanaka, N. Imanishi, T. Matsumura, A. Hirano, Y. Takeda, O. Yamamoto, Journal of Power Sources 180 (2008) 576.
[13] S. T. Lee, K. Raveendranath, R. M. Tomy, N. A George, S. Jayalekshmi and J. Ravi J. Phys. D: Appl. Phys. 40 (2007) 3807.
[14] S. Chitra, P. Kalyani et al. Physical Properties of LiMn2O4 Spinel Prepared at moderate temperature. Ionics 4 (1998)
[15] Howling, A. A. Dorier, J.L. Hollenstein, Ch. Kroll, U. Finger, F. Journal of Vacuum Science & Technology A: Vacuum, Surfaces, and Films 10 (1992) 1080].
[16] J. A.Thornton, Thin Solid Films54 (1978) 23.

[17] RajiveTomy M, Anil Kumar K M, Anand P B and S Jayalekshmi, Journal of Physics and Chemistry of Solids. 72 (2011) 1251

Chapter 4

Post annealing studies of Li-Mn-O films.

Abstract: The performance of a thin film battery is directly related to the structural, electrical and electrochemical properties of the cathode film. This chapter deals with the detailed characterization of the Li-Mn-O cathode films deposited at various sputtering pressures, using high frequency RF excitation source. The effect of post annealing on the properties of the films is discussed. The assembling of a half cell device along with its detailed electrochemical characterization is also addressed in depth.

4.1 Introduction.

Among the various battery technologies, thin film battery technology offers the best performance, with advantages such as ultra small size, lightweight, long life and better capacity. A thin film battery with an all solid state technology design has also been realized, in which all the thin film battery layers are made out of ceramic materials. This design is intrinsically safe and allows operations at low as well as high temperatures without losing much of the capacity [1].Compared to bulk lithium ion battery technology, the thin film battery technology is still in its early stages of development, providing much scope for further developments during the years ahead [2-6].

As described in chapter 2, thin film lithium ion batteries can be realized using a wide variety of techniques, out of which the magnetron sputtering is the most versatile technique identified to deposit thin film battery layers. Even though it is one of the most flexible and widely used techniques, it has got a few disadvantages as well. These include comparatively high initial investment costs, and low rates of deposition of individual layers, which make the battery assembling a lengthy affair, affecting the throughput of production and production cost.

The present work is focused on the development of high quality thin film cathode materials based on spinel oxides, using high frequency (27.12MHz) magnetron sputtering technique. As described in chapter 3, a detailed investigation to optimize the deposition conditions using 27.12MHz excitation source, has been carried out by varying the sputtering power and pressure. The deposition rate has been found to be considerably higher in the present case compared to the conventional lower frequency (13.56MHz) sputtering technique.

The detailed structural, electrical and electrochemical studies of the lithium manganese oxide cathode films deposited by high frequency RF excitation source (27.12MHz) are detailed in this chapter. The studies are confined mainly to three sputtering pressure regimes of 0.005 mbar, 0.01mbar and 0.05mbar.

4.2 Characterization of Li-Mn-O films.

4.2.1 Chemical composition of 'as deposited' Li-Mn-O films.

The chemical composition of the deposited films was confirmed using atomic emission spectroscopy (Thermo Electron IRIS INTREPID II XSP DUO), ICP-AES. Table 4.1 shows the chemical composition of the Li-Mn-O films deposited at various pressures with a power density of 5W/cm^2 using 27.12MHz RF source.

Table 4.1: Chemical composition of Li-Mn-O film deposited at a power density of 5W/cm^2

Sputtering pressure (mbar)	Li	Mn	Li/Mn
0.005	1.01	2	0.505
0.01	0.95	2	0.475
0.05	0.91	2	0.455

It is evident from table 4.1, that the lithium content in the films deposited at higher pressures is lower than that in the films deposited at lower pressures. A possible reason for this may be the re-sputtering of the deposited films by bombarding argon ions. As the pressure increases, the ion bombardment on the growing films also increases resulting in Li ion deficient films. So it is clear that the films deposited at the 0.005mbar pressure have the chemical composition close to that of a stoichiometric $LiMn_2O_4$.

4.2.2 Structural studies of 'as deposited' Li-Mn-O films by XRD.

In order to confirm the structural characteristics and the phase purity of the deposited films, the X-ray diffraction technique (XRD) was used. The crystal structure of the films was characterized using a Rigaku X-ray Diffractometer (Model: D max C) with filtered Cu-Kα radiation having wavelength 1.542Å.

The X-ray diffraction patterns of the as deposited films under various pressures and with an RF power density of 5W/cm^{2}are shown figure 4.1. The 'as deposited' films, for all sputtering pressures, are found to have poor crystallinity with a broad small peak around 20°,which corresponds to the reflection from the (111) plane [7]. The amorphous nature may be because of the lower energy exchange between vapor atoms in the sputtering plasma and the substrate. Moreover, at room temperature deposition, atomic defects in the form of vacancies in the structure are generated, which tend to form amorphous phases in the films. The peaks marked as SS in figure 4.1, represent those of the stainless steel substrate.

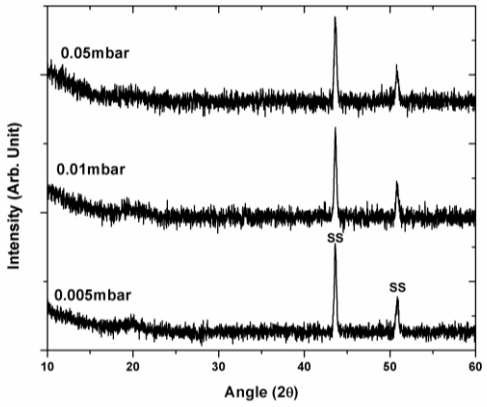

Fig. 4.1: XRD patterns of the as deposited Li-Mn-O films at various deposition pressures for a sputter power density of 5W/cm^2.

4.2.3 Experimental set up for annealing of 'as deposited' Li-Mn-O films.

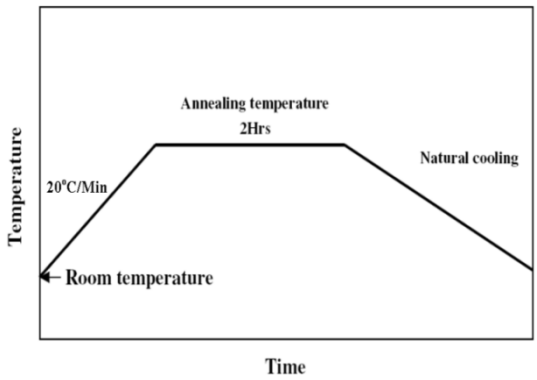

Fig. 4.2: Temperature programming sequence for the annealing process of Li-Mn-O films.

It is clear from figure 4.1 that the as deposited films show amorphous nature. In order to study the effect of post-annealing on the properties of the Li-Mn-O films, the films were annealed in a muffle furnace (Hi-Heat Furnaces & Refractory) capable of measuring temperatures upto 1000°C, with an accuracy of ± 5°C.

The annealing was carried out at various temperatures of 300, 500, 600, 700 and 800°C under atmospheric conditions. The muffle furnace used has a programmable PID controller. The ramping rate for heating during the annealing process was fixed at 20°C per minute as shown in figure 4.2. The specific temperature, for annealing was maintained for a fixed time of 2 hrs. The samples were then cooled to room temperature by natural cooling.

4.2.4 Structural studies of post annealed Li-Mn-O films.

In order to study the effect of post annealing on the structural properties of the films deposited at various sputtering pressures, X-ray diffraction studies were conducted. The XRD patterns of the Li-Mn-O thin films deposited at different sputtering pressures, and annealed at 700°C are shown in figure 4.3.

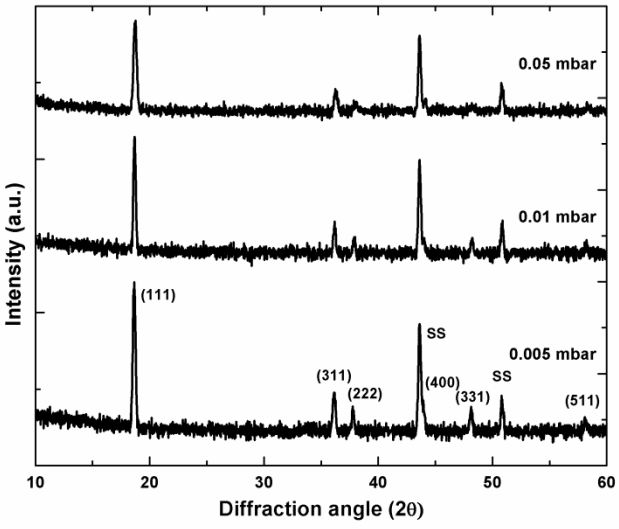

Fig. 4.3: The XRD patterns of the Li-Mn-O thin films deposited at different sputtering pressures, and annealed at 700°C

The XRD patterns show that, with the increase of the sputtering pressure, the relative X-ray peak intensity, lattice parameter and the FWHM (full width at half maximum) of (111) plane are decreasing. The lattice parameter of the films deposited at 0.005mbar pressure and post annealed at 700°C is found to be close to that of bulk $LiMn_2O_4$ [24]. The lattice parameter of the films deposited at higher pressures is found to depart more from the bulk value. It seems that an increase in sputtering rate corresponding to higher pressures may induce a faster reaction rate, which brings about the damage of the surface due to the ion bombardment. This results in poor crystalline quality as well as lithium deficiency. From figure 4.3, it is clear that peak positions of the films deposited at higher pressures are found to be slightly shifted to the higher angles compared to the films deposited at 0.005mbar. However, the XRD data of the high pressure deposited films shows that there are no impurity phases and the spinel structure is undisturbed and preserved. It is clear from figure 4.3, that the films deposited at 0.005mbar pressure show the highest crystallinity. In order to find the optimal annealing temperature, a detailed investigation of the structural characteristics of the Li-Mn-O films, deposited at 0.005mbar pressure and annealed at various temperatures are carried out by X-ray diffraction study and the results are shown in figure 4.4.

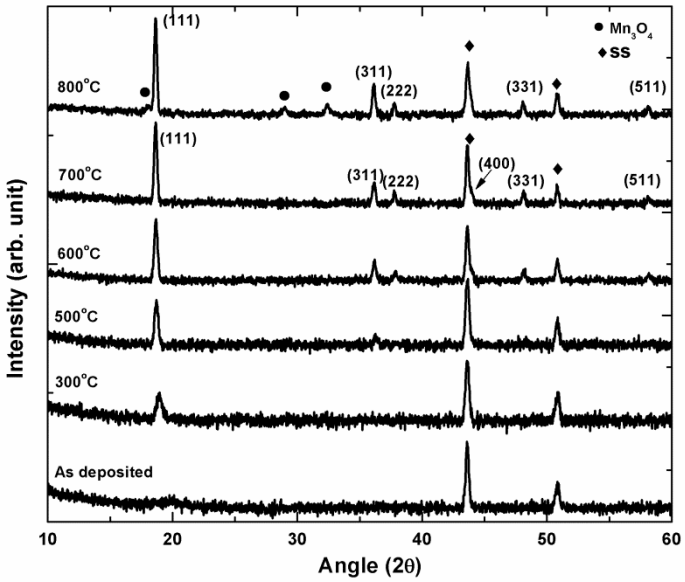

Fig. 4.4: The XRD patterns of the Li-Mn-O thin films deposited at a sputtering pressure of 0.005mbar and annealed at various temperatures.

As described in section 3.2.2, the 'as deposited' films corresponding to a sputtering pressure of 0.005mbar show poor crystalline nature. It is evident from figure 4.4 that, with the increase of annealing temperature, the XRD peaks from the film are getting more intense with respect to those of the substrate, with a slight shift in peak positions towards the lower diffraction angles, indicating an increase in unit cell volume. The FWHM corresponding to all the diffraction peaks is found to be decreasing with the increase in annealing temperature.

In the case of the films annealed at 700°C, the most prominent peak is the one corresponding to $2\theta = 18.64^{\circ}$, which is related to the reflection from the (111) plane. Apart from this, there are five other peaks corresponding to the reflections from (311), (222), (331), (400) and (511) planes. The peaks marked as 'SS' in figure 4.4, belong to those of the stainless steel substrate.

With further increase in annealing temperature, i.e. at 800°C, although the peak intensities are enhanced, some new peaks are found to appear. These extra peaks are due to the presence of the impurity phase Mn_3O_4, which is formed upon heat treatment at higher temperatures [8].

The analysis of XRD data clearly shows that the samples annealed at 700°C, certainly have the closest match with cubic spinel structure corresponding to Fd3m space group, with Li-ions occupying the 8a tetrahedral sites and manganese cations occupying 16d octahedral sites of a cubic closed array represented by the oxygen located at the 32e positions. The lattice parameter of this film is calculated to be around 8.236 Å, which is comparable to that of bulk $LiMn_2O_4$ (8.247 Å). The shift in peak positions with annealing temperature may be due to the strain in the films, which arises from the ion bombardment during sputter deposition [9].

The variation of the XRD peak intensity corresponding to the (111) plane with annealing temperatures for the films deposited at 0.005mbar pressure is shown in figure 4.5. It is clear from figure 4.5 that, with the rise in annealing temperature, the intensity of the peak corresponding to (111) plane is sharply

increasing. This indicates that increase in annealing temperature results in a clear improvement in the crystalline quality of the Li-Mn-O films.

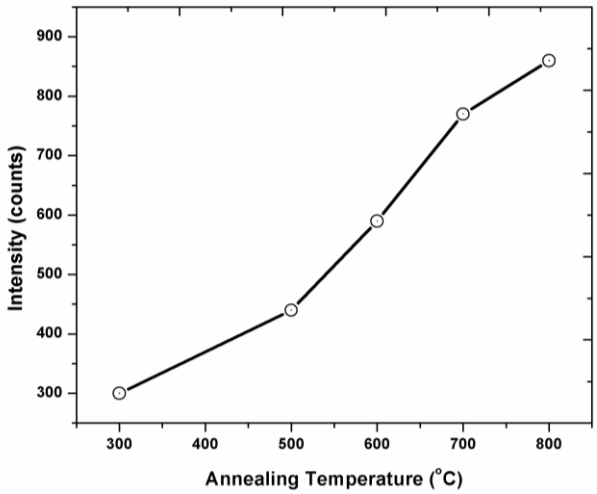

Fig. 4.5: The variation of the XRD peak intensity of the (111) plane with annealing temperature.

The variation of the cell parameter, 'a' obtained from XRD data for the films deposited at 0.005mbar pressure with annealing temperatures is shown in figure 4.6.

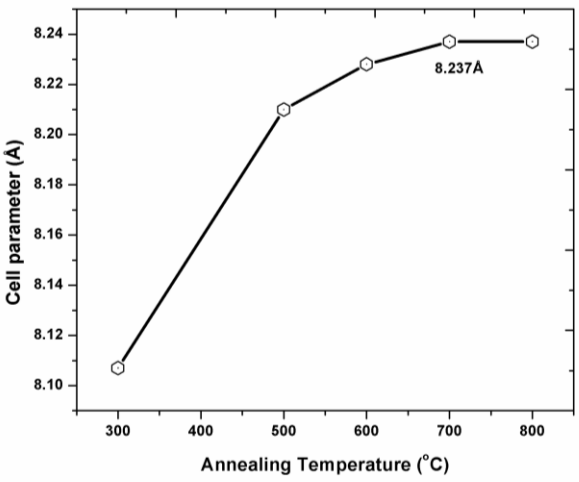

Fig. 4.6: The variation of the cell parameter 'a', with post annealing temperature.

The lattice parameter of the films annealed at lower temperatures is slightly lower than the ideal value. However with the rise in annealing temperature, lattice parameter is found to increase. This is a consequence of the improvement in the crystalline quality of the Li-Mn-O films with increase in annealing temperature. The intrinsic compressional stress in the 'as deposited' films can lead to smaller grain size. As the annealing temperature increases, the strain in the films decreases, because of the increase in particle size, resulting in increased lattice parameter.

The variations of the FWHM of XRD peaks with annealing temperature, and the corresponding crystallite size calculated using the Scherrer formula for the (111) plane are shown in figure 4.7.

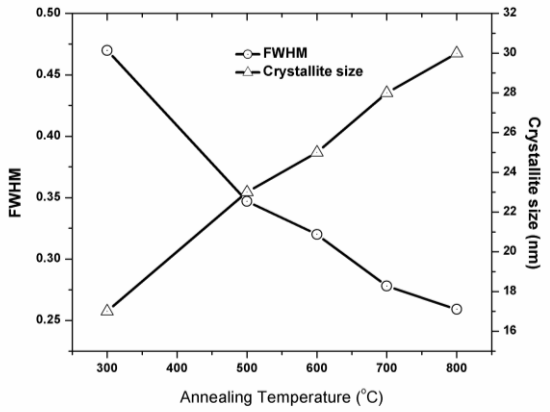

Fig. 4.7: The variations of FWHM of the peak corresponding to the (111) plane and of the crystallite size calculated using the Scherrer formula, with annealing temperature

Figure 4.7 shows that, with the rise in annealing temperature, the FWHM of the peak corresponding to the (111) plane is sharply decreasing, and the crystallite size estimated using Scherrer formula is increasing. A possible reason for this can be attributed to the intrinsic compressional stress developed during the sputtering process of the 'as deposited' films which leads to smaller grain size. As the annealing temperature increases, the strain in the films decreases because of the agglomeration of the neighboring smaller grains into larger ones. This results in lesser strain, and larger grains which in turn decreases the FWHM of the X-ray diffraction lines [9, 10].

4.2.5 Surface morphology of Li-Mn-O films by SEM.

The surface morphology of the deposited films was studied by scanning electron microscopy (SEM- ESEM QUANTA 200, FEI.). The SEM images of the as deposited Li-Mn-O films are shown in figure 4.8.

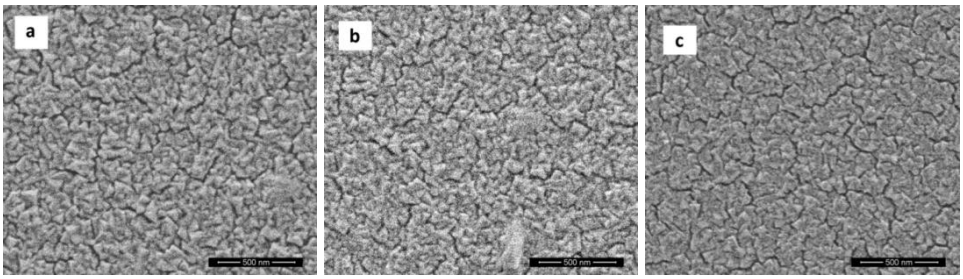

Fig.4.8: Scanning electron micrographs of the Li-Mn-O films deposited at pressures of (a) 0.005mbar, (b) 0.01mbar and(c) 0.05mbar.

The SEM images reveal a homogeneous and uniform film surface with cracks. The films deposited at 0.05mbar (fig. 4.8c) show well defined cracks with larger density, which may be induced by the strain in the films. One possible reason for the strain in the films may be the severe argon ion bombardment on the growing films at higher deposition pressure.

The surface topography of Li-Mn-O films deposited at various pressures and annealed at 700°Cis shown in figure 4.9.

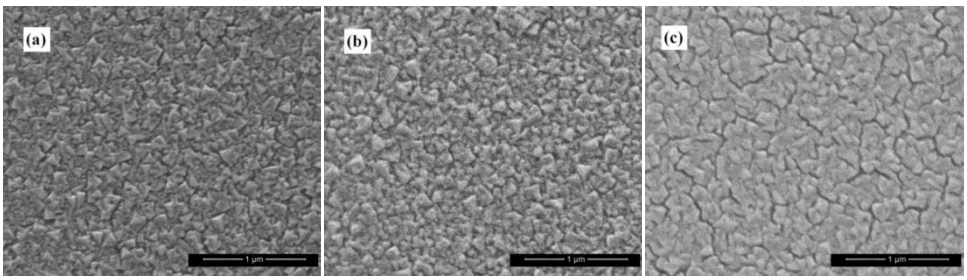

Fig.4.9: Scanning electron micrographs of the Li-Mn-O films deposited at pressures of (a) 0.005mbar, (b) 0.01mbar, (c) 0.05mbar and post annealed at 700°C.

The SEM images of the post annealed films reveal homogeneous and uniform surfaces exhibiting a multi faced polycrystalline flake-like topography. On comparing the XRD results and SEM images, it is seen that, for the post annealed films, the average grain size has increased significantly compared with the 'as deposited' films. The increase in average grain size with increase in annealing temperature is due to the strain in the 'as deposited' films as explained section 4.3

A detailed investigation on the surface topography of Li-Mn-O films, deposited at 0.005mbar and annealed at various temperatures, is carried out by scanning electron microscopy and the images are shown in figure 4.10.

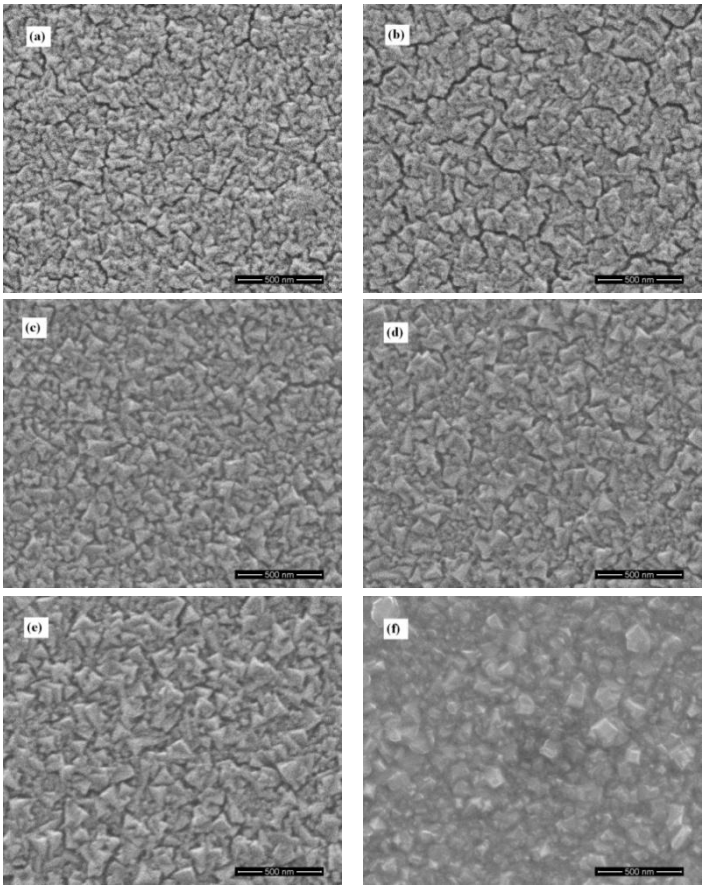

Fig.4.10: Scanning electron micrographs of the Li-Mn-O films deposited at 0.005mbar (a) 'un-annealed' and post annealed at (b) 300°C, (c) 500°C, (d) 600°C, (e) 700°C, (f) 800°C.

The SEM images show that Li-Mn-O films have a homogeneous and uniform surface topography. The 'as deposited' films do not show any clear surface structural features, and cracks are clearly visible in the image which indicates that the films are strained. With the increase of annealing temperature, a clear transition in the surface features is observable. The films annealed at higher temperatures exhibit a multi faced polycrystalline flake-like topography and are devoid of any cracks. As the annealing temperature increases, the average crystallite size also increases. This is a clear indication of strain in the 'as deposited' films. As the annealing temperature increases, strain relaxation takes place due to the agglomeration of smaller strained grains into less strained grains, resulting in larger grain size. The shift in the peak positions and decrease in FWHM of XRD peaks, with the increase in annealing temperature support this theory [9]. The SEM images show that, for a film post annealed at 700°C, the average grain size is in the order of 140nm.

The cross-sectional SEM image of the Li-Mn-O film annealed at 700°C is shown in figure 4.11.

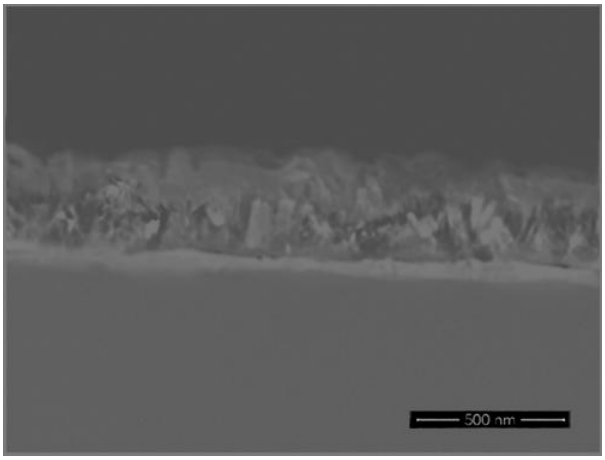

Fig. 4.11: Cross-sectional scanning electron micrograph of the Li-Mn-O films deposited at 0.005mbar pressure and post annealed at 700°C.

The cross sectional morphology of the Li-Mn-O films exhibits a typical structure of randomly distributed flake like crystallites with visible porosity. The

thickness of the film can be roughly estimated as 300nm.Figure 4.11 also shows that the deposited films lack ordered film growth mechanism.

4.2.6 Surface topography of Li-Mn-O films by AFM.

Surface profiles of the Li-Mn-O films annealed at 700°C were studied with an atomic force microscope (AFM) (WITec Alfa) operated in tapping mode using an etched single crystal Si tip. The AFM data was used to calculate the roughness (R_{rms}). Surface images were obtained from 2μm x 2μm area scans. The corresponding image is shown in figure 4.12.

AFM image represents hillocks, scattered randomly at average separations larger than the grain size. Grains and grain boundary grooves can be clearly seen. The roughness (R_{rms}) of the film has been calculated to be 24nm.

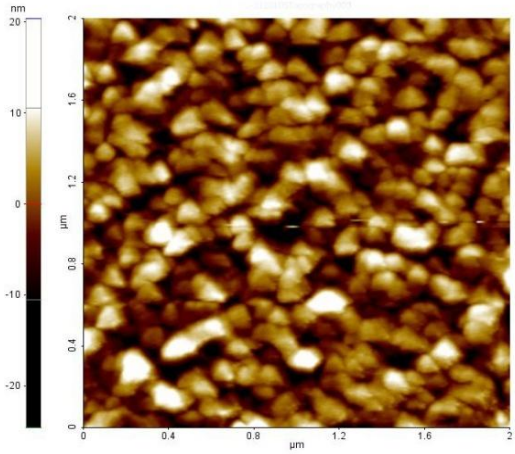

Fig. 4.12: Surface topography of the Li-Mn-O films deposited at 0.005mbar pressure and post annealed at 700°C.

4.2.7 Structural studies of Li-Mn-O films by Raman Spectroscopy.

Raman spectroscopy technique can be effectively employed for probing directly the near-neighbor environment of oxygen coordination around the lithium and manganese cations in $LiMn_2O_4$ system. The lithium manganese oxide, $LiMn_2O_4$, crystallizes with a cubic spinel-like structure and [11] its crystallographic structure possesses the symmetry Fd3m. It has the general

structural formula $A[B_2]O_4$, where the B cations reside on the octahedral 16d sites, the oxygen anions on the 32e sites, and the A cations occupy the tetrahedral 8a sites. The approximately cubic close packed array of oxide ions incorporates MnO_6octahedra sharing two opposing corners with LiO4 tetrahedra as shown in figure 4.13.

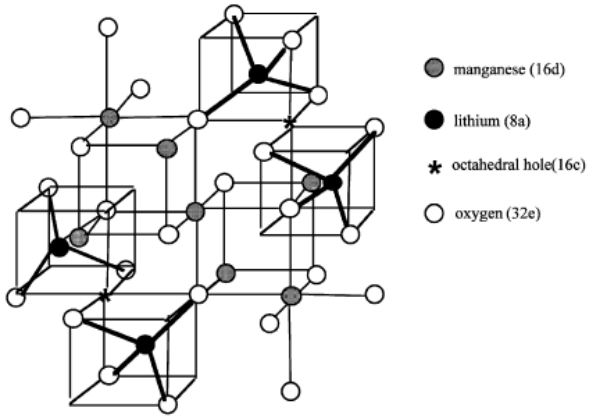

Fig. 4.13: Schematic representation of the spinel structure of $LiMn_2O_4$ [12].

The spinel structure is primarily characterized by structural groups as follows: (1) MnO_6octahedra, connected to one another in three dimensions by edge sharing. (2) LiO_4tetrahedra, sharing each of their four corners with a different MnO_6 unit but essentially isolated from one another. (3) a three-dimensional network of octahedral (16c) and tetrahedral (primarily 8a) sites, in which lithium ions can move through the (1x1) channels of the spinel lattice [12].

Using the group theory, the number of Raman and IR-active (infrared) vibrational modes allowed for a certain crystal structure, has been calculated. Based on this, the free MnO_6 octahedron belongs to the O_h group and displays six fundamental vibrational modes given by$\nu_1(A_{1g})$ symmetric stretching, ν_2 (E_g) symmetric deformation, ν_3 (F_{1u}) asymmetric stretching, ν_4 (F_{1u}) asymmetric bending, ν_5 (F_{2g}) symmetric bending, and ν_6 (F_{2u}) asymmetric bending. The ν_1, ν_2, and ν_5 are Raman active and ν_3 and ν_4 are IR active, while ν_6 is inactive in both IR and Raman. The free LiO_4 tetrahedron belongs to the T_d group and displays four fundamental vibrational modes expressed as$\nu_1(A_1)$ symmetric

stretching, ν_2(E) asymmetric stretching, ν_3(F_2) asymmetric stretching, and ν_4 (F_2) asymmetric deformation. All the fundamentals are Raman active but only ν_3 and ν_4 are active in the IR [13] [14].

The vibrational modes of the Raman active zone-centre phonons of the spinel structure are shown in figure 4.14.

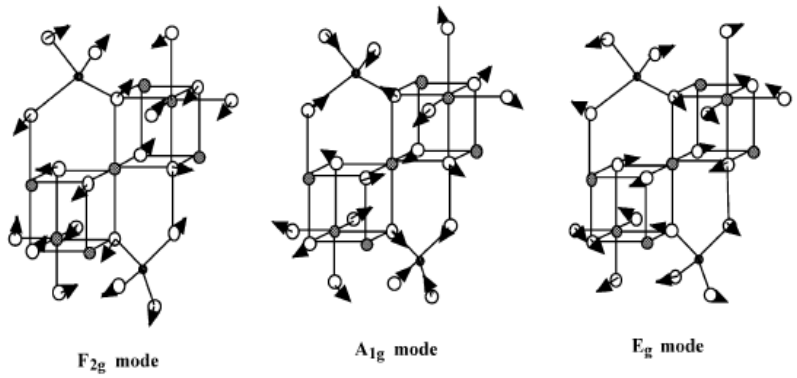

Fig. 4.14: The vibrational modes of the Raman active zone-centre phonons of the spinel structure [12].

Figure 4.15 shows typical Raman spectrum of $LiMn_2O_4$ and assignment of the peaks to the various modes.

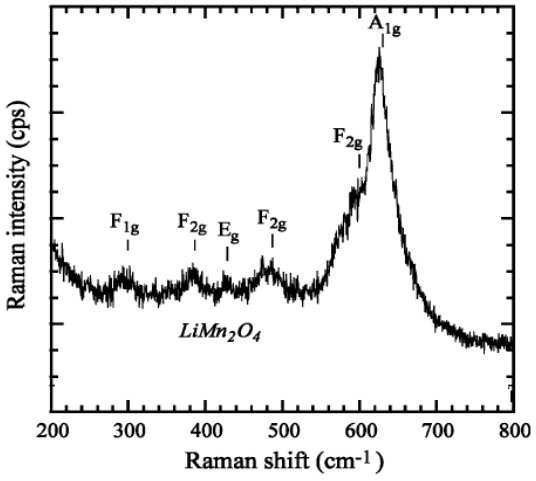

Fig. 4.15: Typical Raman spectrum of $LiMn_2O_4$, and assignment of peaks to the various Raman modes [12].

The Raman spectrum of $LiMn_2O_4$primarily consists of a strong and broad band at approximately 625 cm^{-1} with a shoulder at 580 cm^{-1}. A band with a medium intensity is visible at around 483 cm^{-1}. Three more bands, with lower wave numbers and having weaker intensity are observed at approximately 426, 382, and 300 cm^{-1}. The peak positions and assignments of the Raman active modes of $LiMn_2O_4$ are shown in table 2.

Table 2: Peak positions (in cm^{-1}), intensity, symmetry, and assignments of the Raman active modes of the spinel $LiMn_2O_4$. [12]

Peak positions (cm^{-1})	Intensity	Symmetry species	Assignment
300	Weak	$F^{(4)}_{1u}$	δ(O-Mn-O)
382	Weak	$F^{(3)}_{2g}$	δ(Li-O)
426	Weak	E_g	ν_s(Mn-O)+ ν_s(Li-O)
483	Medium	$F^{(2)}_{2g}$	ν(Mn-O)
583	Shoulder	$F^{(1)}_{2g}$	ν_s(Mn-O)
625	Strong	A_{1g}	ν_s(Mn-O)

The Raman spectra of the Li-Mn-O films were obtained with LabRAM-HR using an argon ion laser of wavelength 514.5 nm as the excitation source (5-10mW power). The Raman spectra of 'as deposited' Li-Mn-O films deposited under different sputtering pressures and at RF power of 5W/cm^2 are shown in figure 4.16.

The Raman spectrum of the 'as deposited' films corresponding to a sputtering pressure of 0.005mbar shows a strong band centered around 627cm^{-1}. The broad Raman band around 627cm^{-1}, corresponds to the A_{1g} mode which belongs to the Mn-O stretching vibration of the MnO_6 group. For the films deposited at higher sputtering pressures, the band corresponding to A_{1g} mode gets shifted progressively towards the higher wave numbers. The reason for this shift is not clear and this could be due to the formation of Mn_3O_4 impurity phase as a result of the deficiency of lithium in the films.

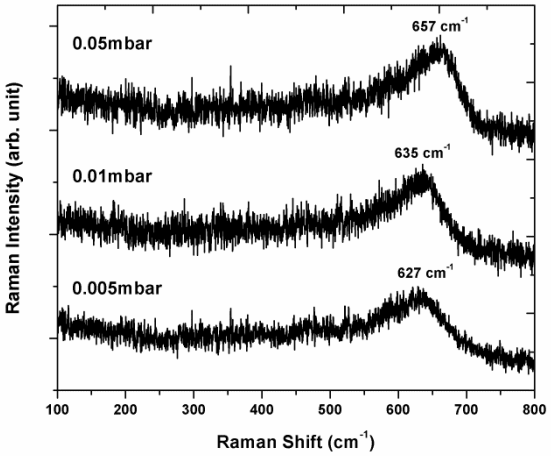

Fig. 4.16: The Raman spectra of as deposited Li-Mn-O films at different sputtering pressures and RF power of 5W/cm^2.

In order to study the effect of annealing temperature on the properties of the Li-Mn-O films, Raman spectra of the films deposited under various pressures and annealed at 700°C are recorded and are shown in figure 4.17.

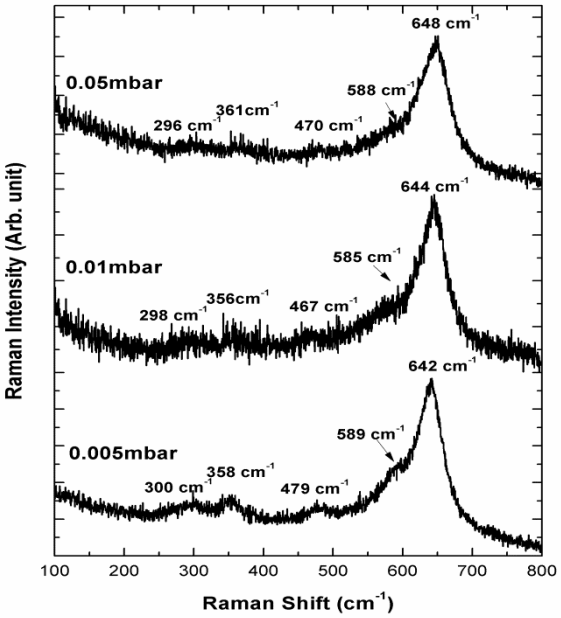

Fig. 4.17: The Raman spectra of the Li-Mn-O thin films deposited at different sputtering pressures and annealed at 700°C

The Raman spectrum of the films deposited at 0.005mbar and annealed at 700°C show a strong band centered at around 642 cm^{-1} and a few less intense bands. For these films, the peak corresponding to the Raman mode A_{1g} which is centered at 642 cm^{-1} is located slightly at a higher wave number compared to the standard Raman spectrum shown in table 2. As observed in figure 4.17, for the films deposited at higher sputtering pressures, the peak corresponding to the Raman mode A_{1g} is shifted to the higher wave number. Accordingly, in the case of the annealed samples as well, the strong band at 642 cm^{-1} corresponding to the sputtering pressure of 0.005mbar is shifted to 648cm^{-1}. This shift in peak positions can be attributed to the lithium deficiency in the films annealed at high temperatures, which is also evident from the ICP-AES data shown in section 3.2.1 [15].

A detailed investigation of the structural features of sputtered Li-Mn-O films deposited at 0.005mbar and annealed at various temperatures was carried out by the micro-Raman spectroscopy and the results are shown in figure 4.18, and the enlarged view of the Raman spectrum of the films annealed at 700°C is shown in figure 4.19

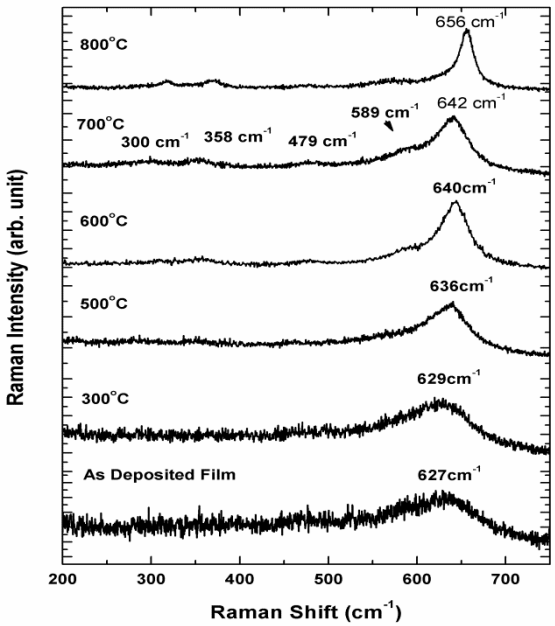

Fig. 4.18: The Raman spectra of the Li-Mn-O thin films deposited at sputtering pressure 0.005mbar and annealed at various temperatures

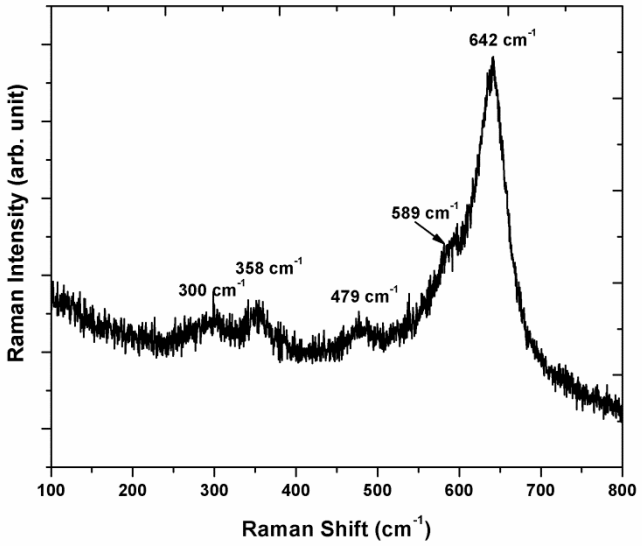

Fig. 4.19: Enlarged view of the Raman spectrum of the Li-Mn-O thin films deposited at sputtering pressure 0.005mbar and annealed 700°C temperature

It is clear from figure 4.18 that the 'as deposited' films show only a broad band centered around 627cm^{-1} and no other peaks are clearly visible, which is due to the amorphous nature of the films. As the annealing temperature increases, other peaks start to evolve and the band at 627cm^{-1} shows a slight shift towards the higher wave numbers.

The films annealed at 700°C (Fig. 4.19) show all the weak bands at their maximum intensity levels. For these films, a strong band corresponding to A_{1g} centered at around 642 cm^{-1}, (which is shifted almost 15cm^{-1} in comparison with the 'as deposited' films) and a few weak bands at 589, 479, 358 and 300 cm^{-1} can be clearly seen. The strong band at around 642 cm^{-1}, accompanied by a small shoulder at around 589 cm^{-1} is closely related to the [MnO_6] octahedron and the Mn oxidation state. These bands are assigned as the A^1_g and F^1_{2g} modes, respectively. The F^1_{2g} shoulder originates mainly from the vibration of the Mn^{4+}- O bond. Its intensity depends on the Mn^{4+} concentration in the material, and hence reflects the Mn average oxidation state [16]. As seen from Fig. 4.19, the A^1_g and F^1_{2g} bands are not well separated in $LiMn_2O_4$ because of the near equal concentrations of Mn^{3+} and Mn^{4+} in the material. The band at 302cm^{-1}

corresponds to F_{1g} symmetry and the bands corresponding to 358, and 478 cm^{-1} have the F_{2g} symmetry [17].

The observed shift in A^1_g band towards the higher wave numbers with increase in annealing temperature can be due to the deficiency of lithium in annealed films. As explained in section 3.2.1, the 'as deposited' films are lithium rich and A^1_g band is centered around 627cm^{-1}. Since lithium is highly volatile, the possibility for lithium deficiency in the films annealed at high temperatures is high.

On further rise in annealing temperature (i.e. 800°C) the band at 478 cm^{-1} diminishes in intensity while the bands at 300cm^{-1} and 360cm^{-1} become slightly stronger. Most importantly, the strong band at 642 cm^{-1} shifts to 656cm^{-1} and becomes narrow and sharp. This shifting may be due to the formation of Mn_3O_4 impurity phase due to the heat treatment at high temperatures, which is evident from the XRD data as well. The observed shift can also be due to some kind of induced structural transformation at high temperatures [12, 17, 18]. For the films annealed at 800°C, the shoulder at 589cm^{-1} becomes slightly less intense with a slight shift towards lower wave numbers, which indicates an unequal concentration of Mn^{3+} and Mn^{4+} in these films.

4.2.8 Electronic transport properties of Li-Mn-O films.

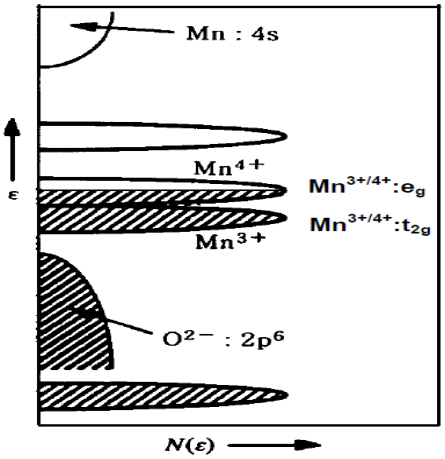

Fig. 4.20: The qualitative energy diagram of $Li_{0.5}Mn_2O_4$

Under ambient conditions, the crystal structure of $LiMn_2O_4$ belongs to the Fd3m space group of a cubic system with lithium ions at the tetrahedral 8a sites, manganese ions at the octahedral 16d sites and oxygen ions at the 32e sites. Because the average valence of manganese ions in $LiMn_2O_4$ is 3.5, equal amounts of $Mn^{4+}(t^3_{2g}e^0_g)$ and $Mn^{3+}(t^3_{2g}e^1_g)$ ions must be distributed randomly on the 16d sites by symmetry. The ionic distribution of this material is then formulated as $(Li^+)_{8a}[Mn^{3+}Mn^{4+}]_{16d}(O^{2-})_{32e}$ [19].

In the case of transition metal compounds, a general explanation for semiconducting behavior is that the transition metal ion can exhibit several valence states so that the electron hopping from low to high valence state can take place (see figure 4.20) [20, 21]. Experimental results are usually discussed in terms of Mott's theory for electrical conductivity in transition metal oxides [22, 23]. In the temperature range from 177 to 450 °K, the electrical conduction in $LiMn_2O_4$ spinel takes place in two parallel regimes by (a) hopping conduction in the localized states and (b) by electron tunneling [24]. The former mechanism tends to take place at high temperatures, where carriers are excited beyond the mobility edges into localized states and dominate the transport, while the latter mechanism may be due to a variable-range hopping mechanism for the small-polaron transport appearing in the low-temperature region. According to the electronic considerations put forward by Goodenough et al. [20], the small-polaron semiconducting character of the $Li[Mn^{3+}Mn^{4+}]O_4$ compound is due to weak Mn-Mn interactions, which in turn prevents an itinerant-electron bandwidth, giving localized electronic configurations. According to the model of small-polaron transport, suggested by Austin and Mott [[22, 23.], the d.c. conductivity should be given by

$$\sigma_{dc} = (\sigma_o/k_BT)\, e^{(-W/k_BT)} \qquad (4.1)$$

where $\sigma_o = \nu_{ph}Ne^2R^2C(1-C)e^{(-2\alpha R)}$, where N is the number of transition metal ions per unit volume (the density of states at the Fermi level), C is the ratio of the transition metal ion concentration in low valance state to the total transition metal ion concentration, ν_{ph} is an optical-phonon frequency ($\sim 10^{13}$) assisting the hops, e is the electronic charge, R the average interionic spacing, α the wave

function decay constant, W the activation energy, k_B the Boltzmann constant and T the absolute temperature.

The above equation (4.1) can be compared to the well-known Arrhenius equation, where the activation energy is given by

$$W = W_h + 1/2W_d \qquad (4.2)$$

W_h is the polaron-hopping energy equal to $W_{p/2}$;W_p is the polaron binding energy and W_d is the disorder energy arising from the energy difference of the neighboring sites [25].

The conductivity measurements of the 'as deposited' and annealed Li-Mn-O films were carried out in the temperature range of 25 to 100°C. For a given film, with the increase of temperature, the conductivity increases, and the conduction is thermally activated which can be attributed to the semiconducting nature of the Li-Mn-O films. The temperature dependence of the conductivity (σ_{dc}) was studied by using Arrhenius equation, by plotting $\ln(\sigma_{dc})$ vs. (1000/T).

The temperature dependence of dc electrical conductivity of the 'as deposited' Li-Mn-O films for various sputtering pressures is shown as Arrhenius plots in figure 4.21.

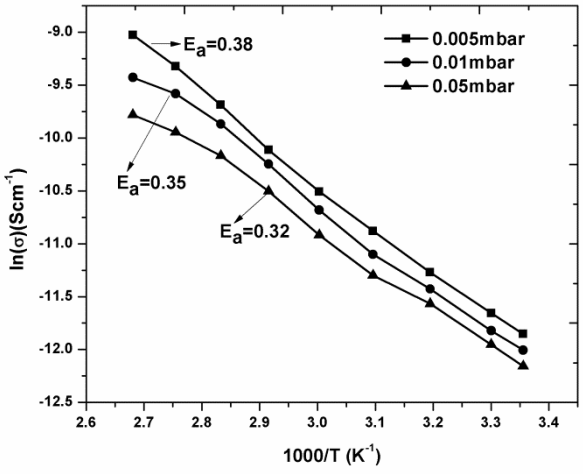

Fig. 4.21: Arrhenius plots of the 'as deposited' Li-Mn-O films deposited at various pressures, for RF power 5W/cm^2

The results show that, for films deposited at different sputtering pressures, conductivity increases with the increase in temperature. This shows the semiconducting nature of the Li-Mn-O films. For as deposited Li-Mn-O films, the conductivity increases with decrease in sputtering pressure. The Arrhenius plot between $\ln(\sigma_{dc})$ and (1000/T) shows that the activation energy increases with the decrease of sputtering pressure.

The temperature dependence of the dc electrical conductivity of the Li-Mn-O films deposited at various pressures and annealed at 700°C is shown as Arrhenius plots in figure 4.22. It is seen that the ambient temperature conductivity increases with decrease in sputtering pressure and the activation energy increases with the decrease of sputtering pressure.

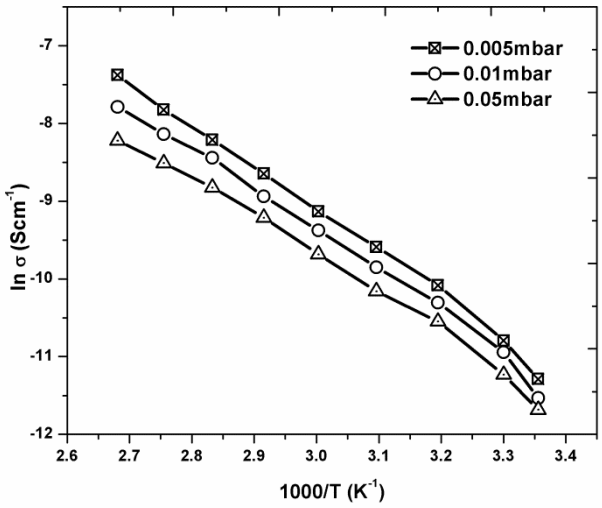

Fig. 4.22: Arrhenius plots showing the temperature dependence of the dc electrical conductivity of the Li-Mn-O films deposited at various pressures and annealed at 700°C

A detailed investigation on the temperature dependence of the dc electrical conductivity of the Li-Mn-O films deposited at 0.005mbar and annealed at various temperatures is shown as Arrhenius plots in figure 4.23.

Figure 4.24 shows that the room temperature conductivity of 'as deposited' Li-Mn-O films is of the order of 10^{-6} S/cm. It is observed that with the increase of

annealing temperature, the ambient temperature conductivity and the thermal activation energy also increase. The highest conductivity is obtained for the films annealed at 700°C. For the films annealed at 800°C, even though the conductivity decreases, the activation energy is slightly higher than that of the films annealed at 700°C. A straight line behavior is observed for all the films, as seen from figures 4.22 and 4.23, with the lower temperature conductivity (near ambient temperature) values slightly deviated from the straight line. This is probably due to the phase transition, induced by Jahn-Teller effect associated with the $LiMn_2O_4$ at around room temperature. [24, 26, 27]

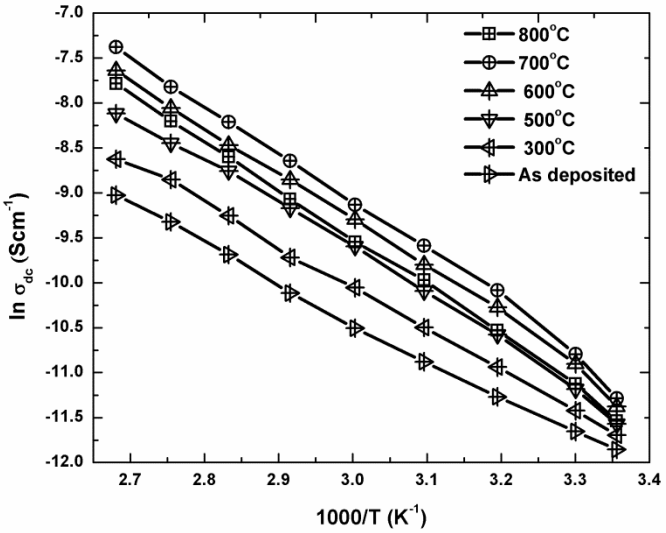

Fig. 4.23: Arrhenius plots showing the temperature dependence of the dc electrical conductivity of the Li-Mn-O films deposited at 0.005mbar and post annealed at various temperatures.

The variation of conductivity and activation energy with annealing temperature is shown in figure 4.24.

There are two reasons for the increase in conductivity with increase in annealing temperature, the first one being the increase in crystallinity of Li-Mn-O films upon annealing. The second reason is the increase in grain size with the increase in annealing temperature, which may reduce the grain boundary scattering of charge carriers, as evident from the XRD and SEM data.

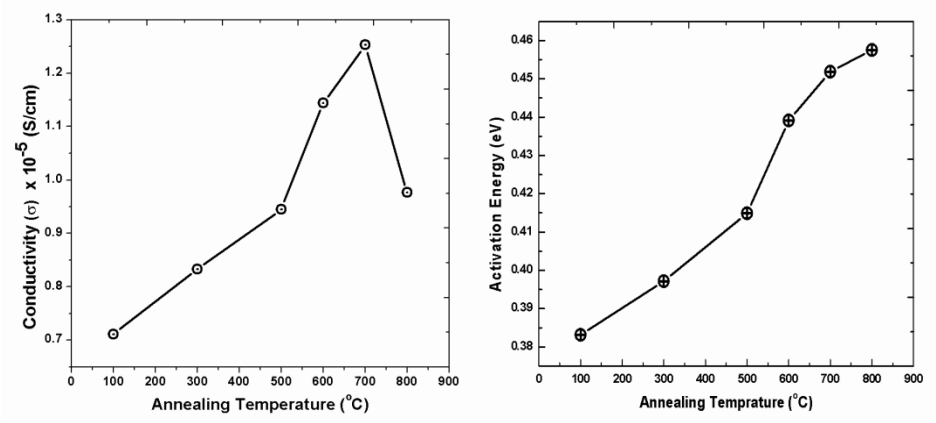

Fig. 4.24: Variation of room temperature conductivity and activation energy of Li-Mn-O films deposited at 0.005mbar and post annealed at various temperatures.

The increase in activation energy with the increase of annealing temperature may be connected with the increase in lattice parameter, a. It is clear from the XRD data that, the lattice parameter of the Li-Mn-O films increases with increase in annealing temperature (see section 3.2.4).Hence the increase in activation energy with the increase in annealing temperature, which is closely related to increase in lattice parameter can be interpreted in terms of the hopping model of manganese oxide-based materials, which predicts that smaller Mn-Mn distance leads to a lower activation barrier [28, 29]. However, more detailed investigations are needed to unravel the actual mechanism behind this phenomenon [20].

4.3 Electrochemical properties of Li-Mn-O films.

4.3.1 Assembling of test cell for electrochemical characterization.

In order to test the electrochemical performance of the cathode films, one has to make a test cell and the best way to do this is by making a Swagelok®cell. The schematic diagram of the Swagelok cell is shown in figure4.25. The Swagelok cell consists of a Teflon® cylindrical union connector with ferrule and nut for hermetic sealing of the electrodes inside the body. The contacts from the electrodes (cathode and anode) can be taken externally using stainless steel rods

which are in contact with the electrodes. In this setup the cathode electrode is in the form of a cylindrical disc of diameter 12mm and thickness 0.5mm. In the Swagelok cell, the cathode, the anode and the separator should be in thin disc forms [30].

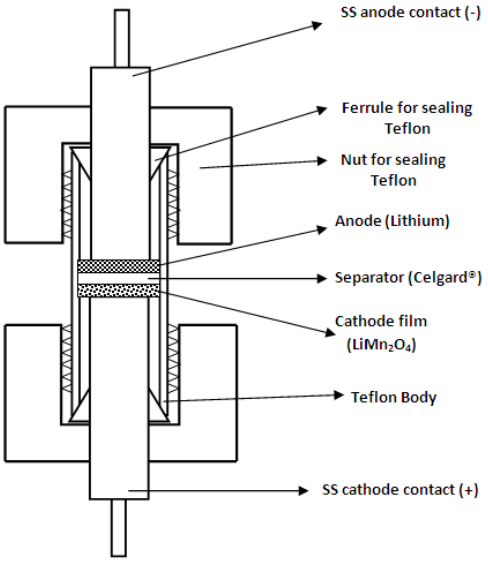

Fig. 4.25. Swagelok type cell for studying the electrochemical performance of cathode films.

For studying the electrochemical performance of Li-Mn-O films, the Swagelok cell assembling was done by transferring all the cell components to the glove box (MTI, USA).The H_2O and O_2 levels inside the glove box were maintained at less than 0.5 ppm. Lithium foil was used (Alfa Aesar) as anode. It was cut in to the required size using a punching machine. The anode and cathode were separated by inserting the separator, Cellguard®. A 1M $LiPF_6$ in 1:1 ethylene carbonate (EC) and diethyl carbonate (DEC) solution (Targray) was used as the electrolyte.

The specimen cell was prepared by carefully inserting the cathode disk and separator in to the Swagelok cell and a few drops of electrolyte were added to the cell and then the lithium foil was placed. The stainless steel contact rods were inserted on both sides of the cell. Then sealing was done with Swagelok ferrule and nut as shown in figure 4.25. Once the cell was sealed, the voltage of

the cell was measured and then the cell was transferred from the glove-box. The cell thus prepared was kept for 24 hours before doing any testing.

4.3.2 Cyclic voltammetry of Li-Mn-O films.

Cyclic voltammetry is a potentiodynamic electrochemical measurement technique that acquires information on the electrochemical behavior of an electrochemical cell. It is helpful to study the thermodynamics of redox processes and kinetics of heterogeneous electron-transfer reactions. The characteristic shapes of the voltammetric waves and the unique positions on the potential scale act as a "fingerprint" for the electrochemical properties of a redox system, and CV is therefore sometimes referred to as "electrochemical spectroscopy".

In the cyclic voltammetry (CV) experiment, the voltage of a working electrode, in the present case Li-Mn-O film, vs. a reference electrode (metallic lithium foil) is measured. The voltage of the working electrode with respect to the reference electrode is increased linearly with time. The current response of the voltaic cell is measured and the resulting I vs. V data can be plotted as a cylic voltammogram (CV). A CV can provide valuable information on a redox reaction, in that the current response vs. voltage data is the evidence supporting the occurrence of a certain redox reaction.

The electrochemical behavior of the cathode material needs to be extensively studied for assessing its prospects of application in thin film batteries. The best way to access the electrochemical properties is by studying the CV and the galvanostatic charge discharge cycling. For this study half cells were fabricated with Li-Mn-O films coated on stainless steel substrates.

The cyclic voltammograms of the as deposited Li-Mn-O thin film samples on stainless steel substrates, deposited at different sputtering pressures, obtained with a voltage scan speed of 0.1mV/s between a voltage window of 3.2V and 4.3V are shown in figure 4.26. The CV curves show that the films are electrochemically active. The curves show distinct and broad oxidation peaks at around 4.16V for the cathodic scan and the reduction peaks at around 4.08V for

the anodic scan. The cathodic peaks correspond to lithium ion deintercalation process to form λ-MnO_2 from $LiMn_2O_4$. The anodic peaks represent the lithium ion intercalation to form $LiMn_2O_4$ from λ-MnO_2.

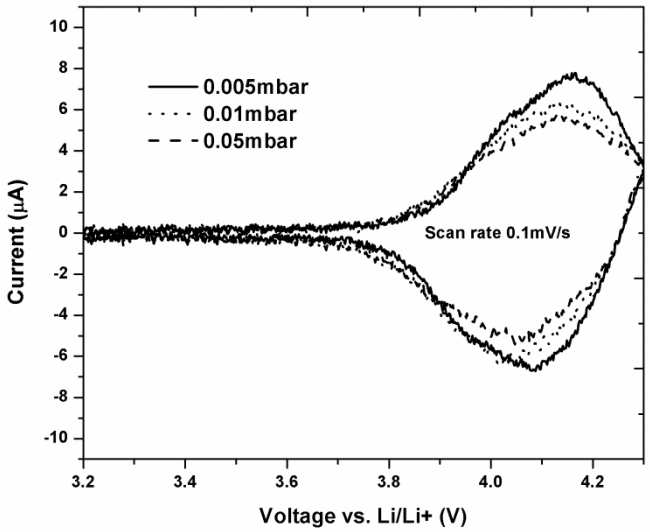

Fig. 4.26: The cyclic voltammograms of as deposited Li-Mn-O thin films, at different sputtering pressures.

For an ideal $LiMn_2O_4$ cathode material, the oxidation and reduction curves consist of two distinct peaks, but in the as deposited Li-Mn-O films, the peaks are not resolved, due to the amorphous nature of the films. It is evident from the CV curves that, as the sputtering pressure increases, the area enclosed by the oxidation and reductions curves decreases, showing a decreased electrochemical capacity.

Cyclic voltammograms of Li-Mn-O films deposited at different sputtering pressures and post annealed at 700°C are shown in figure 4.27. It is clear from figure 4.27 that, Li-Mn-O films deposited at various pressures and annealed at 700°C are electrochemically active. Two distinct oxidation as well as reduction peaks for both the cathodic and anodic scans can be clearly seen. The area under the CV curve is decreasing with the increase of the sputtering pressure, indicating a decrease in capacity with increase in pressure. Moreover, as the sputtering pressure increases, the oxidation and the reduction peaks show a merging trend with a slight shift in the respective peak positions.

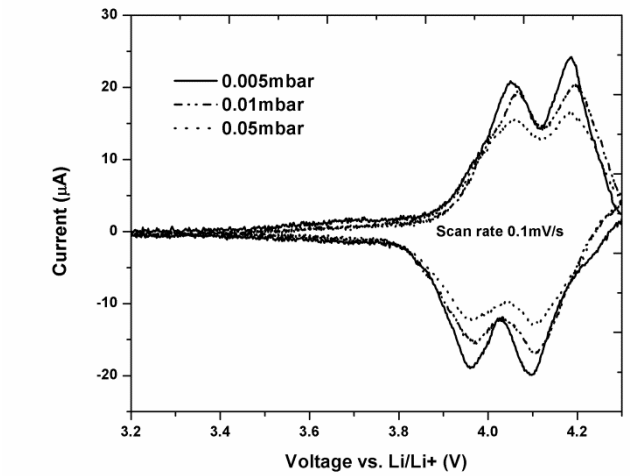

Fig. 4.27: Cyclic voltammograms of Li-Mn-O films deposited at different sputtering pressures and post annealed at 700^{o}C

The results of the detailed investigations on the cyclic voltammetry of Li-Mn-O films deposited at 0.005mbar and post annealed at various temperatures are shown in figure 4.28.

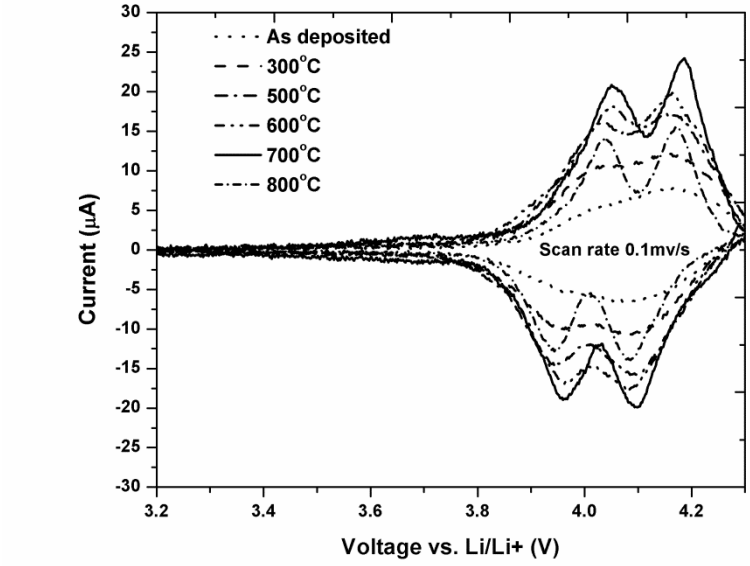

Fig. 4.28: Cyclic voltammograms of Li-Mn-O films deposited at 0.005mbar and post annealed at various temperatures.

It has been observed earlier (from figure 4.26) that the ‘‘as deposited’ films show some reversible capacity with two broad unresolved peaks corresponding to anodic and cathodic scans. It is quite evident from figure 4.28 that, as the annealing temperature increases, the anodic/cathodic peaks become stronger and sharper with an increase in the area under the curve.

The films annealed at 700°C display the most intense peaks (see figure 4.29) and these peaks are located at about 4.05V and 4.18V for oxidation cycle and 4.1V and 3.96V for reduction cycle which are in good agreement with the previously reported values [31].

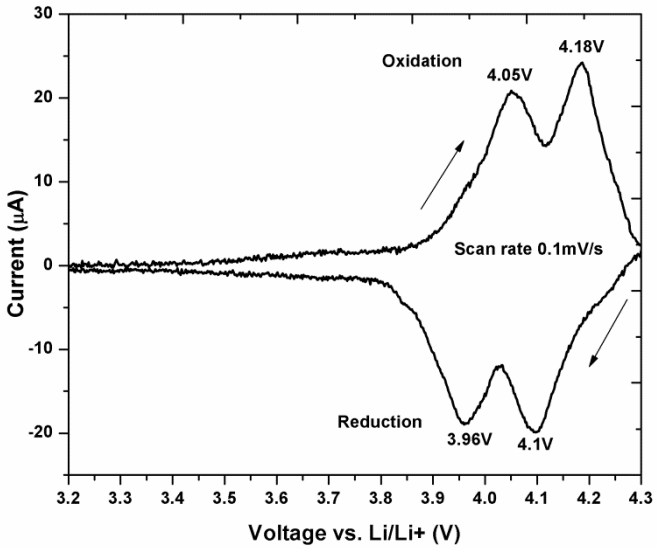

Fig 4.29: Enlarged view of the cyclic voltammogram of Li-Mn-O films deposited at 0.005mbar pressure and annealed at 700°C

These two pairs of redox peaks indicate the two stages of the Li-ion extraction and insertion processes. The cathodic peaks correspond to a two step lithium ion deintercalation process to form λ-MnO_2 from $LiMn_2O_4$. The first oxidation peak at 4.00 V vs. Li/Li+ is attributed to the removal of Li+ from one-half of the tetrahedral 8a sites. The second oxidation peak at 4.18 V vs. Li/Li+ is the removal of Li+ from the remaining tetrahedral 8a sites. Similarly the anodic peaks represent the two stage lithium ion intercalation to form $LiMn_2O_4$ from λ-MnO_2.

It is evident from figure 4.28 that, with the rise of annealing temperature, the FWHM of all the cathodic and anodic peaks is decreasing and the area under the curve is increasing. The increase in area under the curve corresponds to an increase in capacity, and so the films annealed at 700°C have got the highest capacity compared to all the other films. The films annealed at 800°C show lesser capacity. This could be attributed to the formation of Mn_3O_4 impurity phase at higher annealing temperatures as observed from the XRD data. These results indicate that the electrochemical properties of Li-Mn-O films are greatly influenced by the annealing temperature. [32]

4.3.3 Charge discharge cycling studies on Li-Mn-O films.

Galvanostatic charge/discharge cycling is an experiment to determine the capacity of the battery by applying a constant current between the cathode and the anode. The current is applied until the required upper or lower potential limits are reached and the corresponding cell voltage and time are recorded in regular intervals. For the working electrode, a negative current would cause reduction and a positive current oxidation. The investigation of the variation of potential with time for an electrochemical system is also called 'chronopotentiometry'. The charge discharge curves of the as deposited Li-Mn-O thin films, obtained at a constant current of 5μA are shown in figure 4.30.

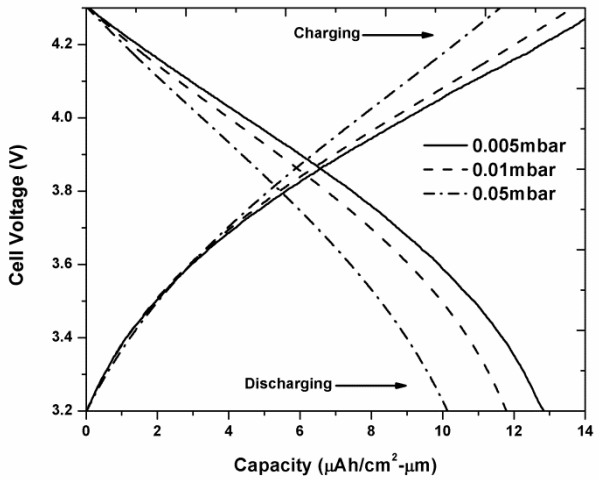

Fig. 4.30: The charge discharge curves of the as deposited Li-Mn-O thin films, deposited at various sputtering pressures.

The cycling profile of the as deposited films shows a smooth curve without any distinct potential plateaus, which may be due to the amorphous nature of the films. The charge discharge curves suggest that the films are electrochemically active, and comparatively stable with extraction and reinsertion of lithium ions during cycling. Further, figure 4.30 shows that the films deposited at a lower sputtering pressure give the highest capacity of ~13μAh/cm^2/μm; it is also observed that the capacity gradually decreases with the increase of sputtering pressure.

The charge discharge curves of the Li-Mn-O thin films deposited at various sputtering pressures, and annealed at 700°C were obtained at a constant current of 5μA and are shown in figure 4.31.

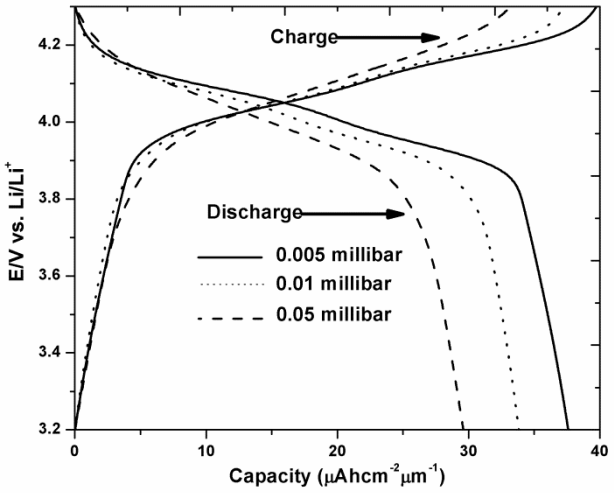

Fig. 4.31: Charge-discharge curves of Li-Mn-O films deposited at different sputtering pressures and post annealed at 700°C

The cycling profile displays two potential plateaus at around 4 and 4.2 V and is in good agreement with the earlier reports [31]. The nature of the curve suggests a good cycling behavior, and the films are stable with extraction and reinsertion of lithium ions during cycling. Further, it is also seen that as the sputtering pressure increases, the discharge capacity decreases. The films deposited at a lower sputtering pressure of 0.005mbar give the highest capacity. There are two main reasons for this behavior. The low pressure deposited films have better crystallinity and the smaller grain size observed at lower pressures

increases the total area available for the electrolyte contact, which facilitates better Li ion diffusion. The high pressure deposited films show poor capacity, possibly due to the poor crystallinity of the films.

In order to study the effect of annealing on the capacity of Li-Mn-O films, a quantitative study of the actual capacity vs. annealing temperature is necessary. Figure 4.32 shows the charge/discharge curves of the Li-Mn-O films deposited at 0.005mbar pressure and annealed at various temperatures, obtained with a charge/discharge current of 5μA.

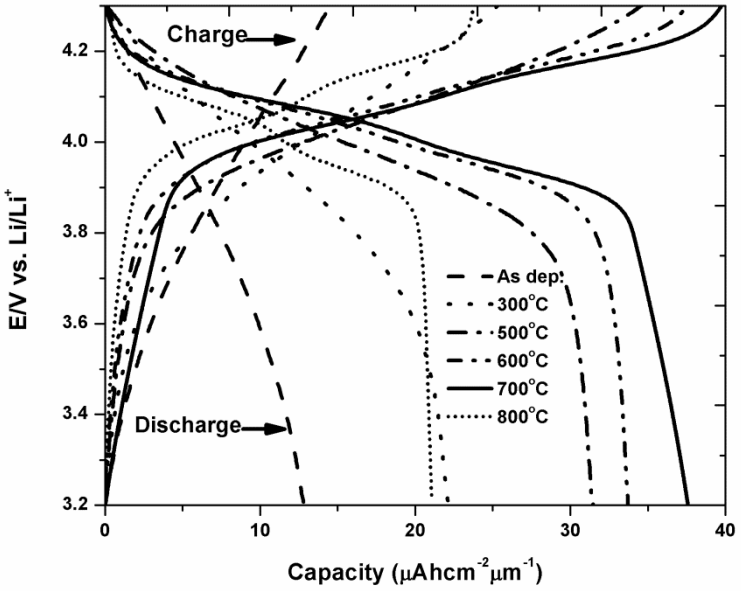

Fig. 4.32: Charge-discharge curves of Li-Mn-O films deposited at 0.005mbar pressure and post annealed at various temperatures.

The charge-discharge cycling profile displays two potential plateaus at around 4 and 4.1 V and is in good agreement with the earlier reports and matches well with the results of cyclic voltammetry data shown in figure 4.28. There is a steady increase of capacity with the rise of annealing temperature, with a maximum capacity of ~37μAh/cm^2/μm observed for the films annealed at 700°C. Moreover the nature of the curves suggests a good cycling behavior, and that the films are stable with extraction and reinsertion of lithium ions during cycling. The observed high capacity for the films annealed at 700°C is due to

the improved crystallinity as well as a high lithium ion diffusion coefficient. The films annealed at 800°C are found to exhibit almost half of the capacity of the films annealed at 700°C. This may be due to the formation of impurity phases at high annealing temperatures.

The variation of discharge capacity with annealing temperature is shown in figure 4.33.

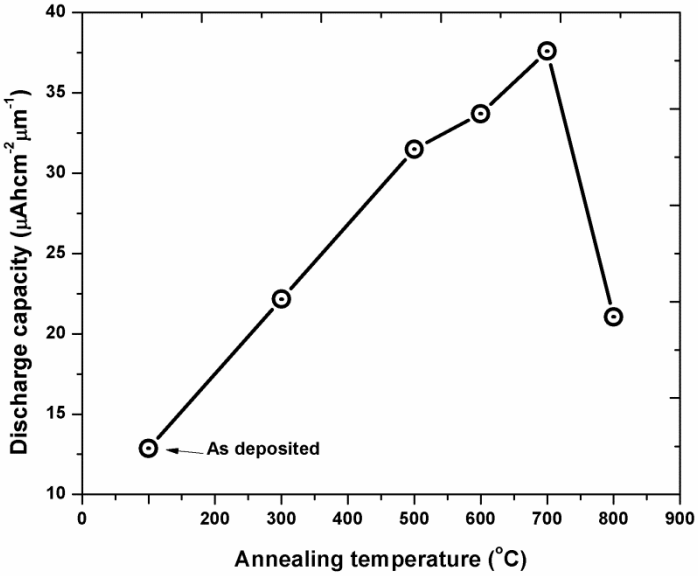

Fig. 4.33: The variation of discharge capacity of Li-Mn-O films deposited at 0.005mbar pressure and post annealed at various temperatures.

Although the films annealed at 700°C are showing the highest capacity, it is only 60% of the specific capacity reported by Tang *et al.*[33]. It is clear from figures 4.32 and 4.33 that, as the annealing temperature rises, the initial capacity increases, due to the increase in the film crystallinity, but the increase in initial capacity is not significant enough, compared to the increase in crystallinity, which means that, for the films annealed at 500, 600 and 700°C, the variation in initial capacity is approximately 15% only. The possible reason for this behavior can be the contamination of Li-Mn-O films by thermal diffusion of iron and chromium from the stainless steel substrate material during annealing above 500°C. Similar observations have been reported by Komaba *et al* [7, 34]

4.3.4 Cycle performance of Li-Mn-O films.

The swagelok cell was charged/discharged between 3.2 and 4.3V with a constant charging and discharging current of 5μA for about 20 cycles. Figure 4.34 shows the specific capacity (in $\mu Ahcm^{-2}\mu m^{-1}$) as a function of cycle number for the Li-Mn-O films deposited at various sputtering pressures and annealed at 700°C.

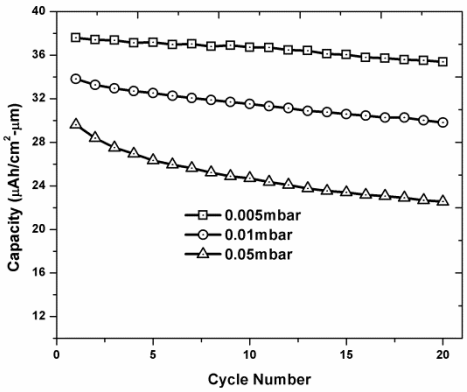

Fig. 4.34: Cycle performance study of Li-Mn-O films deposited at different sputtering pressures and post annealed at 700°C

It is clear from figure 4.34 that the films deposited at a sputtering pressure of 0.005mbar show the minimum cycle degradation (0.29%/cycle). The films deposited at 0.05mbar pressure show the maximum cycle degradation of 1.1% per cycle.

The specific capacity (in $\mu Ahcm^{-2}\mu m^{-1}$) of Li-Mn-O films deposited at 0.005mbar pressure and annealed at various temperatures is plotted as a function of cycle number and the plots are shown in figure 4.35.

It is seen from figure 4.35 that, the 'as deposited' films show very poor capacity retention, which is mainly due to the amorphous nature of the films. For the films annealed at 300°C the capacity retention is better compared to the 'as deposited' films. An average capacity fading of 1.28% per cycle is observed for these films. The capacity fading for the films annealed at 500 and 600°C is 0.51% and 0.35% respectively.

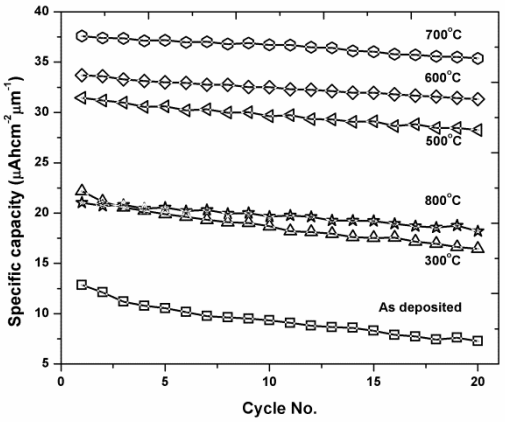

Fig. 4.35: Cycle performance study of Li-Mn-O films deposited at 0.005mbar pressure and post annealed at various temperatures.

The films annealed at 700°C show the highest capacity as well as maximum capacity retention and the discharge capacity after 20 cycles is about 94.1% of the initial value. The average capacity loss per cycle is about 0.29%. The good capacity retention is because of a stable Mn_2O_4 skeleton which remains intact over repeated lithium extraction/insertion during the cycling process. The films annealed at 800°C are showing much lower capacity compared to those annealed at 700°C, which is mainly due to the presence of impurity phases.

The variation of capacity fading with annealing temperature for discharge cycle for the Li-Mn-O films deposited at 0.005mbar pressure is shown in figure 4.36.

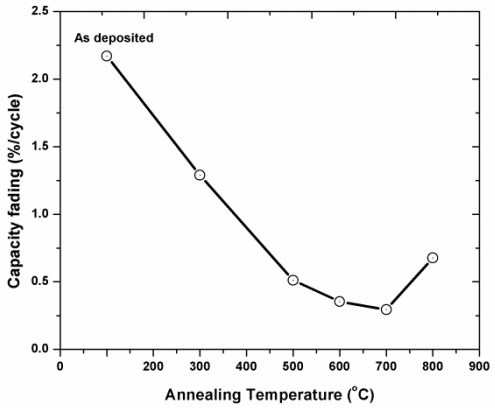

Fig. 4.36: The variation of capacity fading with annealing temperature for discharge cycle for the Li-Mn-O films deposited at 0.005mbar pressure.

Figure 4.37 shows the variation of Coulombic efficiency of Li-Mn-O films with annealing temperature, after 20 cycles.

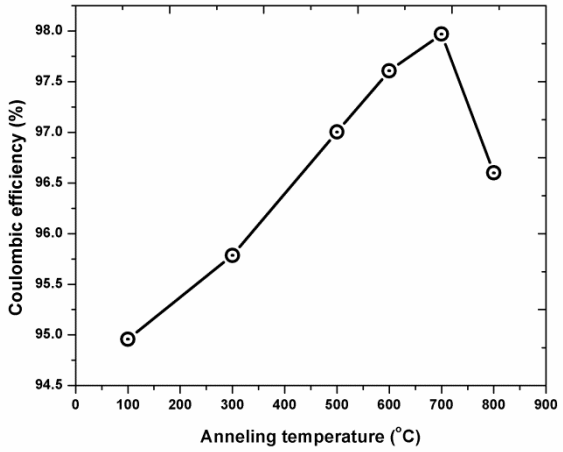

Fig. 4.37: The variation of Coulombic efficiency of Li-Mn-O films with annealing temperature, after 20 cycles.

The electrochemical performance of the Li-Mn-O films annealed at different temperatures depends on the electrical conductivity. Son and Kim [35] have reported that the spinel $LiMn_2O_4$ with a high electronic conductivity shows better cycle performance than that with lower electronic conductivity, which is consistent with the result of Guan et al. [36]. Moreover, when the conductivity increases the polarization effect is reduced, thereby increasing the Columbic efficiency. The reduced polarization is also beneficial for the decrease of the charge transfer resistance of active materials, which finally improves the cycle performance of the spinel $LiMn_2O_4$ [37]. It clear from figure 4.37 that, the columbic efficiency of the Li-Mn-O films annealed at different temperatures, after 20 cycles, increases with the increase in electronic conductivity, as shown in figure 4.24.

4.4 Conclusions

The present investigations show that the properties of the ‘as deposited’ Li-Mn-O films grown by high frequency RF (27.12MHz) sputtering exhibit a strong dependence on the sputtering pressure. It is quite evident from table 4.1, that with the increase of the sputtering pressure, the lithium content in the Li-Mn-O

films decreases. Moreover, the films deposited using the 27.12MHz excitation frequencies are found to be amorphous for all the sputtering pressures. The structural, electrical and electrochemical characteristics of the as deposited films also show a strong dependence on the sputtering pressure. It is also evident that, the room temperature electrical conductivity of the films deposited at 0.005mbar pressure is higher than that for films deposited at other pressures. It is seen that the thermal activation energy for electrical conduction is decreases with the increase of the sputtering pressure. The electrochemical studies of the 'as deposited' films show that, the low pressure deposited films have the highest discharge capacity compared to higher pressure deposited films. The main reason for the inferior performance of the films deposited at higher sputtering pressures is the lithium deficiency in these films. The lithium deficiency arises due to the re-sputtering of the deposited films by the argon ion bombardment at higher pressures.

A detailed post annealing study of the films deposited at 0.005mbar pressure was conducted and the annealed films were characterized. The structural studies conducted on the annealed films show that, as the annealing temperature increases, the crystallinity is also increasing, with a slight shift in the peak positions towards the lower diffraction angles. The films with the best structural properties were obtained upon annealing at a temperature of 700°C. The results of the XRD, SEM and the Raman spectral analysis are found to support each other. The DC electrical conductivity studies show an increase in conductivity, as well as thermal activation energy, with the increase of annealing temperature. The present study reveals that the sputtered films, post annealed at 700°C exhibit the best characteristics as far as structural, morphological and electrical properties are concerned.

The cyclic voltammograms of post annealed films show improvement in electrochemical performance with increasing annealing temperature. The charge discharge cycling displays highest capacity for the films annealed at 700°C.However the highest capacity obtained in the present work is low compared to the earlier reported values. The reason for the reduction in capacity is possibly the contamination of Li-Mn-O films by the thermal diffusion of iron and chromium from the stainless steel substrate material

during annealing. The films annealed at 700°C, are found to show quite stable cycling behavior and even after 20 cycles, the capacity fading is only about 0.29% per cycle.

It can be concluded that the ‘as deposited’ Li-Mn-O films show inferior properties compared to annealed films. The present studies indicate that thermal annealing has significant effect on the structural, electrical and electrochemical properties of Li-Mn-O thin films.

4.5 References

[1] N. J. Dudney,The Electrochemical Society's Interface, 17 (2008) 44.
[2] Y. J. Park, J. G. Kim, M. K. Kim, H. T. Chung, H. G. Kim, Solid State Ionics 130 (2000) 203.
[3] B. J. Neudecker, N. J. Dudney, J. B. Bates, J. Electrochem Soc. 147(2000) 517.
[4] J. B Bates, G. R. Gruzalski, N. J. Dudney, C. F. Luck, X. Yu, Solid State Ionics 70/71 (1994) 619.
[5] S. D. Jones, J. R. Akridge, F. K. Shokoohi, Solid State Ionics 69 (1994) 357.
[6] A. Patil, V. Patil, D.W. Shin, J. W. Choi, D. S. Paik, S. J. Yoon, Materials Research Bulletin 43 (2008) 1913
[7] S. Komaba, N. Kumagai, M. Baba, F. Miura, N. Fujita, H. Groult, D. Devilliers and B.Kaplan, Journal of Applied Electrochemistry 30 (2000) 1179.
[8] Fu-Yun Shih, Kuan-Zong Fung, Journal of Power Sources 159 (2006) 179–185
[9] S. Surampudi, Lithium batteries, Electrochem. Soc. Proc. 98-16 (1999) 280.
[10] RajiveTomy M, Anil Kumar K M, Anand P B and S Jayalekshmi, Journal of Physics and Chemistry of Solids. 72 (2011) 1251
[11] J.C. Hunter, J. Solid State Chem. 39 (1981) 142.
[12] C.M. Julien, M. Massot, Materials Science and Engineering B97 (2003) 217.
[13] P. Tarte, J. Preudhomme, Spectrochim. Acta 26A (1970) 747.
[14] J. Preudhomme, P. Tarte, Spectrochim. Acta 27A (1971) 845.
[15] M. A. Camacho-López,. E. Haro-Poniatowski et al. Superficies y Vacío 17(1), 7-12, marzo de 2004]
[16] Lithium ion rechargeable batteries, by Kazunori Ozawa, Wiley VCH (2009), ISBN-97-8-3-527-31-983-1
[17] S.B. Tanga, H. Xiaa, M.O. Laia and L. Lu.Journal of Alloys and Compounds 449 (2008) 322.
[18]K.F. Chiu, H.H. Hsiao, G.S. Chen, H.L. Liu, J.L. Her, H.C. Lin, J. Electrochem. Soc. 151 (2004) A452.
[19] E Iguchi, Nakamura and A Aoki, Philosophical magazine, 1998, Vol.78, No. 1, 65-77
[20] J.B. Goodenough, A. Manthiran and B. Wnetrzewsld, J. Power Sources 43-44, 269 (1993).

[21] G. Pistoia, D. Zane and Y. Zhang, J. Electrochem. Soc. 142, 2551 (1995).
[22] N.F. Mott, J. Non-Crystal. Solids 1, 1 (1968)
[23] I.G. Austin and N.F. Mott, Adv. Phys. 18, 41(1969).
[24] S. Chitra, P. Kalyani, T. Mohan, M. Massot, S. Ziolkiewicz, R. Gangandharan, M. Eddrief and C. Julien, Ionics 4 (1998) 8.
[25] D K Shukla& S Mollah, Indian Journal of Pure & Applied Physics 45 (2007) 52.
[26]A. Yamada and M. Tanaka, Mater. Res. Bull. 30, 715 (1995).
[27] A. Yamada, J. Solid State Chem. 122, 160 (1996).
[28] J. Molenda, K. Swierczek, W. Kucza, J. Marzec, A. StoklosaSolid State Ionics 123 (1999) 155–163
[29] O. M. Hussain, K. Hari Krishna V. KalaiVani& C. M. Julien, Ionics (2007) 13:455–459
[30] Rajive Tomy M, Anil Kumar K M and S Jayalekshmi, Journal of Instrument Society of India, Vol 41, No. 2, June 20.
[31] J. Xie, T. Tanaka, N. Imanishi, T. Matsumura, A. Hirano, Y. Takeda, O. Yamamoto, Journal of Power Sources 180 (2008) 576.
[32] F.Y. Shih, K. Z. Fung, Journal of Power Sources 159, (2006) 179
[33] S.B. Tang, M.O. Laia, L. Lua, S. Tripathy, Journal of Solid State Chemistry 179 (2006) 3831.
[34] Hee-Soo Moon and Jong-Wan Park, Journal of the Korean Physical Society, Vol. 41, No. 6, December 2002, pp. 872.
[35] J.T. Son, H.G. Kim, J. Power Sources 147 (2005) 220
[36] J. Guan, M. Liu, Solid State Ionics 110 (1998) 21
[37] Xifei Li, Youlong Xu Electrochemistry Communications 9 (2007) 2023

Chapter 5

Studies on Li-Mn-O films with in-situ substrate bias

Abstract: As seen in the previous chapter, the structural, electrical and electrochemical properties of the Li-Mn-O cathode films are very much dependent on the crystallinity of the films. This chapter initially addresses the effects of in-situ dc substrate bias on the crystallinity of the Li-Mn-O films, during film deposition. It is followed by detailed characterization studies of the Li-Mn-O films deposited under various substrate bias conditions, using high frequency RF excitation source. The effects of post annealing on the properties of the Li-Mn-O films deposited under dc bias condition are analyzed. The details of assembling and electrochemical characterization of half cell devices also form a significant part of this chapter.

5.1 Introduction.

As seen in the chapter 4, the electrochemical properties of the 'as deposited' Li-Mn-O cathode films are inferior due to the amorphous nature of these cathode films, deposited using high frequency magnetron sputtering technique. Since the electrochemical properties are very much dependent on the crystallinity and other related properties of the cathode materials,, these 'as deposited films' should undergo post annealing treatments to improve their quality. The post annealing studies previously conducted on Li-Mn-O films indicate that films have to be annealed at very high temperatures to obtain good crystallinity followed by good electrochemical properties [1, 2].This high temperature annealing requirement limits the type of substrates that can be used for depositing Li-Mn-O films and hence increases the complexity of the deposition system and process. It is well known that in biased sputtering technique, in situ substrate bias makes the cathode thin films denser, resulting in much reduced concentration of defects, which can have prominent effects on the electrical and electrochemical properties of these films. This technique can be effectively employed to get void-free film microstructure and can be used deposit crystalline films even at room temperature. In bias sputtering, either a negative DC or RF bias voltage is applied externally to the substrate. The presence of the bias modifies the electric fields near the substrate, which in turn can vary the flux and energy of the incident charged species, enhancing the quality of the deposited material [3-5].

In the present work, the sputtering has been carried out under various substrate bias conditions and this chapter is devoted to the detailed structural, electrical and electrochemical studies of the Li-Mn-O films deposited under in-situ dc substrate bias. The present chapter also addresses the effects of post annealing on the various properties of the films, and the details of assembling and electrochemical characterization of the half cell devices.

5.2 Characterization of Li-Mn-O films with in-situ bias

In this study, various negative, dc, substrate bias voltages were applied, while depositing the Li-Mn-O films. Though substrate bias voltages in the range -5V

to 100V were used for the present study, only significant results are included in this section. The sputter deposited films were annealed at different temperatures of 300, 400, 500, 600, and 700°C under atmospheric conditions. All other parameters used for the annealing were the same as discussed in section 4.2.3. The Li-Mn-O films used for the present studies were deposited at a sputtering pressure of 0.005mbar with RF power density 5W/cm^2.

5.2.1 Chemical composition studies.

The results of the ICP-AES studies to determine the chemical composition of the films deposited under different substrate bias conditions are shown in table 5.1

Table 5.1: Chemical composition of Li-Mn-O films with in-situ substrate bias

In-situ substrate bias (V)	Li	Mn	Li/Mn
-25V	1.02	2	0.51
-50V	0.74	2	0.37
-100V	0.31	2	0.16

It is clear from table 5.1that, the films deposited at lower bias voltages show higher lithium content compared to films deposited at higher bias voltages. It can be deduced that as the substrate bias increases, the number of ions bombarding the growing film increases, which causes the re-sputtering of the films. Lithium is highly volatile and so the possible reason for the lithium deficiency at higher bias voltages can be the increased re-sputtering of the films due to the severe Ar ion bombardment, arising as a result of the higher substrate bias voltage.

5.2.2 Structural studies

In order to study the structural characteristics and phase purity of the deposited films, the X-ray diffraction technique was used. XRD studies were conducted on the Li-Mn-O films deposited on stainless steel substrates. The diffraction

patterns were recorded between diffraction angles (2θ), 10 and 60°, at a scan speed of 2 degrees per minute. Figure 5.1shows the X-ray diffraction patterns of the un-annealed (as deposited) films deposited at 5W/cm^2 RF power.

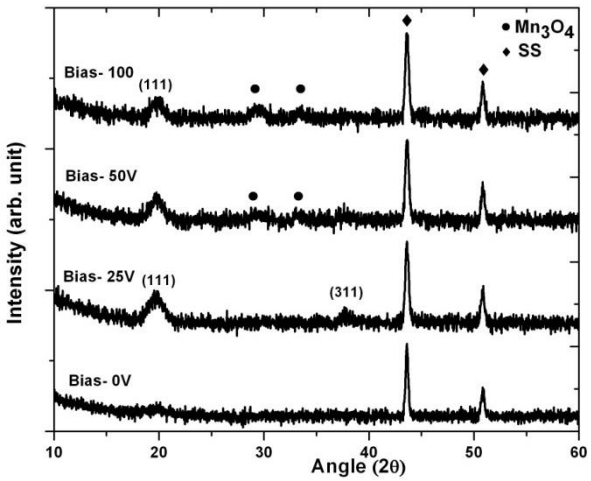

Fig. 5.1: XRD patterns of the as deposited Li-Mn-O films under various bias voltages for a sputtering pressure of 0.005mbar and sputtering power density of 5W/cm^2

The as deposited films, with substrate bias voltages, are found to be significantly crystalline compared to the films deposited without bias voltages. All the films deposited with in-situ substrate bias, show a broad small peak around 19.6°, which corresponds to the reflection from the (111) plane of the spinel phase. The films deposited with in-situ substrate bias voltage of -25V are found to be stoichiometrically superior to the films deposited at higher substrate bias voltages.

It is clear from figure 5.1 that, the 'as deposited' films with in-situ bias voltage of -25V show a peak significant intensity around 19.6° and another weak peak at around 37°, which correspond to the reflections from the (111) and (311) planes respectively. The films deposited with higher bias voltages of -50V and -100V, are found to have a less intense peak corresponding to (111) plane and a few impurity peaks corresponding to the Mn_3O_4 phase, which are marked as (•). The peaks marked as (♦) represent those of the stainless steel substrate.

Since the films deposited with substrate bias -25V show the best structural features without any impurity phase, detailed investigations on the structural characteristics of the Li-Mn-O films, deposited at 0.005mbar pressure and under the substrate bias of -25V,are carried out by X-ray diffraction technique, after subjecting to post annealing at different temperatures. The results are shown in figure 5.2.

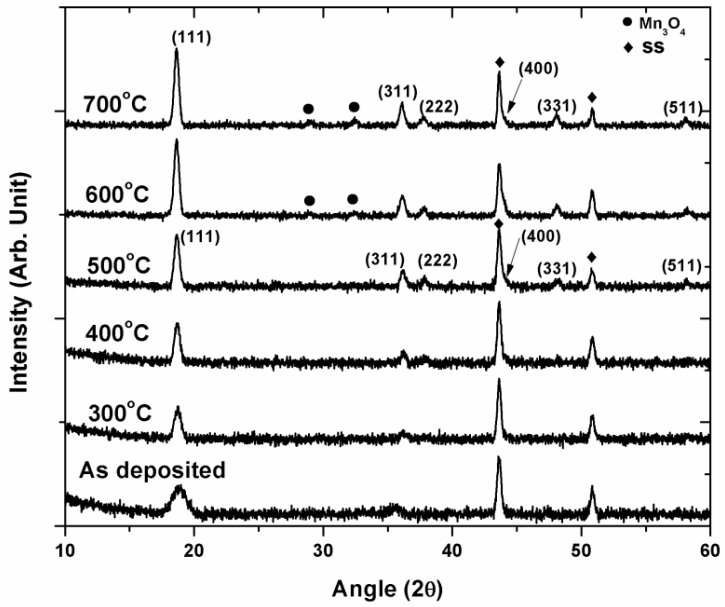

Fig.5.2: The XRD patterns of the Li-Mn-O films deposited at a pressure of 0.005mbar, with substrate bias -25V and annealed at various temperatures.

It is seen from figure 5.2 that, the 'as deposited' films, grown at 0.005mbar pressure, with a substrate bias of -25V show comparatively good crystalline nature. It is also evident from figure 5.2, that, with the increase of annealing temperature, the XRD peaks get stronger and sharper with a slight shift in peak positions towards the lower diffraction angles.

The full width at half maximum (FWHM) of the peak corresponding to the (111) plane is found to decrease with the increase in annealing temperature. For the films annealed at 500^{o}C, the most prominent peak is at $2\theta = 18.66^o$, which corresponds to the reflection from the (111) plane. Apart from this, there are five other peaks corresponding to the reflections from, (311), (222), (331),

(400) and (511) planes. The peaks marked as 'SS' belong to those of the stainless steel substrate. With further rise in post annealing temperature to 600^{o}C and 700^{o}C, although the peak intensities are enhanced, some new peaks are found to appear. These extra peaks correspond to the presence of the Mn_3O_4 phase, which is formed due to the heat treatment at high temperatures.

The analysis of XRD data shows that the films annealed at 500^{o}C, certainly have the closest match with the cubic spinel structure corresponding to Fd3m space group. The lattice parameter of the film annealed at 500^{0}C is calculated to be around 8.2280 Å, which is slightly lower than that of bulk $LiMn_2O_4$ (8.247 Å). The shift in peak positions with increase in annealing temperature may be due to the strain in the films, which arises from the ion bombardment during sputter deposition. [6, 7]

The variation of the peak intensity with annealing temperature corresponding to the (111) plane is shown in figure 5.3.

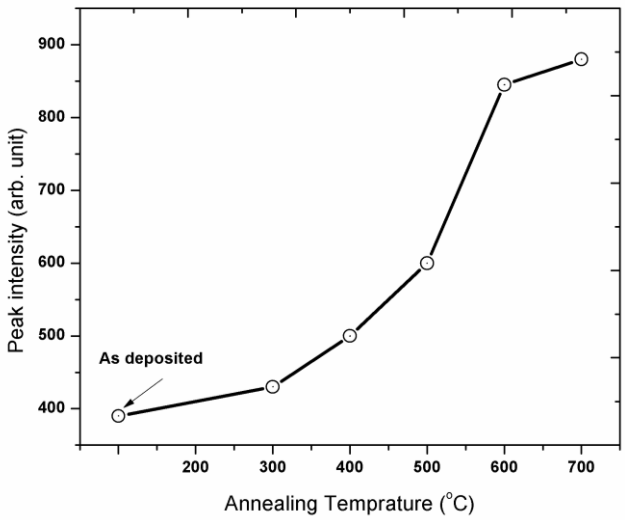

Fig. 5.3: The variation of the XRD peak intensity of the (111) plane with annealing temperature for the films deposited with substrate bias -25V.

It is clear from figure 5.3, that, with the rise in post annealing temperature, the intensity of the peak corresponding to the (111) plane is increasing. This

clearly shows that the post deposition heat treatment definitely improves crystallinity.

The variation of the cell parameter (a) with the annealing temperature is shown in figure 5.4. It is clear from figure 5.4 that, with the rise in annealing temperature the unit cell parameter increases. This is mainly due to the improvement in crystallinity of the films with the increase in annealing temperature which brings about relaxation of the strain in the films, as explained in section 4.2.4.

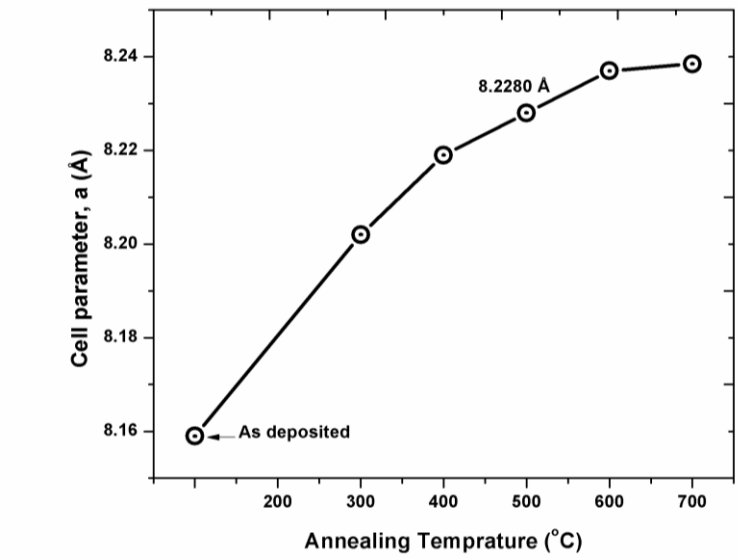

Fig. 5.4: The variation of the cell parameter 'a', with post annealing temperatures for the films deposited with substrate bias -25V.

The variations of the FWHM of the peak corresponding to the (111) plane and crystallite size, calculated using Scherrer formula with increase in annealing temperature are shown in figure 5.5. It is clear from figure5.5 that, with the rise in annealing temperature, the FWHM of the peak corresponding to the (111) plane sharply decreases, while the crystallite size estimated using Scherrer formula increases [7]. A possible explanation for this is given in section 4.2.4.

On comparison of the FWHM of the XRD peaks of the films deposited with substrate bias and films without substrate bias, it is clear that the films with bias

show higher FWHM of the peaks for the same annealing temperature. This indicates that the films deposited with bias are having smaller crystallite size in comparison with the films deposited without bias. The crystallite size calculated using Scherrer formula, for the films with bias is 18.3nm, while for the films without bias, the size is 28nm. The smaller particle size or crystallite size observed in films deposited with bias is a consequence of the comparatively smaller strain in these films.

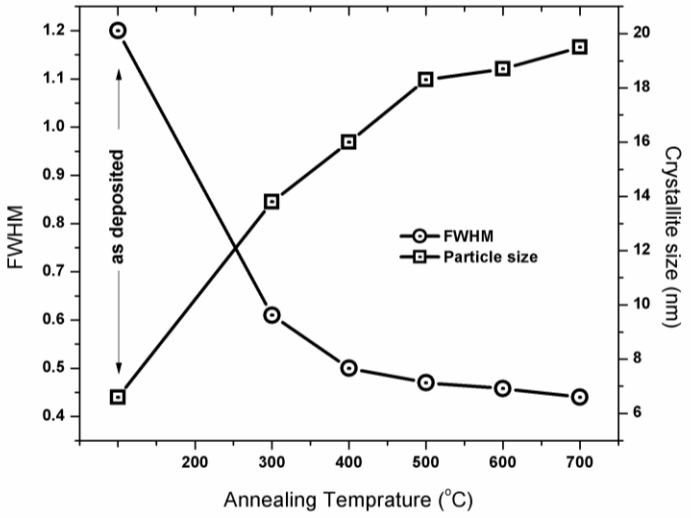

Fig. 5.5: The variations of the FWHM, and crystallite size calculated using Scherrer formula with annealing temperature corresponding to the (111) plane for the films deposited with substrate bias -25V.

In section 4.2.4 it is seen that, as the annealing temperature increases, the strain in the films decreases due to the agglomeration of the neighboring smaller grains in to larger ones. When strain is less the agglomeration of the neighboring particles will be less and the change in particle size will be also less. This indicates that bias sputtering can reduce crystallite size and thereby it increases the surface area available for the electrochemical reaction.

5.2.3 Surface topography studies by SEM

The scanning electron microscope (SEM) images of the as deposited Li-Mn-O films with in-situ substrate bias are shown in figure 5.6.

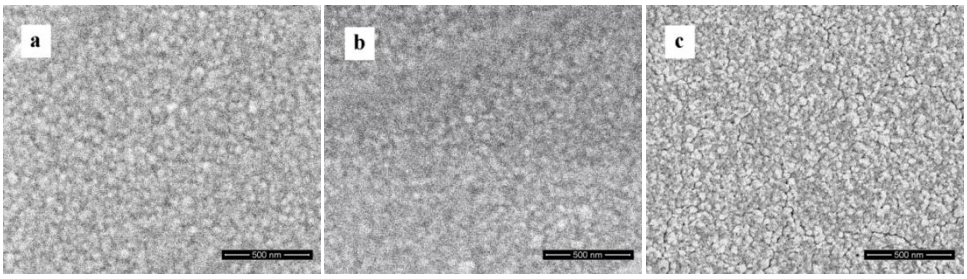

Fig.5.6: Scanning electron micrographs of the Li-Mn-O films deposited at (a) -25V, (b) -50V and (c) -100V at a pressure of 0.005mbar and power density 5W/cm^2

The SEM images reveal a homogeneous and uniform film surface, exhibiting a smooth surface topography. The surface topography of Li-Mn-O films deposited with substrate bias -25V and post annealed at 500^{o}C was investigated using scanning electron microscope image (SEM), which is shown in figure 5.7.

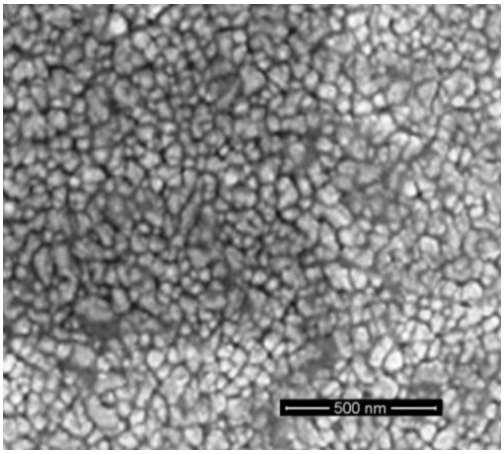

Fig. 5.7: Scanning electron micrograph of the Li-Mn-O films deposited at a sputtering pressure of0.005mbar, with substrate bias -25V and post annealed at 500^{o}C.

The surface morphology of the films deposited with bias voltage -25V and annealed at 500^{0}C is almost homogeneous, with regular and round grains having approximately 80 nm average diameters and is devoid of any cracks. The cross-sectional SEM image of the Li-Mn-O films deposited at 0.005mbar

pressure, with substrate bias -25V, and annealed at 500^{o}C is shown in figure 5.8.

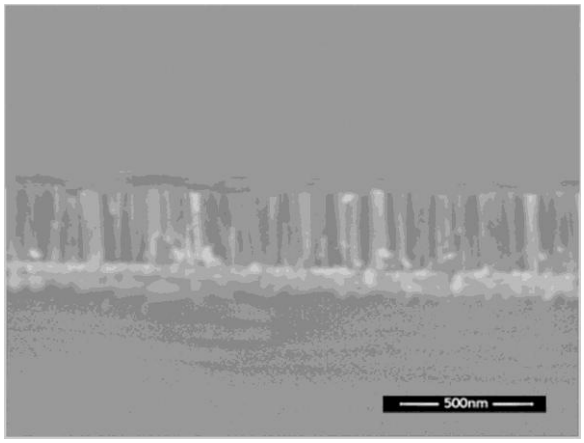

Fig.5.8:Cross-sectional scanning electron micrograph of the Li-Mn-O films deposited at 0.005mbar pressure, with substrate bias -25V, and annealed at 500^{o}C.

The cross sectional morphology of the Li-Mn-O films exhibits a pronounced columnar crystalline habit with a clear orientation perpendicular to the substrate surface. It also indicates that the film is highly dense and the thickness of the film can be roughly estimated as 300nm.The cross sectional image of the Li-Mn-O films deposited with substrate bias shows a significant change in the orientation of the film growth direction compared to the films deposited without substrate bias. The columnar growth may be due to self-shadowing of the incident atoms by those already incorporated into the growing film or due to the re-sputtering of the growing film, as a consequence of the increased Ar^{+} ion collisions on the substrate, in the presence of the substrate bias.

5.2.4 Surface topography by Atomic force microscopy (AFM).

Surface profiles of the Li-Mn-O films deposited with bias -25V and annealed at 500^{o}C were studied with an atomic force microscope (AFM) (WITec Alfa) operated in tapping mode using an etched single crystal Si tip with a radius of 10 nm. The AFM data was used to calculate the surface roughness (R_{rms}).

Surface images were obtained from the 2μm x 2μm area scans and image is shown in figure 5.9.

AFM image features reveal a smooth surface. The R_{rms} roughness of the film I estimated as 9nm.

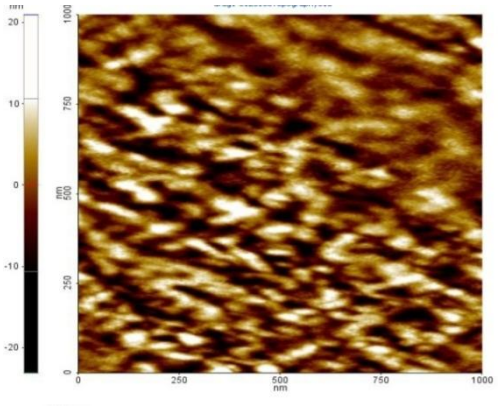

Fig.5.9: Surface topography of the Li-Mn-O films deposited at 0.005mbar pressure with a substrate bias -25V and post annealed at 500^{o}C.

5.2.5 Raman spectroscopy

The micro-Raman spectra of high frequency RF sputtered Li-Mn-O films deposited at different substrate bias voltages and at a sputtering pressure of 0.005mbar are shown in figure 5.10.

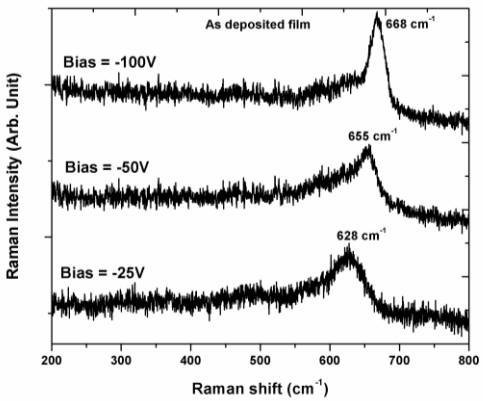

Fig. 5.10: The Raman spectra of the 'as deposited' Li-Mn-O films with various substrate biases, at a sputtering pressure of 0.005mbar and RF power density 5W/cm^2.

The Raman spectrum of the as deposited films, for a sputtering pressure of 0.005mbar, with substrate bias -25V, shows a strong band centered at around 628 cm^{-1}. For the films deposited at higher substrate bias voltages, the band gets shifted progressively towards the higher wave numbers. The reason for this shift could be the formation of Mn_3O_4 impurity phase as a result of the deficiency of lithium in the films deposited at higher substrate bias conditions. [28]

The micro-Raman spectra of Li-Mn-O films deposited at 0.005mbar pressure with substrate bias -25V and annealed at various temperatures are shown in figure 5.11. The Raman spectrum of 'as deposited' films with substrate bias -25V, shows a broad band at around 630cm^{-1}. As seen in section 4.2.7, this broad peak corresponds to the Raman mode A_{1g}, and as the annealing temperature increases this strong band gets shifted towards the higher wave number. For the films annealed at 500°C, apart from the Raman mode A_{1g}, the spectrum is featured by a few more weak bands at 583, 476, 354 and 296 cm^{-1}.

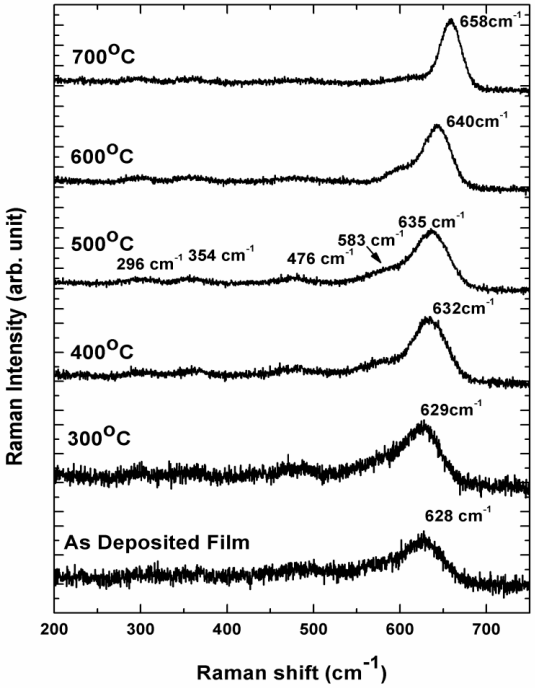

Fig. 5.11: The Raman spectra of the Li-Mn-O thin films deposited at sputtering pressure 0.005mbar with substrate bias -25V and annealed at various temperatures

On further rise in annealing temperature, (i.e. 700^{o}C) the band at 478 cm^{-1} diminishes in intensity and the strong band at 635 cm^{-1} shift to 658cm^{-1}. This shifting may be due to the formation of Mn_3O_4 impurity phase due to the heat treatment at high temperature as explained in section 4.2.7 [8, 9]. However, with the application of substrate bias, the effects of the annealing temperature show up from lower temperatures, compared to the situation without the substrate bias.

5.2.6 DC conductivity studies

The electrical conductivity measurements of the Li-Mn-O films deposited on platinum coated Si wafers were carried out by two probe sandwich method with Al as the top electrode. Keithley 2400 source measuring unit was used to measure current and voltage of the device under test (DUT), which was kept under dynamic vacuum condition. The measurements were repeated at different temperatures between 25 and 100^{o}C and the conductivity was calculated as described in section 2.5.7.

The temperature dependence of dc electrical conductivity of the 'as deposited' Li-Mn-O films, deposited at a sputtering pressure of 0.005mbar and at various substrate bias voltages is shown as Arrhenius plots in figure 5.12.

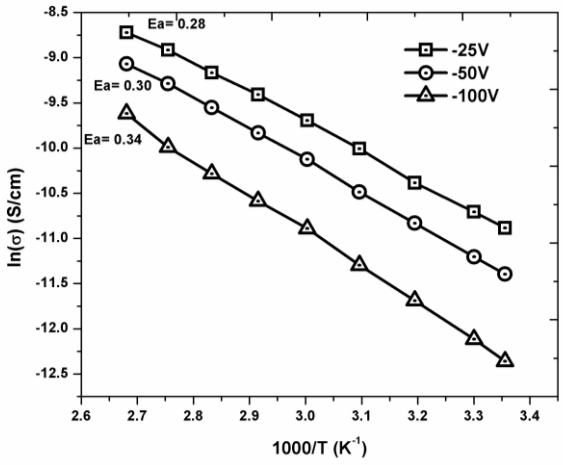

Fig. 5.12: Arrhenius plots of the 'as deposited' Li-Mn-O films with various substrate bias voltages and at a sputtering pressure of 0.005mbar and RF power density 5W/cm^2

For films deposited under different substrate bias conditions, the conductivity increases with the increase of temperature, which shows the semiconducting nature of the Li-Mn-O films. Moreover, for 'as deposited' Li-Mn-O films, the conductivity decreases with increase in substrate bias. The Arrhenius plots between $\ln(\sigma_{dc})$ and (1000/T) show that the thermal activation energy increases with the increase in substrate bias.

The temperature dependence of the dc electrical conductivity of the Li-Mn-O films deposited at 0.005mbar with substrate bias -25V and annealed at various temperatures is shown as Arrhenius plots in figure 5.13.

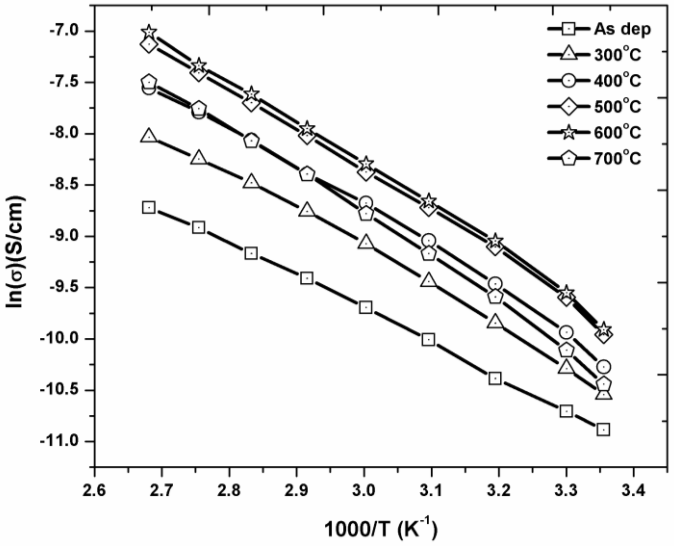

Fig. 5.13: Arrhenius plots showing the temperature dependence of the dc electrical conductivity of the Li-Mn-O films deposited at 0.005mbar pressure with substrate bias and post annealed at various temperatures.

From figure 5.13 it is seen that, with the increase of temperature, the conductivity increases, and the temperature dependence of conductivity (σ_{dc}) satisfies Arrhenius equation, which is depicted as the plot of $\ln(\sigma_{dc})$ vs. (1000/T). A straight line behavior is observed for all the films, with the lower temperature conductivity values slightly deviated from the straight line. This may be due to the phase transition, induced by Jahn-Teller effect, as explained in section 4.2.8.

The variation of room temperature electrical conductivity and thermal activation energy with annealing temperature for the Li-Mn-O films deposited under substrate bias conditions is shown in figure 5.14.

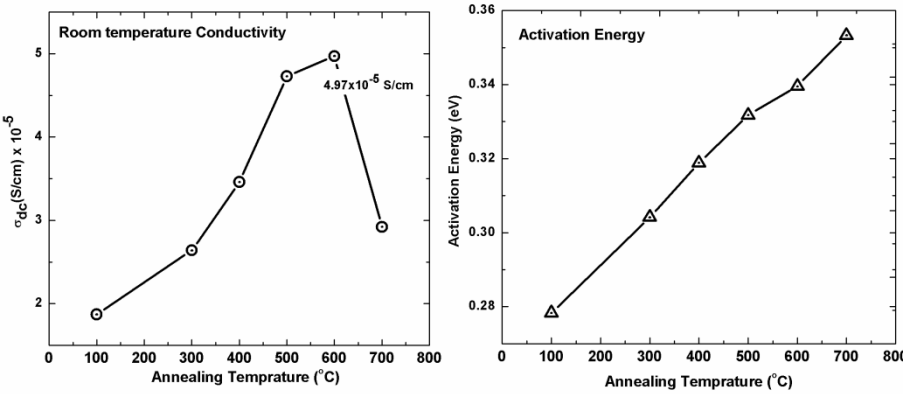

Fig. 5.14: Variation of room temperature dc electrical conductivity and activation energy with annealing temperature for the Li-Mn-O films deposited at 0.005mbar pressure under substrate bias -25V.

It is observed that, with the increase of annealing temperature, the activation energy linearly increases, whereas the electrical conductivity increases upto the annealing temperature of 600°C and thereafter decreases. The films annealed at 500°C and 600°C show almost similar values of electrical conductivity, while the activation energy values are different.

On comparing the conductivity data of films deposited with and without substrate bias, it is found that, the conductivity of the former is much higher than that of the latter. However, the activation energy of the films deposited with substrate bias is lower than that of the films without bias. The maximum room temperature conductivity is observed for the films deposited with substrate bias and annealed at 500°C, which is ~ $5x10^{-6}$S/cm. For the films without substrate bias, the maximum conductivity is observed for the ones annealed at 700°C, which is ~$1x10^{-6}$S/cm. The presence of substrate bias not only enhances the electrical conductivity considerably, but reduces the required optimum annealing temperature as well.

The cross sectional SEM images clearly establish ordered and columnar growth, perpendicular to the substrate, for the films deposited with substrate bias. Such an ordered growth mechanism is not observed for the films deposited without substrate bias. Definitely the difference in growth mechanism is the prime factor contributing towards the better quality and superior properties of the films deposited under substrate bias conditions [10, 11].

5.2.7 Cyclic voltammetry studies.

The cyclic voltammograms of the as deposited Li-Mn-O thin films with various substrate bias voltages, coated on stainless steel substrates, obtained with voltage scan speed of 0.1mV/s (see section 4.3.2) are shown in figure 5.15.

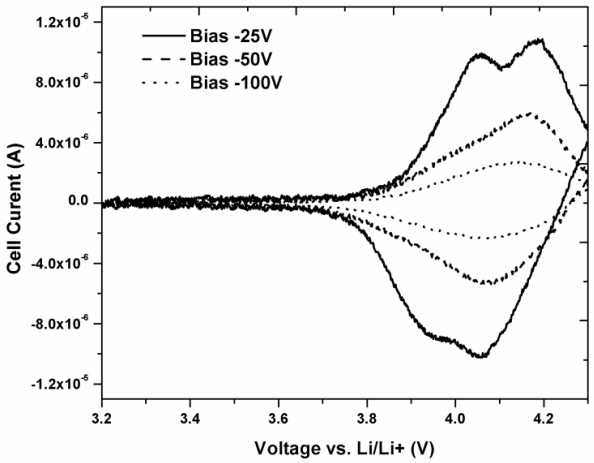

Fig. 5.15 The cyclic voltammograms of ‘as deposited’ Li-Mn-O films with various substrate bias voltages.

The cyclic voltammograms (CV) shown in figure 5.15, indicate that the films deposited at lower substrates bias voltages are electrochemically more active, where as the films deposited at higher bias voltages are much less active.

The CV curve of the ‘as deposited’ films with substrate bias voltage of -25V shows two distinct oxidation peaks at around 4.05V and 4.17V for the cathodic scan and two less resolved reduction peaks at around 3.4V and 4.06V for the anodic scan. The cathodic peaks correspond to lithium ion deintercalation

process to form λ-MnO_2 from $LiMn_2O_4$. The anodic peak represents the lithium ion intercalation to form $LiMn_2O_4$ from λ-MnO_2. The films deposited under higher bias voltages of -50 and -100V show only one broad peak for the cathodic and anodic scans. It is evident from the CV curves that, as the bias voltage increases, the area enclosed by the oxidation and the reductions curves decreases, showing a decreased electrochemical capacity.

Cyclic voltammograms of Li-Mn-O films deposited at 0.005mbar pressure under substrate bias of -25V and post annealed at various temperatures are shown in the figure 5.16.

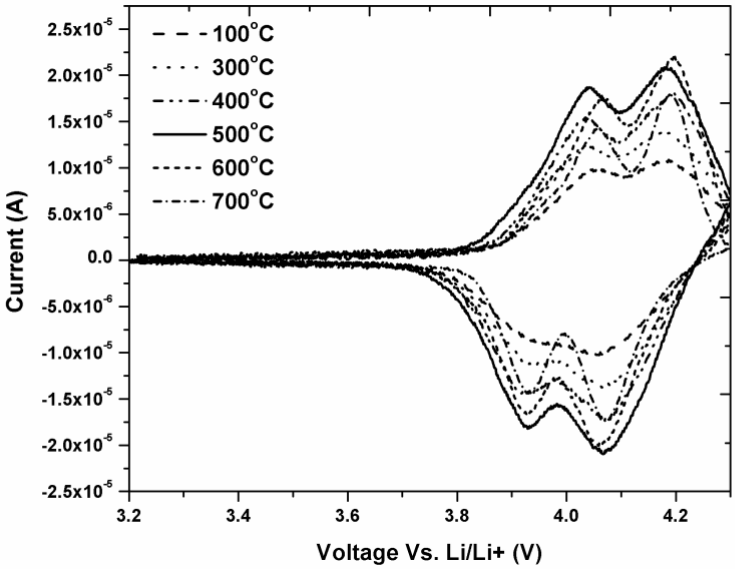

Fig. 5.16: Cyclic voltammograms of Li-Mn-O films deposited at 0.005mbar pressure with substrate bias of -25V and post annealed at various temperatures.

The cyclic voltammogram of the Li-Mn-O films deposited with substrate bias of -25V is significantly different from that of the films deposited without substrate bias. For the films deposited with substrate bias of -25V both the cathodic and anodic peaks are more resolved and the area under the CV curve is significantly enhanced. The effect of annealing has more or less the same effect on the films deposited with and without substrate bias. With annealing anodic/cathodic peaks become stronger and sharper and the area under the CV curve increases. The films deposited with substrate bias of -25V and annealed at

500°C display the best CV results (see figure 5.17), for which the peaks are located at about 4.05 and 4.18V for oxidation cycle and 4.07 and 3.93V for reduction cycle. These two pairs of redox peaks indicate the two stages of the Li-ion extraction and insertion process as explained in section 4.3.2.

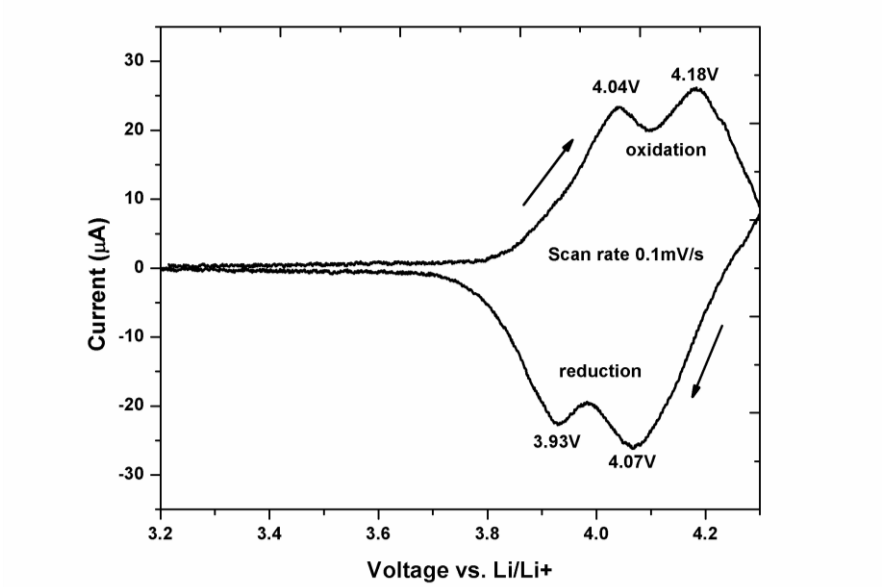

Fig. 5.17: Enlarged view of the cyclic voltammogram of Li-Mn-O films deposited at pressure of 0.005mbar, with substrate bias of -25V and annealed at 500^{o}C

It is also evident from the figure that with the rise of annealing temperature the FWHM of all the cathodic and anodic peaks decreases and the area under the CV curve is increases. The major difference between the cyclic voltammograms of the Li-Mn-O films deposited with and without substrate bias is that the films deposited with substrate bias is electrochemically much more active than the other, which is quite evident from the area under the CV curves. The increase in area under the curve can be interpreted as the increase in capacity, and hence the films annealed at 500°C have got the highest capacity compared to all other films. The films annealed at 600 and 700°C show lesser capacity, which may be due to the formation of Mn_3O_4 impurity phase at higher annealing temperatures. This is evident from the XRD data as well [12].

5.2.8 Charge discharge cycling studies.

The charge discharge curves of the as deposited Li-Mn-O thin films, grown under various substrates bias voltages, obtained at a constant current of 5μA are shown in figure 5.18.

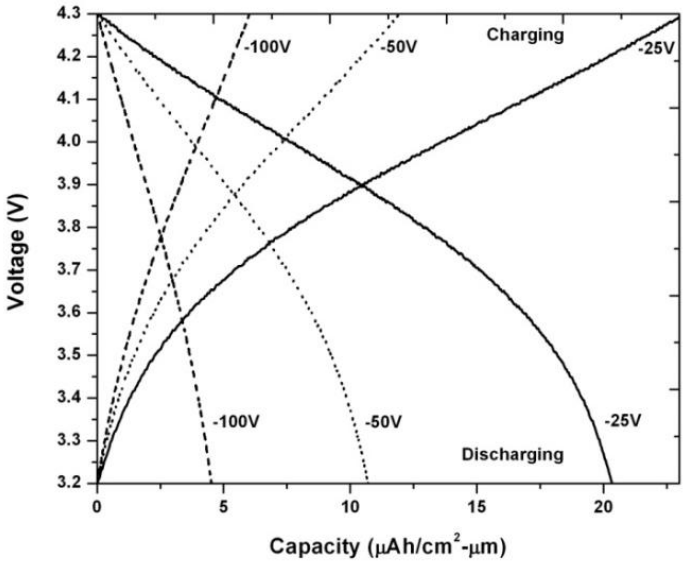

Fig. 5.18: The charge discharge curves of 'as deposited' Li-Mn-O films with various substrate bias voltages for a sputtering pressure of 0.005mbar and RF power density 5W/cm^2.

The cycling profile of the 'as deposited' films shows smooth curves without any distinct potential plateaus. The charge discharge curves show that the films deposited with bias voltage of -25V are electrochemically most active and stable with extraction and reinsertion of lithium ions during cycling, compared to the ones deposited at higher bias voltages.

The films deposited at the lower substrate bias of -25V have the highest capacity of ~20μAh/cm^2/μm. It is also observed that the capacity drastically decreases with the increase of substrate bias voltage. The superior properties of the films deposited at lower substrate bias of -25V can be a consequence of the better crystallinity of these films.

Figure 5.19 shows the charge/discharge curves of the Li-Mn-O films deposited with substrate bias of -25V and annealed at various temperatures, obtained with a constant current of 5μA.

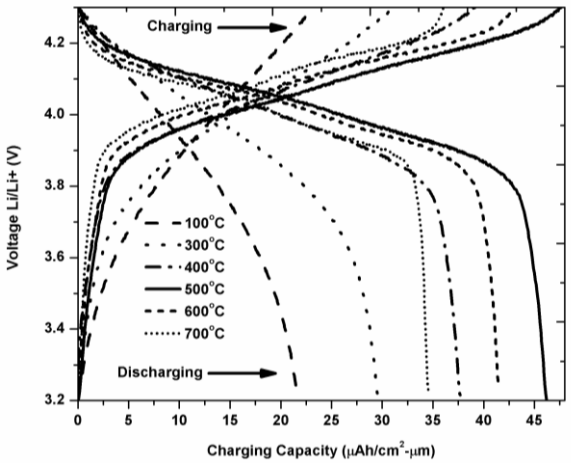

Fig. 5.19: The charge-discharge curves of Li-Mn-O films deposited at 0.005mbar pressure with substrate bias -25V and post annealed at various temperatures.

Similar to the charge discharge profile of Li-Mn-O films without bias, the charge-discharge cycling profile of the films with bias also displays two potential plateaus at around 4 and 4.1 V. It is clear from figure 5.19 that, there is a steady increase of capacity with the rise of annealing temperature, with a maximum capacity of ~47μAh/cm^2/μm obtained for the films annealed at 500^{o}C. The capacities of these films are much higher than those of the films deposited without substrate bias. As in the case of CV the experiment, the best results are obtained for the films deposited with substrate bias of -25V and annealed at a lower temperature of 500°C. In the case of the films deposited without substrate bias, the best results are obtained for films annealed at a higher temperature of 700°C. The reason for the improved capacity can be attributed to the improvement in crystallinity at lower annealing temperature and reduced substrate contamination due to lower annealing temperature. The films annealed above 500°C show lower capacity, which may be due to the formation of impurity phases at high annealing temperatures as evident from the XRD data.

The variation of discharge capacity of the films deposited under substrate bias of -25V, with annealing temperature is shown in figure 5.20.

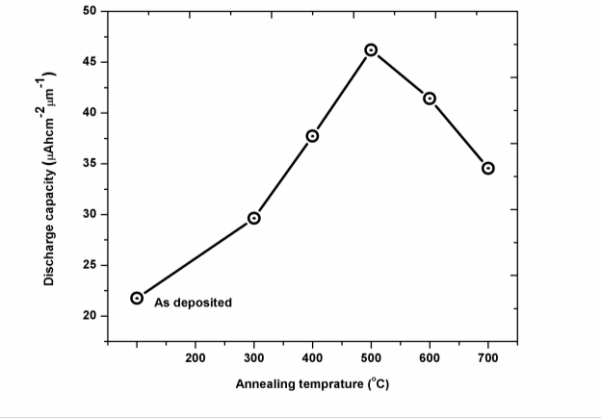

Fig. 5.20: The variation discharge capacity of Li-Mn-O films deposited at 0.005mbar pressure, with substrate bias of -25V and post annealed at various temperatures.

5.2.9 Cycle performance studies.

The specific capacity (in $\mu Ahcm^{-2}\mu m^{-1}$) of Li-Mn-O films deposited at a pressure of 0.005mbar with substrate bias of -25V and annealed at various temperatures is plotted as a function of cycle number and is shown in figure 5.21.

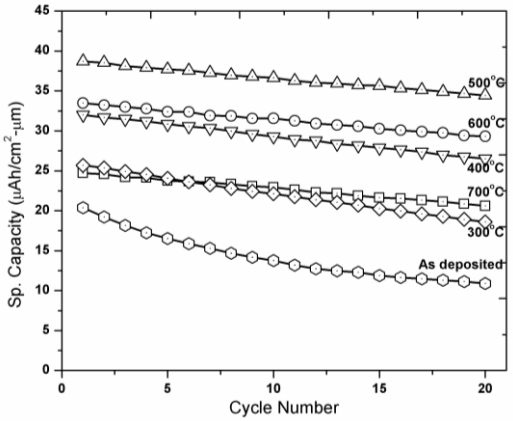

Fig 5.21: Cycle performance study of Li-Mn-O films deposited at 0.005mbar pressure, with substrate bias of -25V and post annealed at various temperatures.

Figure 5.21 shows that the 'as deposited' films have very poor capacity retention, which is mainly due to the poor crystalline nature of the films. The capacity fading for the films annealed at 300 and 400°C is 1.38% and 0.86% respectively. The films annealed at 500°C show the highest capacity as well as maximum capacity retention and its discharge capacity after 20 cycles is about 88.0% of the initial value. The average capacity loss per cycle for these films is about 0.55%. The films annealed at higher temperature also show poor capacity retention, which may be due to the presence of impurity phases in these films.

The films deposited with -25V substrate bias and annealed at 500°C show higher initial capacity than the films deposited without substrate bias and annealed at 700°C. However, in the case of capacity retention, the films deposited without substrate bias and annealed at 700°C show better results. The reason for this is not clear, but it is believed that the films deposited with substrate bias and annealed at 500°C have smaller grain size and larger surface area, which can enhance both the capacity and capacity degradation. The enhanced capacity degradation is assumed to be arising due to the Mn dissolution as described in section 1.6.4

The variation of discharge capacity fading with annealing temperature is shown in figure 5.22.

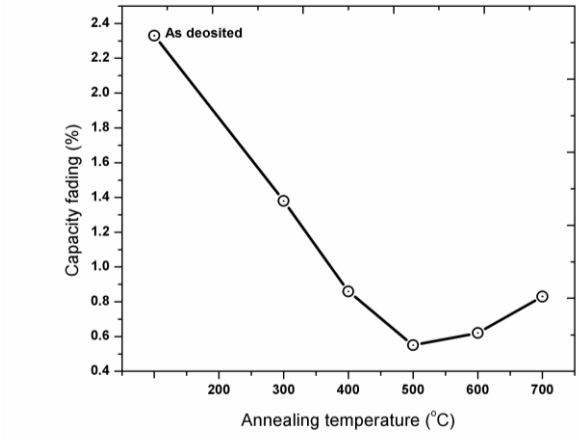

Fig. 5.22: The variation of discharge capacity fading for the Li-Mn-O films deposited at 0.005mbar pressure with substrate bias of -25V and post annealed at various temperatures.

Figure 5.23 shows the variation of Coulombic efficiency with annealing temperature of Li-Mn-O films deposited under bias of -25V, after 20 cycles.

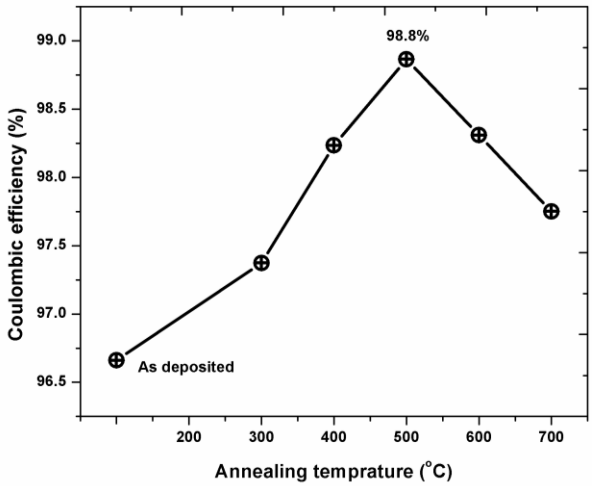

Fig. 5.23: The variation of Coulombic efficiency for the Li-Mn-O films deposited at 0.005mbar pressure with substrate bias of -25V and post annealed at various temperatures.

5.3 Conclusions.

The results presented in this chapter show that the in-situ dc substrate bias has significant impact on the growth mechanism and other properties of the ‘as deposited’ Li-Mn-O films grown by high frequency RF (27.12MHz) magnetron sputtering. The most striking feature of the in-situ dc bias is the improvement in the crystalline nature of the ‘as deposited’ films compared to the films deposited without substrate bias. It is also observed that the compositional, structural, electrical and electrochemical characteristics of the as deposited films show a strong dependence on the substrate bias voltage. The room temperature electrical conductivity of the films deposited at 0.005mbar pressure with a substrate bias of -25V is found to be higher than that of the films deposited without substrate bias. The electrochemical studies of the ‘as deposited’ films with substrate bias show significantly higher discharge capacity than the films deposited without substrate bias. The improved electrochemical performance of the films deposited with substrate bias can be attributed to the enhanced crystallinity and ordered growth mechanism in these

films. It is also observed that films deposited with higher bias voltages result in lithium deficient films.

A detailed post annealing study of the films deposited at 0.005mbar pressure with substrate bias of -25V was also carried out. The structural studies conducted on the annealed films show that, as the annealing temperature increases, the crystallinity is also increasing, with a slight shift in the peak positions towards the lower diffraction angles. The results of XRD, SEM and Raman spectral analysis are found to complement each other. The DC electrical conductivity studies of the films deposited with in-situ substrate bias, show an increase in electrical conductivity, and a decrease in thermal activation energy, compared to the films deposited without bias. The films deposited with substrate bias of -25V and annealed at 500°C exhibit the best structural, morphological and electrical characteristics.

The cyclic voltammograms of post annealed films show improvement in electrochemical performance with the rise of annealing temperature. The charge discharge cycling displays highest capacity for the films annealed at 500°C. Most importantly, films deposited with substrate bias of -25V and annealed at 500°C show significantly higher discharge capacities, compared to the films deposited without bias. However the capacity fading observed in these films is slightly higher than that in the films deposited without bias.

The best structural, morphological, electrical, and electrochemical characteristics are observed for the films deposited with a substrate bias of -25V and annealed at 500°C. In the absence of any substrate bias, similar characteristics are observable only at higher post annealing temperatures around 700°C. The presence of substrate bias can considerably reduce the optimum post annealing temperature, required for the best film characteristics.

5.4 Reference.

[1] Rajive Tomy M, Anil Kumar K M, Anand P B and S Jayalekshmi, Journal of Physics and Chemistry of Solids. 73 (2012) 559
[2] Rajive Tomy M, Anil Kumar K M, Anand P B and S Jayalekshmi, Journal of Physics and Chemistry of Solids. 72 (2011) 1251
[3] Li et al, J. Vac. Sci. Technol. A, 18(2000)2333
[4] Jun et al., Appl. Phys. Lett. 87(2005)132108
[5] K. F. Chiu et al, Journal of The Electrochemical Society, 152(2005)A2058
[6] Fu-Yun Shih, Kuan-Zong Fung, Journal of Power Sources 159 (2006) 179–185.
[7] S. Surampudi, Lithium batteries, Electrochem. Soc. Proc. 98-16 (1999) 280.
[8] S.B. Tanga, H. Xiaa, M.O. Laia and L. Lu.Journal of Alloys and Compounds 449 (2008) 322.
[9] K.F. Chiu, H.H. Hsiao, G.S. Chen, H.L. Liu, J.L. Her, H.C. Lin, J. Electrochem. Soc. 151 (2004) A452.
[10] J. Molenda, K. Swierczek, W. Kucza, J. Marzec, A. StoklosaSolid State Ionics 123 (1999) 155–163
[11] O. M. Hussain, K. Hari Krishna V. KalaiVani& C. M. Julien, Ionics (2007) 13:455–459
[12] F.Y. Shih, K. Z. Fung, Journal of Power Sources 159, (2006) 179

Chapter 6

Characteristics of doped Li-Mn-O films

Abstract: The major problem with the spinel $LiMn_2O_4$ as a cathode material for lithium ion battery is its capacity loss during repeated cycling process. There have been several studies to overcome this drawback of $LiMn_2O_4$ by partial substation of Mn ions with other transition metal ions. This chapter deals with the studies on the effects of Zn and Ni doping on the characteristics of the Li-Mn-O films deposited by high frequency magnetron sputtering. The analysis of the improved electrochemical performance and enhanced cyclability of the half cell devices assembled using the doped Li-Mn-O film is also discussed in detail.

6.1 Introduction.

As discussed before, the major problem with the spinel $LiMn_2O_4$ cathode is the capacity loss during the cycling. This is the key hurdle which prevents the wider use of $LiMn_2O_4$ as a cathode material for lithium secondary batteries [1-4]. The cyclability of lithium secondary batteries greatly relays on the structural integrity of the host materials during charging and discharging processes. $LiMn_2O_4$ has a cubic spinel structure with space group symmetry Fd3m. The extraction/insertion of lithium ions from/into the $Li[Mn_2]O_4$ spinel framework occurs in two distinct steps. The lithium extraction/insertion from/into the 8a tetrahedral sites occur at around 4V with the maintenance of the initial cubic spinel symmetry. The extraction/insertion from/into the 16c octahedral sites occurs at around 3V by a two phase mechanism involving the cubic spinel $Li[Mn_2]O_4$ and tetragonal lithiated spinel $Li_2[Mn_2]O_4$. Although both mechanisms involve the same $Mn^{3+/4+}$ couple, the 1V difference between the two processes is a reflection of the difference in the site energies.

The cubic to tetragonal transition on going from $Li[Mn_2]O_4$ to $Li_2[Mn_2]O_4$ is due to the Jahn-Teller distortion associated with the single electron in the e_g orbitals of the high spin Mn^{3+}:$3d^4(t^3_{2g}e^1_g)$ ion. The cubic to tetragonal transition is accompanied by a 16% increase in c/a ratio and 6.5% increase in the unit cell volume. This change is too severe for the electrodes to maintain the structural integrity during the charge discharge cycling process. This has been considered as one of the important causes for the fading of capacity at room temperature. This aspect restricts the use of $LiMn_2O_4$ to the 4V region (i.e. 4.2 -3.2V) with a limited capacity of 120mAh.

Even with the operation around 4V, the $LiMn_2O_4$ exhibits capacity fading especially at slightly elevated temperatures (50^oC) above room temperature. The factors such as Jahn Teller distortion occurring on the surface of the particles under conditions of non equilibrium cycling, manganese dissolution in to the electrolyte, formation of two cubic faces in 4V region and the loss of crystallinity and development of micro-strain during cycling process have been suggested to be the sources of the capacity fading.

In order to improve the cycle performance of the Li-ion batteries with Li-Mn-O spinel cathode, several research groups have investigated the prospects of metal substituted Li-Me-Mn-O compounds (Me = Al, Cr, Ga, Ti, Ge, Fe, Co, Zn, Ni, Mg). It has been pointed out that the substitution of metal cations for Mn enhances the stability of the spinel structure, since the average Mn valence increases and the Jahn-Teller distortion gets suppressed.

It is generally accepted that the metal cation doped stoichiometric Li-Mn-O compounds have the common formula Li_{8a} $[Me_yMn_{2-y}]16_dO_4$, and possess a cubic spinel structure. The doped metal ions substitute the manganese ions on the octahedral 16*d* sites, and the lithium ions keep the tetrahedral 8*a* location.

In this chapter a detailed discussion about the effect of doping, on the structural electrical and electrochemical characteristics of the Li-Mn-O film is given. In the present work, Zn and Ni are used dopants for the $LiMn_2O_4$ cathode materials.

Zinc and nickel have been chosen as dopants because of their comparable atomic radius with the manganese atom. The use of Zn and Ni as dopants in $LiMn_2O_4$ electrode is beneficial in stabilizing the structural changes, because the Ni and Zn ions increase the average ionic valance of the Mn and together with lithium ions maintain the interlayer distance. Moreover, Zn and Ni are cheaper and less toxic than several other transition elements.

There are many reports of using Ni and Zn as substitution elements for the structural stability of $LiMn_2O_4$, by introducing around 25-30% of the substitution elements. However the effect of using Zn and Ni as dopants by introducing only 2.5-3% of these elements in to the host $LiMn_2O_4$ material has not been investigated in depth. The present work is an attempt to maintain the structural integrity of $LiMn_2O_4$ spinel phase by the low concentration doping of Zn and Ni.

The results of the detailed characterization studies carried out on Zn and Ni doped Li-Mn-O films deposited under the optimized conditions as described in chapter 4 and 5 are given in the following sections.

6.2 Characterization of Li-Mn-O films doped with Zinc (Zn).

The Zn doped Li-Mn-O films were deposited at 0.005mbar pressure with (-25V) and without (0V) substrate bias. The films deposited without bias were annealed at 700℃ and the films deposited with -25V substrate biaswere annealed at 500℃. These annealing temperatures were selected as per the results given in chapters 4 and 5 and were identified as the optimum annealing temperatures for achieving the best structural, electrical and electrochemical film characteristics.

6.2.1 Chemical composition.

The atomic emission spectroscopy was used to determine the elemental composition of the films. The chemical composition of the Zn doped Li-Mn-O films with and without substrate bias is shown in Table 6.1.

Table 6.1: Chemical composition of the Zn doped Li-Mn-O films

Substrate Bias (V)	Li	Mn	Zn
0V	1.03	2	0.049
-25V	0.98	2	0.047

6.2.2 X-ray diffraction studies.

The structural properties of the Zn doped Li-Mn-O films were studied by X-ray diffraction technique. The XRD patterns of the Zn doped and annealed Li-Mn-O thin films are shown in figure 6.1. The XRD patterns of Zn doped spinel Li-Mn-O films show that only the cubic spinel phase with a space group Fd3m is present and all the peak positions are in good agreement with the standard spectrum of $LiMn_2O_4$. For both the film samples (with and without bias), the most prominent peak corresponds to the reflection from the (111) plane. Apart from this, there are five other peaks corresponding to the reflections from (311), (222), (331), (400) and (511) planes. The peaks marked as ‘SS’ belong to those of the stainless steel substrate.

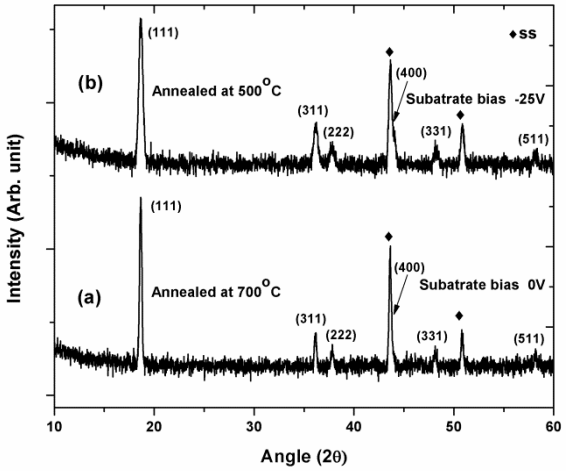

Fig. 6.1:XRD patterns of the Zn doped Li-Mn-O thin films deposited at sputtering pressure of 0.005mbar and (a) with substrate bias 0V and annealed at 700^{o}C and (b) with substrate bias of -25Vand annealed at 500^{o}C

The summary of the XRD data is shown in table 6.2.

Table 6.2: The lattice constants and the full width at half maximum (FWHM) of Zn doped Li-Mn-O films.

Substrate Bias (V)	Post annealing temperature (^{o}C)	a (Å)	FWHM (111) plane
0	700	8.2324	0.276
-25	500	8.2258	0.472

In figure 6.1, no peaks of Zn related materials have been detected. It is also observed that the diffraction lines are shifted slightly towards higher angles with Zn substitution, indicating a smaller lattice parameter for the Zn-doped films. The decreased lattice parameter of Zn doped Li-Mn-O films may be a consequence of the increased concentration of Mn^{4+}ions in the spinel structure, which has a much smaller ionic radius (r=0.053nm) thanMn^{3+} (r=0.064nm) [5]. It is well known that the Jahn-Teller distortion of the [MnO_6] octahedron

in$LiMn_2O_4$ is caused by the Mn^{3+}cations at the 16d sites and the decreased amount of Mn^{3+} in $LiMn_2O_4$ can suppress the Jahn-Teller distortion [6-7].

On a comparative study of the XRD patterns of the films deposited with and without substrate bias, it is seen that, the films deposited with substrate bias have lower cell parameter compared to the films deposited without substrate bias. The FWHM of the XRD peaks also shows a significant difference, which may be due to the difference in grain size of the films deposited with and without substrate bias. The decrease in cell parameter in the films deposited with substrate bias can be attributed to the comparatively higher strain in the films.

6.2.3 Surface morphology studies.

The surface topography of Zn doped Li-Mn-O films was investigated by scanning electron microscopy technique and the images are shown in figure 6.2.

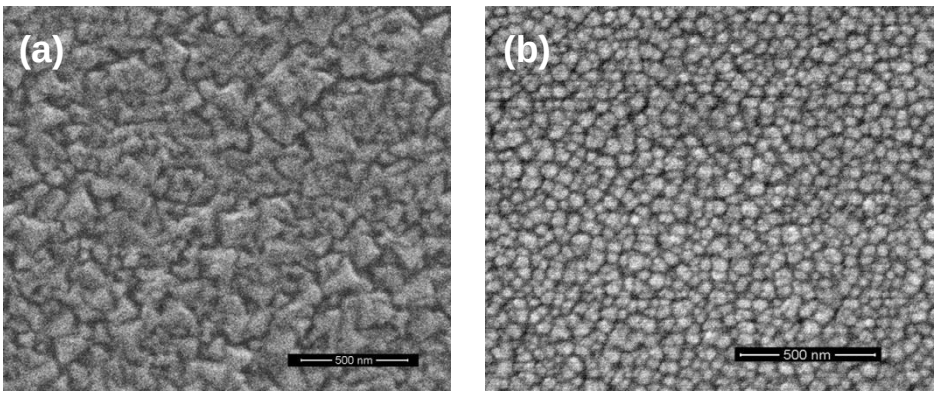

Fig. 6.2: Scanning electron micrographs of the Zn doped Li-Mn-O thin films deposited with sputtering pressure of 0.005mbar and (a) with substrate bias 0V and annealed at 700°C and (b) with substrate bias of -25Vand annealed at 500°C.

The surface morphology of Zn doped Li-Mn-O films indicates that films deposited without bias (0V) and annealed at 700°C have a multi faced polycrystalline flake-like topography. The surface morphology of the films

deposited with bias voltage of -25V and annealed at 500°C is almost homogeneous with regular and round grains of approximately 80 nm average diameter and the surface is devoid of any cracks.

6.2.4 Raman spectroscopy studies.

The micro-Raman spectra of Zn doped Li-Mn-O films are shown in figure 6.3.The Raman spectrum shows a broad band at around 628cm^{-1}, and a few weak bands at 482, 354 and 296 cm^{-1}. The broad band at around 628 cm^{-1} is accompanied by a small band at around 585 cm^{-1}. These bands are closely related to the [MnO_6] octahedron and the Mn oxidation state, and are assigned as the A^1_g and F^1_{2g} modes, respectively. The F^1_{2g} shoulder originates mainly from the vibration of the Mn^{4+}-O bond and in the case of the Zn doped films it is sharper and resolved compared to the pristine Li-Mn-O films [8].

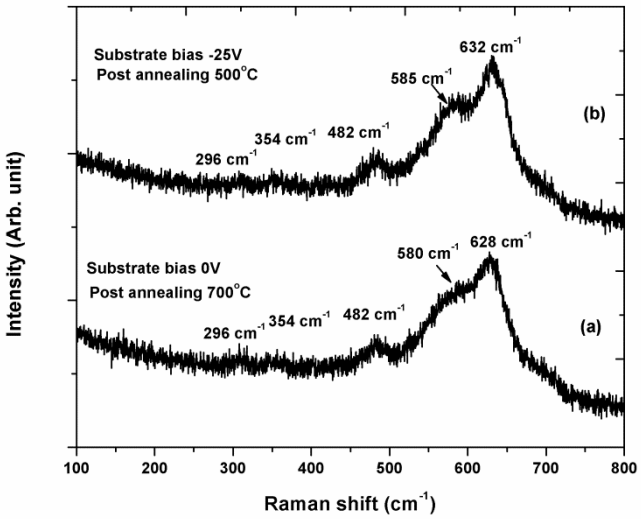

Fig. 6.3: Raman spectra of the Zn doped Li-Mn-O thin films deposited at sputtering pressure of 0.005mbar and (a) with substrate bias 0V and annealed at 700°C and (b) with substrate bias of -25Vand annealed at 500°C

In general, Raman features corresponding to the Zn^{2+}/Mn^{4+}cation ordering are not well resolved for Zn doped Li-Mn-O films, possibly because of the low level of Zn doping. Moreover, there is apparently not much difference in the Raman spectra of the Li-Mn-O films deposited with and without substrate bias.

6.2.5 DC conductivity studies.

The temperature dependence of the dc electrical conductivity of the Zn doped Li-Mn-O films is shown as Arrhenius plots in figure 6.4.The conductivity measurements of the Zn doped Li-Mn-O films were carried out at various temperatures between 25 and 100°C. The temperature dependence of electrical conductivity of the Zn doped Li-Mn-O films exhibits a semiconductor behavior, which can be well described by a typical thermal activation model satisfying Arrhenius equation.

The Arrhenius plot between ln(σ) and 1000/T shows a straight line behavior for the Zn doped films and more importantly all the conductivity values perfectly fit in to the straight line. This behavior is different from that of the pristine Li-Mn-O films, where the lower temperature conductivity values are found to be slightly deviated from the straight line. This behavior can be attributed to the phase transition, induced by Jahn-Teller effect around room temperature [9, 10], as explained in section 4.2.8.

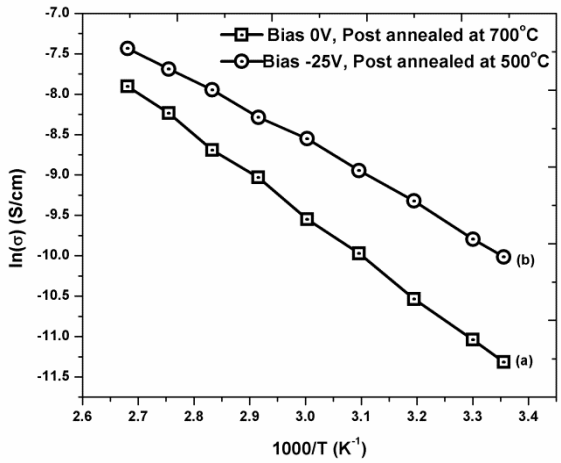

Fig. 6.4: Arrhenius plots showing the temperature dependence of the dc electrical conductivity of Zn doped Li-Mn-O thin films deposited (a) with substrate bias 0V and annealed at 700°C and (b) with substrate bias of -25Vand annealed at 500°C.

In Zn doped Li-Mn-O films it can be assumed that Jahn-Teller effect is somewhat suppressed, which is very important for the stability and good

cyclability of the cathode material. The results of electrical conductivity studies of Zn doped Li-Mn-O films are summarized in table 6.3.

Table 6.3: Results of electrical conductivity studies of Zn doped Li-Mn-O films deposited with and without substrate bias.

Substrate Bias (V)	Annealing temperature ℃	Room temperature conductivity S/cm	Activation energy eV
0V	700	1.22×10^{-5}	0.44
-25V	500	4.48×10^{-5}	0.33

The present investigations show that the room temperature conductivity of Zn doped Li-Mn-O film is slightly less than that of the conductivity of the pristine Li-Mn-O films. This could be due to the unequal 16d site occupancy of Mn^{3+} and Mn^{4+}ions in Zn doped Li-Mn-O films, which decreases the electron hopping rate between the cations, and could not be fully compensated by the Zn cations[11].

6.2.6 Cyclic voltammetry studies.

Cyclicvoltammetry experiments were carried out on Zn doped Li-Mn-O films at a voltage scan speed of 0.1mV/s and the CV curves are shown in figure 6.5. Cyclic voltammogram of Zn doped Li-Mn-O films shows two well-resolved peaks centered at 4.05V/4.188V (oxidation peaks) and 4.106V/3.955V (reduction peaks), which correspond to theMn^{3+}/Mn^{4+} redox couple. The different potentials associated with the two oxidation/reduction peaks are attributed to the different lithium content in $Li_{\delta}Mn_2O_4$ below and above δ = 0.5,due to the disorder-order phase transitions of Li+ at the tetrahedral sites [12,13].

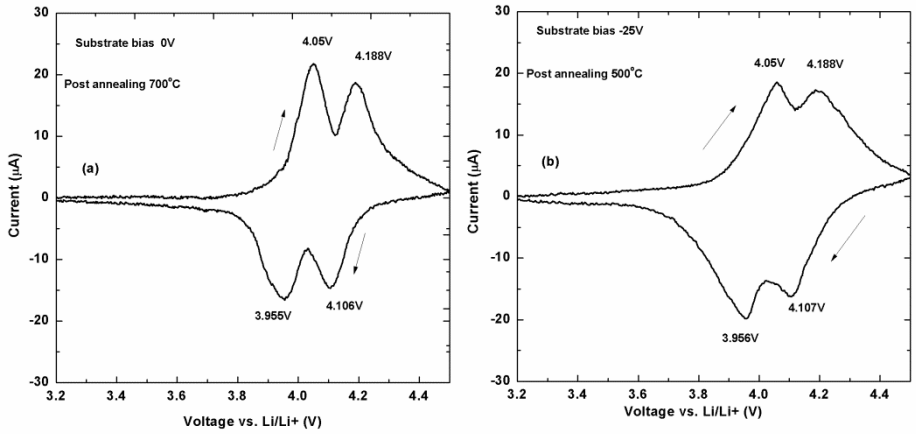

Fig. 6.5: Cyclic voltammograms of the Zn doped Li-Mn-O thin films deposited (a) with substrate bias 0V and annealed at 700^{o}C and (b) with substrate bias of -25Vand annealed at 500^{o}C

It is clear from the CV curve that, with the doping of Zn, the sweeping area of the Mn^{3+}/Mn^{4+} redox couple is reduced compared to pristine Li-Mn-O. Moreover it is also observable that the lower voltage oxidation peak and lower voltage reduction peak positions remain almost unchanged in comparison with pristine Li-Mn-O films. However the higher voltage oxidation and reduction peak positions are shifted to higher voltages. This could be because of the high voltage behavior of the Zn doped films. It is also apparent that all the Zn doped films show electrochemical activity almost upto 4.5V while the pristine films show activity only up to 4.3V.

6.2.7 Charge discharge cycling studies.

The charge discharge curves of the Zn doped Li-Mn-O films were obtained at a constant current of 5μA and are shown in figure 6.6. The charge discharge curve of the Zn doped Li-Mn-O films shows two distinctive voltage plateaus, located at 4.1V and 4V respectively, which is the basic characteristic of the spinel $LiMn_2O_4$ cathode material. Moreover, there is a steep curve between 4.5 and 4.1V, which may probably be due to high voltage behavior as a result of Zn doping [14].

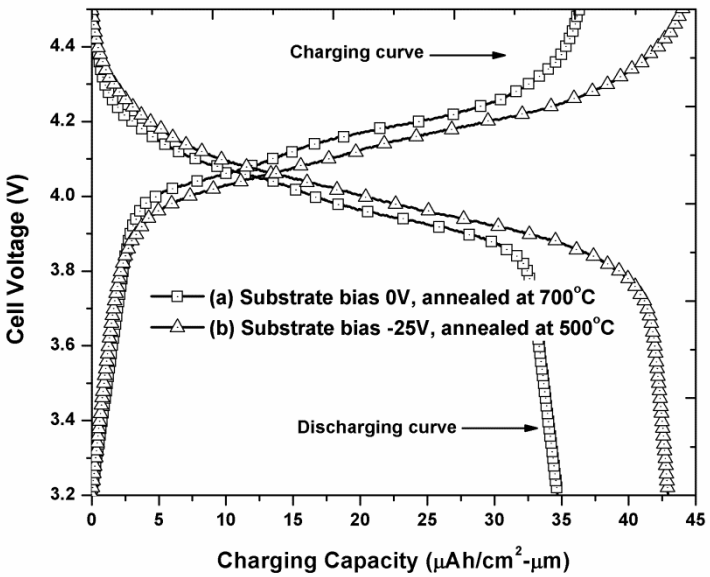

Fig. 6.6: Charge discharge curves of the Zn doped Li-Mn-O thin films deposited with sputtering pressure of 0.005mbar and (a) with substrate bias 0V and annealed at 700°C and (b) with substrate bias of -25Vand annealed at 500°C

It is observed that the discharge capacity of Zn doped films is slightly less than that of the pristine Li-Mn-O films. The doped films show only 93% of the capacity of the pristine films. This behavior is similar in both the Zn doped films, deposited with and without substrate bias. A decrease in Mn^{3+}concentration as a result of Zn doping can be a possible reason for this behavior [15]. The formation of a primitive cubic structure from the FCC spinel as suggested by Y. Ein-Eli *et al*[14] has also been cited as another possible reason. However the XRD data does not show any evidence for the existence of this phase.

The films deposited without substrate bias and annealed at 700°C show an initial charge capacity of 36.32 μAh $cm^{-2}\mu m^{-1}$and discharge capacity of 34.7 μAh $cm^{-2}\mu m^{-1}$and the films deposited with substrate bias (-25V) and annealed at 500°C show a charge capacity of 44.0μAh $cm^{-2}\mu m^{-1}$and discharge capacity of 42.9μAh $cm^{-2}\mu m^{-1}$. The large difference in capacity between the films deposited with and without bias voltage can be attributed to the possible contamination of

Li-Mn-O films by the thermal diffusion of iron and chromium from the stainless steel substrate material, during annealing above 500°C, as explained in section4.3.3.

6.2.8 Cycle performance studies.

The cycling studies of the Zn doped Li-Mn-O films were carried out between 3.2 and 4.5V with a constant charging and discharging current of 5μA for about 20 cycles and the curves are shown in figure 6.7. It is observed that Zn doping considerably improves the capacity retention of the Li-Mn-O films. This result holds for the films deposited with and without substrate bias.

In the case of the films deposited without substrate bias and annealed at 700°C, the capacity decay is 0.13% per cycle and the discharge capacity after 20 cycles is almost 97% of the initial capacity. For the films deposited with substrate bias (-25V) and annealed at 500°C the capacity decay is 0.19% per cycle and the discharge capacity after 20 cycles is almost 96% of the initial capacity.

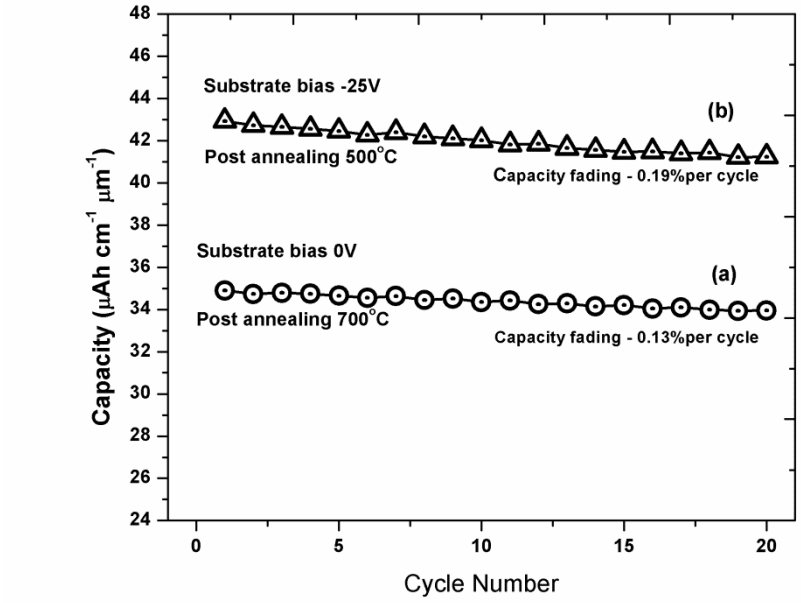

Fig. 6.7: Cycle performance of the Zn doped Li-Mn-O thin films deposited (a) without substrate bias (0V) and annealed at 700°C and (b) with substrate bias of-25Vand annealed at 500°C

Table 6.4: Summary of the charge/discharge cycling studies on Zn doped Li-Mn-O films deposited with and without substrate bias.

Substrate Bias (V)	Annealing temperature (^oC)	Initial charge capacity ($\mu Ah\ cm^{-2}\mu m^{-1}$)	Initial discharge capacity ($\mu Ah\ cm^{-2}\mu m^{-1}$)	Capacity fading	Colu eff.
0	700	36.32	34.7	0.13	98
-25	500	44	42.9	0.19	98.6

The improvement in cycle performance of Zn doped Li-Mn-O films can be attributed to the structural stability of the doped spinel, resulting from the suppression of the Jahn-Teller distortion and the creation of stronger Mn(Zn)-O bonds as Mn ions are substituted by Zn ions. Upon Zn doping, the concentration of the redox species $Mn^{3+}$of modified $LiMn_2O_4$ decreases, which results in the decrease of the maximum discharge capacity. However, $LiZn_xMn_{2-x}O_4$ solid solution formed on the surface of the spinel $LiMn_2O_4$ particles, stabilizes the spinel structure[16]. The manganese ions in $LiMn_2O_4$ are in two oxidation states, consisting of 50% Mn^{3+} and 50% Mn^{4+}. When the amount of Mn^{3+} is more than 50%, the spinel $LiMn_2O_4$ is susceptible to Jahn–Teller distortion [17]. During the discharge process at high rates, the diffusion rate of lithium ions in electrolyte solution is much rapid than that of Li ions inside the spinel $LiMn_2O_4$ [18].As a result of this, a non-equilibrium dynamic condition occurs, in which lithium ions heap on the surface of spinel $LiMn_2O_4$ particles resulting in Mn^{3+}rich region, which induces Jahn–Teller distortion. The Zn doping almost eliminates Jahn–Teller distortion by stabilizing the spinel structure as a result of the decrease in the concentration of Mn^{3+} ions [19].

6.3 Characterization of Li-Mn-O films doped with Nickel (Ni).

Similar to the Zn doped films, the Ni doped Li-Mn-O films were deposited at 0.005mbar pressure with substrate bias voltage of 0V (i.e. without substrate bias) and -25V. The films deposited without substrate bias were annealed at 700°C and films deposited with substrate bias of -25V were annealed at 500°C.

6.3.1 Chemical composition.

The atomic emission (ICP-AES) spectroscopy was used to determine the elemental composition of the Ni doped Li-Mn-O films deposited with and without substrate bias and the results are shown in table 6.5.

Table 6.5: Chemical composition of the Ni doped Li-Mn-O films

Substrate Bias (V)	Li	Mn	Ni
0V	1.02	1.947	0.048
-25V	0.98	1.946	0.047

6.3.2 X-ray diffraction studies.

The structural properties of the Ni doped Li-Mn-O films were studied by X-ray diffraction technique. The XRD patterns of the Ni doped and annealed Li-Mn-O thin films are shown in figure 6.8.

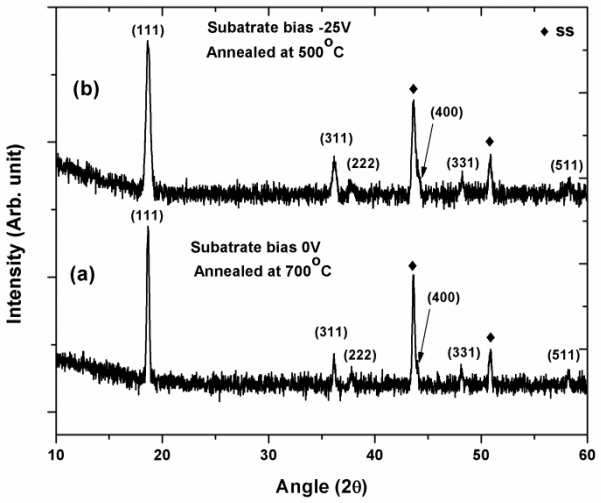

Fig. 6.8: The XRD patterns of the Ni doped Li-Mn-O thin films deposited at sputtering pressure of 0.005mbar and (a) with substrate bias 0V and annealed at 700^{o}C and (b) with substrate bias of -25Vand annealed at 500^{o}C

The XRD patterns of Ni doped Li-Mn-O films correspond to an ordered cubic spinel structure with space group Fd3m and none of the secondary phase or impurity phases are detected. The most prominent diffraction peak is the line corresponding to the (111) plane. Apart from this, there are five other peaks corresponding to the reflections from, (311), (222), (331), (400) and (511) planes. The peaks marked as 'SS' belong to those of the stainless steel substrate.

One of the main observations with the XRD pattern is the slight shifting of the diffraction lines towards higher diffraction angles with Ni substitution, indicating a smaller lattice parameter for the Ni-doped films compared to the un-doped films. The calculated lattice parameters of the Ni doped films are shown in table 6.6.

Table 6.6: The lattice constants and the full width at half maximum (FWHM) of the XRD peaks of Ni doped Li-Mn-O films deposited with and without substrate bias.

Substrate Bias (V)	Post annealing temperature (°C)	a (Å)	FWHM (111) plane
0	700	8.2323	0.28
-25	500	8.2258	0.468

The decreased lattice parameter of Ni doped Li-Mn-O films may be due to the increased concentration of Mn^{4+} in the spinel structure, which has a much smaller ionic radius (r=0.053nm) thanMn^{3+} (r=0.064nm) [5].The Jahn-Teller distortion of the [MnO_6] octahedron in$LiMn_2O_4$ is caused by the Mn^{3+}cations at the 16d sites and the decrease in the concentration of Mn^{3+} in $LiMn_2O_4$can suppress the Jahn-Teller distortion [6, 7, 14]

It is clear from table 6.6, that the films deposited with and without substrate bias show a difference in the values of lattice parameter. The films deposited with substrate bias have lower cell parameter compared to the films deposited without substrate bias. The decrease in cell parameter in the films deposited

with substrate bias is due to the comparatively higher strain in the films. The FWHM of the XRD peaks also shows a significant difference, as in the case of Zn doped samples, which can be attributed to the difference in grain size of the films deposited with and without substrate bias.

6.3.3 Surface morphology studies.

The surface morphology of Ni doped Li-Mn-O films was investigated by scanning electron microscopy technique and the images are shown in figure 6.9.The films deposited without (0V) bias and annealed at 700°C exhibit a multi faced polycrystalline flake-like topography. For the films deposited with substrate bias and annealed at 500°C, a homogeneous surface with regular and round grains of approximately 80 nm average diameter is observed, which is devoid of any cracks.

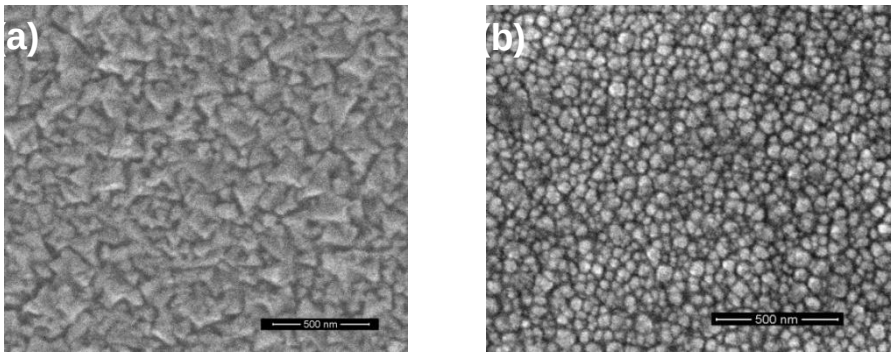

Fig. 6.9: Scanning electron micrographs of the Ni doped Li-Mn-O thin films deposited with sputtering pressure of 0.005mbar and (a) with substrate bias 0V and annealed at 700°C and (b) with substrate bias of -25Vand annealed at 500°C.

6.3.4 Raman spectroscopy studies.

The micro-Raman spectra of Ni doped Li-Mn-O films are shown in figure 6.10. The Raman spectra of the Ni doped Li-Mn-O films (with and without substrate bias) are nearly identical with those of Zn doped films. As in the case of Zn doped films the vibrations corresponding to A^1_g and F^1_{2g} modes give rise to the

prominent peaks[8].The spectra do not show any major Raman features corresponding to the Ni^{2+}/Mn^{4+}cationordering for Ni doped Li-Mn-O films, also.

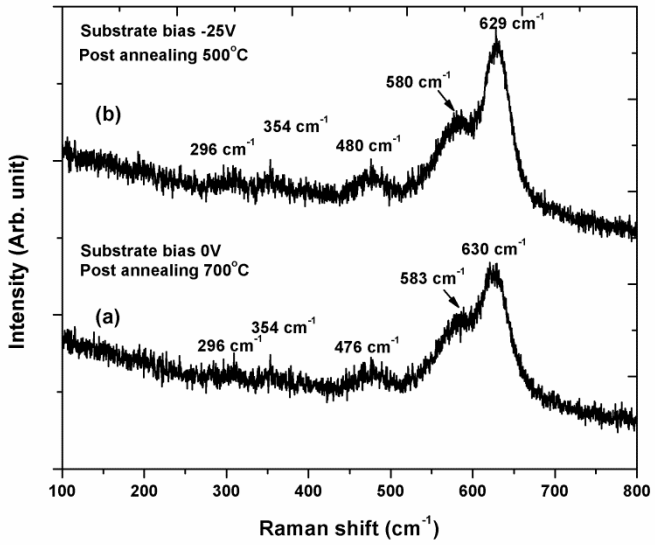

Fig.6.10:Raman spectra of the Ni doped Li-Mn-O thin films deposited with sputtering pressure of 0.005mbar and (a) with substrate bias 0V and annealed at 700°C and (b) with substrate bias of -25Vand annealed at 500°C

6.3.5 DC conductivity studies.

The temperature dependence of the dc electrical conductivity of the Ni doped Li-Mn-O films is shown as Arrhenius plots in figure 6.11. Similar to the pristine Li-Mn-O films, the Ni doped films also show a semiconductor behavior, which can be well fitted to a typical thermal activation model using Arrhenius equation.

The Arrhenius plot between ln(σ) and 1000/T shows a straight line behavior for the Ni doped films and more importantly, all the conductivity values perfectly fit into the straight line, similar to the behavior of Zn doped films. As in the case of Zn doped Li-Mn-O films, Ni doping also suppresses the Jahn-Teller effect, which is very important for the stability and cyclablity of the cathode material.

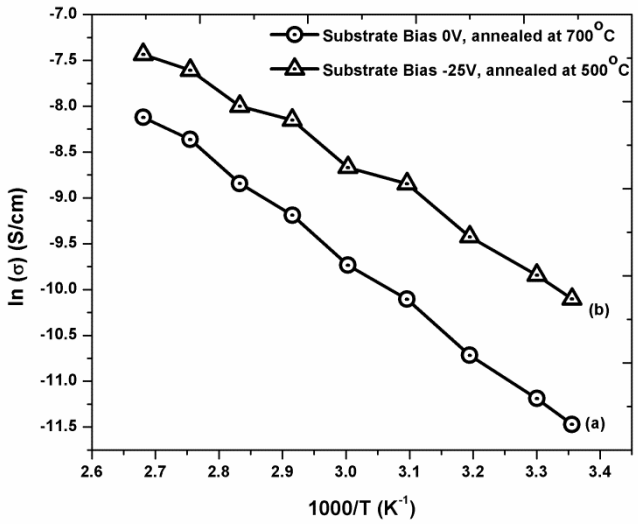

Fig. 6.11: Arrhenius plots showing the temperature dependence of the dc electrical conductivity of the Ni doped Li-Mn-O thin films deposited with sputtering pressure of 0.005mbar and (a) with substrate bias 0V and annealed at 700°C and (b) with substrate bias of -25Vand annealed at 500°C.

The room temperature electrical conductivity of Ni doped Li-Mn-O films is slightly less than the conductivity of the pristine films, similar to Zn doped films. An exactly similar explanation as in the case of Zn doping seems to support this observation [11]. The results of electrical conductivity studies of Ni doped Li-Mn-O films are summarized in table 6.7.

Table 6.7: Results of electrical conductivity studies of Ni doped Li-Mn-O films deposited with and without substrate bias.

Substrate Bias (V)	Annealing temperature ^{o}C	Room temperature conductivity S/cm	Activation energy eV
0V	700	1.04×10^{-5}	0.44
-25V	500	4.09×10^{-5}	0.34

6.3.6 Cyclic voltammetry studies.

Cyclicvoltammetry experiments were carried out on Ni doped Li-Mn-O films at a voltage scan speed of 0.1mV/s and the CV curves are shown in figure 6.12. Cyclic voltammogram of Ni doped Li-Mn-O films shows two well-resolved current peaks centered at4.05 V/4.195V (oxidation peaks) and 4.105 V/3.956V (reduction peaks), which correspond to theMn^{3+}/Mn^{4+} redox couple. [12, 13].The CV curves of Ni doped Li-Mn-O films show characteristics almost identical to those of Zn doped films.

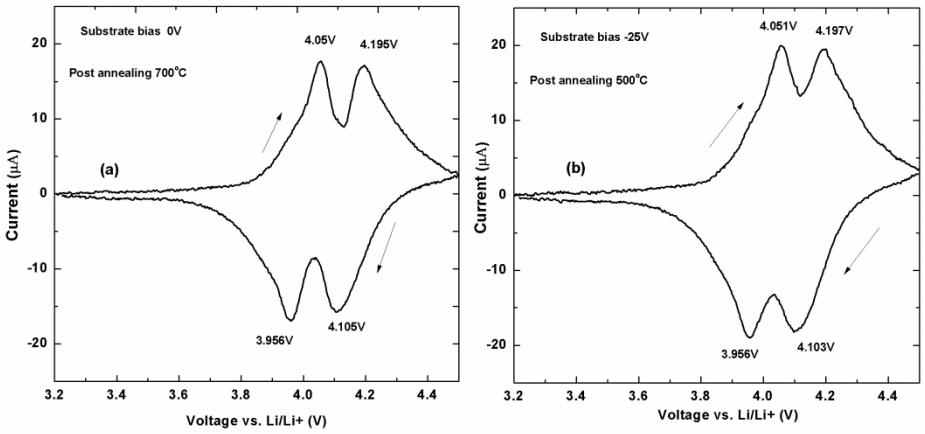

Fig. 6.12: Cyclic voltammograms of the Ni doped Li-Mn-O thin films deposited at sputtering pressure of 0.005mbar and (a) with substrate bias 0V and annealed at 700°C and (b) with substrate bias of -25Vand annealed at 500°C.

As in the case of Zn doping, the area of the CV curve is reduced in the case of Ni doping as well indicating a reduction in capacity. It is also observed that all the Ni doped films show electrochemical activity almost upto 4.5V while the pristine films show activity only up to 4.3V, similar to the case of Zn doped films.

6.3.7 Charge discharge studies.

The charge discharge curves of the Ni doped Li-Mn-O films were obtained at a constant current of 5μA and are shown in figure 6.13. As in the case of Zn doped films, the charge discharge curve of the Ni doped Li-Mn-O films shows

two distinctive voltage plateaus located at 4.1V and 4V respectively. There is also a steep curve between 4.5 and 4.1V, probably due to the high voltage behavior of the Ni doped films, which is exactly similar to the behavior of the Zn doped samples [14, 15]

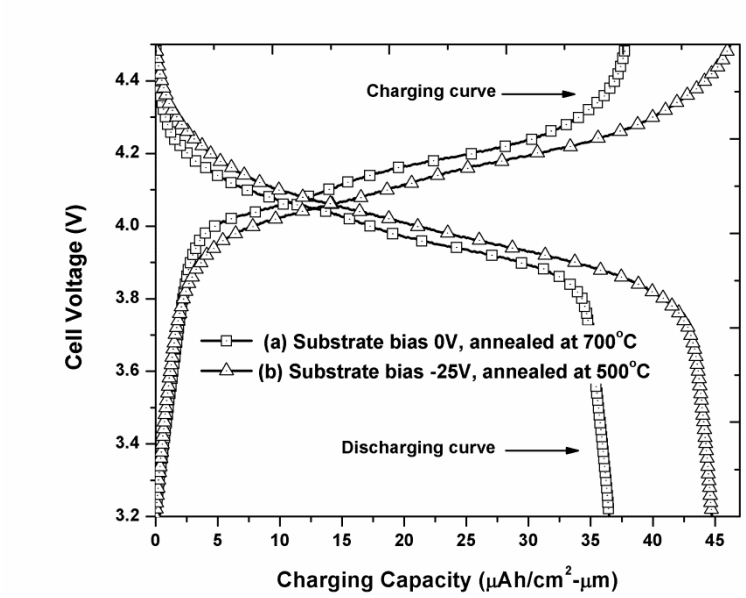

Fig. 6.13: Charge discharge curves of the Ni doped Li-Mn-O thin films deposited at sputtering pressure of 0.005mbar and (a) with substrate bias 0V and annealed at 700°C and (b) with substrate bias of -25Vand annealed at 500°C

The films deposited without substrate bias and annealed at 700°C show an initial charge capacity of 37.87 μAh $cm^{-2}\mu m^{-1}$and discharge capacity of 36.5 μAh $cm^{-2}\mu m^{-1}$and the films deposited with substrate bias (-25V) and annealed at 500°C show an initial charge capacity of 46.26 μAh $cm^{-2}\mu m^{-1}$and discharge capacity of 44.75μAh $cm^{-2}\mu m^{-1}$.

The significant difference in capacity between the films deposited with and without bias voltage is a consequence of the possible contamination of the Li-Mn-O films by the thermal diffusion of iron and chromium from the stainless steel substrate material, during annealing above 500°C, as explained in the case of Zn doped films.

6.3.8 Cycle performance studies.

The cycling studies of the Ni doped Li-Mn-O films were carried out between 3.2 and 4.5V with a constant charging and discharging current of 5μA for about 20 cycles and the results are shown in figure 6.14.

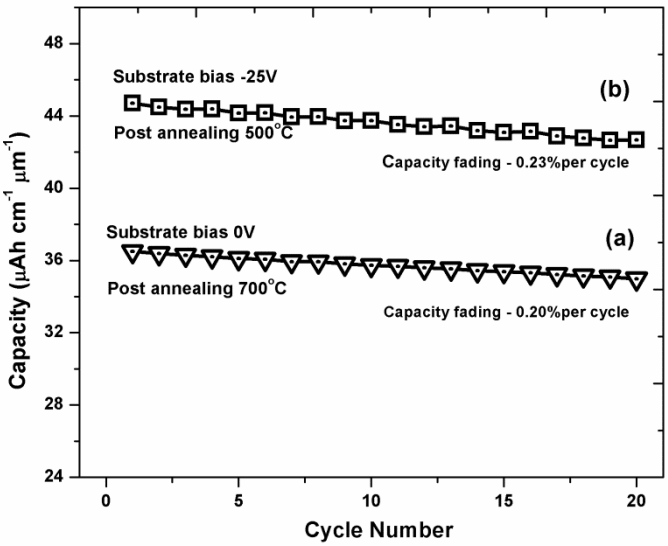

Fig. 6.14: Cycle performance of the Ni doped Li-Mn-O thin films deposited (a) without substrate bias (0V) and annealed at 700°C and (b) with substrate bias of-25Vand annealed at 500°C

As in the case of Zn doped films, Ni doping also improves the capacity retention of the Li-Mn-O films, deposited with and without substrate bias. In the case of the films deposited without substrate bias and annealed at 700°C, the capacity decay is 0.20% per cycle and the discharge capacity after 20 cycles is almost 94% of the initial capacity. For the films deposited with substrate bias (-25V) and annealed at 500°C the capacity decay is 0.23% per cycle and the discharge capacity after 20 cycles is almost 95% of the initial capacity. The improvement in cycle performance of the Ni doped Li-Mn-O films can be analyzed in the way exactly similar to the case of Zn doped films [16].

Summary of the charge/discharge cycling studies on Ni doped Li-Mn-O films deposited with and without substrate bias is given in table 6.8

Table 6.8: Summary of the charge/discharge cycling studies on Ni doped Li-Mn-O films deposited with and without substrate bias.

Substrate Bias (V)	Annealing temperature (^oC)	Initial charge capacity ($\mu Ah\ cm^{-2}\mu m^{-1}$)	Initial discharge capacity ($\mu Ah\ cm^{-2}\mu m^{-1}$)	Capacity fading	Colu eff.
0	700	37.87	36.5	0.20	98.3
-25	500	46.75	44.75	0.23	98.4

6.4 Conclusions.

High frequency (27.12MHz) magnetron sputtering technique was successfully employed to deposit good quality doped, Li-Mn-O films with required doping levels of Zn and Ni. These films were deposited with and without substrate bias and were also post annealed. The structural, electrical and electrochemical characteristics of these doped films are found to be comparable to those of the un-doped films ones with a few exceptions.

The Arrhenius plots of electrical conductivity, between ln(σ) and 1000/T fit in to a straight line for all the Zn and Ni doped films. This behavior is different from that of the pristine Li-Mn-O films, where the lower temperature conductivity values show slight deviations from the straight line due to the phase transition induced by Jahn-Teller effect. It is obvious that for the both the Zn and Ni doped Li-Mn-O films the Jahn-Teller effect is somewhat suppressed, which is very important for the stability and cyclability of the cathode material.

The electrochemical studies of the Zn and Ni doped films with and without substrate bias show slight decrease in capacity compared to the pristine films. It is also observed that the films doped with Zn show lesser capacity compared to the films doped with Ni. The CV curves of both the Zn and Ni doped films show response upto 4.5V compared to the 4.3V of the pristine films. This is a consequence of the possible high voltage behavior of the doped Li-Mn-O films.

The highlight of the present investigations on Zn and Ni doped Li-Mn-O films is the observation that both the Zn and Ni doping can substantially improve the capacity retention of the magnetron sputtered Li-Mn-O cathode films. In the case of pristine Li-Mn-O films deposited with and without substrate bias, the capacity fading per cycle is found to be 0.55% and 0.29% respectively. Upon doping with Zn, the capacitive fading with and without bias, gets reduced to 0.19% and 0.13% respectively. In the case of Ni doping, the capacity fading per cycle for the films deposited with and without bias, is 0.23% and 0.2% respectively. With proper optimization of the doping conditions, it should be possible to achieve excellent capacity retention along with higher capacity for the Zn and Ni doped Li-Mn-O films.

6.5 Reference.

[1] D. Guyomard and J. M. Tarascon, *Solid State Ionics*, **69**, 222 (1994).
[2] D. H. Jang, Y. J. Shin, and S. M. Oh, *J. Electrochem. Soc.*, **143**, 2204 (1996).
[3] M. M. Thackeray, *Prog. Solid State Chem.*, **25**, 1 (1997).
[4] M. M. Thackeray, A. de Kock, M. H. Rossouw, D. Liles, R. Bittihn, and D. Hoge, *J. Electrochem. Soc.*, **139**, 363 (1992).
[5] Wei y J, Nam k W, Kim K B, Chen G. Solid State Ionics, 2006, 177(1): 29−35.
[6] Lee J F, Tsai Y W, Santhanam R, Hwang B J, Yang M H, Liu D G., Journal of Power Sources, 2003, 119/121(6): 721−726.
[7] HE Xiang-ming, LI Jian-jun, CAI Yan, WANG Yao-wu, YING Jie-rong, JIANG Chang-yin, WAN Chun-rong., Journal of Power Sources, 2005, 150(10): 216−222.
[8] P. Strobel, A. Ibarra Palos, M. Anne, C. Poinsignon, A. Crisci, Solid State Sci. 5 (2003) 1009.
[9] J. Rodriguez-Carvajal, G. Rousse, C. Masquelier, M. Hervieu, Phys. Rev. Lett. 81 (1998) 4660.
[10] J. Molenda, K. Swierczek, M. Molenda, J. Marzec, Solid State Ionics 135 (2000) 53.
[11] J. Molenda, J. Marzec, K. ´ Swierczek, D. Pałubiak, W. Ojczyk, M. Ziemnicki, Solid State Ionics, 175 (2004) 297
[12] G. Yuan, J.N Reimers, J.R. Dahn, Phys. Rev. B 54 (1996) 3878.
[13] K.A. Striebel, A. Rougier, C.R. Horne, R.P. Reade, E.J. Cairns, J. Electrochem. Soc. 146 (1999) 339.
[14] Y. Ein-Eli, W. Wen and S. Mukerjee, Electrochemical and Solid-State Letters, 8 (3) (2005) A141.
[15] Park D H, Lim S T, Hwang S J, Choy J H, Choi J H, Choo J. J Power Sources, 2006, 159(2):1346−1352.
[16] Y.W. Tsai, R. Santhanam, B.J. Hwang, S.K. Hu, H.S. Sheu, J. Power Sources 119–121, (2003) 701.
[17] A. Yamada, J. Solid State Chem. 122 (1996) 160.
[18] K.Y. Chung, C.W. Ryu, K.B. Kim, J. Electrochem. Soc. 152 (2005) 791.
[19] Xifei Li, YoulongXu, Chunlei Wang, Applied Surface Science 255 (2009) 5651

Chapter 7

Summary and scope for further studies

Abstract: The conclusions drawn from the present investigations are summarized in this chapter. The significant outcomes of the present study are highlighted. The prospects for further investigations in this direction are also discussed.

7.1 Introduction

One of the most promising methods to power autonomous micro-electronic devices is the use of integrated thin film micro-batteries. In this context, thin film lithium-ion batteries, have garnered a lot of appeal in scientific and technological research, due to their various advantages such as, high cell voltage, high gravimetric and volumetric energy density, lack of memory effects, good thermal stability, low self discharge and absence of possible pollution due to toxic metals and electrolytes. Thin film lithium ion batteries offer higher current densities and cell efficiencies than bulk batteries because of the higher ionic conductivity of thin films. The recent developments in nanoscience and technology have marked significant advancements in miniaturizing the electronic components and devices. There are many devices and gadgets which require power supplies with low power outputs in communication and medical fields, such as implantable medical devices, CMOS-based integrated circuits, anti-theft protection devices, gas sensors, microcoulometers etc. Due to the growing tendency in the microelectronic industry towards complete integration of all functional devices onto a single chip, secondary rechargeable thin film solid state batteries of small dimensions are envisaged to be suitable energy sources. In such applications thin film technology can offer many advantages since it is well adapted to possible device designs and problems such as high interface resistances can be minimized due to the absence of the electrolyte-electrode interfaces.

The thin film lithium ion battery technology is based on the use of suitable lithium intercalation compounds for the electrodes and electrolytes. Among these compounds spinel $LiMn_2O_4$is highly attractive as a cathode material because of its favorable properties such as high specific capacity, high cell voltage and better structural stability. Additionally, it has an advantage in terms of cost as it is abundant in nature and is being perceived as a ‘green’ source of energy as it is non-toxic.

Thin film batteries based on $LiMn_2O_4$ cathode material can be developed by using a variety of techniques among which RF magnetron sputtering is a versatile technique offering the possibilities to micro-fabricate the thin film batteries directly onto chips in any shape or size, and on flexible substrates, with

good capacity and cycle life. However, the deposition of thin film battery layers by RF sputtering is always challenging due the low deposition rates of the individual layers, complexity in the optimization of device quality layers and ultimately the difficulty in attaining electrochemical stability of the device.

The objectives of the present investigations primarily include the optimization of the deposition conditions of magnetron sputtered $LiMn_2O_4$as cathode films for use in thin film lithium ion battery applications. Along with pristine $LiMn_2O_4$ its doped variants have also been investigated in detail. Advanced deposition techniques using high frequency (27.12MHz) magnetron sputtering, and substrate-biased sputtering have been developed to improve the rate of deposition and cyclability of the cathode materials and reduce the required optimum post annealing temperatures for achieving excellent film characteristics.

7.2 Summary and conclusions

Pristine and doped (Zn and Ni) Li-Mn-O films were deposited by using conventional RF excitation frequency as well as high frequency magnetron sputtering technique. Higher rates of deposition have been obtained in sputtered films grown using a 27.12MHz RF excitation source, compared to the films deposited with conventional frequency (13.56MHz) RF source. It seems that higher frequency RF magnetron discharge appreciably improves the nucleation and the rate of growth of the Li-Mn-O films without compromising the quality of the films. It is believed that the beneficial effects of the high discharge frequency can be a consequence of the reduced DC voltage at the target surface, which in turn reduces the energy of reflected argon ions bombarding the growing films. The higher energy of the Ar ions would otherwise lead to defects in the films followed by a disturbed film growth. More investigations are required to conclusively prove the actual mechanism underlining this phenomenon.

The influence of the sputter deposition parameters, especially the deposition pressure and power on the structural, electrical and electrochemical characteristics of the Li-Mn-O films was investigated in detail and the optimum

pressure and power ranges were identified. Additionally, the influence of the in-situ substrate bias on high frequency sputter deposition was investigated for various substrate bias voltages. It was observed that the films deposited without any substrate bias were amorphous, while those deposited with substrate bias were crystalline. Moreover, the structural, electrical and electrochemical characteristics of the films were found to show a strong dependence on the sputtering pressure and bias voltage. It was also observed that with the increase of sputtering pressure and bias voltage, the films had the tendency to show inferior structural, electrical and electrochemical characteristics owing to the lithium deficiency in these films..The lithium deficiency mainly arises due to the re-sputtering of the deposited films by the argon ion bombardment at higher pressures and higher substrate bias voltages. This signifies that, a balanced ion bombardment on the growing film is necessary, in which the energy of the bombarding ions plays a major role in the development of a high quality cathode film.

In general, the properties of the 'as deposited' Li-Mn-O films were found to be inferior. Hence detailed post annealing studies of the films deposited with, and without substrate bias were conducted. The structural studies conducted on the annealed films have shown that, as the annealing temperature increases, the crystallinity also increases. However there is an optimum annealing temperature range, above which the film characteristics tend to be inferior due to the formation of impurity phases. One of the striking results from the annealing studies is that the films grown with substrate bias show superior performance compared to films grown without substrate bias even at comparatively lower annealing temperatures. This signifies that the films grown with substrate bias can significantly reduce the required optimum post annealing temperatures for achieving desired film characteristics, which facilitates the reduction of thermal budget in the manufacturing process.

Even though the electrochemical properties of the films deposited with in-situ substrate bias and annealed at lower temperatures show high capacity, the capacity fading (per cycle) is found to be slightly more than that of the films deposited without substrate bias. The reason for the poor cycle performance is attributed to structural instability of the cathode films during charging and discharging processes. In the case of $LiMn_2O_4$, the structural instability arises

due to the Jahn-Teller distortion, in which the cubic to tetragonal transition occurring at near room temperature results in the distortion of the spinel cubic structure.

In order to improve the capacity retention of these films, Li-Mn-O films were grown with Ni and Zn doping. The doped films show more or less similar characteristics compared to the pristine films. The results of dc electrical conductivity studies carried out on these doped films, deposited with and without in-situ bias show that the doping considerably suppresses the Jahn-Teller distortion and helps in attaining structural stability of the cathode film.

The electrochemical studies of the doped films shows light decrease in capacity compared to the pristine ones. Most importantly, the cycle performance studies of the doped Li-Mn-O films show a significant improvement in the capacity retention, compared to the un-doped films. The reason for the improvement in the cycle performance in doped Li-Mn-O films can be attributed to the structural stability of the doped spinel films, as a result of the suppression of the Jahn-Teller distortion.

7.3 Scope for further investigations.

The outcomes of the present work extend ample scope for further investigations, as every new finding can open the door for additional scientific questions and technical improvements. The present study has demonstrated the advantages of using high frequency RF excitation sources, to obtain good device quality cathode films with higher deposition rates. It is believed that there is still room to improve the rate of sputtering by using VHF (Very High Frequency) excitation sources with frequencies40MHz and 60 MHz It may also be possible to further enhance the capacity of the devices by understanding the characteristics of the VHF plasma. Moreover, using the VHF sputtering process, the deposition conditions of the solid electrolyte layer and the anode layer also need to be optimized. Another important point is to reduce the post annealing temperature, as observed in the biased sputtering studies. In this regard it is proposed to deposit films with an ion assisted sputtering process (which is superior and highly controllable compared to simple substrate bias technique)

by which it is possible to precisely control the properties of the films without lithium deficiency. It is believed that the ion assisted sputter deposition can improve the crystallinity of the films significantly, there by considerably reducing the required high post annealing temperatures.